INVESTIGATIONS OF METAL AND METAL–ORGANIC BILAYER NANOSTRUCTURES EMPLOYING ATOMIC FORCE MICROSCOPY AND RELATED TECHNIQUES

A Thesis

Submitted for the Degree of

Doctor of Philosophy

By

Neena Susan John

Chemistry and Physics of Materials Unit

JAWAHARLAL NEHRU CENTRE FOR ADVANCED SCIENTIFIC RESEARCH

(A Deemed University)

BANGALORE, INDIA

March 2007

Dedicated to my

parents & sisters

DECLARATION

I hereby declare that this thesis entitled **"INVESTIGATIONS OF METAL AND METAL–ORGANIC BILAYER NANOSTRUCTURES EMPLOYING ATOMIC FORCE MICROSCOPY AND RELATED TECHNIQUES"** is an authentic record of research work carried out by me under the supervision of ***Prof. G. U. Kulkarni*** at the Chemistry and Physics of Materials Unit, Jawaharlal Nehru Centre for Advanced Scientific Research, Bangalore, India, and it has not been submitted elsewhere for the award of any degree or diploma.

In keeping with the general practice of reporting scientific observations, due acknowledgement has been made whenever work described here has been based on the findings of other investigators. Any omission that might have occurred due to oversight or error in judgement, is regretted.

Neena Susan John

CERTIFICATE

Certified that the work described in this thesis entitled **"INVESTIGATIONS OF METAL AND METAL–ORGANIC BILAYER NANOSTRUCTURES EMPLOYING ATOMIC FORCE MICROSCOPY AND RELATED TECHNIQUES"** has been carried out by **Neena Susan John**, under my supervision at the Chemistry and Physics of Materials Unit, Jawaharlal Nehru Centre for Advanced Scientific Research, Bangalore, India.

Prof. G. U. Kulkarni
(Research Supervisor)

Acknowledgements

I express my heartfelt gratitude to my research supervisor, Prof. G. U. Kulkarni for his invaluable guidance and constant encouragement. I am extremely grateful to him for suggesting the research projects as well as propelling it in the right direction. His optimistic and imaginative approach in scientific research is awe-inspiring. I am indebted to him for the acquired skills in several instrumental techniques. His methodical approach with the instruments and his creative ideas have helped in the efficient use of them. I also thank him for his care and concern in my personal matters. We were always welcome at home at any point of time for discussions. I thank Mrs. Indira Kulkarni for her warmth and hospitality.

I am grateful to the chairman of CPMU, Prof. C. N. R. Rao, FRS for his constant support and encouragement in various ways. He has been a source of inspiration to all of us with his boundless enthusiasm, up-to date knowledge, dedication and commitment to science. I am thankful to him for the opportunities to collaborate with him. I thank Mrs. Rao for her affection and hospitality.

I express my sincere thanks to various collaborators during my research work, Prof. Swapan K. Pati and Dr. Ayan Datta (TSU, JNCASR), Prof. Milan K. Sanyal and Dr. Sudipta Pal (Saha Institute, Kolkata), Prof. Rama Govindarajan, Manikandan, Ratul (EMU, JNCASR), Dr. N. Chandrabhas & G. Kavitha (CPMU, JNCASR). Special note of thanks to Prof. Pati & Ayan for many useful discussions and readiness to help.

It's a pleasure to thank Dr. Stefan Heun and Prof. Lucia Sorba (TASC-INFM, Trieste) for hosting me in Italy and for helpful discussions and suggestions. I am also grateful to Dr. Luca Gavioli, Dr. Mattia, Dr. Iskander & Emmanuele (Università Cattolica, Brescia) for help with AES measurements. I thank Mattia, Iskander, Emmanuel and Michele for their valuable help and company. Support from Indo-Italian Scientific cooperation programme is acknowledged. I am equally thankful to Prof. F. Komori (university of Tokyo) for SQUID measurements.

I thank all the faculty members of CPMU for their cordiality, especially my teachers, Profs. K. S. Narayan, N. Chandrabhas, S. Natarajan, Dr. A. R. Raju for courses. Thanks to Dr. Govindaraj for various helps. I thank Profs. A. G. Menon, Ashokan (IISC) for course work. I express my thanks to Dr. G. V. Shivashankar, Feroz & Aprotim (NCBS, Bangalore) and Dr. Venkataraman & O. V. S. N. Moorthy (IISc, Physics Dept.) for assistance in various measurements. I thank Dr. George Thomas (RRL, TVM) for his timely advice and suggestions.

I would like to thank all of my teachers, who have guided me till now, especially Profs of CUSAT, Sugunan sir, Pratapan sir, Kurup sir, Yusuff sir and Nalini teacher who have prompted me to take up research.

I take this opportunity to thank my lab seniors Dr. C. P. Vinod and Vijayalakshmi for introducing me to the various aspects of the surface science lab and equipments and their helpful and friendly mentality.

I express my special thanks to my senior Dr. John Thomas who has helped me immensely with AFM and other experiments. Thanks to him for useful discussions and cheerful company. I thank Dr. Anupama & Dr. Gargi Raina for their care and affection and support during lowly times. I thank Dr. Sudheendra and Dr. Vanita for help in project work. Fruitful collaboration with Dr. Gautam and Dr. Leonard is acknowledged.

I am grateful to my present labmates, Ved, Reji, Vijay & Bhuvana for assistance in experiments, discussions and cheerful atmosphere. Special note of thanks to Selvi for help with laser ablation and optimization that accelerated the femto-cup project.

I thank my past labmates, Dr. Angappane, Ramesh, Girish, Sravani, Dr. Sailaja, for cooperation and friendly atmosphere.

Timely and ready assistance and also friendly attitude from technical staff, Mr. Srinath and Mr. Srinivas is acknowledged. I am very thankful to Mr. Basavaraj (SEM), Mr. Anil (XRD), Mr. Vasu, Mr. Srinivasa Rao (UV), Mr. Arokianathan, Mrs. Usha (TEM), Mr. Shashikiran, Mrs. B. S. Suma (confocal) for their invaluable technical assistance.

I thank the staff of academic and administrative section in JNC for their assistance. I also thank the library staff for their help. I am thankful to the staff of the computer lab, Shithal, Masanam, Vikas, for computer lab assistance.

Financial assistance from Council of Scientific and Industrial Research (CSIR), JNCASR and DST is acknowledged.

I thank Reji, Neenu, Lakshmi, Vivek, Asish Kundu, N. Vinod, Sameen, Selvi, Kalyani, Nimmi, Gomathi, Harish, Raja, Kavitha G, Behera, Meenakshi, Rinki, Manoj, Ujjal, Moumita G for a memorable and joyous JNC life.

I also thank my friends in JNCASR, Dash, Pearl, Dhanasree, Pushpa, Thiru, Motin, Bhat, Chandu, Pavan, Gayathri, Shailaja, Kapoor, Ram, Srilekha, Kavitha Siva, Shoba, Keerti, Parvati, Nidhina, Arati, Soumya and Gargi Dutta.

I thank Daly, Raji, Manju, Seba, Swaroop & Cherry for their invaluable friendship. I also thank my M.Sc and B.Sc batchmates, Radhu, Ish, Sanu, Regi, Srikant, Betty, Mily for moral support and encouragement.

There are no words to express my gratitude to Chachan & Amma, my sisters Maemol, Sheena, Mini & their families, whose endearing support, love and prayers have made this thesis a reality. This thesis is dedicated to them.

Preface

The thesis pertains to investigations on metal and metal-organic bilayer nanostructures employing atomic force microscopy and related techniques. It is organized into six chapters. **Chapter 1** introduces the concept of nanoscale materials, their important properties and atomic force microscopy as an enabling tool for the study.

Chapter 2 discusses the optimization and performance of gold-coated cantilever probes for use in conducting-atomic force microscopy (C-AFM), which is essentially a two-probe multimeter with nanometer precision. The mechanical and electrical stability of the nanocontact between a gold-coated tip and a graphite substrate has been studied in relation to the contact force and circuit current.

The nature of electrical conduction in a nanorectifier system–a Langmuir-Blodgett (L-B) film of alkanethiol capped Au nanocrystals supported on an organic monolayer deposited on a SiO_2-Si substrate – are described in relation to the film morphology **in Chapter 3** employing C-AFM. The effect of monolayer compression on the morphology of the L-B films and the monolayer-bilayer transition has been studied. The I-V plots acquired at different locations on the nanocrystal film are analyzed and the large rectification ratios observed, have been explained on the basis of asymmetric tunnel junction model.

Chapter 4 presents the structural aspects of lamellar bilayer systems of Pd(II)- and Ni(II) alkanethiolates (PdSR, NiSR) and their electrical and magnetic properties respectively. Hybrid bilayers, consisting of binary mixtures of PdSR, have been prepared for the first time and the structural aspects relating to bilayer spacing and chain conformation have been studied. The electrical properties of individual bundles of PdSR at room temperature are investigated by C-AFM and the influence of chain length is discussed. A solventless thermolysis method for producing Pd nanocrystals and metallic Pd films from PdSR and the effect of chain length on nanocrystal size have also been studied. The magnetic properties of lamellar NiSR of different chain lengths exhibiting intralayer and interlayer interactions at low temperatures have also been examined.

Deposition of metal cuplike structures with femtoliter capacity by pulsed laser ablation, their characterization using scanning electron microscopy and AFM and also their applications as containers, are discussed in **Chapter 5**. The optimal conditions for obtaining femto-cups of various metals on different substrates are explored. An understanding of the underlying mechanism is also provided in terms of droplet flow dynamics. Transforming the metal cups to oxide ones and their chemical mapping by scanning Auger microscopy are also discussed.

In **Chapter 6**, dip-pen lithography (DPN), an AFM based technique is demonstrated for patterning of–colloids of luminescent doped $LaPO_4$ and ZnO on different substrates, precursors for metal and semiconductor nanopatterns and also molecules. A laboratory method has been developed to produce AFM tips of different sizes by laser irradiation of commercial tips. A study of colloidal ink deposition from such blunt tips is also presented.

CONTENTS

6. Generating patterned nanostructures by dip pen nanolithography

LIST OF ABBREVIATIONS

AFM	Atomic Force Microscopy
APTMS	Amino propyl trimethoxy silane
C-AFM	Conducting-Atomic Force Microscopy
CTAB	Cetyl trimethyl ammonium bromide
dia	diameter
DMSO	Dimethyl sulfoxide
DNA	Deoxy-ribonucleic acid
DPN	Dip Pen Nanolithography
EA	Electron affinity
EDX	Energy Dispersive X-ray spectroscopy
EFM	Electric Force Microscopy
FET	Field-effect transistor
FESEM	Field Emission Scanning Electron Microscopy
FC	Field cooled
F-D	Force- Distance
FT-IR	Fourier Transform Infrared Spectroscopy
GdSt	Gadolinium stearate
HOMO	Highest occupied molecular orbital
HOPG	Highly oriented pyrolytic graphite
HRTEM	High Resolution Transmission Electron Micrograph
IP	Ionization potential
I-V	Current-Voltage
KE	Kinetic energy
LAO	Local Anodic Oxidation
L-B	Langmuir-Blodgett
LEEM	Low Energy Electron Microscopy
LFM	Lateral Force Microscopy
LUMO	Lowest unoccupied molecular orbital
MFM	Magnetic Force Microscopy

MO	Molecular orbital
MP	Melting point
MWCNT	Multi-walled carbon nanotube
NC	Nanocrystal
NDR	Negative differential resistance
NTS	Nonadecenyl trichlorosilane
OTS	Octadecyl trichlorosilane
PdSR	Palladium alkanethiolate (R-alkylchain)
PVP	Poly(vinylpyrrolidone)
QD	Quantum dot
SAED	Selected Area Electron Diffraction
SAM	Scanning Auger Microscopy
SAMs	Self-assembled monolayers
SEM	Scanning Electron Microscopy
SFM	Scanning Force Microscopy
SNOM	Scanning Near-field Optical Microscopy
SPL	Scanning Probe Lithography
SPM	Scanning Probe Microscopy
SQUID	Superconducting Quantum Interference Device
SR-AES	Spatially Resolved Scanning Auger Spectroscopy
STM	Scanning Tunneling Microscopy
STS	Scanning Tunneling Spectroscopy
SWCNT	Single-walled carbon nanotube
TEM	Transmission Electron Microscopy
TOABr	Tetra octyl ammonium bromide
UHV	Ultra-high vacuum
UV	Ultra-Violet
XPEEM	X-ray Photo Emission Electron Microscopy
XPS	X-ray Photoelectron Spectroscopy
XRD	X-ray diffraction
ZFC	Zero field cooled

Chapter 1

Nanomaterials and Atomic Force Microscopy

1.1 Nanoscale Materials – Concept, Evolution and Significance

Materials with extensions in the range of nanometers, i.e, one billionth of a meter, are to be known as nanomaterials. Figure 1.1 gives a comparison of different length scales involving features that are familiar. A strand of a hair measures 50 micrometer in diameter, which is the minimum size that we can see in detail with our naked eye.

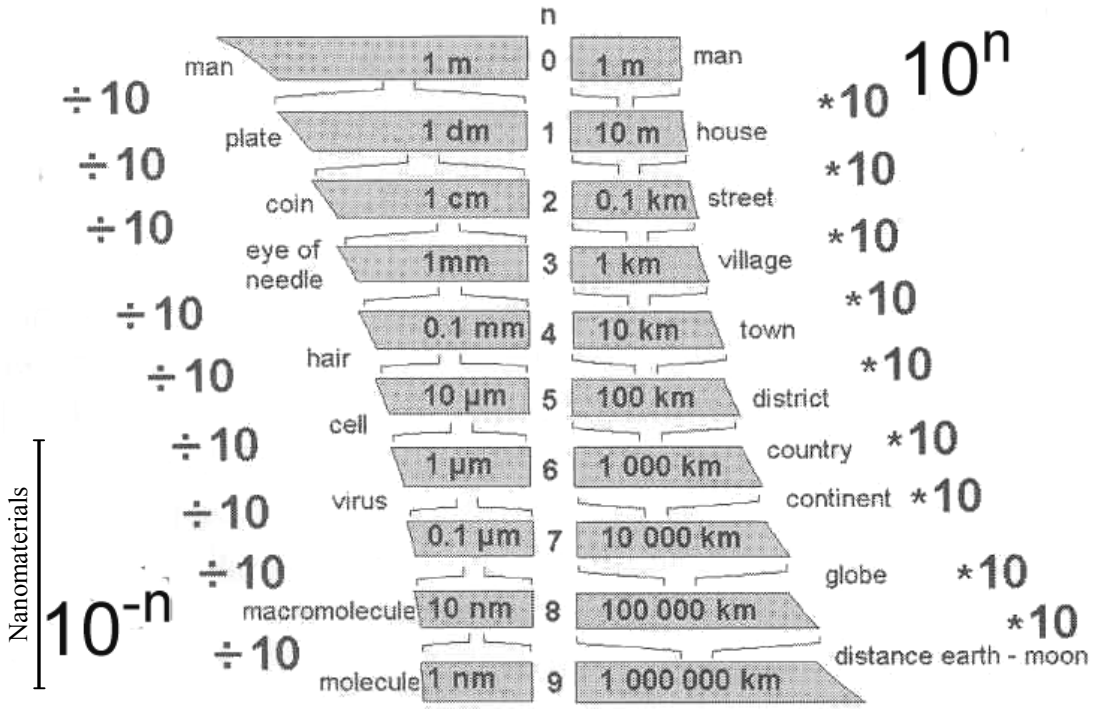

Figure 1.1. Size comparison of macroscopic and microscopic objects [adopted from ref. 1].

Microorganisms and many biological entities measure below this dimension and are called microscopic implying that the size range falls around a few microns and a microscope is needed to view such structures. Below is the nanometer range. In 19th

century, materials were classified being macro, meso or micro. With the advent of nanoscience, the originally used term, mesoscale is now expanded to include a wide range between nano and milli (10 nm to 0.1 mm).

Strictly, nanomaterials are objects with at least one of their physical dimensions below 100 nm. When the physical dimensions of a solid become comparable to the mean free path of the electrons in it, the electrons begin to feel confined and therefore, the properties of the solid undergo a dramatic change critically depending on the number of atoms and electrons, in contrast to the average properties arising from the large scale periodic arrangement of atoms in the bulk state. Although this fact has been known since the development of quantum mechanics in the early part of the last century, a direct visualization of the quantum confinement became possible only recently. A schematic diagram of the density of states of a solid with electrons confined to one, two and three dimensions, named as 2D, 1D and 0D materials respectively, is given in Figure 1.2. Thus, unique electrical, optical and magnetic properties are expected from nanoscale materials that have driven the whole field to such an amounting progress as we see today. Thus, materials that come under this regime are ultra-thin films (2D), nanotubes and nanorods (1D), nanoparticles or quantum dots (0D) of metals, semiconductors etc. Table 1.1 lists a few nanoobjects and their geometric dimensions. To have an idea of the scale, a 100 nm nanocrystal contains 100 million atoms, which is small when compared with bulk.

Table 1.1. Commonly known nanoscale objects

Object	Diameter
Hydrogen atom	0.1 nm
Fullerene (C_{60})	0.7 nm
Single-walled carbon nanotubes (SWCNT)	0.4-1.8 nm
DNA	2 nm
Multi-walled carbon nanotube (MWCNT)	5-100 nm
Proteins	5-50 nm
CdSe Quantum dot	2-10 nm
Ribosome	25 nm

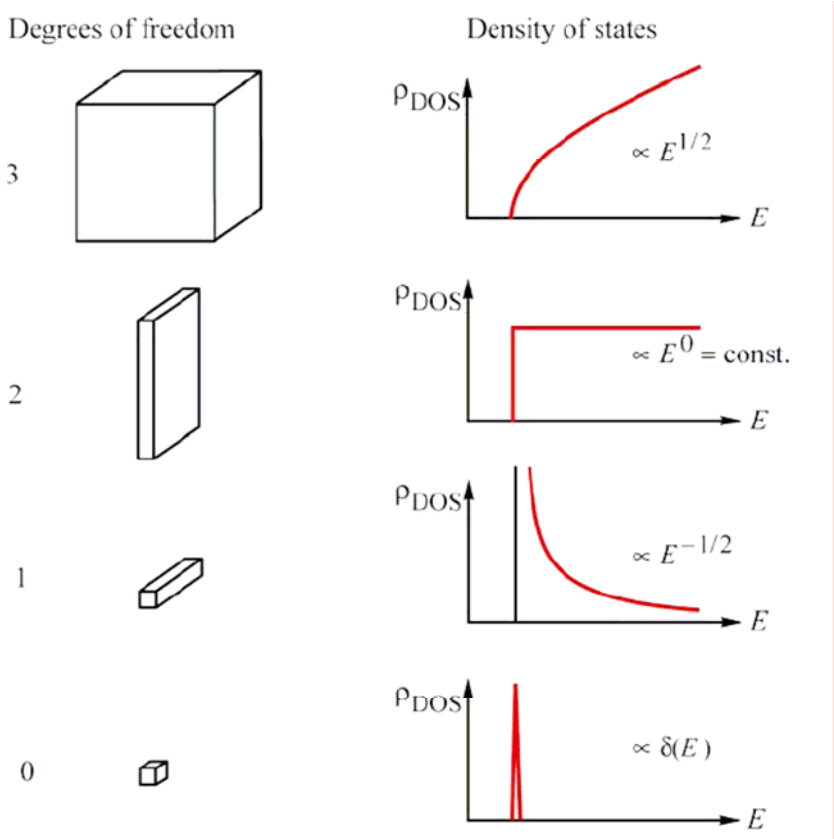

Figure 1.2. Density of states for reduced dimensions [reproduced from ref. 2].

Nanoparticles of metals and oxides were known even before the emergence of quantum mechanics, in the name of colloid chemistry. Because of the attractive colors the colloids exhibit, in the ancient times they were used as dyes to stain glasses and fabrics, though the scientific aspects were not known until Faraday (1857). Purple of Cassius, a popular dye mentioned in 17th century work of Andreas Cassius was found to consist of tin oxide and Au nanocrystals. The color of the Lycurgus cup, a roman glass artifact dated to 4 A. D, that appears red in transmitted light and green in reflected light, is attributed to the impregnated Au and Ag nanocrystals. The colloidal form of the metals was first established by Michael Faraday in 1857 in his Bakerian lecture on the 'Experimental Relations of Gold (and other Metals) to Light' [3]. Faraday's studies of metal hydrosols and aerosols led him to conclude that "*the gold is reduced in exceedingly fine particles, which becoming diffused, produce a beautiful ruby fluid…the various preparations of gold, whether ruby, green, violet or blue…consist of that substance in a*

metallic divided state". And yet the precise mechanism of that coloration was not established until Mie in 1908 [4], who showed that the colors of spherical particles were a consequence of the absorption and scattering of light by the metal core in a dielectric medium, which in today's terminology is known as surface plasmon excitation. These studies on colloidal systems were further augmented by Gans [5,6], Einstein [7], Kubo [8] and Ostwald [9].

The colloidal chemistry was still at its infancy when Feynman, one of the great physicists and visionaries, delivered his famous lecture in the 1959 ACS meeting titled 'There is Plenty of Room at the Bottom' [10]. The basic inspiration for his speech was derived from the biological systems consisting of proteins and DNA (Watson and Crick discovered DNA in 1950) that are able to do a variety of mechanical and electrical functions, "*the biological example of writing information on a small scale has inspired me…..a biological system can be exceedingly small. Many of the cells are very tiny, but they are very active; they manufacture various substances; they walk around; they wiggle; and they do all kinds of marvelous things-all on a very small scale. Also they store information…in DNA molecules in which approximately 50 atoms are used for one bit of information. Consider the possibility that we too can make a thing very small that does what we want-that we can manufacture an object that maneuvers at that level*!" His vision was to write the entire 24 volumes of *Encyclopedia Britannica* on the head of a pin and ultimately in terms of small bits to record 24 million books in a space width of 1/200 of an inch. He suggested miniaturization in terms of top-down and bottom-up approaches and even gave guidance as to how to achieve it, thus introducing the concept of nanotechnology. The subsequent silicon revolution and microfabrication was a giant leap in technology. Scanning probe microscopic techniques (invented in 1980s) with nanometer dimension probe capable of atomic level resolution and manipulation gave more insights into the nanostructures. The discovery of fullerenes and carbon nanotubes in 1990s further accelerated the quest to make other materials in similar dimensions and also to explore the technological aspects of these materials. In a nutshell, the application of quantum mechanics for explaining the processes in the *small world,* detailed understanding of biological functions, chemical pathways for synthesis and powerful instrumentation resulted in the explosion of the nanoscience field as we see today.

With the development of efficient microscopes and computer automation, complex systems belonging to nanoworld became more accessible. The study of nanoscale phenomena has caught the attention for two important reasons,

1) the property of matter bearing nanodimensions becomes size dependent. This is exemplified in Figure 1.3 for metals that undergo metal-insulator transition as the size is reduced to form clusters. The emergence of Kubo gap (see Section 1.3.2 for more details) is illustrated.
2) most of the biological functions originate from the hierarchy of small molecules (see Figure 1.4).

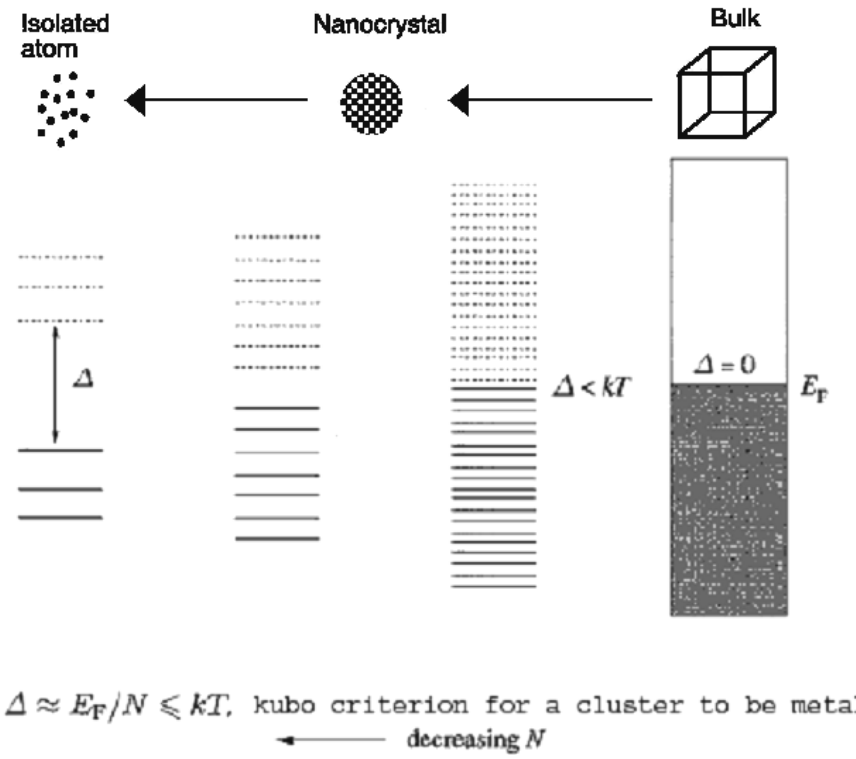

Figure 1.3. Size induced effects in a metallic nanocrystal [reproduced from ref. 11].

In addition to the size dependence, the shape of the materials and the form in which they are obtained also influence their properties. Hence, there has been greater interest to put any type of material into the desired nanogeometry by exploiting chemical pathways. For example, ZnO, an important semiconducting and piezoelectric material, has the richest family of nanostructures consisting of nanoparticles, nanotubes, nanowires

nanorings and even other exotic forms such as nanosprings, nanocombs, nanobelts and nanocages [12]. Other interesting shapes include Ag and Au nanotriangles and nanoprisms, nanodisks and nanorings [13,14], junction nanotubes [15], GaS nanowalls [16], nanoflowers [17] etc. Figure 1.5 gives electron micrographs of some interesting shapes of nanoobjects.

Equally important aspect is how to exploit such properties in applications where the novel properties are achieved not only by varying constituent components but also by varying effective sizes. Examples include device fabrication, membrane and filtering systems, sensors and actuators, optoelectronics etc. Integrating nanostructures with macroscopic forms to form a functional environment is equally challenging and importance of various lithographic techniques walks in here. An analogy with biological systems is given in Figure 1.4.

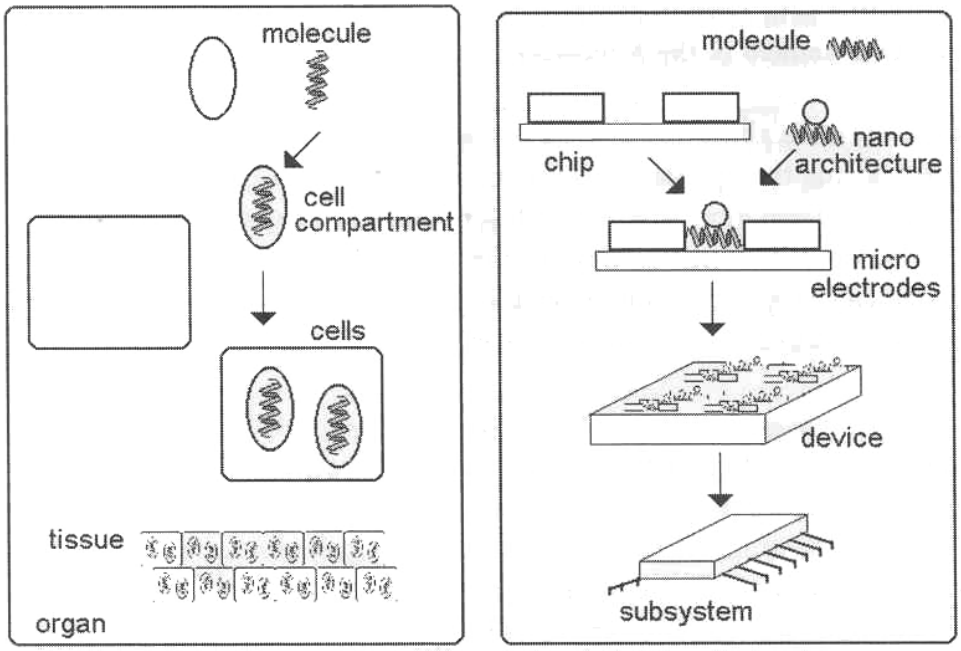

Figure 1.4. Integration of natural and technical nanosystems in a functional microstructured environment [reproduced from ref. 1].

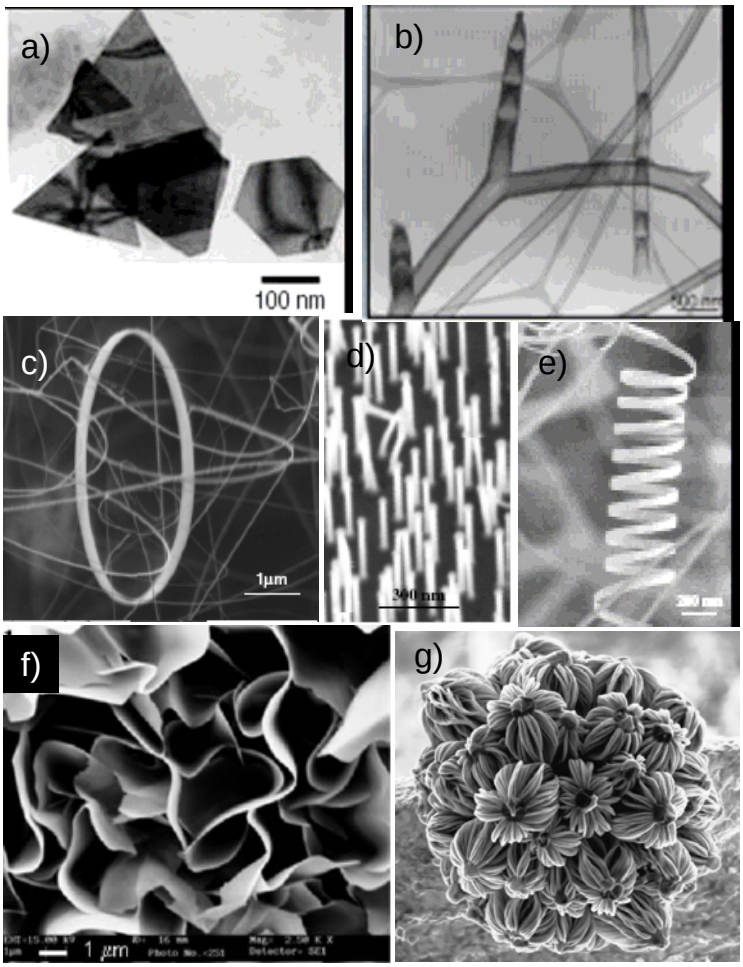

Figure 1.5. Electron micrographs of nanomaterials in different shapes. a) Au nanotriangles. b) Y-junction CNTs. c), d) and e) ZnO nanoring, nanowires and nanospring. f) GaS nanowalls. g) SiC nanoflowers, [reproduced from refs. 13, 15, 12, 16, 17 respectively].

With the progress in the understanding of nanoworld, the horizon of 'nanostructures and nanomaterials' has become vast to include any system that exhibits unique properties owing to their nanoscale components. This definition is extremely wide as it includes everything listed below:

a) All isolated nanosystems- rods, tubes, particles and other shapes and assembly of these nanosystems,

b) Nanocomposites (inorganic-organic hybrid systems, polymer-nanostructure composites…),

c) Porous solids with diameters in nanoscale (zeolites, open framework materials, mesoporous fibers and spheres..),

d) Thin film devices (also organic monolayers),

e) Interfaces (multilayers, solid-solid-, but also solid-liquid interfaces, wetting and growth phenomena), internal interfaces, domain (state-of-the art transistors, research devices for transport studies),
f) Surface science (lattice, reconstructions, adhesion, growth), boundaries, type II superconductors, phase segregation, grain boundaries, dislocations...), defects (atomic defects, line defects, compositional defects...),
g) All scanning-probe microscopy (SPM) techniques (STM, SFM, SNOM,..), metrology (nanometer as a measuring standard),
h) Macromolecules, and single atoms/molecules, fullerenes, (atomic manipulation), biological systems (DNA, proteins, molecular motors, Abalone shell) and many more.

The immediate goals of the science and technology of nanomaterials is to fully master the synthesis of isolated nanostructures (building blocks) and their ensembles and assemblies with the desired properties, to explore and establish nanodevice concepts and systems architecture, to generate new classes of high-performance materials, including biologically-inspired systems, to connect nanoscience to molecular electronics and biology and to improve known investigative methods while discovering better tools for the characterization of nanostructures.

1.2 Synthesis and Assembly of Nanomaterials

The synthesis of nanomaterials spans inorganic, organic and biological systems, all with control of size, shape and structure. Two main approaches for the synthesis are *top-down* and *bottom-up* methods. The basic concept behind these approaches is given in Figure 1.6. Top-down approach includes all physical methods involving breaking down the bulk by machining methods and lithography. Many other methods like resistive evaporation, laser ablation, arc discharge involve a combination of top-down and bottom-up approaches. Clusters and films of noble metals like Pd, Ni, Cu, Zn, Cd etc, important nitrides and oxides, semiconductors etc, have been obtained by laser ablation and supersonic jet expansion methods [18,19]. The major issue with this method is the poor control on the size distribution of the nanosystems as they form larger aggregates when collected on solid supports. Carbon nanotubes and nanotubes of other materials are generally prepared by arc discharge/thermal evaporation of graphite or powders of other

materials under a gas flow in a tubular furnace [20,21]. Here, by controlling the evaporation rate and the gas flow rate, one can achieve some control on shape and size.

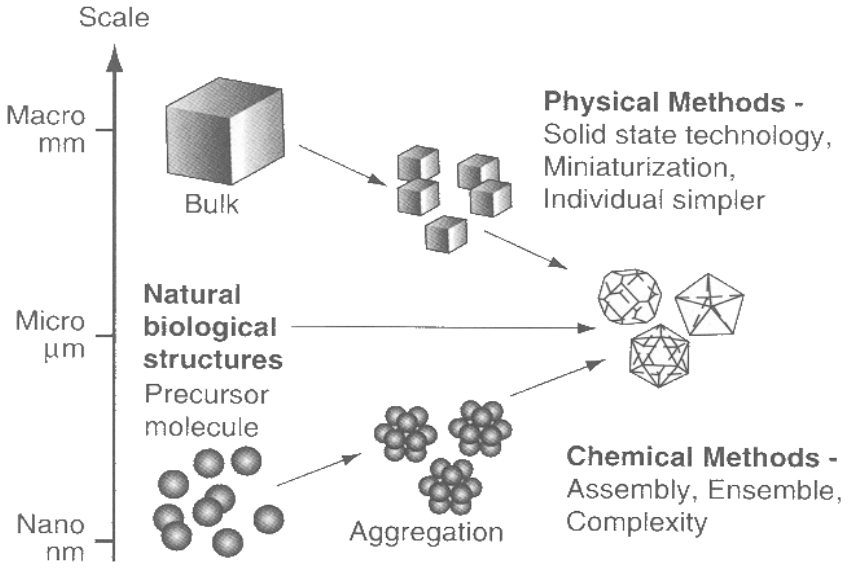

Figure 1.6. Schematic representation of the top-down and bottom-up processes [reproduced from ref. 22].

Lithographic methods are at advantage in this respect since ultimate size control can be realized depending on the resolution of the technique. Hence, a variety of lithographic techniques, photolithography, electron beam and ion beam lithography [23,24], colloidal/nanosphere lithography [25,26], soft lithography [27], host of scanning probe techniques [28] or a combination of these are used extensively to produce nanostructures in various shapes and sizes fixed on to solid supports and also to assemble them over large scales for device applications [29].

Bottom-up approaches for synthesizing nanomaterials include mainly the chemical methods. This usually involves reduction reactions in a solvent medium for producing metal nanocrystals and sulfidation, nitridation or hydrolysis for producing metal sulfides, nitrides or oxides (semiconducting nanocrystals) respectively, followed by capping with ligand molecules for stabilizing the sol [30-32]. Heat, light or chemical reducing agents act as the external stimuli for the reactions. Typical ligand or capping agents (sometimes called as surfactants) employed are ionic species like sodium citrate, or polymers such as

poly(vinylpyrrolidone), poly(vinylalcohol), block copolymers and dendrimers, fatty acids, long chain thiols or amines. Sols can be stabilized either by electrostatic or steric forces [33]. Electrostatic stabilization involves the formation of an electric double layer around the nanopaticles, thereby preventing aggregation. The double layer is affected by factors such as ionic strength of the solvent and the temperature. In the case of covalently bound long chain ligands, the steric repulsion owing to the interpenetration of chains stabilizes the nanoparticles against coagulation. Excellent size control is possible with this method by adjusting the ratio of reactant salt, surfactant and reducing agent. Efficient phase transfer methods to move nanocrystals in and out of aqueous and organic solvents to make them suitable for specific applications for example, fluorescent tagging of cells, are also available in literature [34].

Nanostructures have also been made in constrained environments such as surfactant micelles, reverse micelles, vesicles, bilayers, microemulsions, nanoporous alumina [32]. Microorganisms such as bacteria and fungi also have been harnessed to synthesize nanostructures [35,36]. Decomposition of organometallic precursors that act as a single source for the constituent elements in the nanomaterial, in reactive high boiling solvents also provides an efficient route for synthesis of semiconductor quantum dots [37,38]. Hydrothermal and solvothermal methods involving high pressure and temperature conditions are easy pathways for producing semiconductor nanocrystals, nanorods and other shapes [39,40]. In addition to these solution phase methods, the template-assisted approach utilizing porous alumina membranes and polymer fibers, is also used for synthesizing monodisperse nanotubes and nanorods of many materials [41,42].

Assembling the nanostructures into ordered arrays is often necessary to render them functional and operational [43]. It is by a combination of novel nanobuilding units and strategies for assembling that nanostructured materials and devices with new capabilities can be generated. The construction of ordered arrays of nanostructures by employing organic self-assembly techniques provide alternative strategies for the production of nanodevices. Two- and three-dimensional arrays of nanocrystals of semiconductors [44,45], metals [46,47] and magnetic materials [48], linear chains of metal nanorods [49], have been assembled by using suitable organic reagents, the spacing being controlled by the length of the ligand molecules. The assembly is facilitated by strong chemical interactions or even weak interactions between ligands [50-52]. Typical assemblies of

nanocrystals and rods are shown in Figure 1.7. Assembling nanocrystals at air-water interface, namely Langmuir-Blodgett method [53] and at liquid-liquid interface [54]

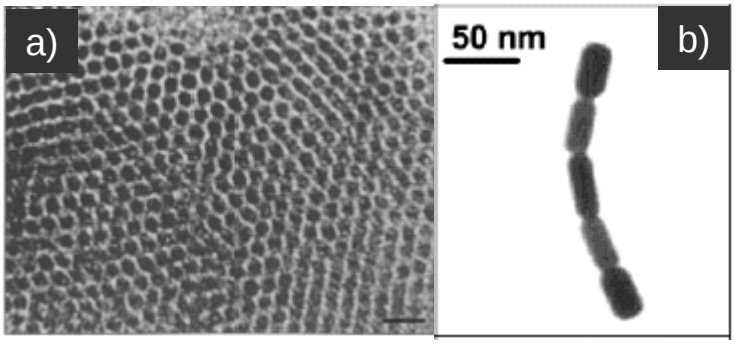

Figure 1.7. Electron micrographs of nanomaterial assemblies a) Pd nanocrystals capped with alkanedithiol. b) Linear chains of Au nanorods facilitated by hydrogen bonding of mercapto-propanoic acid [reproduced from refs. 46 and 49 respectively].

followed by transfer to solid supports are also good methods for getting mesoscopic arrays for applications. L-B method has the advantage of on-site tuning of interparticle spacing by adjusting surface pressure of the monolayer. Template directed assembly using monolayers of molecules [55], oligonucleotides, natural self-assembly of proteins like chaperonins [56], etc are also known. Lithography induced assembly is attracting wide attention due to its compatibility with device fabrication techniques [43,57,58].

1.3 Properties of Nanomaterials and Emerging Applications in Nanotechnology

The relation between structure and properties, which is the foundation of materials science, has become increasingly important in the age of nanoscale science and technology. As the size of the materials is reduced, the properties become increasingly size dependent and constitute the fascinating aspect of nanomaterials. Size effects can be classified into two types, one dealing with the advantage of having small size with direct implications in miniaturization and surface-area increase, and the other dealing with the evolution of new electronic, optical, mechanical and magnetic features owing to the quantum confinement.

1.3.1 Physical Properties

In the nanosize regime, the effective surface to volume ratio increases i.e, the percentage of surface atoms increases and this variation with particle diameter is shown graphically for sodium atoms in Figure 1.8. The increase in surface area and surface free energy with decreasing particle size leads to changes in interatomic spacings, which get manifested in the thermodynamic properties. For instance, the melting point of gold particles has been observed to decrease rapidly for particle sizes less than 10 nm [22]. Nanomaterials find applications related to catalysis and sensors. Nanocatalysis by gold particles of diameter 1-2 nm, which are otherwise noble, is an example [59]. Other examples are sensing actions of particles and rods of ZnO or SnO_2 to many gases like NO_2, ethanol, ammonia, hydrocarbons etc [12]. Many transition metal nanoparticles are supported on oxide supports or zeolites to form nanocomposites to assist in catalysis [60]. Nanotubes and fibres of carbon have also been harnessed as supports for metal catalysts since they have several advantages such as high resistance to acidic and basic media, easy recovery of spent catalyst and readily modifiable surface by chemical functionalization [61].

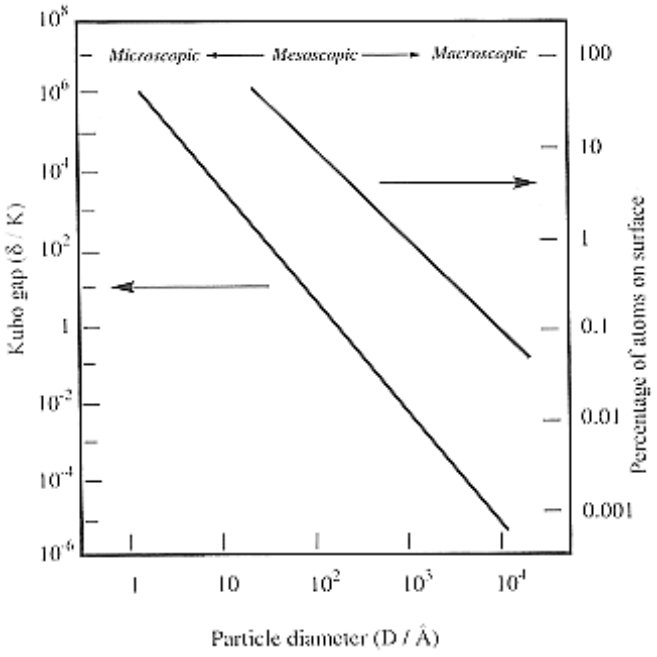

Figure 1.8. The fragmentation of bulk sodium; a plot of percentage of surface atoms with particle diameter. The figure also gives the variation of average electronic energy level spacing (the Kubo gap, see Section 1.3.2 for discussion) against particle diameter [reproduced from ref. 11].

The developments in nanoscience and nanotechnology have great impacts in biotechnology and medicine. Polymer nanoparticles and spheres and other metal nanoparticles are used as drug delivery agents [62]. Carbon nanotubes with suitable chemical functionalization can act as scaffolds for bioreceptors and hence assist in biosensing [63].

Self-assembling molecules can be used for engineering surface properties making them sensitive to different environments and also find applications in patterning [64].

Mechanical properties also get modified in a nanostructured material [22]. For example, SWCNTs and MWCNTs show high mechanical strengths and high elastic limits that lead to considerable mechanical flexibility and reversible deformation. Many nanostructured metals, ceramics and nanocomposites of layered materials have good yield strength and are observed to be superplastic in that they are able to undergo extensive deformation without fracture. This is presumed to arise from grain boundary diffusion and sliding and can be engineered in a nanocomposite. Super hard materials like carbides have been made into nano. Ceramic coatings on CNTs and their composites with polymers [65] are found to be promising materials for mechanical purposes. Materials like MoS_2 nanotubes and fullerenes find potential applications as solid lubricants [66].

1.3.2 Electronic Properties

In the nanometric domain, the electronic structure undergoes various changes and is evident from the density of states obtained for different dimension by quantum mechanical calculations (see Figure 1.2). The electronic properties of metal nanocrystals, carbon nanotubes and molecular systems have been well investigated and they form the foundation for nanoelectronics.

Bulk metals possess a partially filled electronic band and their ability to conduct electrons is due to the availability of a continuum of energy levels below E_f, the Fermi level that gets populated on application of electric field. When the size is reduced, the energy level also becomes discrete and is estimated as Kubo gap, Δ [8].

$$\Delta = E_f/3n, \tag{1.1}$$

n being the number of free electrons in the nanoparticle (a contribution of one electron per atom is usually assumed). The Kubo gap will manifest itself when $\Delta > kT$. A plot of

the variation of Kubo gap with particle size in the case of sodium is given in Figure 1.8. Hence, a natural consequence of the emergence of Kubo gap is a size-induced metal–insulator transition when the diameter of the particle is decreased to below a few nanometers as schematically explained in Figure 1.3 [11]. Photoelectron spectroscopic studies of Hg clusters showed that the nonmetallic gap in very small clusters closes when the number of atoms increases to 400. In the case of semiconductors, the energy levels at the band edges become discrete with size reduction, effectively increasing the band gap. Generally, quantum confinement manifests when the size becomes comparable to de-Broglie wavelength of conduction electrons in the case of metals and when it is comparable to exciton Bohr radius in the case of semiconductors.

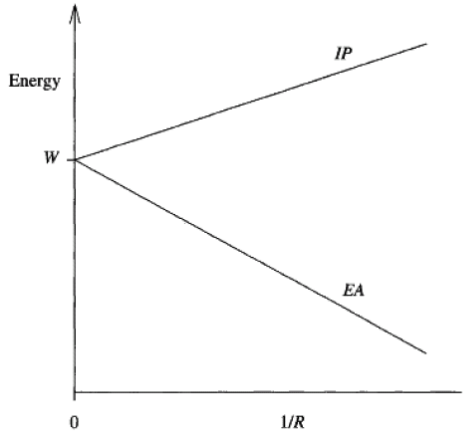

Figure 1.9. Dependence of cluster IP and EA on cluster radius predicted by the liquid drop model [reproduced from ref. 67].

The energy required to add or remove an electron, called work function in bulk metals, become nonequivalent upon size reduction and are termed as ionization potential (IP) and electron affinity (EA) respectively, as in the case of molecules. The variation of IP and EA with cluster size is given in Figure 1.9. The difference between two energies is called charging energy (U), which depends on the diameter and chemical identity of the material. U is related to capacitance (typically ~10^{-18} F for organic ligand covered metal nanocrystal) as $C = U/2e$. When electrons are allowed to tunnel through a potential barrier into the cluster, the capacitance changes sufficiently to block the entry of the next electron till an observable change in the potential of the charging field is applied. This

leads to Coulomb gap and Coulomb staircase in the I-V spectra (see Figure 1.10, $U \sim 100$ meV). It has been proposed that, by using nanocrystals, single electron devices such as supersensitive electrometers and memory devices could be fabricated. True to this, single-electron transistors have been demonstrated with one or a few nanocrystals at the gap between electrodes [68].

Augmented by the prediction by Moore that the number of transistors in a chip will grow exponentially with time [69], there has been a greater thrust towards miniaturization of devices and the existing silicon technology pose several practical problems when the thickness comes below 40 nm. This boosted the development of nanotechnology and molecular electronics and current research focuses mainly on electronic properties of nanomaterials. Arrays of nanocrystals behave differently from isolated ones due to interparticle interaction and are considered as *artificial solids*. Many studies on one, two, and three dimensional arrays of metal nanocrystals like Au, Ag, Co, etc have revealed that the transport can be tuned by simply varying the diameter of the

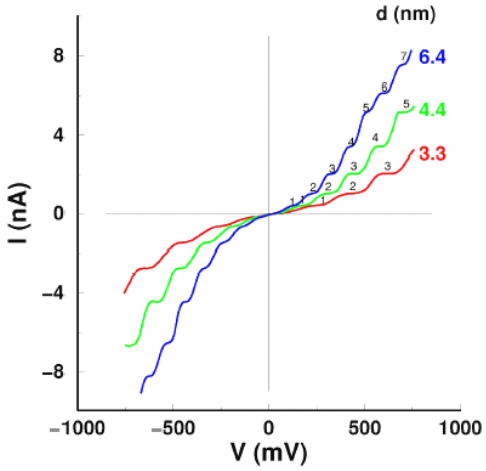

Figure 1.10. I-V spectra of Pd nanocrystals of different sizes exhibiting Coulomb staircase phenomena [reproduced from ref. 70].

nanocrystals, interparticle separation, type of capping ligand and structural disorder in the system [71-73]. Heath and coworkers have shown reversible insulator-metal transition by compressing a monolayer of Ag nanocrystals in L-B trough [72]. By employing nanocrystal ensembles, nonvolatile memories [74], field-effect transistors [75],

nanoswitch [76], etc have been demonstrated. Composites of nanocrystals with molecules, polymers and nanotubes have been used for sensing action as well [77].

Buckminsterfullerene, C_{60}, a spherical organic solid with unsaturated π-molecular orbitals, has a rich electronic and vibrational structure [78]. Electronic properties of fullerenes and its doped varieties have been thoroughly probed. By controlling the alkali metal dopants it is possible to get metal-semiconducting transition and some of they are found to be high temperature superconductors. When mixed with conducting polymers they are useful materials for plastic solar cells, since they are excellent acceptors in the excited state [79].

Interesting electronic properties exhibited by carbon nanotubes (CNTs) are due to the inherent folding of the graphitic sheets as in the case of fullerenes and its one-dimensional nature [20]. Electronic structure of CNTs is well-investigated and major contribution is from the π-derived electronic states. Calculations and experimental studies show that CNTs may be as good conductors as copper, although the degree of helicity together with the number of six-membered rings per turn decides their electronic properties [80]. Electron transport in metallic CNTs occurs ballistically with quantized conductance over long nanotube lengths, enabling them to carry high currents with essentially no heating. Hence, they can carry high current densities and field-effect transistors and logic circuits have been demonstrated by employing cross-wire configuration of CNTs [81]. Ghosh *et al*. [82] demonstrated flow sensors from CNTs. The high electrochemically accessible surface area of porous CNT arrays combined with their good conductivity and mechanical properties render them attractive as electrodes for making supercapacitors [83] and electromechanical actuators [84]. The variation in the conductivity on adsorption of gases or attachment of molecules inherent to the material of the nanotube or nanowire is utilized in sensing action [85]. One of the most important applications of CNTs that is already commercialized is its field emission property with low emission threshold potentials and high local field due to their sharp tip. They have longer lifetimes and are exploited in flat panel displays [86].

Molecules are attractive components for the ultimate miniaturization of devices since they can be easily tuned to perform many complex electronic functions. Polymer electronic devices, where in films of doped conducting polymers are used as FETs and light-emission devices, are becoming popular due to their light-weight and flexible

aspects [87]. Single molecules started gaining attention since the proposal of a molecular rectifier by Aviram and Ratner in 1974 [88]. Molecules have been a part of chemistry from its origin and the properties are clearly understood in terms of energy scales of the molecular orbitals. Essentially all electronic processes in nature, from photosynthesis to signal transduction, occur in molecular structures. For electronics applications, molecular structures have four major advantages [89-91]:

- *Size*. The size scale of molecules is 1-100 nm, a scale that permits functional nanostructures with accompanying advantages in cost, efficiency, and power dissipation.
- *Assembly and recognition*. One can exploit specific intermolecular interactions to form structures by nanoscale self-assembly. Molecular recognition can be used to modify electronic behavior, providing both switching and sensing capabilities on the single-molecule scale.
- *Dynamical stereochemistry*. Many molecules have multiple distinct stable geometric structures or isomers (an example is the rotaxane molecule in which a rectangular slider has two stable binding sites along a linear track). Such geometric isomers can have distinct optical and electronic properties. For example, the retinal molecule switches between two stable structures, a process that transduces light into a chemoelectrical pulse and allows vision.
- *Synthetic tailorability*. By choice of composition and geometry, one can extensively vary a molecule's transport, binding, optical and structural properties. The tools of molecular synthesis are highly developed.

Molecules have disadvantages, though, such as instability at high temperatures.

Current research in this field has demonstrated the use of molecular components as interconnects, switches, rectifiers, transistors, nonlinear optical elements, dielectrics, photovoltaic elements, and memory bits [90]. Theoretical studies have provided a good understanding of the mechanism of transport through molecules [92]. The molecules could be attached to other nanosystems or interspersed with inorganics to improve their conductance and sensitivity to light [93].

1.3.3 Optical Properties

The colour of the nanocrystals, metal or semiconductor is the first striking observation that one would make after synthesizing them. Mie [4] was the first to study

the scattering of light by small particles based on classical Maxwell equations. The electronic absorption spectra of nanocrystals is dominated by the surface plasmon band which arises due to the collective coherent excitation of the free electrons within the conduction band [94] (see Figure 1.11). From Mie theory, for small particles (neglecting the scattering term and higher order extinction terms), the extinction coefficient is given by

$$C_{ext} = \frac{24\pi^2 R^3 \varepsilon_m^{3/2}}{\lambda} \frac{\varepsilon'}{(\varepsilon + 2\varepsilon_m)^2 + \varepsilon'^2} \qquad (1.2)$$

where ε_m is the dielectric constant of the surrounding medium, ε and ε' are the real and imaginary parts of the frequency dependent dielectric constant of the substance. The dielectric constant of the substance in turn depends on the mean free path of the electrons, which becomes diameter dependent for small sizes. This is the case of spherical particles, where only dipolar plasmon resonance is prominent. In the case of nonspheroid shapes, multipole oscillations also becomes important and higher order terms have to be considered. Thus, metal nanocrystals of various sizes exhibit

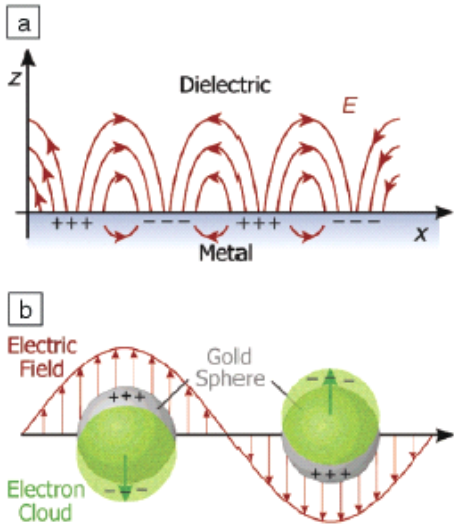

Figure 1.11. Schematic illustration of the collective oscillations of free electrons for (a) a metal–dielectric interface and (b) a spherical gold colloid. Excited by the electric field of incident light, the free electrons can be collectively displaced from the lattice of positive ions (consisting of nuclei and core electrons). While the plasmon shown in (a) can propagate across the surface as a charge density wave, the plasmon depicted in (b) is localized to each particle [reproduced from ref. 94].

characteristic colors depending on their diameters and shape [94,95]. Modifications to Mie theory explain the optical properties of spheroid/nonspheroid metal particles in complex dielectric environments [96]. The surface plasmon characteristics of gold nanorods of various aspect ratios and linear chains formed by them are gaining attention [97]. Surface plasmon phenomenon has given rise to a new applied field namely plasmonics [98]. It also finds major application in the detection of biomolecules by surface enhanced Raman spectroscopy [99]. Events that alter the surrounding dielectric and the number of free electrons on the metal such as the solvent refractive index and binding of molecules on the surface of nanocrystals have been successfully studied using the plasmon resonance band [95,100].

In the case of semiconductor and other particles, the free electron concentration is much smaller and the plasmon absorption band is shifted to the infrared region. Brus and coworkers recognized the inadequacy of Mie's theory in explaining the electronic absorption spectra of semiconductor nanocrystals and proposed an independent theory based on effective mass approximation [101]. They proposed that the absorption band in the visible region is due to excitons. In fact in semiconductors, there is a direct correlation between the excitonic band gap and the absorption edge. Thus, CdS an yellow solid, exhibits an excitonic absorption around 600 nm, which gradually shifts into the UV region as the nanocrystal diameter is varied below 10 nm. The absorption band can be systematically varied across ranges of a few 100 nm by changing the size of the nanocrystals. They also exhibit luminescence behavior. The emission spectra are generally intense, narrow and can be brought about by excitation in a broad range of wavelengths in contrast to the organic dyes whose emission spectra have tails and very narrow excitation spectra. Furthermore, the emission can be tuned by altering the diameter of the nanocrystal. For example, the emission and the absorption spectra of CdSe QDs for various sizes are given in Figure 1.12. Thus, these semiconductor quantum dots find important biological applications in fluorescent tagging of cells and multiple tagging is possible with nanocrystals of different sizes since they can be excited with the same wavelength [102]. By changing the material of the QD and the size, it is possible to get fluorescence ranging from UV region to visible extending to IR region. Surface defect states are found to affect the luminescence properties, which can be

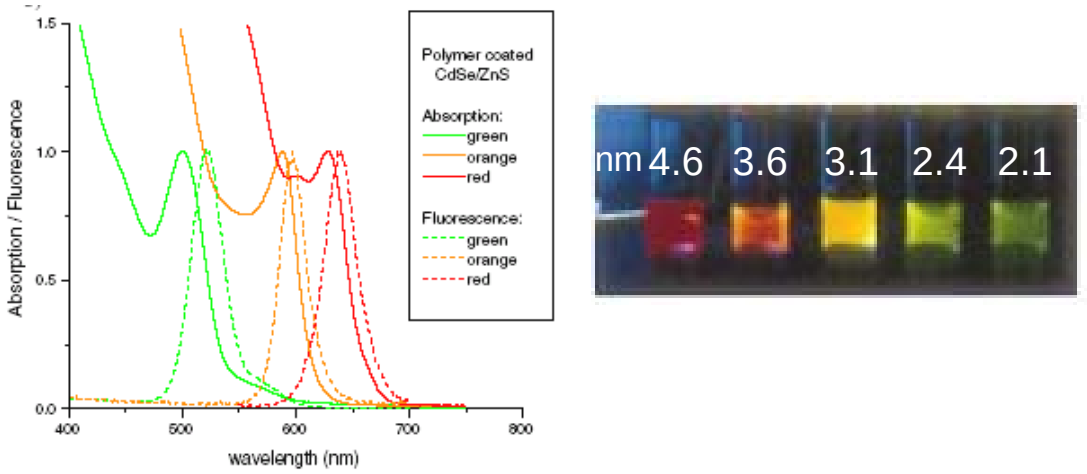

Figure 1.12. Normalized absorption and fluorescence spectra in water of polymer-coated CdSe/ZnS quantum dots of different size [adopted from ref. 102]. A photograph of the emission from the solutions composed of QDs of different sizes is given alongside.

avoided by coating the nanocrystals with a wide band gap inorganic material like ZnS. Optical properties of other important materials Si and III-V compounds of GaN, GaAs, InN have also been studied [103]. Nanocrystals and rods of various transition metal oxides with dopants examples, $Y_2O_3:Er^{3+}$, $ZnS:Mn^{2+}$ that exhibit upconversion luminescence have far reaching applications in solid state lighting [104].

Optical properties of a superlattice of nanocrystals are different from that of isolated ones due to interparticle interactions. The surface plasmon absorption of metal nanocrystals [105] and absorption spectra of semiconductor nanocrystals when present in a close packed organization such as the case of films of nanocrystals are found to be red-shifted due to interparticle dipolar interactions [106]. Delocalization of electronic states of nanocrystals in ensembles due to strong exchange interactions have been observed in experiments with CdSe nanocrystals [107].

Fullerenes functionalized with molecules and polymers are useful in optical devices as optical limiting materials [79]. Optical properties of carbon nanotubes [20,108] and other inorganic nanotubes and nanowires [20,108] are also interesting. As expected for 1D systems, sharp signatures of absorption and luminescence features are seen depending on the type of CNTs and their sizes. Electric field induced optical infrared emission from CNT FETs have been demonstrated and are promising for ultrasmall integrated photonic

devices [109]. Aniostropy in photoluminescence intensity when recorded parallel and perpendicular to the long axis of InP nanowires can be utilized to create polarization-sensitive nanoscale photodetectors. Huang *et al*. have demonstrated the room temperature ultra-violet lasing of ZnO nanowires [110]. The observed lasing action indicates that these nanowires can act as natural resonant cavities. Electroluminescence from ZnO nanowires in n-ZnO film/ZnO nanowire array/p-GaN film heterojunction light-emitting diodes has been observed [111]. A high concentration of electrons supplied from the n-ZnO films activated the radiative recombination in the ZnO nanowires, i.e., increased the light-emitting efficiency of the heterojunction diode. Single-crystal ZnO nanowires can be used as ultraviolet photodetectors [112]. Nanoscale light-emitting diodes with colors ranging from ultraviolet to near-infrared have been prepared using a solution based approach in which electron-doped semiconductors are assembled with hole-doped silicon nanowires in crossed nanowire architecture [113]. Hybrid metal dielectric 1D nanostructures consisting of noble metal nanoparticles embedded in dielectric matrices are considered to have practical applications in ultra fast all-optical switching devices owing to their enhanced third-order nonlinear susceptibility, especially near the surface plasmon resonance frequency [114].

Hybrid materials composed of inorganic and organic parts are interesting since they combine the optical, electronic, magnetic properties and thermal stability of inorganic framework and also the flexibility, tunability and light-weight aspects of organic molecules. For instance, the non-linear optical response of organic molecules is shown to increase by confining them in a silicate network. Also, the restricted environment of silicate networks is found to enhance the quantum yield of organic LEDs [115,116].

1.3.4 Magnetic properties

Much of the attraction in synthesis and studies of magnetism in nanomaterials is due to their applications in high-density information storage media [117,118]. In the case of spherical nanocrystals, there is a critical diameter (~10 nm) below which they exhibit single domain characteristics and are said to be superparamagnetic. Superparamagentic behavior is caused by thermal flipping of the anisotropic barrier to magnetization reversal. Below a certain temperature called blocking temperature, this flipping or relaxation can be arrested and the nanocrystals acquire a finite coercivity. Nanocrystals

possess other size dependent magnetic properties such as enhanced atomic magnetic moments and higher magnetic anisotropy. Recently, Sundaresan *et al*. reported ferromagnetism as a universal feature of nonmagnetic oxide nanoparticles (7-30 nm dia), which arises due to exchange interactions between localized electron spin moments resulting from oxygen vacancies at the surfaces of nanoparticles [119]. Figure 1.13 shows the magnetization curves obtained for CeO_2 nanoparticles.

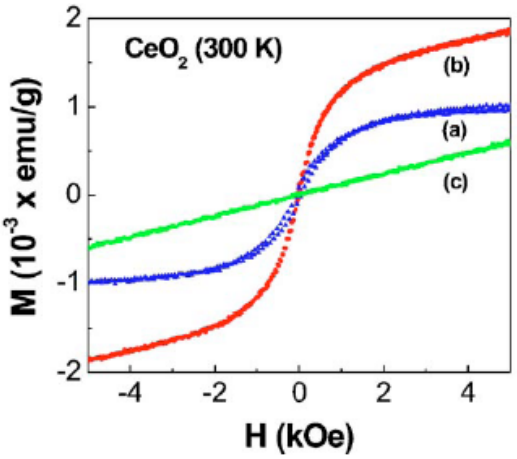

Figure 1.13. Magnetization curves for CeO_2 nanoparticles a) 7 nm, b) 15 nm, c) 500 nm at 300 K. Note the absence of ferromagnetism in the 500 nm nanoparticles, in contrast to the 7 or 15 nm nanoparticles [reproduced from ref. 119].

Assembling nanocrystals of different magnetic materials is still an intensive area of research because of its direct applications in memory devices. Fe/Pt and Co/Pt alloy nanocrystals are found to form ferromagnetic films capable of supporting high-density magnetization reversal transitions. Magnetic semiconductor nanostructures find applications in magneto-optical memory and spintronic devices [120]. Nanomagnetic particles also find applications in biology such as separation and manipulation of biomolecules such as cells, proteins and DNA fragments by immobilizing them on the surface of particles [118]. Accomplishments in the direction of biosampling antigens for on-chip immunoassay systems have also been achieved [121,122].

Molecule based magnets show interesting magnetic ordering phenomena due to low lattice dimensionality, various spin dimensionalities and the presence of structural disorder and competing interactions [123,124]. Especially of interest are polynuclear

metallic complexes with high spin values, called as single molecule magnets (eg. $Mn_{12}O_{12}(CH_3COO)_{16}(H_2O)_4$) and their assembly for use in information storage [125, 126].

1.4 Tools for the Nanoworld: Scanning Probe Microscopy Techniques

The realization that the there are small things in the world that are not visible to the naked eye extends back into human history. The developments in biology and medicine created an interest in the microworld, in order to gain more understanding of the processes and hence, microscopic imaging techniques for direct visualization of objects represent certain milestones in biology. Long before instruments were available for imaging of molecules, an understanding of the spatial arrangements of atoms in molecules and solids had been developed partly due to the intuition of great physicists and chemists and also other bulk spectroscopic measurements exhibiting specific signatures of the arrangement. However, the importance of microscopes was not recognized in physics and chemistry, until the concept of miniaturization started revolutionizing the technical world. Although chemistry dealt with molecules and atoms, it had several tools like infrared spectroscopy, nuclear magnetic resonance, mass spectroscopy to arrive at the structure and bonding and other surface sensitive techniques like X-ray photoelectron spectroscopy to study the interaction of molecules with surfaces. X-ray diffraction pattern from crystals was considered to be the ultimate in chemistry to understand the position and arrangement of atoms and packing of molecules. With the resolution limit of optical microscopes, chemists were clearly not interested in microscopes until electron microscopes (1930) and their high-resolution modes like field-emission guns and transmission electron microscopy were developed. With the progress in nanoscience, material scientists started using these extensively to study various nanostructures.

The resolution of a light microscope is limited by the higher wavelength of the visible light and being electromagnetic wave, the frequency cannot be varied so easily. By Abbe's law,

$$\text{Resolution, } d = 0.612\lambda/n \sin\alpha \qquad (1.3)$$

where λ is the wavelength of the radiation used to view specimen, n is the refractive index of the medium through which radiation travels and α is the aperture angle.

Electrons being charged particles, the wavelength can be manipulated to about 0.1 nm and can be focused to a beam diameter of about 1-5 nm. Electron beams interact with sample (see Figure 1.14) and undergo 1) elastic scattering (no loss of KE) 2) inelastic scattering 3) diffraction [127,128]. Much information about sample surface, composition and structure can be gained by harnessing the scattered beam.

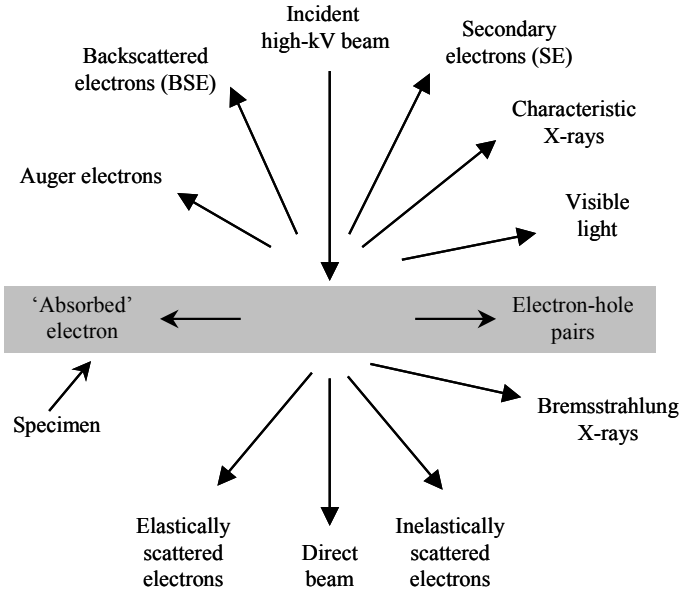

Figure 1.14. Signals generated when a high-energy beam of electrons interacts with a thin specimen. The arrows indicate in a relative manner, where the signals can be detected [adopted from 129].

Transmission electron microscope (TEM)

The first electron microscope was achieved in the transmission mode, where the diffracted beam from a thin specimen is used to image a selected area of the specimen [129]. A resolution of the order of 0.2 nm is achieved, which is atomic resolution. The diffraction pattern as such helps to identify the crystal structure of the sample. This requires extensive instrumentation such as electron optics, vacuum system (~10^{-9} Torr) and high accelerating voltages (~300 keV). TEM is routinely used in nanoscience research for imaging nanostructures and to understand local structure and can be

integrated with other techniques like electron energy loss spectroscopy and energy dispersive X-ray spectroscopy for information on the local chemical composition.

Scanning electron microscopy (SEM)

In SEM, the scattered beams from the sample surface are collected and amplified using a detector, when the probing e-beam scans over the surface in a raster fashion. The elastic scattering produces backscattered electrons (energy>50 eV) and inelastic scattering produces secondary electrons (<50 eV), X-rays and also Auger electrons. These signals are obtained from specific emission volumes within the sample and can be used to examine many characteristics of the sample. X-rays emitted are characteristic of the elements present in the sample, hence can be used to study the chemical composition and is called **energy dispersive X-ray spectroscopy.** The Auger electrons can be used to map local chemical composition of nanostructures with good spatial resolution and is called **scanning auger microscopy and spectroscopy.**

Backscattered and secondary electrons are utilized in imaging surface topography. Topography contrast arises because the number and trajectories of backscattered electrons and the number of secondary electrons depend on the angle of incidence between the beam and specimen surface. 3D appearance is possible due to the large depth of focus of SEM. The backscattered image can provide a contrast of the chemical composition in terms of variation in atomic number. Although the probe beam diameter can be made to 1 nm and high currents can be generated using field-emission electron sources, the ultimate resolution depends on the interaction volume of the sample from where the scattered beams are generated. The instrumentation has advanced to such an extend that even biological samples can be imaged without metal coating under low vacuum conditions and also scanning TEM is possible with the present day FESEMs.

Electron beam lithography is another major advantage with field-emission SEMs. Due to higher possible resolutions, it has become the popular method for fabrication of nanodevices [130]. It can be used for direct patterning on e-beam active surfaces or indirect patterning by employing e-beam resist polymers coated on metal or semiconductor surfaces.

Scanning Probe Microscopes (SPM)

Scanning probe microscopes, discovered by Binnig and Röhrer in 1980s, began a new paradigm in the concept of microscopy and they have become an integral part of nanoscience and nanotechnology. This new generation microscope consists of a nanometric dimension probe or a tip that is capable of interacting with surface through electrons, force or photons, atom by atom and hence giving ultimate resolution. True to the adage, 'seeing is believing', SPM aids us to see atoms! The concept of lenses, magnification and depth of focus in a normal beam microscope is completely changed in this case. The first type of SPM was a scanning tunneling microscope (STM) that exploits the quantum mechanical phenomenon of electron tunneling from tip atoms to surface atoms [131]. Later on, other powerful variants, like atomic force or scanning force microscopy (AFM or SFM) that employs the force experienced by the tip grafted to a cantilever capable of deflection [132], when brought close to surface atoms and scanning near-field optical microscope (SNOM) that employs the interaction of light coming through a hole with the surface in close proximity or rather near field, were developed.

1.4.1 Scanning Tunneling Microscopy and Spectroscopy (STM & STS)

STMs use a sharp, conducting tip with a bias voltage applied between the tip and the sample. When the tip is brought within about 10 Å of the sample, electrons from the sample begin to "tunnel" through the 10 Å gap into the tip or vice versa, depending upon the sign of the bias voltage (see Figure 1.15). The resulting tunneling current varies with tip-to-sample spacing, and it is the signal used to create an STM image. For tunneling to take place, both the sample and the tip must be conductors or semiconductors. Unlike AFMs, which are discussed in the next section, STMs cannot image insulating materials. The tunneling current is an exponential function of distance; if the separation between the tip and the sample changes by 10% (on the order of 1 Å), the tunneling current changes by an order of magnitude.

$$\text{Tunnel current, } I \propto \exp(-2kd) \tag{1.4}$$

where d is the distance between tip and sample surface and

$$\kappa = (2m\phi)^{1/2}/\hbar\,, \tag{1.5}$$

ϕ being the density of states at the Fermi level of the tip (for a small bias applied to the sample). This exponential dependence gives STMs their remarkable sensitivity. STMs can image the surface of the sample with sub-angstrom precision vertically, and atomic resolution laterally [133].

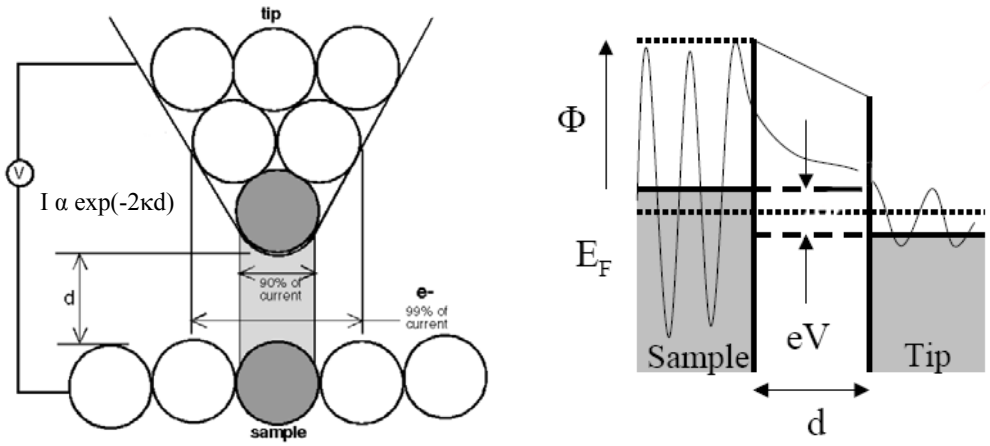

Figure 1.15. Schematic of the tip-sample interaction in STM and the mechanism of tunneling.

In the tunneling regime, the tip and the sample can be regarded as independent and the electron transfer between them is described by the perturbation approach, using the wave functions of the free electrodes. Representing the tip by an atom with a single s-orbital and assuming a small bias voltage between the tip and the sample, Tersoff and Hamman [134] showed on the basis of perturbation approach that the spatial variation of the tunnel current is proportional to the partial electron density distribution of the sample surface. The partial electron density is associated with the energy levels lying in the vicinity of the Fermi level, E_f.

For obtaining an image of the surface, the tip is scanned over the sample surface with the help of a piezoelectric scanner attached either to the tip or the sample. Voltage can be applied in X, Y and Z directions of the scanner so that the tip moves laterally as well as vertically. The vertical movement is controlled through a feedback loop giving height information. The complete layout of the instrument is given in Figure 1.16. The tips generally used in STM are mechanically cut Pt/Ir or chemically etched tungsten (for use in UHV).

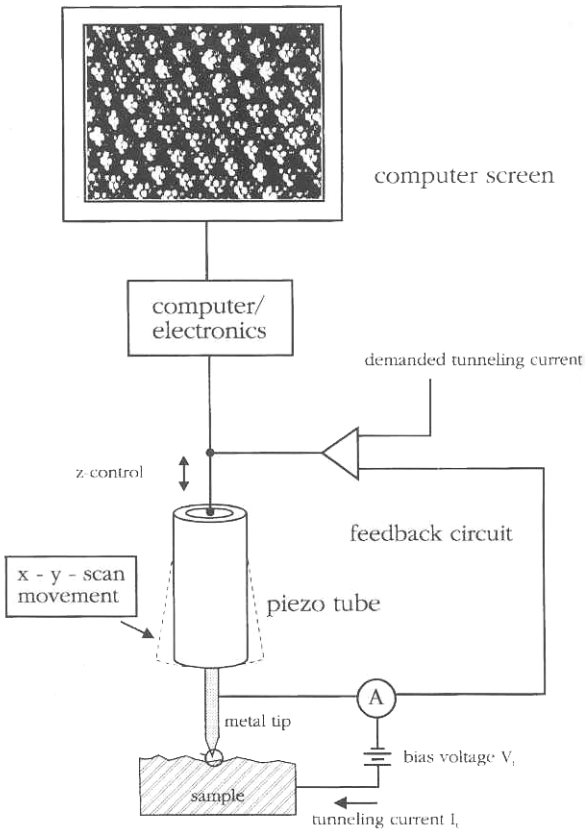

Figure 1.16. Schematic of the complete layout of STM [reproduced from ref. 133].

STMs can be designed to scan a sample in either of two modes: *constant-height* or *constant-current* mode. In constant-height mode, the tip travels in a horizontal plane above the sample and the tunneling current varies depending on topography and the local surface electronic properties of the sample. The tunneling current measured at each location on the sample surface constitutes the data set, the topographic image. In constant-current mode, a feedback is used to keep the tunneling current constant by adjusting the height of the scanner at each measurement point. For example, when the system detects an increase in tunneling current, it adjusts the voltage applied to the piezoelectric scanner to increase the distance between the tip and the sample. In this case, the motion of the scanner constitutes the data set.

The sensitivity to the local electronic structure makes STM imaging tricky especially when mapping the topography of a sample, which has oxidized regions since the tunnel current, will drop at those places and creates a valley like appearance.

Scanning tunneling spectroscopy (STS) studies the local electronic structure of a sample's surface. The electronic structure of an atom depends upon its atomic species (for instance, whether it is a gallium atom or an arsenic atom in the case of GaAs surface) and also upon its local chemical environment (how many neighbors it has, what kind of atoms they are, and the symmetry of their distribution).

STS encompasses many methods: taking "topographic" (constant-current) images using different bias voltages and comparing them; taking current (constant-height) images at different heights. The most popular method is ramping the bias voltage with the tip positioned over a feature of interest while recording the tunneling current. This results in current vs. voltage (I-V) curves characteristic of the electronic structure at a specific x,y location on the sample surface. It is possible to collect I-V curves at every point in a data set, providing a three-dimensional map of electronic structure. With a lock-in amplifier, dI/dV (conductivity) or dI/dz (work function) vs. V curves can be collected. The normalized quantity (dI/dV)/I/V reflects the local density of states. Bias dependence of the tunnel current is extremely informative to probe the occupied and unoccupied states in semiconductor surfaces. A classical example is the observation of the empty and occupied states of GaAs(110), which are localized at Ga and As atoms respectively. These states appear selectively in the images obtained at bias voltages of opposite polarities [135].

STM has been extensively used to study the interactions of adsorbate gases on metal surfaces, surface atomic structure and electron density of layered compounds and self-assembled monolayers of alkanes, organic conductors and conducting polymers [136,137]. It has been possible to study the dynamics of molecules on metal surfaces [138] and hence to observe chemical reactions and study kinetics, which has great implications in catalysis. STM and STS have been extensively used to probe electronic structure and view atomic resolution of nanomaterials for example, metal clusters [139], carbon nanotubes and their junctions [140] and perovskites [141].

Beyond a simple topographical imaging, STM can be used to manipulate atoms and pattern materials [142]. A classic example is the construction of a quantum corral structure using Fe atoms (see Figure 1.17) and the direct visualization of stationary waves inside the corral [143]. Manipulation of single porphyrins [144] and fullerenes [145] at room temperature in UHV has been demonstrated. In this latter experiment, a

molecular scale prototype of an abacus was fabricated, where single fullerenes were translated along the Cu(111) monoatomic steps by using the STM tip as manipulator.

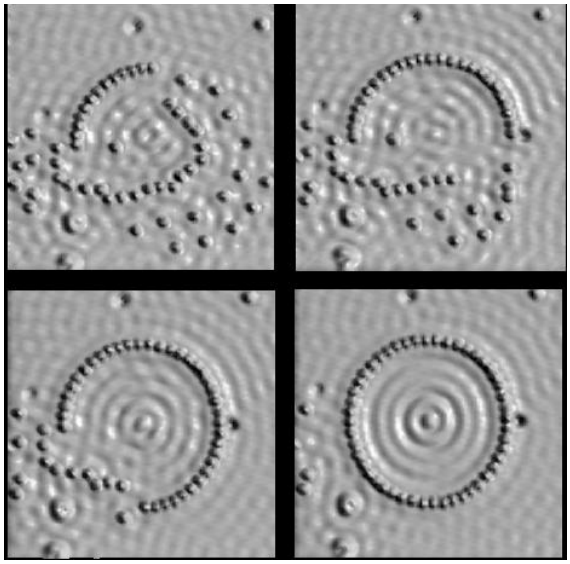

Figure 1.17. The making of Quantum Corral: Fe atoms on Cu(111) [reproduced from ref. 143].

Nanolithography by applying bias to metal tips to detach atoms from the tip and deposit them on the surface in a periodic manner has also been demonstrated [146]. Modifications in instrumentation have made it possible to perform STM and STS under UHV conditions at low temperature or higher temperatures. Lately, electrochemical STM [147] in which the tip acts as a working electrode with sample immersed in electrolyte, has been employed to do nanoscale oxidation/reduction or chemical etching reactions that can locally modify the surfaces of metals, semiconductors [148,149] or the electronic structure of molecules [150]. Tao *et al*. have devised a STM break junction technique to create metal-molecule junctions where in an STM tip is moved in and out of an Au substrate in the presence of molecules, and have successfully measured single molecule conductance of a variety of systems [151, 152].

1.4.2 Atomic Force Microscopy (AFM)

A force microscope detects forces acting between a sample surface and a sharp tip (< 10 nm), which is located at the free end of a 100 to 200 μm long cantilever (see Figure 1.18). A feedback system, which controls the vertical z-position of the tip on the sample

surface, keeps the deflection of the cantilever (and thus the force between the tip and sample) constant. Moving the tip relative to the sample in the (x,y) plane of the surface by means of piezoelectric drives, the actual position of the tip can be recorded as a function of the lateral position. In typical AFMs, cantilever deflections in the range from 0.1 Å to a few micrometers are measured, corresponding to forces from 10^{-13} to 10^{-5} N [153,154]. The most widely used method to measure cantilever deflection technique is beam deflection technique. A light beam from a laser diode is reflected from the rear side of the cantilever and focused on to a four-segment photodiode. If I_A, I_B, I_C and I_D are the currents, which are induced by the light in segments A-D of the photodiode, then the current $(I_A + I_B)–(I_C + I_D)$ represents a measure of the deflection of the cantilever. Additionally, the torsion of the cantilever can be measured through the analysis of the $(I_A + I_C)–(I_B+ I_D)$ current, which is proportional to the lateral force acting on the tip.

Several forces typically contribute to the deflection of an AFM cantilever. The force most commonly associated with atomic force microscopy is an interatomic force called the van der Waals force. The variation of the van der Waals force on the distance between the tip and the sample follows Lennard-Jones potential given by,

$$V(r) = \underset{\text{repulsive}}{\underset{\downarrow}{a/r^{12}}} - \underset{\text{attractive}}{\underset{\downarrow}{b/r^{6}}}, \; r \text{ being the distance,} \qquad (1.6)$$

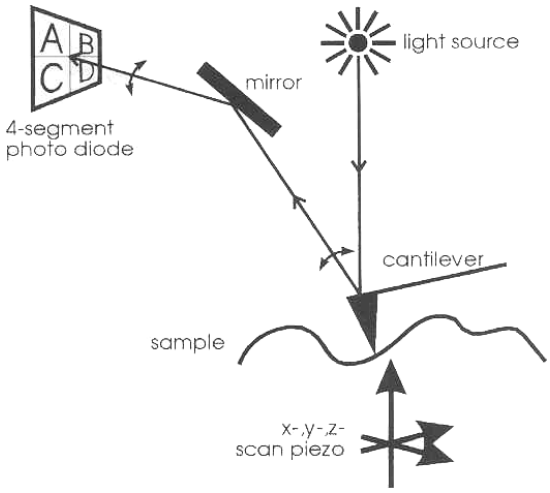

Figure 1.18. A schematic illustration of the principle behind AFM. The beam deflection technique for sensing cantilever deflections is shown [reproduced from ref. 153].

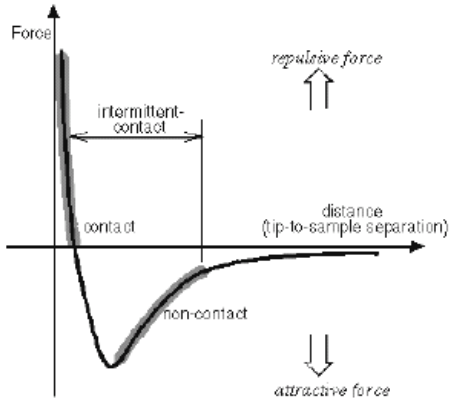

Figure 1.19. Interatomic force vs. distance curve. The different regimes corresponding to different modes of AFM operation is also indicated.

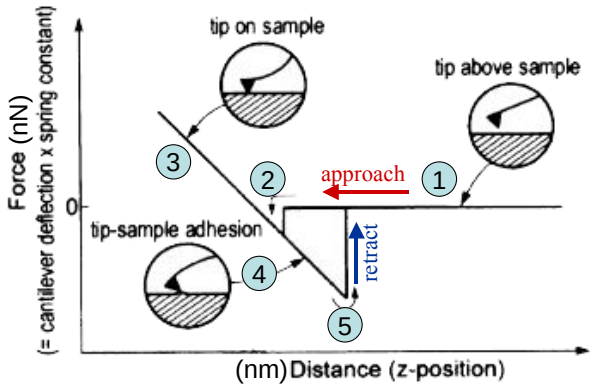

Figure 1.20. Force-distance plot acquired in AFM when tip approaches and retracts. Cartoons shown describe the interactions at different points of the curve. See text for explanation.

as shown in Figure 1.19. The typical working modes for AFM are named for their detection range in the Van der Waals force regime, i.e. 1) contact mode for repulsive regime, 2) non-contact for purely attractive regime and 3) tapping or intermittent mode for switching between the two regimes as indicated in the figure. Force-distance plot acquired in AFM by extending and retracting piezo also follow a similar behavior, except that the sample adhesion forces will also come into the picture and is given in Figure 1.20. Contact force is calculated by Hook's law,

$$F = -kz \tag{1.7}$$

k is the spring constant of the cantilever and z is the displacement. Various interactions happening are (1) large tip-sample distances; no interaction (2) as the tip approaches the attractive force overcomes the restoring force; 'jump to contact' point (3) tip pushes

farther into surface; a positive linear cantilever deflection is observed. With the retraction of tip, it traces the same path. (4) hysteresis is observed; the sample adhesion forces bends the cantilever (5) restoring force overcomes the adhesion force.

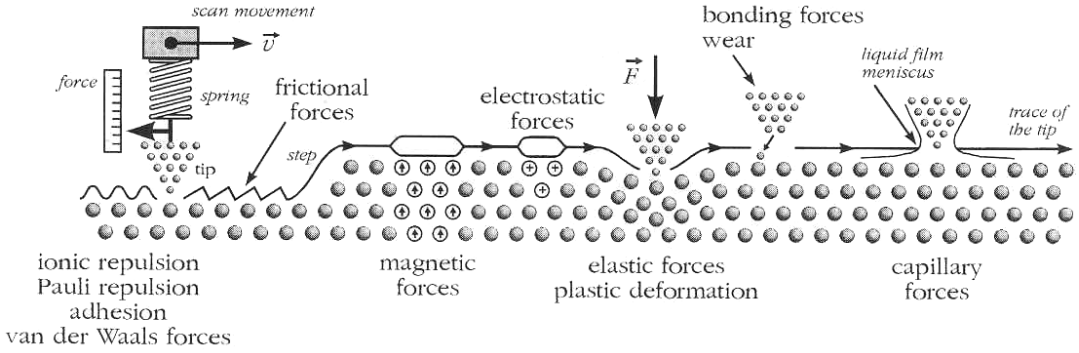

Figure 1.21. A summary of the relevant forces acting in AFM [reproduced from ref. 153].

Table 1.2. A compilation of forces and different application modes*

Forces (range of influence)	Application mode
[a, L] Magnetic forces (100 nm)	Magentic Force Microscopy (to probe magnetic domains)
[a, L] Electrostatic forces (100-500 nm)	Electric Force Micrsocopy (to probe electric field distribution) Local Anodic Oxidation (lithography)
Elastic forces, deformation	Nanoindentation, nanoscratching (to study mechanical properties)
[a, L] Capillary forces (10-200 nm)	Dip-pen nanolithography
Adhesion forces	Force spectroscopy (nature of surfaces)
Frictional forces	Lateral Force Microscopy (to probe samples with constituents of different chemical nature)
[a, S] Chemical binding forces (0.1-10 nm)	Force spectroscopy (to study different bonding/nonbonding forces in molecules)
[a, S] Van der waals forces (10 nm)	
[r, S] Pauli repulsion (0.1 nm)	Topography (contact mode AFM)
[r, S] Ionic repulsion	

*(a-attractive, r-repulsive, L-long range, S-short range)

The van der Waals forces are not the only force acting when a tip approaches a sample surface. Depending on the sample characteristics, several type of forces long-

range or short-range, attractive or repulsive, come into play that can be exploited to obtain other properties of sample surface and is of utmost significance in nanotechnology. A cartoon displaying the different forces is given in Figure 1.21. Table 1.2 lists the various forces, their range of influence and the AFM technique utilizing the force. Various applications require modifications in the tip and the electronics of the standard AFM. For instance, in order to do a magnetic mapping, the normally insulating probe made up of Si or Si_3N_4 is coated with a thin film of magnetic material and tapping mode scan is done in the 'lift mode'. Hence, any type of sample surface can be examined under AFM (roughness within the range of *z* range of piezo). Since various types of forces can be mapped, AFM is given a more general name, scanning force microscopy (SFM). Furthermore, AFM can be performed under UHV, air or liquid media.

AFM in contact mode

In contact-AFM mode, also known as repulsive mode, an AFM tip makes soft "physical contact" with the sample. The tip is attached to the end of a cantilever with a low spring constant (0.01-0.5 N/m), usually made of Si_3N_4. As the scanner gently traces the tip across the sample (or the sample under the tip), the contact force causes the cantilever to bend to accommodate changes in topography. Once the AFM has detected the cantilever deflection, it can generate the topographic data set by operating in one of two modes-*constant-height* or *constant-force* mode. In constant-height mode, the spatial variation of the cantilever deflection can be used directly to generate the topographic data set because the height of the scanner is fixed as it scans. In constant-force mode, the deflection of the cantilever can be used as input to a feedback circuit that moves the scanner up and down in z, responding to the topography by keeping the cantilever deflection constant. In this case, the image is generated from the scanner's motion. With the cantilever deflection held constant, the total force applied to the sample is constant.

If the cantilever is coated with a thin film of a metal, it can be used to measure electrical characteristics of the sample and it is called **conducting-atomic force microscopy (C-AFM)**. This technique has been employed lately to obtain conductance mapping of nanocomposites, I-V characteristics of molecules, nanotubes and other nanostructures. See Chapter 2, for a detailed description of C-AFM.

Lateral force microscopy (LFM)

In contact mode AFM, it is possible to measure the torsional motion of the cantilever during the scanning. The torsion of the cantilever depends on the lateral force or friction acting on the scanning probe. Lateral deflections of the cantilever usually arise from two sources: changes in surface friction and changes in slope. In the first case, the tip may experience greater friction as it traverses some areas, causing the cantilever to twist more strongly. In the second case, the cantilever may twist when it encounters a steep slope. To separate one effect from the other, LFM and AFM images should be collected simultaneously. This is possible in modern day AFMs, by employing a quad-cell position sensitive photodiode to measure the lateral component of deflection as explained in Section 1.4.2. The cantilever probe is most susceptible to the frictional effect when the scan direction is perpendicular to the major axis of the cantilever and therefore, the scan angle must be set to 90^o or 270^o to get a high quality friction image.

LFM studies are useful for imaging variations in surface friction, especially at nanometer scale that can arise from inhomogeneity in surface material, and also for obtaining edge-enhanced images of any surface. Hence, LFM mode has been used for characterizing nanocomposites to differentiate the component distribution and also patterns of two different molecules where height differences are not prominent [155].

AFM in noncontact mode

Non-contact AFM is one of several vibrating cantilever techniques in which an AFM cantilever is vibrated near the surface of a sample. The spacing between the tip and the sample is on the order of tens to hundreds of angstroms. A stiff cantilever (k-100 N/m) is vibrated close to its resonance frequency (100-400 kHz) by a piezo element. The resonance frequency

$$f_O = \sqrt{\frac{keff}{m}} \tag{1.8}$$

where

$$k_{eff} = k - {}^{\partial F}\!/_{\partial z}\,, \tag{1.9}$$

is the effective spring constant determined by the force gradient experienced by the cantilever. The change in the force gradient, expected when the tip is approaching the sample surface shifts the resonance frequency, which subsequently alters the amplitude of the cantilever vibration (see Figure 1.22). The signal obtained by the deflection sensor

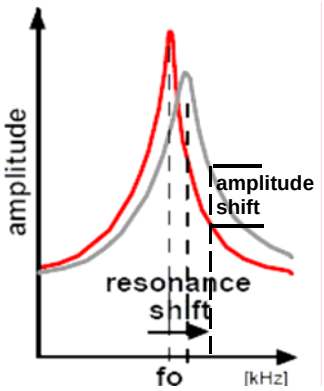

Figure 1.22. The shift in the resonance frequency caused by an external force gradient that results in a change of amplitude at a given frequency.

is analyzed by the lock-in technique. A subsequent feedback circuit regulates on a constant phase shift between the signal of the deflection sensor and the original driving signal or on a constant amplitude of the modulated deflection sensor signal. Both methods keep resonance frequency constant. Since the tip does not touch the sample during scanning, surface deformations and lateral forces are minimized. Hence this mode is suitable for imaging soft and elastic materials, monolayers of molecules etc. Also since a surface can be traced for a distance of several tens of nanometers, long-range forces can be imaged separated from the surface topography.

Recently, there has been considerable interest in phase imaging [156], which works by monitoring the phase differences between the driving oscillation of the cantilever and the actual cantilever oscillation during imaging. In phase imaging, the phase lag of the cantilever oscillation relative to the driving signal is simultaneously monitored. The phase lag is very sensitive to the variations in material properties of the surface such as elastic, electrostatic, magnetic, and thermal properties. Therefore, it provides us more than topographical information: variation in composition, adhesion, viscoelasticity and others.

Intermittent-contact AFM (Tapping mode AFM)

Intermittent-contact atomic force microscopy is similar to noncontact AFM, except that for intermittent contact the vibrating cantilever tip is brought closer to the sample so that at the bottom of its travel it just barely hits, or "taps," the sample. The cantilever's

oscillation amplitude changes in response to tip-to-sample spacing. An image representing surface topography is obtained by monitoring these changes. In this mode also, the friction or drag between the tip and the sample is eliminated and is more sensitive than noncontact mode.

Magnetic and electric force microscopy (MFM & EFM)

MFM or EFM images the spatial variation of magnetic forces or electric forces on a sample surface. For MFM, the tip is coated with a ferromagnetic thin film (Co/Cr) and magnetized before scanning. For EFM, tip is coated with any conductive material or doped in the case of Si tips and a bias is applied to the tip. The system operates in non-contact mode, detecting changes in the phase of the cantilever oscillation induced by the magnetic field's or electric field's dependence on tip-to-sample separation.

An image taken with a magnetic tip/conducting tip contains information about both the topography and the magnetic/electric properties of a surface. Which effect dominates depends upon the distance of the tip from the surface, because the interatomic magnetic/electric force persists for greater tip-to-sample separations than the van der Waals force. If the tip is close to the surface, in the region where standard noncontact AFM is operated, the image will be predominantly topographic. As you increase the separation between the tip and the sample, magnetic/electric effects become apparent. Typically, imaging is done in interleave mode, with phase image captured by lifting the cantilever to a particular height (lift mode) [157]. Monitoring the phase shift at different lift heights gives an idea of the field influence.

MFM can be used to image naturally occurring and deliberately written domain structures in magnetic materials [158]. It is routinely used to study the domain structure in thin films of magnetic materials and nanostructures [159]. EFM is useful to image various components in an electronic circuitry and conducting properties of nanomaterials [160].

Several other AFM modes have also been developed like scanning capacitance microscopy (capacitance mapping), scanning thermal microscopy (thermal conductivity mapping), Kelvin probe microscopy (work function mapping).

Scanning near-field optical microscopy (SNOM or NSOM)

SNOM is another important technique developed around AFM that has many potential applications in nanoscience. This technique enables users to work with standard optical tools in near field beyond the diffraction limit that normally restricts the resolution capability of such methods [161]. It works by exciting the sample with light passing through a sub-micron aperture formed at the end of a single-mode drawn optical fiber or an AFM tip. Typically, the aperture is a few tens of nanometers in diameter. The fiber is coated with aluminum to prevent light loss, thus ensuring a focused beam from the tip. The topography can be attained using normal force feedback. Scattered light from the sample is collected in reflectance or transmittance mode to get information. The most commonly chosen imaging mode is fluorescence, but there have been other examples including UV-visible, IR and Raman techniques.

Nanolithography also has been performed by modifying the molecular films or polymers by phototreatment with good resolution using SNOM [162].

Chemical Force Spectroscopy

Force-distance curve obtained when the tip approaches the sample in AFM reflects the interatomic interactions between them and a typical force curve is explained in the previous section. The specialty of AFM is its sensitivity to piconewton forces and

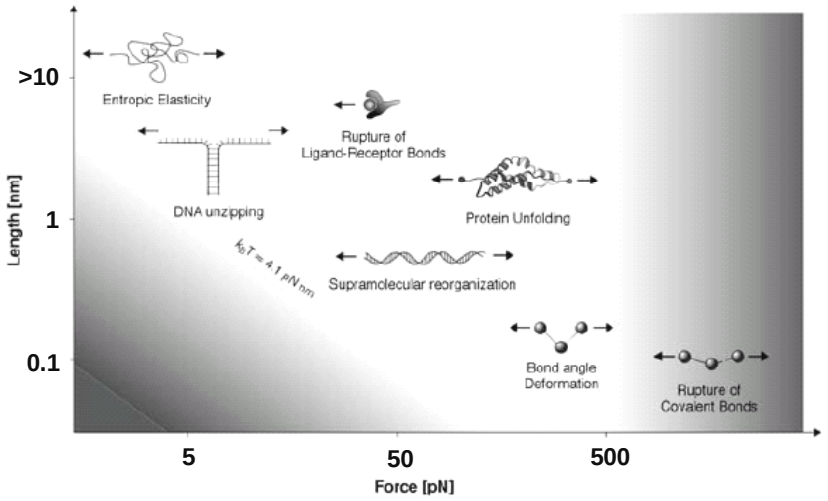

Figure 1.23. Force and length scales in different biological processes [reproduced from ref. 163].

nanometer precision, which can be exploited to probe molecular interactions, especially molecular recognition forces that are significant for gaining insight into many biological processes. Force range and length scales of different molecular processes are given in Figure 1.23. Furthermore, their selectivity and specificity are widely exploited in nanobiotechnology for developing bioanalytical and biomedical devices such as biosensors [164].

For this purpose, the AFM tip is functionalized with molecules for example; one counter part of the recognition pair and the other part is immobilized on a flat surface. Several factors have to be considered for the experiment, the foremost being the strong binding of the molecules to the surfaces, which should be stronger than the intermolecular force being studied [165]. Hence, AFM has been used to detect intermolecular forces between complementary DNA oligonucleotides [166], between ferritin antibody and ferritin [167], between concanavalin and oligosaccharides [168], and between fibronectin and bacterial cells [169]. The hysteresis portion of the F-D curve

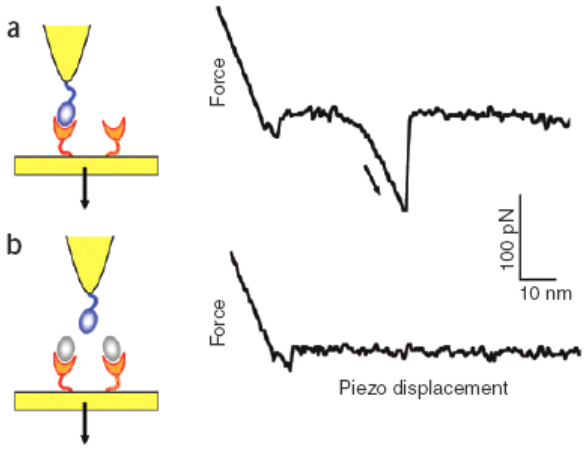

Figure 1.24. Measurement of molecular recognition interaction forces. (a) Typical force-displacement curve obtained upon retracting (down arrow) an AFM tip functionalized with oligoglucose carbohydrates from a surface modified with the lectin concanavalin A. b) Blocking experiment confirming the specificity of the interaction [reproduced from ref. 165].

(refer to Figure 1.20) gives a measure of the pull-off force or adhesion characteristics and its value is most important in molecular recognition studies. This is illustrated in the case of lectin-carbohydrate interaction, where in a force of 100 pN is attributed to the rupture of a single carbohydrate-lectin pair (see Figure 1.24). The unbinding event is accompanied by a nonlinear elongation force reflecting essentially the stretching of the

flexible spacer. In order to demonstrate the specificity of the measured unbinding force, F-D plot is acquired by bringing the carbohydrate functionalized AFM tip towards the surface immobilized lectin, already blocked with glucose. Force spectroscopy has also been applied to study DNA mechanics [170], protein folding/unfolding [171] and adhesion forces [172].

1.4.3 AFM based Nanolithography

The core and strength of AFM is the nanometer resolution probe that is capable of imaging and modifying surfaces. Since resolution mainly depends on the probe dimensions, it has become an attractive tool for generating nanoscale patterns [28, 137,142,173].

Physical Probe Lithography

This includes the formation of patterns by the physical movement of material on a substrate (for example, by applying a high contact force or through modifications induced by locally applied heat).

Mechanical patterning (nanoscratching or force lithography) has successfully been applied to substrates and films of soft metals such as copper, gold, nickel, and silver [173-175]. The structures that have been created include thin lines and pits. High-force AFM has also been applied to polymer substrates and polycarbonate films, both in contact as well as intermittent operation [176,177]. Besides the mechanically induced deformation of substrates and films, SPM techniques can also be used for the gentle movement of metallic [178–180] or latex [181] nanoparticles into dimers, trimers, linear structures and letters.

Thermomechanic patterning for data storage was demonstrated by heating poly(methylmethacrylate) film above its glass transition temperature using an AFM tip heated with the aid of a laser diode, in contact with the polymer. Indents of 100 nm size with densities up to 30 $Gbin^{-2}$ were achieved [182].

Nanoshaving and nanografting

In nanoshaving (Figure 1.25A) the AFM tip exerts a high shear force during the scan, which causes displacement of the SAM adsorbates. Performing this manipulation at the solid–liquid interface using a solution containing a different alkanethiol or nanoparticles,

one can induce the occurrence of chemisorption in the newly exposed gold surface as the tip ploughs through the matrix SAM, in the so called nanografting mode (Figure 1.25B). In both cases reducing the interaction forces between the tip and the sample surface, one can visualize the nanostructures in a non-invasive fashion [183,184]. Positive and negative pattern transfer has been demonstrated by nanografting of molecules with different lengths with respect to the surrounding matrix [185]. If the tip is conducting, after the grafting process, electron transfer properties of the patterned surface can be explored [186].

Dip pen nanolithography involves transfer of molecules or materials through a water meniscus formed between the AFM tip and substrate. It can be considered to be a combination of physical and chemical techniques since it involves physical transfer of materials to chemically modify a surface. This has been proved to be a versatile technique for nanopatterning and is reviewed in Chapter 6, Section 6.1.

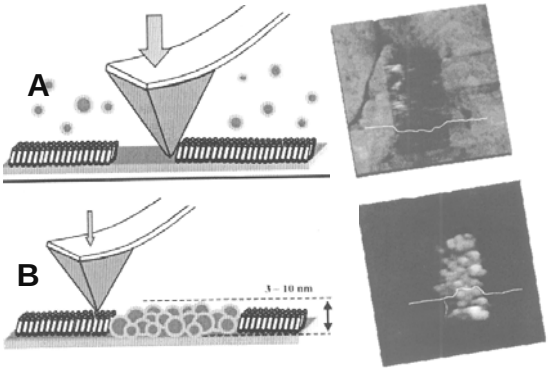

Figure 1.25. Schematics showing the nanoshaving of thiol molecules (A) and nanografting of Au nanoparticles (B). The corresponding AFM topography images are also shown [reproduced from ref. 184].

Oxidative Probe Lithography

This involves tip-induced electrochemical patterning, where in an electric field is applied between the tip and the substrate and the water meniscus formed at ambient conditions as the electrolyte (see Figure 1.26). Field-effect induced oxidation has been applied to Si [187-189], GaAs [190], Ti [191,192], Ta [193], Mo and Cr [194] and is popularly termed as local anodic oxidation (LAO). Electron-induced oxidation has been applied to organic resists [195], SAMs [196], and L-B films [197]. Such lithographically

produced oxides have been employed as gates in transistor devices [198]. Using a tip bias of 12 V (negative at the tip) and patterning speeds of 0.55 mms^{-1}, a MOSFET with an effective channel length of 0.1 mm was formed (with a patterning width of 0.21 mm).

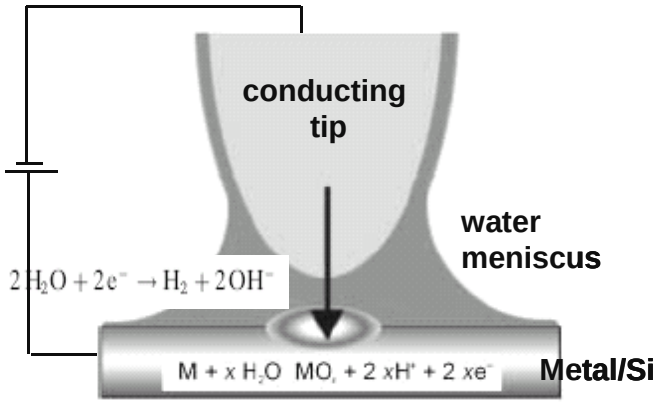

Figure 1.26. Schematic representation of the tip-induced oxidation of surfaces (LAO). Reaction schemes at anode and cathode are also given [adopted from ref. 28].

Avouris *et al*. reported the preparation of a single-electron transistor from constricted thin metal wires (Ti and Nb) by means of the local probe oxidation of a thin metal film [199]. Substrates can be oxidized through thin films of organic resists as well. Liu *et al*. reported a method to create assemblies of gold nanoparticles on patterned SAMs of octadecyltrichlorosilane (OTS) on SiO_2/Si [200]. LAO was employed to create SiO_2 protrusions through OTS and Au particles were adsorbed on aminosilane functionalized protrusions.

Oxidative probe lithography can also be employed to oxidize molecular monoalyers, introducing functionality rather than destroying them. Sagiv and coworkers demonstrated this for different silane molecules and subsequently functionalized them with other organic (amines, cationic species, thiols) molecules and inorganic substances yielding a variety of nanopatterned substrates [201,202]. The various possibilities are summarized in Figure 1.27. The terminal vinylic end group of 18-nonadecenyltrichlorosilane (NTS) on a p-doped silicon wafer could be oxidized to carboxylic group. The oxidation could be followed by friction imaging or phase imaging since carboxyl groups and alkyl groups have different interactions with tip. The oxidized region could be coupled with a second layer of OTS or with other metallic ions that can be reduced to metal, with aid of probe

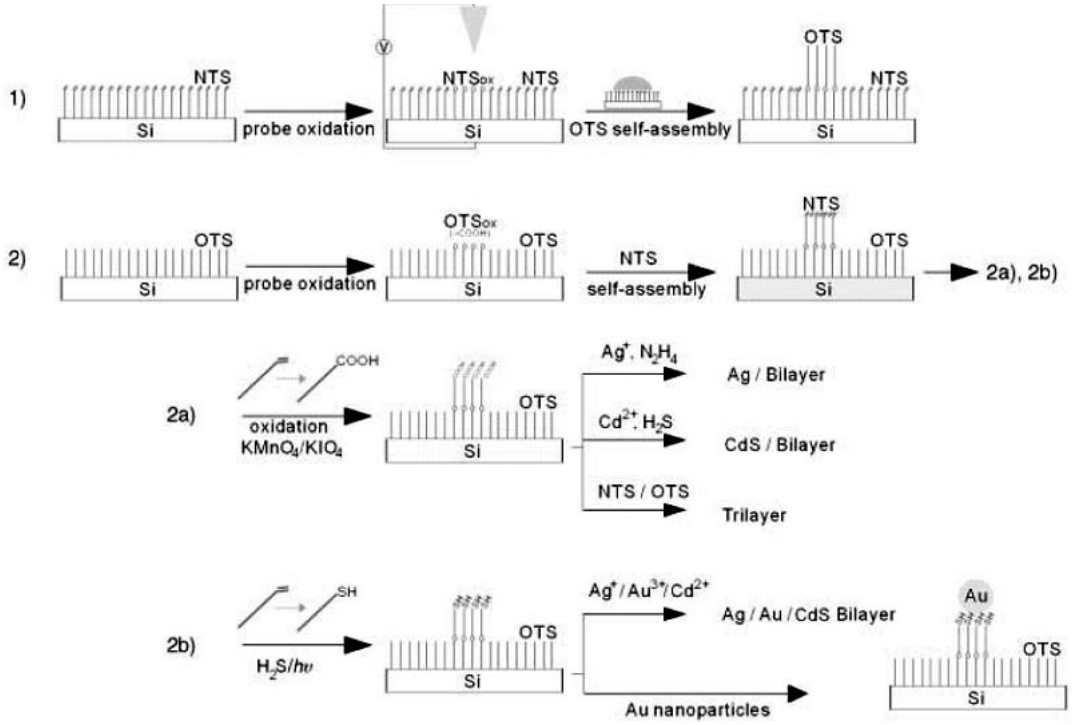

Figure 1.27. A schematic showing the various possibilities of using the tip-induced functionalized molecular patterns for producing inorganic nanopatterns [adopted from ref. 28].

or reducing agents. The terminal vinyl groups could also be converted to thiol groups by UV irradiation H_2S/Ar (1:1) atmosphere and employing thiol chemistry one can assemble metal or metal sulfide nanostructures. Poly-L-lysine coated gold nanoparticles assembled on oxidized OTS have been employed for coupling with proteins [28]. Possible applications may be found in nanosensor array devices.

In another variation called redox probe microscopy, the tip is coated with redox active materials like hydroquinone and ferrocenyl complexes [203]. Tip coated with poly (vinylferrocene) can be converted to positively charged ferricenium state by applying bias, which in turn is used to pick up negatively charged beads or particles to drop at specific locations by reduction. In the case of hydroquinone modified tip, the protons released during oxidation is used to pattern a pH sensitive block copolymer film.

AFM assisted electrostatic nanolithography has been demonstrated for polymers like poly(methylmethacrylate) and polystyrene, by applying electric field to the conducting tip [204]. The basis for feature generation is associated with mass transport of softened

polymer liquid in non-uniform electric field. An increase of carrier density, potentially arising from localized dielectric breakdown within the films, creates a 'cylinder' of polymer under the AFM tip susceptible to Joule heating arising from increased current flow. The strong electric field gradient polarizes the viscoelastic polymer, drawing it towards the AFM tip.

Although high-resolution patterns and nanostructures can be achieved on a variety of substrates by SPM lithography methods, their major drawback is the low patterning speed resulting in small area patterns. Current attempts have resulted in the development of multiple tip arrays capable of parallel processing [205,206].

References

[1] M. Köhler & W. Fritzsche, *Nanotechnology*, Wiley VCH, Weinheim (**2004**).

[2] http://www.ecse.rpi.edu/~schubert/Course-ECSE-6968 Quantum mechanics/

[3] M. Faraday, *Philos. Trans. R. Soc. Lond.*, 147, 145 (**1857**).

[4] G. Mie, *Ann. Phys.*, 25, 377 (**1908**).

[5] R. Gans, *Ann. Phys.*, 31, 881 (**1911**).

[6] R. Gans, *Ann. Phys.*, 47, 270 (**1915**).

[7] A. Einstein, *Ann. Phys*., 17, 549 (**1905**).

[8] R. Kubo, *J. Phys. Soc. Jap*. 17, 975 (**1962**).

[9] W. Ostwald, "Die Welt der Vernachl¨assigten Dimensionen", Steinkopf, Dresden (**1915**)

[10] R. Feynman, *Eng. Sci.*, Caltech, 23, 22 (**1960**), reprinted in *J. Micromech. Systems*, 1, 60 (**1992**).

[11] P. P. Edwards, R. L. Johnston & C. N. R. Rao in *Metal Clusters in Chemistry*, P. Braunstein, L. A. Oro, P. R. Raithby Eds, Wiley VCH, Weinheim (**1999**).

[12] Z. L. Wang, *J. Phys.: Condens. Matter*, 16, R829 (**2004**).

[13] S. Shivshankar, A. Rai, B. Ankamwar, A. Singh, A. Ahmad & M. Sastry, *Nat. Mater.*, 3, 482 (**2004**).

[14] A. A. Zinchenko, K. Yoshikawa & D. Baigl, *Adv. Mater*., 17, 2820 (**2005**).

[15] C. N. R. Rao & A. Govindaraj, *Acc. Chem. Res.,* 35, 998 (**2002**).

[16] U. K. Gautam, S. R. C. Vivekchand, A. Govindaraj & C. N. R. Rao, *Chem. Commun.*, 3995 (**2005**).

[17] G. W. Ho, A. S. W. Wong, D. -J. Kang & M. E Welland, *Nanotechnology*, 15, 996, (**2004**).

[18] H. Haberland, *Clusters of Atoms and Molecules I*, Springer Series in Chemical Physics, Springer-Verlag, Berlin (**1995**).

[19] D. B. Chrisey & G. K. Hubler, *Pulsed Laser Deposition of Thin Films*, Wiley VCH, New York (**1994**).

[20] C. N. R. Rao & A. Govindaraj, *Nanotubes and Nanowires*, RSC Series on Nanoscience, Royal society, London (**2005**).

[21] C. N. R. Rao, A. Govindaraj & S. R. C. Vivekchand, *Annu. Rep. Prog. Chem., Sect. A*, 102, 20 (**2006**).

[22] R. M. Brydson & C. Hammond in *Nanoscale Science and Technology*, R. Keisall, I. Hamley, M. Geohegen Eds., Wiley VCH, England (**2005**).

[23] A. A. Tseng, C. D. Chen & K. J. Ma, *IEEE Transactions on Electronics Packaging Manufacturing*, 26, 141 (**2003**).

[24] S. Matsui & Y. Ochiai *Nanotechnology*, 7, 247 (**1996**).

[25] H. W. Deckman, J. H. Dunsmuir, S. Garoff, J. A. McHenry & D. G. Peiffer, *J. Vac. Sci. Technol. B*, 6, 333 (**1988**).

[26] W. Frey, C. K. Woods & A. Chilkoti, *Adv. Mater.*, 12, 1515 (**2000**).

[27] Y. Xia & G. M. Whitesides, *Angew. Chem. Int. Ed.*, 37, 550, (**1998**).

[28] D. Wouters & U. S. Schubert, *Angew. Chem. Int. Ed.*, 43, 2480 (**2004**).

[29] X. Zhang, C. Sun & N. Fang, *J. Nanoparticle Res*., 6, 125 (**2004**).

[30] C. N. R. Rao, G. U. Kulkarni, P. J. Thomas & P. P. Edwards, *Chem. Soc. Rev.*, 29, 27 (**2000**).

[31] M. –I. Baraton, Synthesis, *Functionalization and Surface Treatment of Nanoparticles*, American Scientific Publishers, USA (**2003**).

[32] C. Burda, X. Chen, R. Narayanan & M. A. El-Sayed, *Chem. Rev.*, 105, 1025 (**2005**).

[33] G. Schmid, *Clusters and Colloids: From Theory to Applications*, Wiley VCH, Weinheim (**1994**).

[34] M. Sastry in *The Chemistry of Nanomaterials*, vol.1, C. N. R. Rao, A. Müller, A. K. Cheetham Eds., Wiley VCH, Weinheim (**2004**).

[35] C. T. Dameron, R. N. Reese, R. K. Mehra, A. R. Kortan, P. J. Carroll et al., *Nature*, 338, 596 (**1989**).

[36] P. Mukherjee, A. Ahmad, D. Mandal, S. Senapati, S. R. Sainkar et al., *Angew. Chem. Int. Ed.,* 40, 3585 (**2001**).

[37] M. Green, *Curr. Opin. Solid State Mater. Sci.*, 355 (**2002**).

[38] T. Trindade, *Curr. Opin. Solid State Mater. Sci.*, 347 (**2002**) & refs. there in.

[39] M. Rajamathi & R. Seshadiri, *Curr. Opin. Solid State Mater. Sci.*, 6, 337 (**2002**).

[40] G. R. Patzke, F. Krumeich & R. Nesper, *Angew Chem Int Ed Engl.*, 41, 2446 (**2002**).

[41] C. R. Martin, *Science*, 266, 1961 (**1994**).

[42] D. Almawlawi, C. Z. Liu & M. Moskovits, *J. Mater. Res.*, 9, 1014 (**1994**).

[43] G. A. Ozin & A. C. Arsenault, *Nanochemistry*, RSC publishing, Cambridge, UK, 2005.

[44] C. B. Murray, C. R. Kagan & M. G. Bawendi, *Science*, 270, 1335 (**1995**).

[45] E. V. Shevchenko, D. V. Talapin, N. A. Kotov, S. O'Brien & C. B. Murray, *Nature*, 439, 55 (**2006**).

[46] F. Caruso, *Colloids and Colloid Assemblies*, wiley VCH, Weinheim, 2004.

[47] G. U. Kulkarni, P. J. Thomas & C. N. R. Rao in *The Chemistry of Nanomaterials*, vol. 1, C. N. R. Rao, A. Müller, A. K. Cheetham Eds., Wiley VCH, Weinheim (**2004**).

[48] F. X. Redl, K.-S. Cho, C. B. Murray, & S. O'Brien, *Nature*, 423, 968 (**2003**).

[49] K. G. Thomas, S. Barazzouk, B. I. Ipe, S. T. S. Joseph & P. V. Kamat, *J. Phys. Chem. B*, 108, 13066 (**2004**).

[50] C. P. Collier, T. Vossmeyer & J. R. Heath, *Annu. Rev. Phys. Chem.,* 49, 371 (**1998**).

[51] Z. L. Wang, *J. Phys. Chem. B*, 104, 1153 (**2000**).

[52] A. N. Shipway, E. Katz & I. Willner, *ChemPhysChem*, 1, 18 (**2000**).

[53] K. Nørgaard & T. Bjørnholm, *Chem. Commun.*, 1812 (**2005**).

[54] C. N. R. Rao, G. U. Kulkarni, V. V. Agrawal, U. K. Gautam, M. Ghosh & U. Tumkurkar, *J. Collo. Inter. Sci.*, 289, 305 (**2005**)

[55] K. V. Sarathy, P. J. Thomas, G. U. Kulkarni & C. N. R. Rao, *J. Phys. Chem B*, 103, 399 (**1999**).

[56] R. A. Mcmillan, C. D. Paavola, J. Howard, S. L. Chan, N. J. Zaluzec & J. D. Trent, *Nat. Mater.*, 1, 247 (**2002**)

[57] M. –P. Pileni, *Nanocrystals forming Mesoscopic structures*, Wiley VCH, Weinheim (**2005**).

[58] M. Geissler & Y. Xia, *Adv. Mater.*, 16, 1249 (**2004**).

[59] J. V. Barth, G. Costantini & K. Kern, *Nature*, 437, 671 (**2005**).

[60] K. J. Klabunde & R. S. Mulukutla in *Nanoscale Materials in Chemistry*, K. J. Klabunde, Ed.; John Wiley & Sons, Inc., (**2001**).

[61] F. R-. Reinoso, *Carbon*, 36, 159 (**1998**).

[62] I. Z. Hilt & M. E. Byrne in *Dekker Encyclopedia of Nanoscience and Nanotechnology*, Marcel Dekker, Inc. (**2004**).

[63] M. Shim, N. W. S. Kam, R. J. Chen, Y. M. Li & H. J. Dai, *Nano Lett.*, 2, 285 (**2002**).

[64] J. C. Love, L. A. Estroff, J. K. Kriebel, R. G. Nuzzo & G. M. Whitesides, *Chem. Rev.*, 105, 1103 (**2005**).

[65] S. R. C. Vivekchand, U. Ramamurthy & C. N. R. Rao, *Nanotechnology*, 17, S344 (**2006**).

[66] R. Tenne, *Chem. Eur. J.*, 8, 5296 (**2002**).

[67] R. L. Johnston, *Phil. Trans. R. Soc. Lond. A*, 356, 211 (**1998**).

[68] S. H. M. Persson, L. Olofsson & L. A. Hedberg, *Appl. Phys. Lett.*, 74, 2546 (**1999**).

[69] Intel press release. http://www.intel.com/research/silicon/mooreslaw.htm

[70] P. J. Thomas, G. U. Kulkarni & C.N. R. Rao, *Chem. Phys. Lett.*, 321, 163 (**2000**).

[71] F. Remacle & R. D. Levine, *ChemPhysChem*, 2, 20 (**2001**).

[72] S.-H. Kim, G. Medeiros-Ribeiro, D. A. A. Ohlberg, R. S. Williams & J. R. Heath, *J. Phys. Chem. B*, 103, 10341 (**1999**).

[73] A. Taleb, F. Silly, A. O. Gusev, F. Charra & M.-P. Pileni, *Adv. Mater.,* 12, 633 (**2000**).

[74] S. Paul, C. Pearson, A. Molloy, M. A. Cousins, M. Green et al., *Nano Lett.*, 3, 533 (**2003**).

[75] S. Kolliopoulou, D. Tsoukalas, P. Dimitrakis, P. Normand, S. Paul, C. Pearson, A. Molloy & M. C. Petty, *Journal of Physics: Conference Series*, 10, 57 (**2005**).

[76] D. L. Gittins, D. Bethell, D. J. Schiffrin & R. J. Nichols, *Nature*, 408, 67 (**2000**).

[77] Z. Qi, M. Wei, I. Honma & H. Zhou, *ChemPhysChem*, 8, 264 (**2007**).

[78] L. Forró & L. Mihály, *Rep. Prog. Phys.*, 64, 649 (**2001**).

[79] F. Wudl, *J. Mater. Chem.*, 7, 1959 (**2002**).

[80] S. Reich, C. Thomson & J. Maultzsh, *Carbon Nanotubes*, Wiley VCH, Weinheim (**2004**).

[81] V. Derycke, R. Martel, J. Appenzeller & Ph. Avouris, *Nano Lett.,* 1, 453 (**2001**).

[82] S. Ghosh, A. K. Sood & N. Kumar, *Science*, 299, 1042 (**2003**).

[83] K. H. An, W. S. Kim, Y. S. Park et al., *Adv. Funct. Mater.*, 11, 387 (**2001**).

[84] R. H. Baughman, C. Cui, A. A. Zakidov et al., *Science*, 284, 1340 (**1999**).

[85] P. G. Collins, K. Bradley, M. Ishigami et al., *Science*, 287, 1801 (**2000**)

[86] N. S. Lee, D. S. Chung, I. T. Han et al., *Diamond Relat. Mater.*, 10, 265 (**2001**).

[87] W. Brütting, *Physics of Organic Semiconductors*, Wiley VCH, Weinheim, 2005.

[88] A. Aviram & M. A. Ratner, *Chem. Phys. Lett.*, 29, 277 (**1974**).

[89] J. R. Heath & M. A. Ratner, *Phys. Today*, 43 (**2003**).

[90] J. Chen, T. Lee, J. Su, W. Wang, M. A. Reed et al., in *Molecular Nanoelectronics*, M. A. Reed, T. Lee, Eds., American Scientific Publishers (**2003**).

[91] E. Tran, M. Duati, V. Ferri, K. Müllen, M. Zharnikov, G. M. Whitesides & M. A. Rampi, *Adv. Mater.*, 18, 1323 (**2006**).

[92] Y. Selzer & D. L. Allara, *Annu. Rev. Phys. Chem.*, 57, 593 (**2006**).

[93] P. K. Sudeep, B. I. Ipe, K. G. Thomas, M. V. George, S. Barazzouk, S. Hotchandani & P. V. Kamat, *Nano Lett.*, 2, 29 (**2002**).

[94] Y. Xia & N. J. Halas, *MRS Bull.,* 30, 338 (**2005**)

[95] E. Hutter & J. H. Fendler, *Adv. Mater.*, 16, 1685, (**2004**).

[96] K. L. Kelley, E. Coronado, L. L. Zhao & G. C. Schatz, *J. Phys. Chem. B*, 107, 668 (**2003**).

[97] M. A. El-Sayed, *Acc. Chem. Res.*, 34, 257 (**2001**).

[98] S. A. Maier, M. L. Brongersma, P. G. Kik, S. Meltzer, A. A. G. Requicha & H. A. Atwater, *Adv. Mater.*, 13, 1501 (**2001**).

[99] K. Kneipp, H. Kneipp, I. Itzkan, R.R. Dasari & M.S. Feld, *Chem. Rev.*, 99, 2957 (**1999**).

[100] K. G. Thomas & P. V. Kamat, *Acc. Chem. Res.*, 36, 88 (**2003**).

[101] L. E. Brus, *J. Chem. Phys.*, 80, 4403 (**1984**).

[102] W. J. Parak, T. Pellegrino & C. Plank, *Nanotechnology*, 16, 5 (**2005**).

[103] W. Chen, J. Z. Zhang & A. G. Joly, *J. Nanosci. Nanotech.*, 4, 919 (**2004**).

[104] J. Nanda, S. Sapra & D. D. Sarma, *Chem. Mater.*, 12, 1018 (**2000**) ; N. Karar, F. Singh & B. R. Mehta, *J. Appl. Phys.*, 95, 656 (**2004**); X. Wang & Y. Li, *Chem. Eur. J.*, 9, 5627 (**2003**).

[105] W. P. McConnell, J. P. Novak, L. C. Brousseau III, R. R. Fuierer, R. C. Tenent & D. L. Feldheim, *J. Phys. Chem. B*, 104, 8925 (**2000**).

[106] C. R. Kagan, C. B. Murray & M. G. Bawendi, *Phys. Rev. B*, 54, 8633 (**1996**).

[107] M. V. Artemyev, A. I. Bibik, L. I. Gurinovich, S. V. Gaponenko & U. Woggon, *Phys. Rev. B*, 60, 1504 (**1999**).

[108] S. R. C. Vivekchand, A. Govindaraj & C. N. R. Rao in *Nanomaterials Chemistry*, C. N. R. Rao, A. Müller, A. K. Cheetham Eds., Wiley VCH, Weinheim (**2007**).

[109] J. A. Misewich, R. Martel, Ph. Avouris, J. C. Tsang, S. Heinze & J. Tersoff, *Science*, 300, 783 (**2003**).

[110] M. Huang, S. Mao, H. Feick et al., *Science*, 292, 1897 (**2001**).

[111] M.-C. Jeong, B.-Y. Oh, M.-H. Ham & J.-M. Myoung, *Appl. Phys. Lett.*, 88, 202105 (**2006**).

[112] C.-L. Hsu, S.-J. Chang, Y.-R. Lin, P.-C. Li, T.-S. Lin, S.-Y. Tsai, T.-H. Lu & I.-C. Chen, *Chem. Phys. Lett.*, 416, 7578 (**2005**).

[113] Y. Huang, X. Duan & C. M. Lieber, *Small*, 1, 142 (**2005**).

[114] M.-S. Hu, H.-L. Chen, C.-H. Shen, L.-S. Hong, B.-R. Huang, K.-H. Chen & L.-C. Chen, *Nat. Mater.*, 5, 102 (**2006**).

[115] H. K. Kim, S. -J. Kang, S. -K. Choi, Y. -H. Min & C. -S. Yoon, *Chem. Mater.*, 11, 779 (**1999**).

[116] T. D. de Morais, F. Chaput, K. Lahlil & J. -P. Boilot, *Adv. Mater.*, 11, 107 (**1999**).

[117] C. A. Ross, T. A. Savas, H. I. Smith, M. Huang & R. Chantrell, *IEEE Trans. Magn.*, 35, 3781 (**1999**).

[118] A. Carl & E. I. Wassermann in *Magnetic Nanostructures*, H. S. Nalwa Ed., American Scientific Publishers, USA (**2002**).

[119] A. Sundaresan, R. Bhargavi, N. Rangarajan, U. Siddesh & C. N. R. Rao, *Phys. Rev. B*, 74, 161306 (**2006**).

[120] D. J. Norris, N. Yao, F. T. Charnock & T. A. Kennedy, *Nano Lett.*, 1, 3 (**2001**).

[121] J. H. Thomas, W. R. Heineman, H. B. Halsall, J. H. Nevin, A. J. Helmicki, H. T. Henderson & C. H. Ahn, *Lab on a Chip*, 2, 27 (**2002**).

[122] C. H. Ahn, J. –W. choi & H. J. Cho in *Encyclopedia of Nanoscience and Nanotechnology*, H. S. Nalwa Ed., American Scientific Publishers, USA (**2004**).

[123] J. Miller & A. Epstein, *MRS Bull.*, 25, 21 (**2000**).

[124] M. Verdagur, A. Blenzen, V. Marvaud, J. Vaissermann et al., *Coord. Chem. Rev.*, 190, 1023 (**2000**).

[125] S. Aubin, M. Wemple, D. Adams, H. L. Tsai, G. Christan & D. Hendrickson, *J. Am. Chem. Soc.*, 118, 7746 (**1996**).

[126] G. Christan, D. Galtesch, D. Hendrickson & R. Sessoli, *MRS Bull.*, 25, 66 (**2000**).

[127] J. Goldstein, D. Newbury, D. Joy, C. Lyman, D. Echlin et al., *Scanning Electron Microscopy and X-ray Microanalysis*, 3rd Edition, Springer Science and Business Media, Inc., USA (**2003**).

[128] R. E. Lee, *Scanning Electron Microscopy and X-ray Microanalysis*, PTR Prentice-Hall, Inc., New Jersey (**1993**).

[129] D. B. Williams & C. B. Carter, *Transmission Electron Microscopy*, Plenum Press, Newyork (**1996**).

[130] C. Brodsky, J. Byers, W. Conley, R. Hung, S. Yamada et al., *J. Vac. Sci. Technol. B*, 18, 3072 (**2000**).

[131] G. Binnig, H. Rohrer, Ch. Gerber & E. Weibel, *Phys. Rev. Lett.*, 49, 57 (**1982**).

[132] G. Binnig, C. F. Quate & Ch. Gerber, *Phys. Rev. Lett.*, 56, 930 (**1986**).

[133] R. Wiesendanger in *Handbook of Microscopy*,Methods II, S. Amelinckx, D. Van Dyck, J. Van Landuyt, G. Van Tendeloo, Eds., Wiley VCH, Weinheim (**1997**).

[134] J. Tersoff & D. R. Hamman, *Phys. Rev. B*, 31, 805 (**1985**).

[135] R. M. Feenstra, J. A. Stroscio, J. Tersoff & A. P. Fein, *Phys. Rev. Lett.*, 58, 1192 (**1987**).

[136] S. N. Magonov & M. –H. Whangbo, *Surface Analysis with STM and AFM*, Wiley VCH, Weinheim (**1996**).

[137] J. Loos, *Adv. Mater.*, 17, 1821 (**2005**).

[138] A. F. Carley, P. R. Davies, R. V. Jones, G. U. Kulkarni & M. W. Roberts, *Chem. Commun.*, 687 (**1999**).

[139] C. P. Vinod, G. U. Kulkarni & C. N. R. Rao, *Chem. Phys. Lett.,* 289, 329 (**1998**).

[140] P. Kim, T. W. Odom, J. L. Huang & C. M. Lieber, *Phys. Rev. Lett.*, 82, 1225 (**1999**) ; B. C. Satishkumar, P. J. Thomas, A. Govindaraj & C. N. R. Rao, *Appl. Phys. Lett*., 77, 2530 (**2000**).

[141] S. Kar, J. Sarkar, B. Ghosh & A. K. Raychaudhari, *Phys. Rev. B*, 74, 085412 (**2006**).

[142] P. Samorì, *J. Mater. Chem.*, 14, 1353 (**2004**).

[143] M. F. Crommie, C. P. Lutz, & D. M. Eigler, *Science*, 262, 218 (**1993**).

[144] T. A. Jung, R. R. Schlittler, J. K. Gimzewski, H. Tang & C. Joachim, *Science*, 271, 181 (**1996**).

[145] M. T. Cuberes, R. R. Schlittler & J. K. Gimzewski, *Appl. Phys. Lett.*, 69, 3016 (**1996**).

[146] D. Fujita & T. Kumakura, *Appl. Phys. Lett.*, 82, 2329 (**2003**).

[147] N. J. Tao, C. Z. Li & H. X. He, *J. Electroanal. Chem.*, 492, 81 (**2000**).

[148] W. Li, J. A. Virtanen & R. M. Penne, *Appl. Phys. Lett.*, 60, 1181 (**1992**).

[149] R. Schuster, V. Kirchner, X. H. Xia, A. M. Bittner & G. Ertl, *Phys. Rev. Lett.*, 80, 5599 (**1998**).

[150] W. Han, E. N. Durantini, T. A. Moore, A. L. Moore, D. Gust et al, *J. Phys. Chem. B*, 101, 10719 (**1997**).

[151] B. Q. Xu & N. J. Tao, *Science*, 301, 1221 (**2003**).

[152] X. Xiao, B. Xu & N. J. Tao, *Nano Lett*., 4, 267 (**2004**).

[153] U. D. Schwarz in *Handbook of Microscopy*,Methods II, S. Amelinckx, D. Van Dyck, J. Van Landuyt, G. Van Tendeloo, Eds., Wiley VCH, Weinheim (**1997**).

[154] F. J. Giessibl, *Rev. Mod. Phys.*, 75, 949 (**2003**).

[155] R. Overney & E. Meyer, *MRS Bull.*, 19, 26 (**1993**).

[156] G. H. W. Sanders, M. C. Davies, C. J. Roberts, S. J. B. Tendler & P. M. Williams, *Langmuir*, 15, 5433 (**1999**).

[157] X. Zhu & P. Grütter, *MRS Bull.*, 457 (**2004**).

[158] H. W. Van Kesteren, A. J. den Boef, W. B. Zeper, J. H. H. Spruit, B. A. Jacobs et al., *J. Appl. Phys.*, 70, 2413 (**1991**).

[159] R. Wiesendanger, M. Bode, M. Kleiber, M. Löhndorf, R. Pascal, A. Wadas et al., *J. Vac. Sci. Technol. B*, 15, 1330 (**1997**).

[160] A. Bachtold, M. S. Fuhrer, S. Plyasunov, M. Forero, E. H. Anderson et al., *Phys. Rev. Lett.*, 84, 6082 (**2000**).

[161] H. Okamoto & K. Imura, *J. Mater. Chem.*, 16, 3920 (**2006**).

[162] S. Sun & G. J. Leggett, *Nano Lett.*, 4, 1381 (**2004**).

[163] H. C. Schaumann, M. Seitz, R. Krautbauer & H. E. Gaub, *Curr. Opin. Chem. Biol.*, 4, 534 (**2000**).

[164] A. P. Turner, *Science*, 290, 1315 (**2000**).

[165] P. Hinterdorfer & Y. F Dufrêne, *Nat. Meth.*, 3, 347 (**2006**).

[166] G. U. Lee, L. A. Chrisey & R. J. Colton, *Science*, 266, 771 (**1994**).

[167] Y. Harada, M. Kuroda, & A. Ishida, *Langmuir*, 16, 708 (**2000**).

[168] A. Touhami, B. Hoffmann, A. Vasella, F. A. Denis & Y. F. Dufrêne, *Langmuir*, 19, 1745 (**2003**).

[169] Y. Bustanji, et al. *Proc. Natl. Acad. Sci. USA*, 100, 13292 (**2003**).

[170] M. Rief, , H. C-. Schaumann & H. E. Gaub, *Nat. Struct. Biol.*, 6, 346 (**1999**).

[171] A. F.Oberhauser, P. E.Marszalek, H. P. Erickson & J. M. Fernandez, *Nature*, 393, 181 (**1998**).

[172] C. Bai, J. Li, Z. Lin, J. Tang & C. Wang, *Surf. Interface Anal.*, 28, 44 (**1999**).

[173] R. M. Nyffenegger & R. M. Penner, *Chem. Rev.*, 97, 1195 (**1997**).

[174] R.W. Carpick, *Chem. Rev.*, 97, 1163 (**1997**).

[175] J. C. Rosa, M. Wendel, H. Lorenz, J. P. Kotthaus, M. Thomas & H. Kroemer, *Appl. Phys. Lett.*, 73, 2684 (**1998**).

[176] B. Klehn & U. Kunze, *J. Appl. Phys.*, 85, 3897 (**1999**).

[177] M. Heyde, K. Rademann, B. Cappella, M. Geuss, H. Sturm, T. Spangenberg & H. Niehus, *Rev. Sci. Instrum.*, 72, 136 (**2001**).

[178] L. T. Hansen, A. Kuhle, A. H. Sorensen, J. Bohr & P. E. Lindelof, *Nanotechnology*, 9, 337 (**1998**).

[179] T. R. Ramachandran, C. Baur, A. Bugacov, A. Madhukar, B. E. Koel, A. Requicha & C. Gazen, *Nanotechnology*, 9, 237 (**1998**).

[180] T. Junno, K. Deppert, L. Montelius & L. Samuelson, *Appl. Phys. Lett.*, 66, 3627 (**1995**).

[181] C. Ritter, M. Heyde, U. D. Schwarz & K. Rademann, *Langmuir*, 18, 7798 (**2002**).

[182] H. J. Mamin & D. Rugar, *Appl. Phys. Lett.*, 61, 1003 (**1992**).

[183] S. Krämer, R. R. Fuierer & C. B. Gorman, *Chem. Rev.*, 103, 4367 (**2003**).

[184] J. C. Garno, Y.Yang, N. A. Amro, S. Cruchon-Dupeyrat, S. Chen & G. -Y. Liu, *Nano Lett*., 3, 389 (**2003**).

[185] J. –F. Liu, S. C-. Dupeyrat, J. C. Garno, J. Frommer & G. -Y Liu, *Nano Lett.*, 2, 937 (**2002**).

[186] J. W. Zhao & K. Uosaki, *Langmuir*, 17, 7784 (**2001**).

[187] J. A. Dagata, J. Schneir, H. H. Harary, C. J. Evans, M. T. Postek & J. Bennet, *Appl. Phys. Lett.*, 56, 2001 (**1990**).

[188] P. M. Campbell, E. S. Snow & P. J. McMarr, *Appl. Phys. Lett.*, 63, 749 (**1993**).

[189] M. Yasutake &Y. Ejiri, T. Hattori, *Jpn. J. Appl. Phys.*, 32, L1021 (**1993**).

[190] M. Lazzarino, G. Mori, L. Sorba, D. Ercolani, G. Biasiol, S. Heun & A. Locatelli, *Surf. Sci.*, 600, 3739 (**2006**).

[191] S. C. Minne, P. Flueckiger, H. T. Soh & C. F. Quate, *J. Vac. Sci. Technol. B*, 13, 1380 (**1995**).

[192] N. Kramer, H. Birk, J. Jorritsma & C. SchSnenberger, *Appl. Phys. Lett.*, 66, 1325 (**1995**).

[193] H. Sugimura, T. Uchida, N. Kitamura & H. Masuhara, *Appl. Phys. Lett.*, 63, 1288 (**1993**).

[194] H. Sugimura & N. Nakagiri, *Jpn. J. Appl. Phys.*, 34, 3406 (**1995**).

[195] C. R. K. Marrian & E. A. Dobsisz, *J. Vac. Sci. Technol. B*, 10, 2877 (**1992**).

[196] C. R. K. Marrian, F. K. Perkins, S. L. Brandow, T. S. Koloski, E. A. Dobisz & J. M. Calvert, *Appl. Phys. Lett.*, 64, 390 (**1994**).

[197] L. Stockman, G. Neuttiens, C. van Haesendonck & Y. Bruynseraede, *Appl. Phys. Lett*., 62, 2935 (**1993**).

[198] S. C. Minne, H. T. Soh, P. Flueckiger & C. F. Quate, *Appl. Phys. Lett.*, 66, 703 (**1995**).

[199] R. Martel, T. Schmidt, R. L. Sandstrom & P. Avouris, *J. Vac. Sci. Technol. A*, 17, 1451 (**1999**).

[200] Q. Li & J. Zheng, Z. Liu, *Langmuir*, 19, 166 (**2003**).

[201] S. Liu, R. Maoz, G. Schmid & J. Sagiv, *Nano Lett.*, 2, 1055 (**2002**).

[202] R. Maoz, E. Frydman, S. R. Cohen & J. Sagiv, *Adv. Mater.*, 12, 424 (**2000**).

[203] D. J. D. Maz, J. E. Hudson, G. D. Storrier, H. D. Abruna, N. Sundararajan & C. K. Ober, *Langmuir*, 17, 5932 (**2001**).

[204] S. F. Lyuksyutov, R. A. Vaia, P. B. Paramonovi, S. Juhl, L. Waterhouse et al., *Nat. Mater.*, 2, 468 (**2003**).

[205] P. Vettiger & G. Binnig, *Sci. Am.*, 35 (**2003**)

[206] S. C. Minne, J. D. Adams, G. Yaralioglu, S. R. Manalis, A. Atalar & C. F. Quate, *Appl. Phys. Lett.*, 73, 1742 (**1998**).

Chapter 2

Optimization of Gold-Coated Probes for Conducting-Atomic Force Microscopy*

SUMMARY

Conducting–atomic force microscopy (C-AFM) has become a popular tool to measure the current–voltage characteristics as well as to obtain conductivity maps of nanobjects. It is equivalent to a two-probe multimeter with nanometer resolution. In this chapter, some aspects of the performance of gold-coated conductive probes used in C-AFM technique are discussed. The resistance of the nanocontact between the gold-coated AFM tip and the graphite substrate has been monitored at various applied forces. For small forces (<50 nN), resistance of the order of a few kiloohms was observed. Minimal contact resistance was observed for forces in the range 100-150 nN, beyond which the tip seems to undergo plastic deformation. The electrical break down of the Au-coating was also studied. The resistance of the nanocontact increased when current of the order of 100 μA was allowed to pass through, finally resulting in melting of the gold coating.

*A paper based on this work has appeared in J. Nanosci. Nanotech. (2005).

2.1 Introduction

The future growth of nanotechnology critically depends on the current research studies, especially related to electronic transport through single molecules, quantum dot arrays, nanotubes and nanowires as well as thin films of nanocomposites and conducting polymers. Since such measurements demand the probe size also to be of similar dimensions, early efforts to obtain current-voltage (I-V) characteristics of individual nanoobjects focused on employing scanning tunneling microscopy and spectroscopy [1,2]. Since then several methods have been developed such as break junctions [3], conducting atomic force microscopy (C-AFM) [4] and more recently with the aid of nanoelectrode fabrication by a variety of lithographic techniques [5].

Among the various tools for nanoscale measurements, C-AFM has become quite popular in the past decade due to its versatility. This is a modified AFM technique in which the cantilever tips are made conducting as probes of electrical measurement, yet with no compromise on the high-resolution imaging ability of the AFM. Thus, the measured electrical properties using a conducting probe can be directly correlated with the specific topographical features on a surface. C-AFM has an important advantage over the tunneling microscopy based techniques-which have been around for the last two decades [1] in that the measurement is carried out 'in contact' using a force feedback in contrast to tunnel current [4]. Hence the I-V characteristics measured is independent of the tip-sample distance, which is the case in STM. Also the force feedback allows conductivity mapping of samples with high resistances or nanocomposites with insulating regions. Early efforts in this direction are from Beale and Pease [6] and Meepagala *et al*. [7]. Since the demonstration of C-AFM in 1995, reporting band gap and charging energy measurements on individual CdS nanoparticles [8], there have been a few publications in this field. Cui *et al*. [9] have measured conductivity of individual octanedithiol and octanethiol molecules while Wold *et al*. [10] estimated the conductance of alkanethiols of varying chain lengths. Kelley *et al*. [11] have established the nature of charge transport in sexithiophene microdomains. This technique has been also employed to measure the electrical properties of nanotubes dispersed on substrates [12-14]. C-AFM has been extensively used for the conductivity mapping of polymers with different doping levels, which helps in giving an idea of the dopant distribution in the polymer [15,16]. Recently,

C-AFM has been used to study the influence of different base pairs on the electrical characteristics of DNA molecules [17].

Electrical measurements of materials are usually carried out with a set of four probes, the outer pair supplying current through the sample and the inner pair measuring the voltage drop. With a two-probe measurement, the contact resistance is always a matter of great concern. In C-AFM too, being a two-probe technique, the measured resistance values may not be as reliable especially when the resistance of the nanostructure being probed is comparable to the contact resistance between the tip and the object. In an interesting report, Petersen *et al*. [18] have illustrated the use of a specialized four-probe scanning technique for accurate estimation of conductivity of ultra thin films but this technique cannot easily be generalized as nanoobjects occur in all shapes and sizes. In the absence of any other versatile technique, therefore, it becomes imperative to understand how to deal with and manage practical issues related to the use of C-AFM. The issues include importantly, the variation of the contact resistance with the applied force, wearing away of the conductive coating due to either electrical break-down or mechanical damage and also the influence of contaminants under ambient conditions. Trenkler *et al*. [19] have evaluated different tips as probes for "electrical" AFM. There are also other articles in the literature dealing with the electrical and mechanical aspects of the tip contact [20,21]. A table listing the contact resistances of AFM probes with different metal coatings is given in Table 2.1.

Table 2.1. Contact resistances of AFM probes after various treatments [adopted from ref. 20].

Probe type	Contact resistance
50 nm evaporated Au on Si cantilever	120 Ω
2 nm Cr, 48 nm Au on Si	130 Ω
80 nm evaporated Ag on Si (1 day old)	30 Ω
80 nm evaporated Ag on Si (30 days old)	8 kΩ
45 nm sputtered Pt on Si	310 Ω
Phosphorous doped Si	4 MΩ

2.2 Scope of the Present Investigation

The present investigation pertains to a systematic study of the behavior of Au-coated cantilever probes used in C-AFM. C-AFM has become an important tool for probing I-V characteristics of nanoobjects and it is essentially a two-probe technique with the conducting cantilever as one of the electrodes having nanometer resolution. Tips are generally made conducting either by coating with metals or by doping Si. Au-coated tips were employed in our studies since they have low contact resistances as seen from Table 2.1. A few reports are available on the mechanical and electrical stability of different metal coatings on these probes [19-21]. There is no systematic study on the breakdown of the metal coating due to high current. The contact resistance varies with the type and nature of coating as well as with the contact force between the sample and the probe. The substrates chosen were highly oriented pyrolytic graphite and Au(111) film on mica, which are the usual substrates for deposition of nanoobjects for imaging with STM or AFM. We considered it essential to monitor the changes in contact resistance of the Au-coated tip as the current limit through the circuit is controlled that in turn helps to find the point of electrical break down. We have examined using SEM, the tip that had undergone electrical break down to inspect the damage to the coating. The effect of contact force on the contact resistance of the probe is also studied. The optimum conditions for the stability of the nanocontact have been arrived at, with the help of such a study. This has helped us to perform further C-AFM experiments on systems such as Au nanocrystal films, Pd-alkanethiolate bilayers etc. as described in subsequent chapters.

2.3 Experimental Details

The set up for C-AFM consists of a Multimode scanning force microscope attached to a Nanoscope IV controller (Digital Instruments, USA) and an external multimeter (Keithley 236) as the source and measurement unit for current–voltage characteristics. Commercial silicon nitride cantilever probes from Olympus (Japan) (spring constant, 0.61 N/m) were made conducting by coating them with gold (300–400 nm) by sputtering. Another set of tips were coated with 20 nm of Ti followed by 50 nm of Au using resistive evaporation method. The bias ramp was applied to the conducting probe through the tip holder and the current was measured from a terminal connected to the floating substrate.

The substrate was isolated from the scanner by proper insulation. The schematic of the set up is shown in Figure 2.1. The electrical noise was minimized by proper earthing of the instrument. The I-V measurements were done in ambient conditions. A photograph of the experimental set up in our laboratory is given in Figure 2.2.

Highly oriented pyrolytic graphite (HOPG) and Au coated mica were used as the conducting substrates. Silicon substrate was also used after cleaning in piranha solution (1:2 H_2O_2:H_2SO_4, *Caution: this mixture reacts violently with organic matter*) and etching in HF (1:10 HF:water). Scanning electron microscopy (SEM) was carried out with a Leica S-440I scanning electron microscope. Energy-dispersive analysis of X-rays (EDX) was performed with an Oxford Microanalysis Group 5526 system attached to the SEM employing Links (ISIS) software and a Si(Li) detector. EDX was carried out in the spot profile mode with a beam diameter of 1 μm.

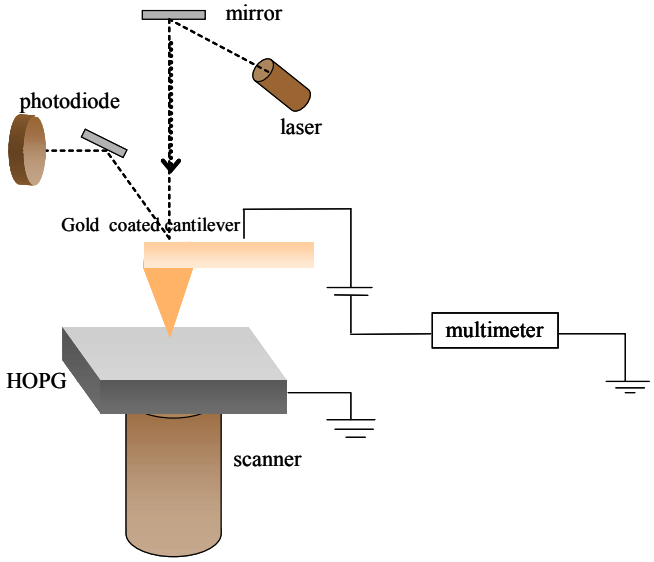

Figure 2.1. Schematic of the C-AFM setup. The bias is applied to the Au-coated cantilever and the current is measured from the terminal connected to the sample (HOPG) using a multimeter.

2.4 Results and Discussion

Prior to an I-V measurement, the conducting cantilever is allowed to come into contact with the substrate using the force feedback of AFM. After a brief scanning, the tip is stopped and held at a point to collect the I-V data. The data obtained for HOPG and

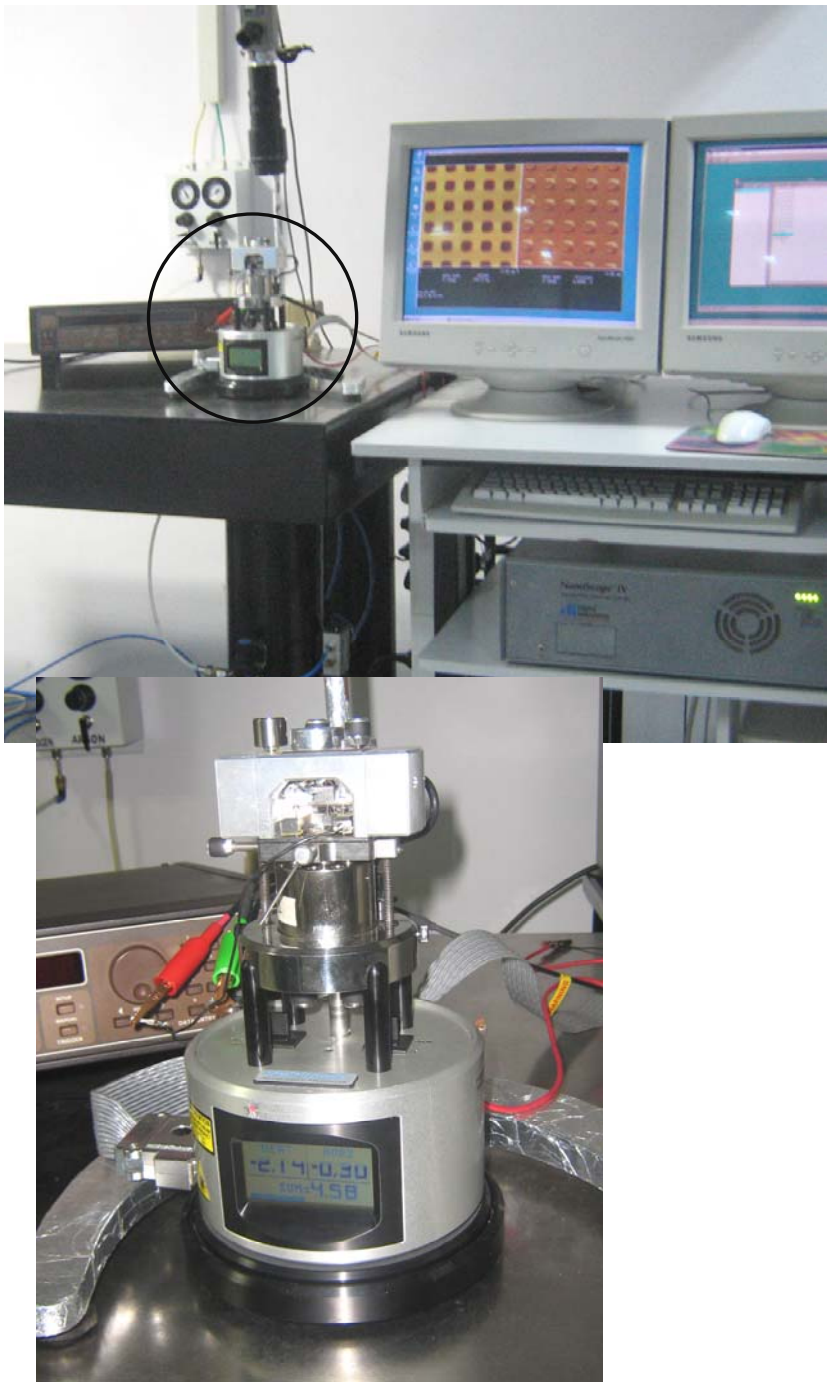

Figure 2.2. A photograph of the completely assembled C-AFM set up for I-V measurements. A magnified view of the Multimode AFM (Digital Instruments, Veeco Metrology group, Santa Barbara) is also shown.

freshly etched Si using a sputter Au-coated cantilever are shown in Figure 2.3. In the case of HOPG (Figure 2.3a), data obtained with two different probes (both prepared under similar conditions) are presented. Although both the probes exhibit linear variation typical of an ohmic contact, the resistance values obtained from the slopes are very different (80 and 400 Ω). However with a given tip, the resistance measured on different portions of the sample is nearly the same for a similar contact force. Therefore, the difference observed could only arise from the variations in the morphology of the sputtered gold film on the cantilever tip. It may be noted that the resistance of the sample itself (HOPG) is much smaller; the in-plane conductivity of graphite being 3×10^4 S/cm [22]. The I-V data of Si in Figure 2.3b is non-linear exhibiting a band gap of 1.1 eV. The measurements on Si were however, insensitive to the choice of tip. This only illustrates that C-AFM can work reproducibly where current involved is small preferably on materials with wide band gaps while for highly conducting materials, the contact resistance can greatly influence the measurement. For Ti/Au coated tip (by thermal evaporation) although the mechanical stability is better than Au coated ones, the contact resistance obtained on HOPG is higher, of the order of 1 kΩ. Sputter coating deposits a thicker and rougher layer of gold which in turn can cause an increase in the contact area of the tip on the substrate and hence less resistance.

For purely ohmic contacts (i.e, metal-metal contacts), the I-V is of the typical spreading resistance form,

$$R = \frac{\rho}{2a} \tag{2.1}$$

where a is the radius of the of tip and ρ is the resistivity of the material. If the mean free path of the electrons, l is much larger than a, which is not uncommon in AFM (typically l ~ 100 Å in metals), the contact resistance is given by Sharvin expression,

$$R = \frac{4\rho l}{3\pi a^2} \tag{2.2}$$

For resistances of about 100 Ω, such as in our case, a contact radius of 1.5 nm is obtained (ρl $=5\times10^{-12}$ Ωcm^2). Because the actual contacts are between two rough and contaminated surfaces, the contact resistance values in experiments are usually larger than calculated [20,23].

The effect of applied force on the resistance of the nanocontact was also studied. Figure 2.4 shows a typical plot of the variation of the measured resistance with the

applied force on the cantilever making contact with the HOPG substrate. In the inset is shown a typical force-distance (F-D) curve obtained by the controlled extension and retraction of the piezo. Graphite surface being non-sticky, the hysteresis in the F-D curve is not well pronounced. The force applied on the tip for the I-V measurement (and also for imaging) is calculated as Δz times the spring constant, where Δz is measured as shown in the inset of Figure 2.4 [24]. The applied force is varied by changing the setpoint value in the deflection setpoint box in the software. When the force applied is gentle,

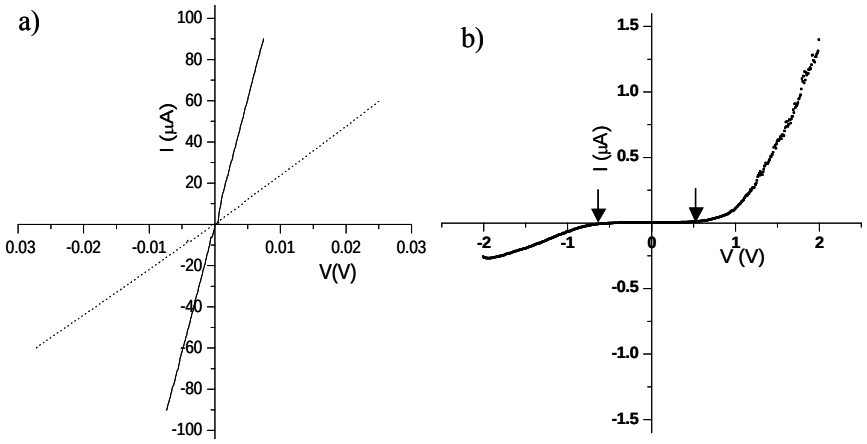

Figure 2.3. a) The I-V curves show the different contact resistances obtained for HOPG with two different gold-coated cantilevers. The solid line indicates a resistance of 80 Ω and the dashed line, 400 Ω. b) A typical I-V curve obtained on Si using C-AFM technique. The band gap of Si is indicated by the arrows.

below 50 nN, the resistance obtained is very high, ~ 20 kΩ and drops rapidly to around 2-3 kΩ with increase of force till 75 nN. A further increase in the force to 100 nN results in a further decrease of resistance to ~ 800 Ω. The rapid decrease in the resistance may be due to an increase in the effective contact area of the tip [20]. Such a rapid increase in conductivity is also observed when the force applied is enough to break the contaminant film on the sample from the ambient. With higher forces (> 200 nN), the resistance reaches a constant value of ~ 1.5 kΩ. The plateau region at higher contact forces can arise due to the plastic deformation of the tip [25]. Although the resistance and force values are tip-dependent, the plot in Figure 2.4 essentially depicts the relation between resistance and the applied force in a nanocontact. A moderate force of 100-150 nN seems to establish a stable contact.

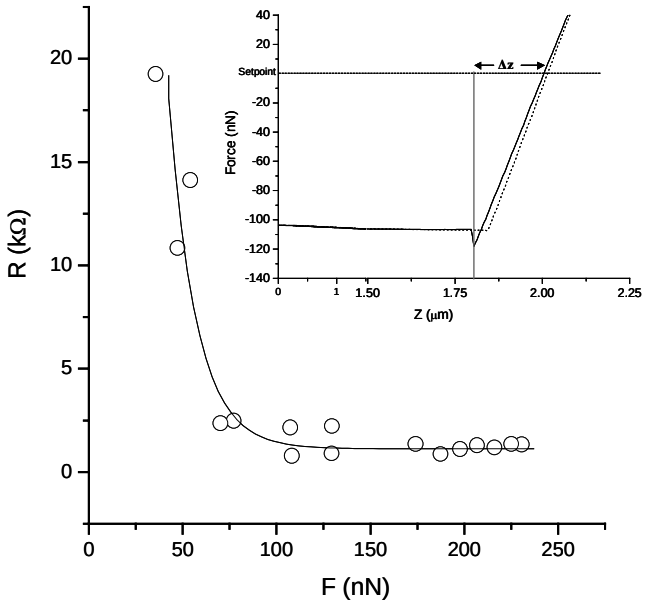

Figure 2.4. A plot of the resistance of HOPG against the contact force of the cantilever. The line joining the points is a guide to the eye. The inset shows a typical force-distance curve. The solid line shows the extension of the piezo (approach of the tip) and the dotted line, the retraction of piezo. The change in displacement with respect to the jump-off contact is indicated as Δz.

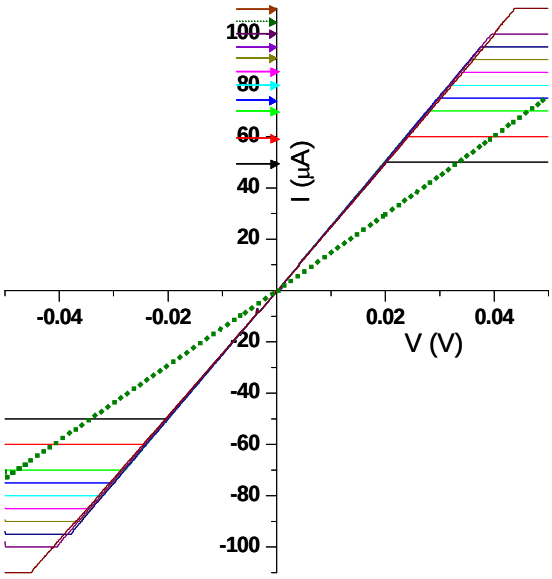

Figure 2.5. The current–voltage curves of graphite obtained using conducting AFM technique for a bias ramp of ±50 mV. The different curves are obtained when the upper current limit of the multimeter as indicated by the arrows, is gradually increased to 110 μA. At 110 μA limit, the current suddenly decreased as indicated by the dotted line. The flattened portions of the data are due to the set current limits.

The choice of voltage and current settings is often difficult due to the unpredictable nature of the contact resistance. This aspect was studied in some detail by carefully limiting the maximum current passing through the contact. In the plot shown in Figure 2.5, the voltage was ramped from -50 to +50 mV each time while increasing the current limit from 50 to 110 μA. Linear characteristics is indicative of the ohmic contact in all the cases. Between current limits of 50 to 80 μA, the I-V data almost overlap each other corresponding to a constant resistance of 390 Ω. As the current limit

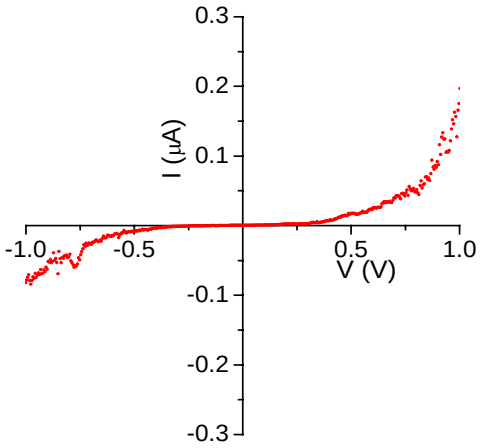

Figure 2.6. The I-V curve obtained with the gold-coated cantilever tip after a passage of current of the order of hundreds of microamps. The bias was increased to ±1V to see an appreciable output current.

was increased to 110 μA, we saw a small increase in the resistance (~ 400 Ω), but at this stage, the tip became unstable. The subsequent I-V (dotted line in Figure 2.5) showed that the resistance had increased to 660 Ω and was still increasing. Finally, in order to produce observable current in the circuit, the bias was increased to a wider range (±1 V), when a nonlinear curve with currents in nA was observed as shown in Figure 2.6. The above observations narrate the behavior of the tip carrying currents that can actually melt away the conductive gold coating and expose the nonconducting Si_3N_4 material inside. The heat generated at the nanocontact is estimated to be 4.8 μW, which amounts to 27 picograms of gold (specific heat of gold, 0.129 J/gK). The nonlinear curve with a blockade as seen in Figure 2.6 can arise due to discontinuous gold patches on the tip and is typical of a metal-insulator-metal tunnel junction. Tip-melting is common with the Au

tips handling currents of a few tens of μA. Similar results were obtained with other conducting substrates such as gold deposited on mica.

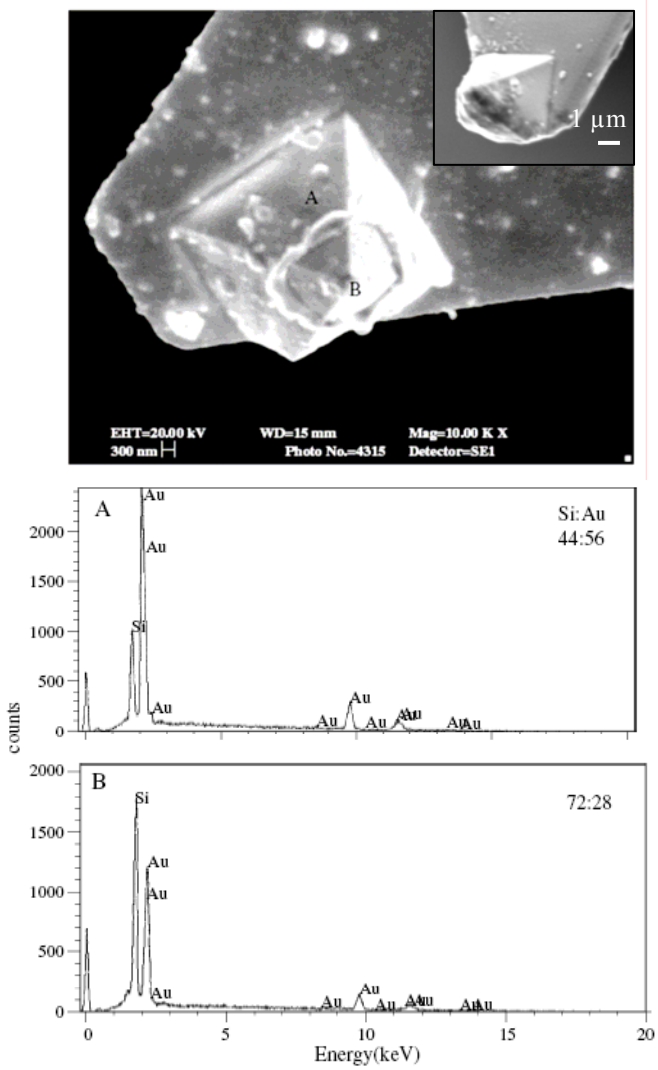

Figure 2.7. Scanning electron micrograph of the Au-coated AFM probe, which has undergone electrical break down. The image clearly shows the melted end of the tip. Inset shows the SEM of the as-coated tip. The EDX measurements done at different portions of the tip (A and B) shown below gives the relative amount of Si and gold at the melted end and at the farther portion.

The Au-coated AFM probe that has been subjected to high current passage (2 mA) is examined under a scanning electron microscope. Figure 2.7 shows the SEM of the used tip. The melted region of the conductive coating is clearly seen in the image. Inset shows the SEM of the as prepared tip coated with Au by sputtering. EDX data collected at the

two locations of the used tip, also shown in Figure 2.7, gives an estimate of the relative contents. In the tip region, the Si to Au ratio is 72:28 while at rare end, where gold coating is still intact, the ratio is 44:56. Gold depletion at the tip region clearly refers to the melting process. The left over gold appears as small islands and patches. From the melted region, we estimate the amount of gold to be 21 picograms which closely matches that calculated (27 picograms) assuming resistive heating. Thus, it is apparent that in C-AFM, a tip in contact with a conducting substrate can reach a situation commonly encountered in break-junctions.

2.5 Conclusions

We have studied some practical issues related to the use of Au-coated probes in conducting-AFM technique, which is a popular tool to measure the I-V characteristics of nanomaterials. We have examined the effect of applied force on the resistance of the nanocontact between the probe and the HOPG substrate. For small forces (< 50 nN), resistance of the order of a few kiloohms was observed. Minimal contact resistance was observed for forces in the range 100-150 nN beyond which the tip seems to undergo plastic deformation. Current passing through the tip too determines the stability of the nanocontact. The electrical stability of the tip coating was studied by carefully controlling the current while measuring the resistance on a conducting substrate. Typically the probes could handle currents of the order of 100 μA and use of higher current resulted in melting of the metal coating of the tip. This knowledge helped us in further experiments with C-AFM for successful measurement of electrical properties of nanomaterials, as detailed in subsequent chapters.

References

[1] D. A. Bonnell, *Scanning Tunneling Microscopy and Spectroscopy*, VCH Publishers Inc., NewYork (**1993**).

[2] M. Ouyang, J. L. Huang & C. M. Lieber, *Acc. Chem. Res.*, 35, 1018 (**2002**).

[3] M. A. Reed, C. Zhou, C. J. Muller, T. P. Burgin & J. M. Tour, *Science*, 278, 252 (**1997**).

[4] T. W. Kelley, E. L. Granstrom & C. D. Frisbie, *Adv. Mater.*, 11, 261 (**1999**).

[5] C. Brodsky, J. Byers, W. Conley, R. Hung, S. Yamada et al., *J. Vac. Sci. Technol. B*, 18, 3072 (**2000**).

[6] J. P. Beale & R. F. W. Pease, *38th IEEE Holm Conference on Electrical Contacts*, 45 (**1992**).

[7] S. C. Meepagala, F. Real & C. B. Reyes, *J. Vac. Sci. Technol. B*, 9, 1340 (**1991**).

[8] B. Alperson, S. Cohen, I. Rubinstein & G. Hodes, *Phys. Rev. B*, 52, R17017 (**1995**).

[9] X. D. Cui, A. Primak, X. Zarate, J. Tomfohr, O. F. Sankey, A. L. Moore, T. A. Moore, D. Gust, G. Harris & S. M. Lindsay, *Science*, 294, 571 (**2001**).

[10] D. J. Wold & C. D. Frisbie, *J. Am. Chem. Soc.*, 122, 2970 (**2000**).

[11] T. W. Kelley & C. D. Frisbie, *J. Vac. Sci. Technol. B*, 18, 632 (**2000**).

[12] P. J. de Pablo, C. Gomez-Navarro, M. T. Martinez, A. M. Benito, W. K. Maser, J. Colchero, J. Gomez-Herrero & A. M. Baro, *Appl. Phys. Lett.*, 80, 1462 (**2002**).

[13] J. G. Park, S. H. Lee, B. Kim & Y. W Park, *Appl. Phys. Lett.*, 81, 4625 (**2002**).

[14] P. J. de Pablo, C. Gomez-Navarro, J. Colchero, P. A. Serena, J. Gomez-Herrero & A. M. Baro, *Phys. Rev. Lett.*, 88, 036804-1 (**2002**).

[15] C. -G. Wu & S. -S. Chang, *J. Phys. Chem. B*, 109, 825 (**2005**).

[16] C. I.-Zanetti, A. Mechler, S. A. Carter & R. Lal, *Adv. Mater.*, 16, 385 (**2004**).

[17] C. Nogues, S. R. Cohen, S. Danube, N. Apter & R. Naaman, *J. Phys. Chem B*, 110, 8910 (**2006**).

[18] C. L. Petersen, T. M. Hansen, P. Bøggild, A. Boisen, O. Hansen, T. Hassenkam & F. Grey, *Sens. Actuators A*, 96, 53 (**2002**).

[19] T. Trenkler, T. Hantschel, R. Stephenson, P. De Wolf, W. Vandervorst *et al.*, *J. Vac. Sci. Technol. B*, 18, 418 (**2000**).

[20] R. E. Thomson & J. Moreland, *J. Vac. Sci. Technol. B*, 13, 1123 (**1995**).

[21] S. P. Jarvis, M. A. Lantz, H. Ogiso, H. Tokumoto & U. Durig, *Appl. Phys. Lett.*, 75**,** 3132 (**1999**)**.**

[22] S. Yoshimura & R. P. H. Chang, *Supercarbon*, Springer Series in Materials Science, Springer-Verlag, Germany (**1998**).

[23] M. A. Lantz, S. J. O'Shea & M. E. Welland, *Phys. Rev. B*, 56, 15345 (**1997**)

[24] Digital Instruments (Veeco) Support Note.

[25] M. J. Loiacono, E. L. Granstrom & C. D. Frisbie, *J. Phys. Chem. B*, 102, 1679 (**1998**).

Chapter 3

Nanoscale Rectifiers: Electrical Characterization of L-B Films of Gold Nanocrystals Supported on an Organic Layer by C-AFM*

SUMMARY

Nanoscale diode would be an integral part of most nanoelectronic devices. In this chapter, we discuss rectifying properties of monolayer and bilayers of dodecanethiol-capped Au nanocrystals studied using C-AFM. A self-assembled Langmuir monolayer of gadolinium stearate (GdSt) held on an oxide passivated Si(001) surface formed the substrate. Au nanocrystals are deposited on the GdSt-SiO_2-Si substrate by Langmuir-Blodgett (L-B) technique, at different surface pressures resulting in monolayer and bilayer formation. The morphology of the films that essentially consists of network of islands and interconnects, strongly depends on the surface pressure of deposition and has been monitored using AFM. The mechanism of rectification is explained on the basis of the spatial asymmetry in two tunnel barriers – one formed by organic tails of thiol molecules lying between a C-AFM tip and Au nanocrystal and the other formed by a thiol-GdSt-SiO_2 barrier in between an Au nanocrystal and Si. This effect is enhanced in the case of the bilayer system with the rectification ratio increasing from 16 in the case of the monolayer, to 128.

*Papers based on this work have appeared in J. Phys. Chem. B (2004) and Phys. Rev. B (2005).

3.1 Introduction

Nanocrystals (NCs) are essentially quantum dot (QD) structures due to their finite size exhibiting interesting size-dependent properties that render them suitable for many optical, electronic, sensor and catalytic applications [1,2]. Single electron transport is a well-studied phenomenon and prototype devices based on nanocrystals have been accomplished [3-5]. Assembling QDs into one, two and three-dimensional arrays offer the promise of "artificial atom" solids with unique properties arising from the collective or individual behavior depending on the inter-QD separation and core sizes [6]. Several methods of obtaining QD superlattices or arrays include self-assembly by simple evaporation of the ligand passivated QDs or by providing suitable functional molecules on substrates for obtaining heterostructures, Langmuir-Blodgett (L-B) method and lithographic techniques [1,7,8]. L-B technique, wherein a monolayer of amphiphilic molecules or NCs is transferred to the substrate at a particular surface pressure, has been extensively used for obtaining NC arrays and probing electron transport through them since it offers easy tuning of the inter-NC separation by monolayer compression. In a pioneering experiment, Heath and coworkers observed Mott-Hubbard type reversible metal-insulator transitions at room temperature by compressing an L-B film of Ag NCs capped with dodecanethiol [9,10]. Since then, there have been a vast deal of studies on the electron transport through NC arrays of different particle sizes and interparticle separations, carefully tuned by chemical synthesis, ligand chain length or L-B compression [11-16]. The above studies have provided an insight into the basic physics of these quantum dot solids. The major energy terms that control the electron transport are the diameter-dependent site energy (α_i) of the highest-lying electron in each NC, the inter-site exchange coupling (β), the inherent fluctuations in the site energy ($\delta\alpha$) due to small but finite nanocrystal size dispersion and the Coulomb charging energy (E_c), which is the energy required to transfer an electron from one NC to an electrically neutral neighbor. Nanocrystal solids in the insulating state are characterized by weak exchange coupling ($\beta << E_c$). In contrast, the formation of strongly coupled arrays with delocalized wave functions characteristic of metallic conduction requires that the exchange coupling dominate both charging energy ($\beta >> E_c$) and also any disorder induced localizations [6, 17,18]. Temperature dependent transport studies have revealed the role of disorder in the

localization of wavefunctions and activated hopping [14,15]. In the case of grossly assembled nanocrystalline films of gold linked by dithiols, a percolation theory is proposed to explain the conduction [18,19]. These studies have led to the design of NC devices capable of lasing and rectification [20,21].

We have undertaken a systematic study to understand the relation between morphology and transport property of gold NC films deposited by L-B technique at different surface pressures. The system consists of Si(001)/SiO_2 on which a monolayer of a fatty acid salt, gadolinium stearate and Au NCs capped with dodecanethiol are deposited sequentially by L-B technique and is hereafter designated as Au-GdSt-SiO_2-Si. The morphology of the top Au film is controlled by choosing an appropriate surface pressure at which the Langmuir monolayer of Au film is deposited. The topography and construction of the films are monitored by atomic force microscopy (AFM). I-V characteristics measured by Conducting AFM, a local probing technique [22], showed non-ohmic transport properties and diode behavior that were dependent on the morphology. We demonstrate that the rectification property arises from the asymmetric spatial configuration in which the thiol capped gold NCs are held. Such rectification properties have been observed rarely in the case of gold NCs. Schmid and co-workers have reported diode behavior in the case of electron beam irradiated Au_{55} cluster monolayer due to asymmetric ordering in the cluster monolayer initiated by charging [23]. Au and Ag nanoparticle films functionalized with donor and acceptor molecules are also reported to exhibit rectification properties [24].

3.2 Scope of the Present Investigation

Nanomaterial-based rectifiers will be important ingredients in nanotechnology and the simplest application of these rectifiers will be in memory devices with enormous storage capacity [25]. The present status of this field is, however, not suitable for immediate technological applications demanding sharp voltage thresholds, large current rectification ratios, small time constants, and above all, easy-to-form stable molecular structure. Experimental and theoretical studies of I-V characteristics of monomolecular films are being carried out extensively to achieve such desired properties and these studies also improve our basic understanding of the electrical transport phenomena in low

dimension. The original concept of molecular rectifier was developed with the assumption that highest occupied molecular orbital (HOMO) and lowest unoccupied molecular orbital (LUMO) can be confined in two parts of a molecule separated by an insulator bridge that prevents orbital overlap or "spilling off" forming a donor-insulator-acceptor (D-σ-A) structure [26]. Since then there have been several attempts to realize these systems experimentally and they have led to D-π-A type systems as well [27-30].

It is now realized that one can form rectifiers easily by connecting a molecule asymmetrically to two tunnel barriers from each side in a line of sight. In this situation, one can, in principle, design a rectifier by altering the spatial asymmetry of the connecting tunnel barriers [25,31-33]. Here, we demonstrate that it is possible to form a rectifier using a dodecanethiol capped gold NC (3.3 nm dia) held in an asymmetric spatial configuration with thiol chains on one side and a monolayer of gadolinium stearate on SiO_2-Si substrate, on the other. The properties of GdSt monolayer itself have been studied in detail [34]. Although electrical properties of metal nanoclusters connected by organic tails are being studied rigorously [11-15,35], so far, a rectifier functionality from such nanocrystal systems has not been reported. Recently, rectification from metal NC film functionalized with donor and acceptor molecules has been reported [24]. Petty and co-workers have reported a FET made up of L-B deposited gold nanoparticles for nonvolatile memories [35-37].

3.3 Experimental Details

3.3.1 Synthesis and characterization of gold NCs

Dodecanethiol encapsulated Au nanocrystals were prepared by Brust method [38]. Briefly, to $HAuCl_4$ solution (1 mL, 25 mM), 10 mL of 10 mM toluene solution of the phase transfer agent tetraoctylammonium bromide (TOABr) was added and stirred vigorously. The phase transfer of $AuCl_4^-$ ions was marked by the change in color of the organic phase from colorless to orange. 82 μL of dodecanethiol was added to the organic phase followed by addition of 10 mL of 0.2 M sodium borohydride ($NaBH_4$) solution, a strong reducing agent, rapidly at room temperature resulting in a brown colored organic phase. The brown sol was washed with deionized water, precipitated with methanol and

filtered using a Nylon filter paper. The particles were redispersed in toluene for further characterization. The reaction scheme is given below:

$$m\mathrm{AuCl_4^-} + m\mathrm{N(C_8H_{17})_4^+}_{(\text{toluene})} \rightarrow m[\mathrm{N(C_8H_{17})_4^+AuCl_4^-}]_{(\text{toluene})}$$

$$m[\mathrm{N(C_8H_{17})_4^+AuCl_4^-}]_{(\text{toluene})} + n(\text{alkanethiol}) + 3me^- \rightarrow 4m\mathrm{Cl^-}_{(\text{aq.})} +$$

$$[(\mathrm{Au_m})(\text{alkanethiol})_{(n-x)(\text{toluene})} + x(\text{alkanethiol})_{(\text{toluene})} + m\mathrm{N(C_8H_{17})_4^+}_{(\text{toluene; aq.})}$$

Transmission electron microscopic (TEM) measurements were carried out with a JEOL-3010 TEM operating at 300 kV. Samples for TEM were prepared by depositing a drop of the toluene sol on a holey carbon copper grid and allowing it to dry in a desiccator overnight. Figure 3.1 shows a typical TEM micrograph obtained from the Au sol. The mean diameter of the particles was found to be ~3.3 nm. The electronic absorption spectra (Perkin-Elmer Lambda 900) of the Au sol reveal the characteristic surface plasmon absorption at 520 nm [38] (see inset of Figure 3.1).

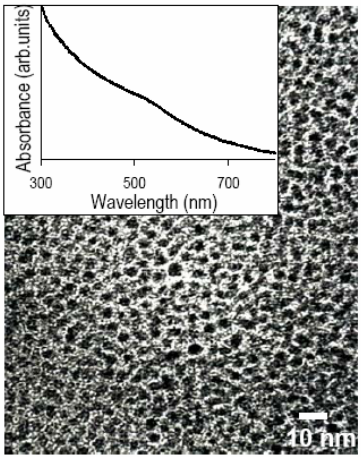

Figure 3.1. TEM image of Au NCs used for L-B deposition. The electronic absorption spectrum of the Au NCs in toluene is shown in the inset.

3.3.2 L-B deposition

Prior to carrying out sequential deposition of GdSt and Au NCs, the n-doped Si(001) was made hydrophilic according to the RCA cleaning procedure using ammonia and hydrogen peroxide solutions (H_2O:NH_4OH:H_2O_2 is 10:1:1). The native oxide layer present on Si surface gets thickened during this process. In the first step of L-B deposition, a monolayer of stearic acid was spread uniformly on the surface of the Milli-

Q water (Millipore) in one of the compartments of an alternating L-B trough (KSV 5000) containing 5×10^{-4} M Gd^{3+} from the dissolved Gd acetate [34]. A schematic of the set-up is shown in Figure 3.2. The GdSt monolayer was deposited on the Si substrate by passing it through the monolayer with a water-to-air upstroke at a speed of 3 mm/min. The surface pressure was maintained at a constant value of 30 mN/m during deposition. For Au NC deposition, 1.5 mL of the toluene solution of NCs (0.2 mg/mL) was spread on the water subphase on the other side of the trough. After the solvent evaporated, the hydrophobic dodecanethiol encapsulated Au NCs remained on the water surface. These were then transferred to the GdSt/SiO_2/Si substrate during a water-to-air upstroke at a speed of 1 mm/min. The pressure-area isotherm of the Langmuir monolayer was recorded during compression and decompression by moving the barriers at a speed of 2 mm/min. Three films, A, B and C were deposited at monolayer pressure of 1.5, 3.5 and 20.0 mN/m, respectively (refer Figure 3.3).

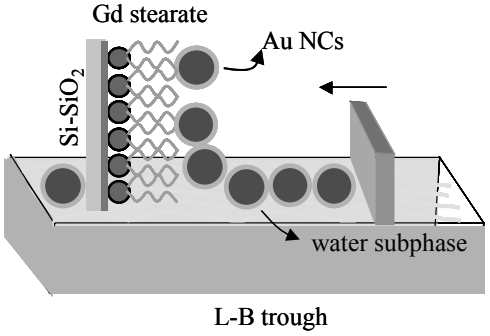

Figure 3.2. A schematic of the L-B deposition process. The barrier is moved across the Langmuir monolayer to increase or decrease the surface pressure.

3.3.3 Characterization of L-B films

The AFM measurements of the films were performed using a scanning probe microscope (Nanoscope IV, Digital Instruments) in both tapping and contact modes. The images were obtained using commercially available etched Si (for tapping mode) and Si_3N_4 (for contact mode) cantilevers. The I-V characteristics of the films GdSt, A, B and C as well as that of the substrate, SiO_2-Si in ambient conditions were probed using the conducting-AFM set up. This was done in the contact mode AFM using a conducting cantilever that was prepared by sputter-coating a commercial silicon nitride probe with

gold (~100 nm thick). A Keithley 236 multimeter was used to collect the I-V data and the details of the set up are explained in Chapter 2, Section 2.2. To ensure that the gold coating on the cantilever had not worn off while scanning, the cantilever was periodically monitored by collecting I-V data from a reference graphite substrate (HOPG). The top Au films were electrically connected to the steel sample holder by silver paint. After obtaining a well-resolved image in the contact mode, the I-V characteristic of the required feature was obtained by positioning the feature to the center of scan area, reducing the scan area to zero, and turning off the feedback.

3.4 Results and Discussion

3.4.1 The pressure-area isotherm

The pressure-area isotherm obtained during compression and decompression of the Au NC Langmuir film (Figure 3.3) show good reversibility and existence of three different regions. This indicates that a monolayer of Au NC is formed upon evaporation

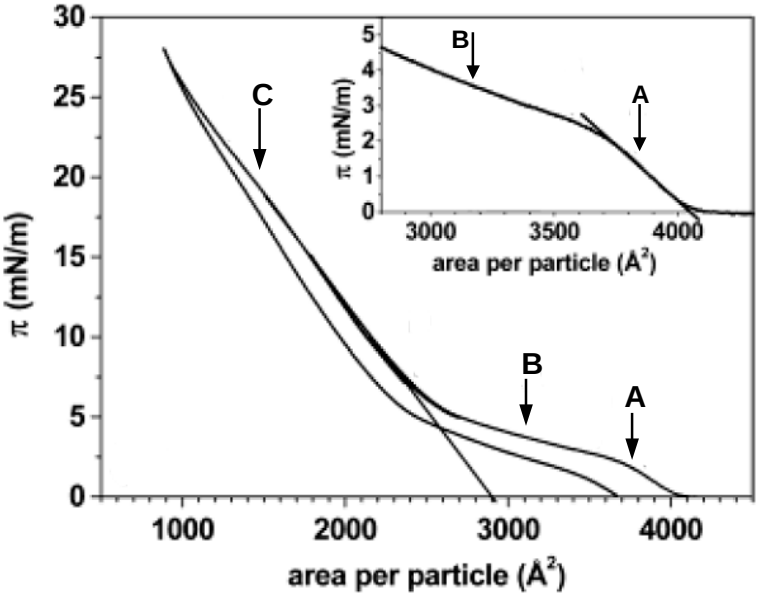

Figure 3.3. π-A isotherms obtained while compressing and decompressing a monolayer of Au NCs in an L-B trough. Samples A, B and C were deposited at pressures indicated by the arrows. Phases A and B are shown clearly in the inset by zooming the low pressure region of the isotherm. The tangents are drawn to indicate the two low compressibility phases.

of toluene from the nanocrystal solution spread on the water-air interface of the trough. The surface pressure-area isotherm is rich in information on stability of the monolayer, the re-orientation of alkyl chains in the two-dimensional system, phase transitions and conformational transitions [40]. In Figure 3.3, there are two low-compressibility phases at two widely different specific particle areas (4000 and 2000 $Å^2$) and there exists a high compressibility phase in between (3500-2500 $Å^2$). The low compressibility low-pressure phase, which extends up to a pressure of 2.0 mN/m (point A), is due to the repulsive interaction arising from the interdigitation of the hydrocarbon tails of dodecanethiol molecules capping the Au cores. This can be compared with the 'liquid-expanded' state normally encountered in the case of amphiphilic molecules, wherein the NCs are stabilized by repulsive interchain interactions. This steric repulsion is sufficient to counter the van der Waals attraction between the metal cores. This is also the reason why the colloidal dispersion of dodecanethiol-capped Au particles remains stable for weeks without aggregation [39,40]. When the surface pressure is increased further, the repulsive interactions are overcome and the chains are susceptible to gauche conformations and interdigitation resulting in a highly compressible phase. This phase transition occurs at 2 mN/m and extends upto 5 mN/m.

Beyond 5 mN/m, the Au NC monolayer undergoes a third phase transition, which is again less compressible due to the formation of a 'liquid-condensed' state. In this state, the chains are highly interdigitated and the monolayer is stabilized by the attractive interaction between Au cores. Since, at this stage, the available volume per cluster in the Langmuir monolayer is reduced drastically with decreased compressibility, the films deposited beyond a certain surface pressure (~6.0 mN/m) has the possibility of forming bilayers of Au NCs. However, it is interesting to note that even beyond this pressure (upto point C in Figure 3.3), the isotherm is retracing the same path during compression and decompression (appears as a thicker line in Figure 3.3 since the trace and retrace coincides). This implies that there is no loss of particles at this pressure range and any deformation of the Langmuir monolayer is reversible. But when the monolayer was decompressed from a surface pressure higher than that at point C, the curve does not follow the same path although the nature of the curve is similar throughout.

3.4.2 AFM analysis of the L-B films

Systematic AFM studies have been performed to extract the real space information regarding height fluctuations and in-plane morphology of the films. For this purpose, films corresponding to the regions A, B and C were chosen as they represent three different phases in the pressure-area isotherm. The tapping mode AFM images of films A, B and C and that of the GdSt prior to NC film deposition, clearly demonstrate the differences in the surface morphology of the films (Figure 3.4). The morphology of the GdSt film is quite different, where the average roughness is low (~4 Å). In the case of Au NC films, the presence of a network of islands is apparent in the images. Both the islands and the interconnects become finer as we go from sample A (Figure 3.4b) to C (Figure 3.4d). The heights of the islands and interconnects estimated from the *z*-profile analysis as shown in Figure 3.4b-d, were ~5±1 nm. The size of the nanocrystal islands as well as of interconnects vary gradually from film A to film C. In sample A, islands are present with a fairly uniform size (300 nm) with interconnects of ~45 nm wide. Each island exhibits one or more number of holes as indicated by arrows in Figure 3.4b. In sample B, the islands are of varied sizes ranging from 60 to 300 nm. Importantly, the holes in the islands are smaller in diameter but are present with a higher number density (Figure 3.4c). A highly porous structure with 50 nm wide interconnects is observed in the case of sample C with almost no islands and holes (Figure 3.4d). Moreover, a large number of bright spots corresponding to the existence of a second Au nanocrystal layer (9 nm height) are observed in this case. The network of Au NCs is more clearly seen in the phase image given in Figure 3.5a where dark holes correspond to Au NCs. The phase image can be contrasted with the topography given in Figure 3.5b, where the brighter regions correspond to NC film. The parameters obtained from the AFM analysis are summarized in Table 3.1.

The monolayer of Au nanocrystals (deposited over GdSt monolayer) goes through substantial restructuring in forming the observed networked membrane. It is interesting to note that despite these variations, the coverage of the islands, estimated on the basis of the area occupied by the island features, is found to be ~60% in all the cases. The growth of the membrane-like structure and its dependence on the surface pressure of the Langmuir monolayer used for deposition, are indeed interesting. Obviously, the surface

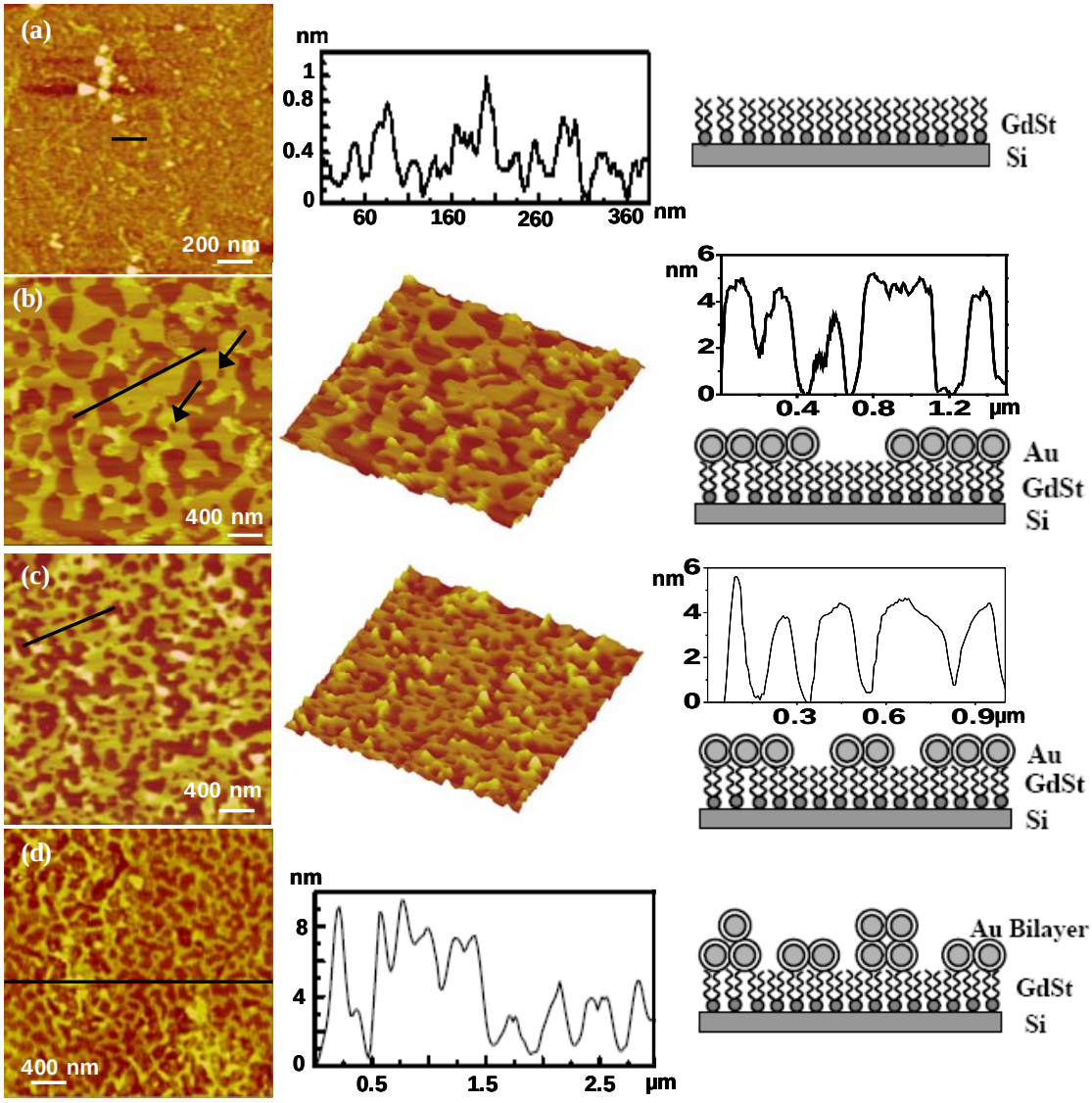

Figure 3.4. Tapping mode AFM images of (a) GdSt/SiO_2-Si(001) substrate. (b) Sample A (c) Sample B (d) Sample C consisting of Au NC/GdSt/SiO_2-Si. The height profiles corresponding to the lines drawn on respective images and the 3D views are shown for each film. The corresponding schematic diagrams of the deposited films are also shown.

pressure of the Langmuir monolayer of Au nanocrystal employed in the deposition process and the interaction between the stearic acid chains and dodecanethiol chains both play an important role in determining the variations of network morphology in these films. The nanocrystal film in A was deposited at a lower pressure region of the isotherm where area occupied by each nanocrystal on water surface is high, corresponding to a loosely net monolayer with diminishing interaction among the particles. This monolayer,

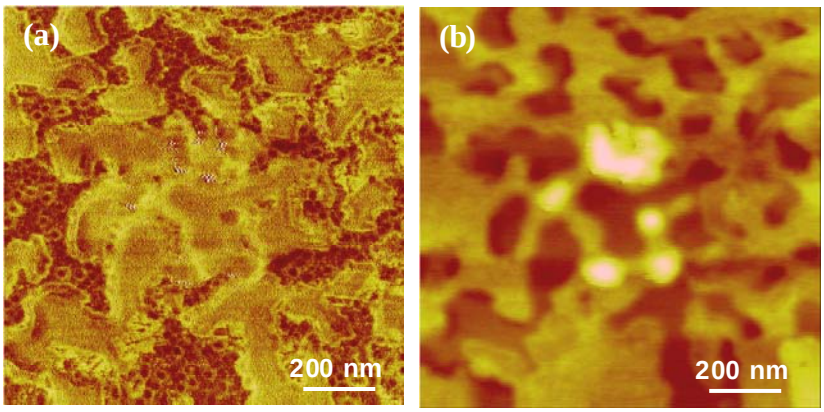

Figure 3.5. (a) The phase contrast image of the Au NC monolayer showing the network of NCs, obtained in tapping mode. The darker regions (holes) in the phase image corresponding to brighter regions in the topography given in (b) constitute Au NCs and the brighter regions comprise of the underlying GdSt film (darker region in (b)). (b) Topography corresponding to (a).

when transferred to the GdSt, appears to spread like a fluid, tolerating the defects and dislocations of the layer below, thereby forming wide islands with thin interconnects. Because films B and C were obtained at progressively higher compressions, the interparticle separation is greatly reduced, enhancing the interaction among the metal cores. Besides, the neighboring nanocrystals get interlocked due to the increasing interdigitations of the dodecanethiol chains surrounding them. Because of this entanglement of Au nanocrystals, the diffusion process [41,42] after transfer, reduces progressively from film B to C and smaller islands with more number of holes are observed.

Table 3.1 Parameters obtained from the AFM analysis

			Sample C	
	Sample A	Sample B	bottom layer	top layer
Heights of the islands and interconnects as obtained from line profile (nm)	~5	~5	~5	~4
Height variation on islands and interconnects (nm)	±1	±1	±1	±1
Coverage of the islands	61%	63%	61%	45%
Saturation value of rms roughness (nm)	2.45	2.41	2.57	
Lateral correlation length (nm)	~620	~460	~320	
Roughness exponent	0.85	0.8	0.6	

The lateral correlation present in these films and its dependence on deposition pressure can be extracted from the AFM images. For isotropic self-affine rough surfaces, the height-height correlation function *g(r)*, can be written as

$$g(r) \equiv \left\langle [z(0) - z(r)]^2 \right\rangle = Ar^{2\alpha} \qquad (0<\alpha<1) \tag{3.1}$$

where $z(r)$ is the height with respect to a mean surface at a lateral distance r from some origin where the height is $z(0)$, and α is the roughness exponent. The exponent α determines the texture of rough surfaces; a lower α indicates a jagged surface, whereas a higher α implies a surface with relatively smooth fluctuations [43]. All physical systems must exhibit this self-affine scaling only over a finite length scale; otherwise the correlation function defined above would diverge, implying that the roughness would grow indefinitely, which is an unphysical situation. The length scale up to which self-affine scaling is observed in a surface is called the correlation length.

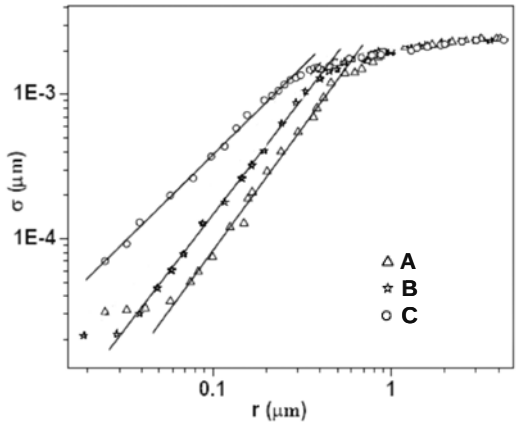

Figure 3.6. RMS roughness (σ) vs scan length (r) obtained from AFM images for A, B and C films. The solid lines are fits to the linear portion of the respective curves in log-log scale.

For actual physical systems, the form of the height-height correlation function is modified from that given above, to

$$g(r) = 2\sigma^2[1 - \exp(r/\xi)^{2\alpha}] \tag{3.2}$$

where σ is the rms roughness of the surface and ξ is the correlation length for self-affine scaling of surface roughness. $g(r)$ has the same form as in eq 3.1 for $r << \xi$. It is well-known that, statistically, the scaling of the rms roughness, σ, is equivalent to the scaling of the height-height correlation function, $g(r)$ [41,44]. Figure 3.6 shows the plot of rms roughness, σ against scan length, r for scans of different sizes for the three cases. The self-affine nature of the films is evident in the log-log plot. In all the cases, σ increases

with r up to a certain cut-off length beyond which it saturates. This cut-off length is the in-plane correlation length, which changes from ~610 nm for film A to ~320 nm for film C. It is interesting to note that in all the cases, σ saturates to a value ~2.4 nm, which is half the layer thickness. A linear fit to the data shows that the scaling exponent α changes from 0.85 to 0.6 as we go from film A to C. A lower value of α implies more rapid fluctuations in the out of plane direction for sample C due to the presence of the upper cluster layer whereas a value of α approaching 1 indicates the presence of relatively smooth islands and valleys in sample A (values are tabulated in Table 3.1). It can be noted that on the wide islands of film A, the rms roughness almost remains unchanged for very small length scales, which is evident from the flat portion of the data for small

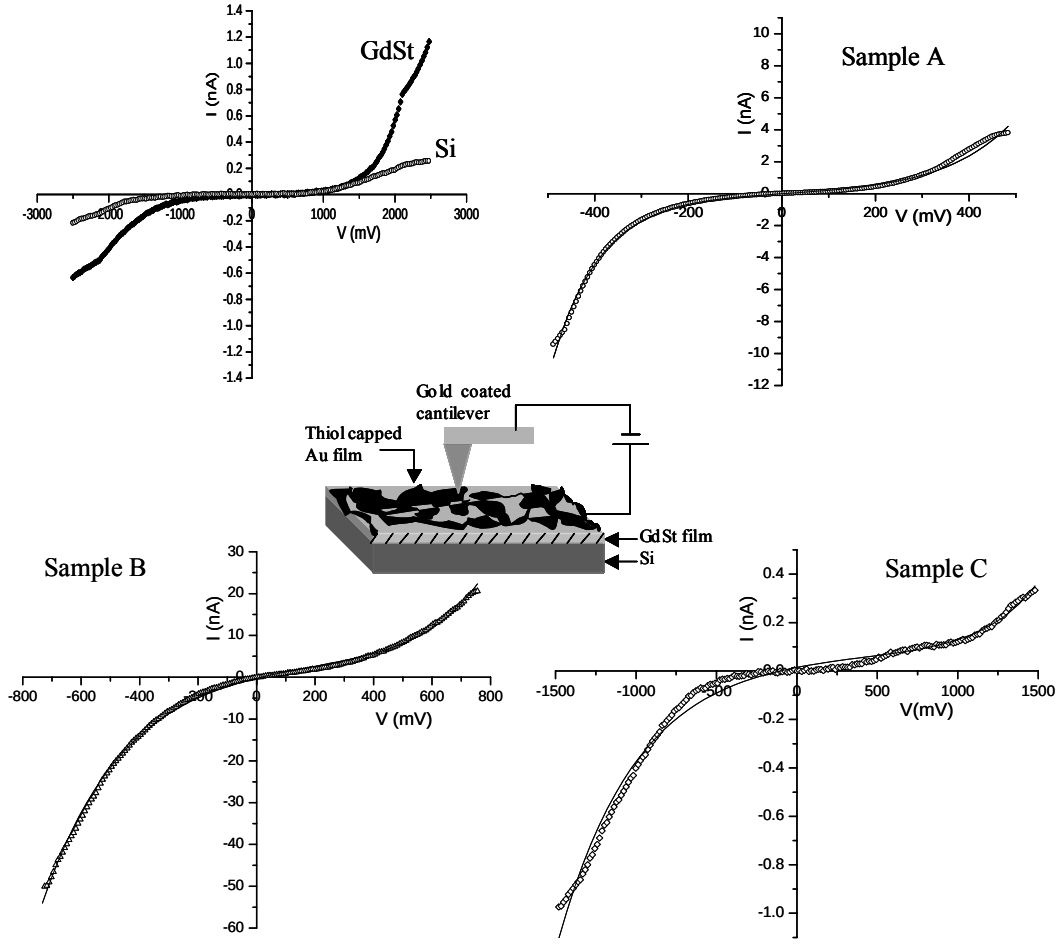

Figure 3.7. I-V spectra obtained from GdSt film-SiO_2-Si and also sample A, sample B and sample C along with the configuration used for acquiring the plots. The fitted curves (solid lines) are also shown.

values of *r*. Such flat portions at low *r* were not observed for other films because the number of smooth wide islands decreases gradually from film A to C. Although a theoretical understanding of the underlying physics giving rise to the membrane-like morphology of the film requires more systematic investigation [41,45], it is gratifying that we could control the morphology of these well-defined bilayer films of Au NC/GdSt on Si(001) substrate.

The I-V characteristics of Au NC/GdSt/SiO_2-Si system were measured for different deposition pressures (A, B and C) as well as for GdSt and the substrate. Using a C-AFM probe, the I-V plots were collected from different regions of the film. The I-V plots given in Figure 3.7 indicate that the transport property of these films depend strongly on the morphology. All the curves are non-linear in nature. A schematic of the configuration used for the measurement is shown alongside. The electrical contact is made to the top portion of the film as well. The I-V curves from the Au films with probe atop the clusters are asymmetric for positive and negative biases. The nature of I-Vs are very different from that obtained from bare substrate n-Si-SiO_2 and the GdSt film. The curves from samples A, B and C can be fitted with an exponential decay and growth function of the type

$$I = I_0 + I_1 \exp(-V/V1) + I_2 \exp(V/V2) \qquad (3.3)$$

It appears that the nanocrystal film behaves like a network of multiple tunnel junctions where the electrons tunnel through the organic ligands between adjacent metal cores [45]. Following an activation bias or trigger voltage, a conduction channel is established through the percolating backbone of nanocrystal interconnects and a stable current is obtained in each case. The current should depend on the interparticle distance, i.e., on the length of the organic linker molecules as well as on the barrier provided by them. Because it is a problem of multiple tunnel junctions, the interparticle distance dependent term in the expression of current will be a summation over the individual tunnel junction [46]. If L_{eff} is the effective interparticle distance and β_{eff} is the effective barrier height, then I_1 and I_2 in eq 3.3 can be written as $I_1 = \exp(-\lambda_1)$ and $I_2 = \exp(-\lambda_2)$ with $\lambda = L_{eff}\beta_{eff}$. The value of λ is found to be ~2.5 and ~6.0 for samples A and C, respectively. Since film C is transferred to the substrate at higher pressure, the organic linker molecules will be compressed in this case, resulting in a smaller interparticle distance in the lateral direction. But the higher value of λ for sample C indicates that this film provides a higher

barrier to the electrons than sample A. It is already shown that in sample C, the Au particles are not aligned in same plane and the fluctuation in the vertical position of the Au core is more as compared to that in film A, giving rise to a lower scaling exponent. This change in morphology in film C may be responsible for the increase in effective barrier for tunneling and hence may reduce the percolation probability for electrons. A more detailed study and a model to explain this morphology dependent electron transport is given in the following section.

3.4.3 Model for the rectifying Au NC films supported on GdSt-SiO_2-Si system

A more careful study was performed on sample C with AFM probe atop the monolayer and bilayer of Au NCs. The configuration used for the study is given in Figure 3.8b along with the AFM topography and the section profile (Figure 3.8a). The positions from which the I-Vs have been collected are marked in the schematic as well as in the image. The corresponding I-V characteristics are plotted in Figure 3.8c. All the curves are rectifying in nature.

The origin of rectification can be due to the heterogeneous nature of the film with Au NCs capped with thiol chains on one side and a monolayer of Gd stearate on SiO_2-Si substrate, on the other. When these are placed asymmetrically spatially, one can, in principle, form a rectifier. This has been demonstrated by Kornilovitch *et al*., in the case of molecules [31]. Such systems require just a conducting molecular level placed closer to one electrode than the other, which can be achieved through insulating tunnel barriers of different widths. Since most of the applied voltage drops on the longer insulating barrier, the conditions for resonant tunneling through the level are achieved at very different voltages for the two opposite polarities. By changing the lengths of the insulating barriers, the rectification ratio can be systematically changed.

Here, it is demonstrated that Au NCs capped with dodecanethiol on GdSt-SiO_2-Si form such a case of asymmetric spatial configuration. The different widths of the tunnel barriers are obtained from the AFM data and are given in the simplified model depicted in Figure 3.8b. When the C-AFM tip is at position **1** (i.e, on the monolayer), the dodecanthiol chains form a tunnel barrier and the tip is, L_t =12 Å away from Au core while the other electrode on doped Si is, L_b > 12 Å constituted by the thiol chains, GdSt layer and SiO_2. The corresponding I-V obtained is shown in Figure 3.8c. This is

comparable to the I-V obtained in the case of sample A, deposited at 1.5 mN/m, where only a monolayer of Au NCs exists (refer to Figures 3.4b and 3.7). We observe a sharp rise in conductance beyond a forward voltage (V_F) of +240 mV but reverse voltage (V_R) comes out to be around -450 mV for obtaining nonzero conductance. The current rectification ratio (R), which is the ratio of forward to reverse currents at a given magnitude of the bias, at ±500 mV is estimated to be 16. The spatial asymmetry becomes more prominent for sample C when the tip is placed on a bilayer of Au NCs (point **2** in Figures 3.8a, b and c). In this condition, the current in the negative bias region was negligible while on the positive bias region, the current was slightly more than that

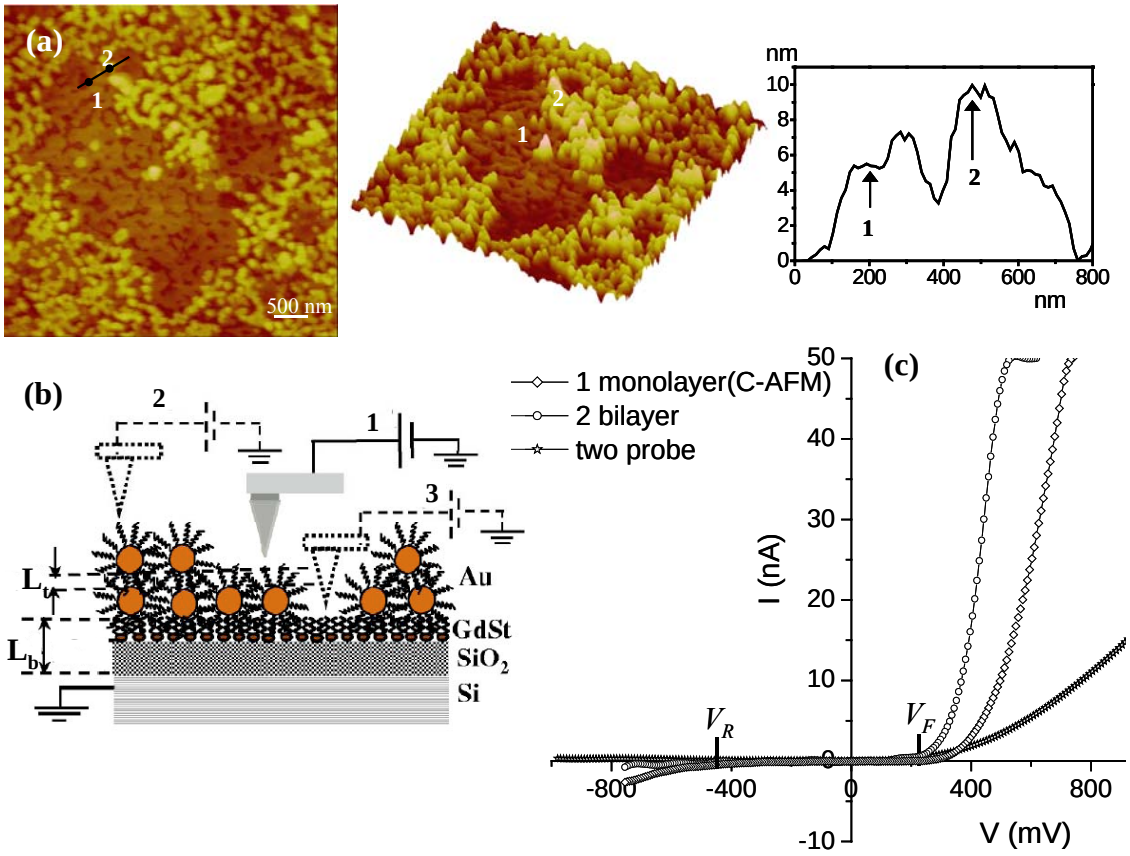

Figure 3.8. Detailed analysis of sample C. (a) Tapping mode AFM image clearly showing the bilayer and monolayer of Au NCs along with a 3D view and height profile across the line marked in the image. (b) Schematic of the Au NC film on GdSt-SiO_2-Si and the configuration used for C-AFM measurements. The different positions from which I-V data have been acquired are marked and the corresponding points are shown in (a). (c) The I-V data from the monolayer and bilayer of Au NCs obtained from C-AFM measurements. The I-V acquired from sample C for a two-probe configuration is also given.

obtained for a monolayer and V_F got shifted to lower bias, +150 mV (Figure 3.8c). The rectification ratio, R in this case is estimated to be 128. This behavior can be contrasted with the rather symmetric I-V profiles obtained for GdSt monolayer (point 3 in Figure 3.8b) and bare SiO_2-Si substrate (refer to Figure 3.7). The above result has been verified by two probe I-V measurements as well with one connection from the top of the film C through a conducting pad and the other from the back of the Si substrate. Rectification is evident in the I-V plot given in Figure 3.8c, but the contrast is less as the conducting pad averages the conductance of the Au NCs with that of GdSt due to the patchy nature of the Au cluster monolayer (see Figure 3.4b). Hence the dominating current carrying paths are tunneling through a C-AFM tip-to-Au NC-to-GdSt-to-SiO_2-doped Si rather than the in-plane conduction through Au-NCs.

The mechanism of rectification due to spatial asymmetry in tunnel barriers is illustrated further with the help of a schematic band diagram (Figure 3.9). The applied voltage, V, drops asymmetrically on the top and bottom barriers giving rise to a diode-like property. Let the voltage drop at the bottom and top barriers be V_b and V_t, respectively, with their ratio, $\eta=V_b/V_t$. In the schematic diagram, the band gap of the n-type (carrier concentration, $\sim 1.6\times10^{17}$ cm^{-3}) Si(001) used, is not shown explicitly and we treat the doped Si as a metallic electrode. In the GdSt-SiO_2-Si system the effect of band bending and the presence of surface states in the Si gap region make it difficult to locate the valence and conduction-band edge accurately with respect to the Fermi level. At equilibrium, the Fermi levels of the C-AFM tip and Si align with the Fermi level of Au NC as shown in Figure 3.9a. The equilibrium Fermi level position obviously depends on the relative work functions of the two electrodes, which are not the same in this case. The difference in the work functions induces a contact potential difference and hence an electric field through the system at zero applied bias. For simplicity, we ignore the field within the nanocrystal and assume that the applied voltage drops only on the two barriers, i.e., $V=V_b+V_t$. In our diagram, the bottom electrode (Si) is always grounded and all the energy levels shift with respect to the Si Fermi level with the applied bias. From density-functional studies, it has been shown earlier [47] that a thiol-passivated Au cluster consisting of 38 Au atoms has a gap of 0.9 eV just above the Fermi energy. We denote this gap as $\Delta=(E_{vac}-E_f)-A_1$, where E_{vac}, E_f, and A_1 are the vacuum level, equilibrium Fermi level position, and electron affinity of Au nanocrystal at zero bias, respectively.

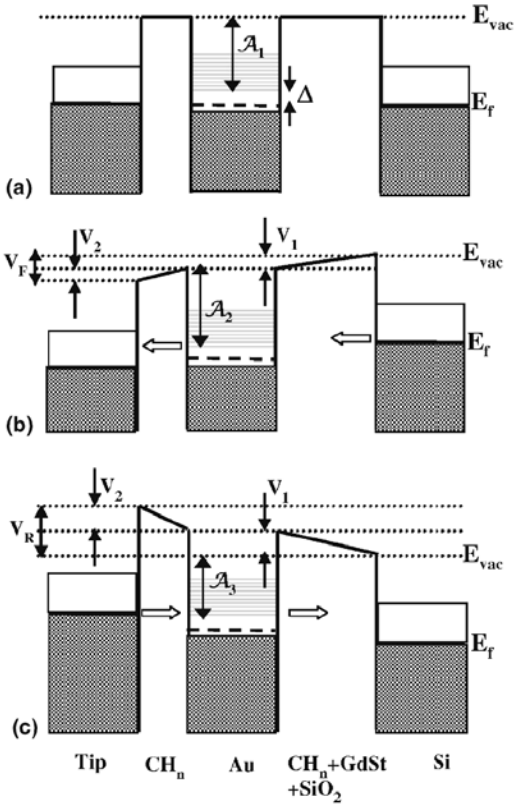

Figure 3.9. (a) Schematic diagram showing the asymmetric tunnel barriers. Fermi levels are aligned at zero bias. (b) At a positive bias (V_F) to tip, the Si Fermi level lines up with the conduction level of the Au nanocrystal. (c) At a negative bias (V_R) to tip, the tip Fermi level aligns with the conduction level of the Au NC. The voltage drops across the top and bottom barriers, and the electron affinity of the Au NC is marked as V_t, V_b, and A_i, respectively.

When positive voltage is applied to the tip, the tip Fermi energy and the energy levels of the Au NCs shift downward, but their relative shifting will depend on η. At a particular forward bias voltage, V_F, the Si Fermi level lines up with the conduction levels of the Au NCs (Figure 3.9b) and a sharp increase in current is observed in I-V spectra due to resonant tunneling [31,32]. Similarly, in reverse bias both the tip Fermi energy and the energy levels of the Au cluster shift upwards and current will start to increase at a voltage (V_R) only when the tip Fermi level lines up with the conduction levels of the Au cluster (Figure 3.9c).

From the expressions [31], $eV_F = \Delta(1+\eta)/\eta$ (3.4)

$$eV_R = \Delta(1+\eta), \quad (3.5)$$

the asymmetric factor $\eta=V_R/V_F$ is found to be 1.9 for sample A. For sample B, current is almost zero in negative bias giving $\eta>>1$. From the above expressions Δ is found out to be 155 meV. This is consistent with earlier reports [2,48], which mentioned that the HOMO-LUMO gap present in a thiol-capped Au nanocrystal of 0.5 and 2 nm dia is 1.8 and 0.3 eV, respectively. The asymmetric factor η can be approximated [32,49] in terms of the parallel-plate capacitances of the two junctions using a simple dielectric model with the widths and relative dielectric constants of the top and bottom barriers L_t, L_b, ε_t, ε_b, respectively. Assuming further that the area associated with the tunneling phenomena for the two barriers is the same, one can write $\eta=(L_b/L_t)(\varepsilon_t/\varepsilon_b)$. By keeping only organic tails on both sides of Au NCs and tuning their tail length, one can get higher η and hence better R.

3.5 Conclusions

The morphology and the I-V characteristics of Au nanocrystal films supported on GdSt-SiO_2-Si, deposited by L-B technique at different surface pressures have been systematically studied employing AFM and its conductive mode. The morphology of the Au NC films that consist of network of islands has been found to depend strongly on the surface pressure of deposition. We have demonstrated that monolayer and bilayer films of thiol-capped Au nanocrystals deposited on GdSt-SiO_2-Si substrate can exhibit rectification properties when the film is asymmetrically coupled to two electrodes. The spatial asymmetry introduced by the different widths of the tunnel barriers at the top and bottom sides of the film plays a key role in generating the asymmetric I-V curves. An obvious extension of our finding is that one can create an array of rectifiers by depositing thiol-capped Au nanocrystals on an organic monolayer attached to a doped silicon or metal substrate. The rectification ratio can then be designed by choosing the desired “tail length” of the organic monolayer. GdSt monolayer, being a 2D ferromagnet, one may exploit it to form possible spintronic devices.

References

[1] A. N. Shipway, E. Katz & I. Willner, *ChemPhysChem*, 1, 18 (**2000**).

[2] C. N. R. Rao, G. U. Kulkarni, P. J. Thomas & P. P. Edwards, *Chem. Eur. J.,* 8, 28 (**2002**).

[3] P. J. Thomas, G. U. Kulkarni & C. N. R. Rao, *Chem. Phys. Lett.*, 321, 163 (**2000**).

[4] D. L. Klein, R. Roth, A. K. L. Lim, A. P. Alivisatos & P. L. McEuen, *Nature*, 389, 699 (**1997**).

[5] U. Simon & G. Schmid, *Nanoparticles: From Theory to Application*, Wiley-VCH, Weinheim (**2004**).

[6] F. Remacle & R. D. Levine, *ChemPhysChem*, 2, 20 (**2001**).

[7] J. H. Fendler, *Chem. Mater.,* 13, 3196 (**2001**).

[8] G. Schmid & U. Simon, *Chem. Commun.*, 697 (**2005**).

[9] G. Markovich, C. P. Collier, S. E. Henrichs, F. Remacle, R. D. Levine & J. R. Heath, *Acc. Chem. Res.*, 32, 415 (**1999**).

[10] G. Medeiros-Ribeiro, D. A. A. Ohlberg, R. S. Williams & J. R. Heath, *Phys. Rev. B*, 59, 1633 (**1999**).

[11] S. -H. Kim, G. Medeiros-Ribeiro, D. A. A. Ohlberg, R. S. Williams & J. R. Heath, *J. Phys. Chem. B*, 103, 10341 (**1999**).

[12] A. Taleb, F. Silly, A. O. Gusev, F. Charra & M. -P. Pileni, *Adv. Mater.*, 12, 633 (**2000**).

[13] D. B. Janes, T. Lee, J. Liu, M. Batistuta, N. -P. Chen, B. L. Wash, R. P. Andres, E. -H. Chen, M. R. Melloch, J. M. Woodall & R. Reifenberger, *J. Electron. Mater.,* 29, 565 (**2000**).

[14] R. Parthasarathy, X. -M. Lin & H. M. Jaeger, *Phys. Rev. Lett.*, 87, 186807 (**2001**).

[15] V. Torma, G. Schmid & U. Simon, *ChemPhysChem* 5, 321 (**2001**).

[16] P. Liljeroth, D. Vanmaekelbergh, V. Ruiz, K. Kontturi, H. Jiang, E. Kauppinen & B. M. Quinn, *J. Am. Chem. Soc.*, 126, 7126 (**2004**).

[17] A. J. Quinn, P. Beecher, D. Iacopino, L. Floyd, G. De Marzi, E. V. Shevchenko, H. Weller & G. Redmond, *Small*, 1, 613 (**2005**).

[18] K. -H. Müller, G. Wei, B. Raguse & J. Myers, *Phys. Rev. B*, 68, 155407 (**2003**).

[19] K. -H. Müller, J. Hermann, B. Raguse, G. Baxter & T. Reda, *Phys. Rev. B*, 66, 075417 (**2002**).

[20] V. C. Sundar, H. -J. Eisler & M. G. Bawendi, *Adv. Mater.*, 14, 739 (**2002**).

[21] T. Cassagneau, T. E. Mallouk & J. H. Fendler, *J. Am. Chem. Soc.*, 120, 7848 (**1998**).

[22] T. W. Kelley, E. L. Granstrom & C. D. Frisbie, *Adv. Mater.*, 11, 261 (**1999**).

[23] V. Torma, T. Reuter, O. Vidoni, M. Schumann, C. Radehaus & G. Schmid, *ChemPhysChem*, 547 (**2001**).

[24] T. Reda, A. F. Collings, C. Barton & P. Lukins, *J. Phys. Chem. B*, 107, 13774 (**2003**).

[25] D. M. Adams, L. Brus, C. E. D. Chidsey, S. Creager, C. Creutz et al., *J. Phys. Chem. B*, 107, 6668 (**2003**).

[26] A. Aviram & M. A. Ratner, *Chem. Phys. Lett.*, 29, 277 (**1974**).

[27] A. S. Martin, J. R. Sambles & G. J. Ashwell, *Phys. Rev. Lett.*, 70, 218 (**1993**)

[28] R. M. Metzger, T. Xu & I. R. Peterson, *J. Phys. Chem. B,* 105, 7280 (**2001**).

[29] R. M. Metzger, B. Chen, U. Höpfner, M. V. Lakshmikanthan, D. Vuillaume, et al., *J. Am. Chem. Soc.*, 119, 10455 (**1997**).

[30] M. L. Chabinyc, X. Chen, R. E. Holmlin, H. Jacobs, H. Skulason, C. D. Frisbie, V. Mujica, M. A. Ratner, M. A. Rampi & G. M. Whitesides, *J. Am. Chem. Soc.*, 124, 11730 (**2002**).

[31] P. E. Kornilovitch, A. M. Bratkovsky & R. S. Williams, *Phys. Rev. B*, 66, 165436 (**2002**).

[32] W. Tian, S. Datta, S. Hong, R. Reifenberger, J. I. Henderson & C. P. Kubiak, *J. Chem. Phys.*, 109, 2874 (**1998**).

[33] S. Lenfant, C. Krzeminski, C. Delerue, G. Allan & D. Vuillaume, *Nano Lett.,* 3, 741 (**2003**).

[34] M. K. Mukhopahdyay, M. K. Sanyal, M. D. Mukadam, S. M. Yusuf & J. K. Basu, *Phys. Rev. B*, 68, 174427 (**2003**).

[35] S. Paul, C. Pearson, A. Molloy, M. A. Cousins, M. Green, S. Kolliopoulou et al., *Nano Lett.,* 3, 533 (**2003**).

[36] S. Kolliopoulou, D. Tsoukalas, P. Dimitrakis and P. Normand, S. Paul, C. Pearson, A. Molloy & M. C. Petty, *Mater. Res. Soc. Symp. Proc.*, 830, D6.7.1 (**2005**).

[37] S. Kolliopoulou, P. Dimitrakis, P. Normand, H. L. Zhang, N. Cant, S. D. Evans, S. Paul, C. Pearson, A. Molloy, M. C. Petty & D. Tsoukalas, *J. Appl. Phys.,* 94, 5234 (**2003**).

[38] M. Brust, M. Walker, D. Bethell, D. J. Schiffrin & R. Whyman, *Chem. Commun.*, 801 (**1994**).

[39] P. C. Ohara, D. V. Leff, J. R. Heath & W. M. Gelbart, *Phys. Rev. Lett.*, 75, 3466 (**1995**).

[40] A. Ulman, *Introduction to Ultrathin Organic films: From Langmuir-Blodgett to Self assembly*, Academic Press, U.S.A. (**1991**).

[41] J. K. Basu, S. Hazra & M. K. Sanyal, *Phys. Rev. Lett.,* 82, 4675 (**1999**).

[42] A. -L. Barabasi & H. E. Stanley, *Fractal Concepts in Surface Growth*, Cambridge University Press, New York (**1995**).

[43] S. K. Sinha, E. B. Sirota, S. Garoff & H. B. Stanley, *Phys. Rev. B*, 38, 2297 (**1988**).

[44] J. K. Basu, M. K. Sanyal, M. Mukherjee & S. Banerjee, *Phys. Rev. B*, 62, 11109 (**2000**).

[45] A. Sharma & R. Khanna, *Phys. Rev. Lett.*, 81, 3463 (**1998**).

[46] R. E. Holmlin, R. Haang, M. L. Chabinyc, R. F. Ismagilov, A. E. Cohen, A. Terfort, M. A. Rampi & G. M. Whitesides, *J. Am. Chem. Soc.,* 123, 5075 (**2001**).

[47] H. Häkkinen, R. N. Barnett & U. Landman, *Phys. Rev. Lett.*, 82, 3264 (**1999**).

[48] O. D. Häberlen, S. -C Chung, M. Stener & N. Rosch, *J. Chem. Phys.*, 106, 5189 (**1997**).

[49] C. Krzeminski, C. Delerue, G. Allan, D. Vuillaume & R. M. Metzger, *Phys. Rev. B*, 64, 085405 (**2001**).

Chapter 4

Lamellar Mesoscopic Systems of Pd and Ni-Alkanethiolates–Structural Aspects, Electrical and Magnetic properties*

SUMMARY

Long chain alkanethiols form lamellar bilayer organizations with transition metals. The structural aspects of Pd(II)- and Ni(II)-alkanethiolates have been studied by X-ray diffraction (XRD), infrared, Raman spectroscopy and UV-Vis spectroscopic techniques, scanning tunneling microscopy and atomic force microscopy. The *d*(001) spacing obtained from XRD is proportional to the chain length and hence, is a measure of the bilayer thickness. The unique electrical and magnetic properties of these hybrid systems arising from a combination of inorganic backbone and organic spacers are also explored.

Unlike other transition metal thiolates, Pd-thiolates are soluble in organic media and this proved to be an advantage while studying self-assembly in mixed thiolates. Binary mixtures of octane (C_8), dodecane (C_{12}), and hexadecane (C_{16}) thiolates of palladium, covering the entire range of compositions, have been prepared from organic media and characterized. All mixed thiolates adopt bilayer configurations with intermediary *d*(001) spacing depending on the binary composition. In C_8-C_{12} and C_{12}-C_{16} bilayers, in which the difference in the chain lengths of the constituent thiols is four methylene units, the thickness varies nearly proportionally to the weighted average of the chain lengths. In contrast, the C_8-C_{16} system shows a step-like behavior with only a few compositions (C_8, 60-80%) exhibiting intermediate *d* values. The alkyl chains are in all-trans conformation in monothiolates, while in hybrid bilayers, especially in C_{12}-C_{16}, gauche defects are observed, their concentration being the highest around the 50:50 composition. Interestingly, these hybrid thiolates seem to provide adequate free volume to trap small molecular species.

---

*Papers based on this work have appeared in J. Phys. Chem. B (2003) and J. Phys. Chem. C (2007).

Palladium alkanethiolates have been employed as precursors for producing stable palladium nanocrystals by a solventless thermolysis route. Transmission electron microscopy analysis revealed that particles form in a close packed arrangement and the size of the particles decrease with increase in chain length. Pd-alkanethiolates decompose to form Pd metal and alkyl disulfides, which in turn assist in stabilizing the colloid. When heated to higher temperatures in air, they decompose completely to form Pd metal films.

The electrical properties of Pd-alkanethiolates are probed by C-AFM technique. AFM images of the thiolate deposited on HOPG showed bundles of string-like features packed in different orientations. I-Vs collected from hexane, octane, decane, dodecane and hexadecane Pd-thiolates were nonlinear and asymmetric in nature with three regimes- a low bias region where the current was linear with bias but small in value, an intermediate bias region where a negative differential resistance (NDR) like feature appeared, beyond which at higher bias the current exhibited sudden jump. The resistance from the low bias region varied exponentially with alkyl chain length with a decay parameter (β) value of 0.2, characteristic of nonresonant tunneling with high tunneling efficiency. The appearance of the NDR peak can be a consequence of the tunneling through the interface states introduced by Pd-S-Pd backbone. A sudden jump in the current at higher bias is due to resonant tunneling.

Nickel alkanethiolates exhibit a lamellar structure similar to Pd-thiolates, but are interesting in terms of the magnetic interactions prevailing in the lattice. Our study on butane, octane, decane, dodecane and hexadecane thiolates of Ni has shown that the susceptibility increases when temperature is lowered below 30 K, reaching a maximum at a particular temperature. This is due to antiferromagnetic coupling along Ni-S-Ni chain and the ordering temperature is found to decrease with increase in chain length, the variation being linear. The study also provides some evidence for interlayer dipolar interactions below 4 K.

4.1 Introduction

Transition metal thiolates constitute a rich class of coordination compounds owing to the strong affinity of the electron rich thiolate (RS^-) ligand and their multifunctional homologues to metal ions binding in the terminal, μ_2-bridging or μ_3-bridging modes. Furthermore, the R part is available for manipulation to effect steric and electronic control to ligation ability. Hence, the early literature is rich with reports of various structures of different dimensionalities where the thiolate ligands exist in different coordination environments [1-14]. Later on, there has been considerable interest in studying the bonding modes of sulfur in these compounds using molecular orbital calculations and density functional theory [15,16]. These studies have revealed that higher polarizability of sulfide and the availability of filled 3p and empty 3d orbitals play a definitive role in the bonding. Thiolate complexes of transition metals have been used as model compounds to represent biologically active centers in nickel-hydrogenases, ferredoxins, nitrogenases, blue copper proteins, metallothioneins etc. that has helped our understanding of the functioning of these systems [17-20]. Another development is the use of volatile molecular thiolates as precursors for the chemical vapor deposition of metallic or sulfidic films [21-26]. Recent developments include generation of various nanostructures from metal thiolate precursors, such as nanocrystals, nanotubes and nanorods [26-31].

Alkanethiolates of metals generally obtained by mixing alkanethiols with metal ions in a protic media, form cyclic cage-like compounds or insoluble complexes with polymeric structures. Cyclic ones, also known as *tiara* or toroidal structures due to their crown like appearance, have been well investigated in terms of structure and bonding [6-16,32,33]. An interesting fact is that such toroidal structures are observed in the case of short chain alkanethiols (number of carbon atoms <4), while long chain thiols (>4) favor the formation of polymeric structures. Due to the lack of availability of single crystals, very little information is available on the polymeric metal alkanethiolates. The very first report on polymeric Pd(II) and Ni(II) mercaptides suggests Ni centers with bridging sulfur in a square planar environment extending in a linear chain [3]. A detailed study of the infinite chain polymers was reported by Dance *et al*. in the case of Ag(I)-alkanethiolate [2,34]. Based on powder XRD measurements, they deduced a layered

structure with two layers of alkyl chains (bilayer) between slabs of Ag-S hexagonal network. Since then, similar layered structures have been reported for Cu(I)-alkanethiolate [35], Pd(II)-alkanethiolate [36], copper hydroxide alkylsulfonates [37], Ni hydroxides and silicates [38, 39] and other such systems [40].

In contrast to most metal (Ag, Cu, Ni etc.) alkanethiolates that precipitate from the organic/protic media, Pd-alkanethiolates remain soluble in the organic media [36]. The other known bilayer systems in organic media are perfluoroalkyl systems [41] and halo-bridged platinum composites [42] linked to long-chain phosphates. The hydrophobic interactions, which are the driving forces for the self-assembly of hydrocarbon chains in aqueous medium are absent in organic media because the chains are completely soluble in the latter. The organizations in organic media are, therefore, considered to be driven by enthalpy rather than entropy [43]. Short chain complexes of metal alkanethiolates are found to be cyclic hexamers while long chains favor extended layered structures. The conformation of the thiol chains and the coordination of metal in these systems have been an interesting topic to structural chemists and detailed analysis of vibrational spectroscopy and NMR (nuclear magnetic resonance) data can be found in the literature [44-49]. The organization of chains in metal alkanethiolates, when chains of different lengths are introduced is interesting and there are very few reports addressing this aspect. Whitesides and coworkers [50-53] obtained mixed monolayers of alkanethiols on gold and characterized them by X-ray photoelectron and infrared spectroscopy, as well as by contact angle measurements. They found preferential adsorption of the longer chain thiols, an observation that goes well with the strong tendency of the longer chains to self-assemble. Some evidence for the aggregation of individual component thiols on a molecular scale was found although a clear phase segregation into macroscopic islands was not observed. In regions where the two thiols coexisted, the terminal portion of the longer chain that extends beyond the terminus of the shorter chain was found to be disordered. The authors suggested that, by using chains of different lengths, it is possible to control the degree of disorder in the monolayers and to introduce free volume in the outer part of the monolayers, where the chains are disordered.

Furthermore, the presence of organic part and inorganic framework should render unique properties to these systems, which are to be explored. Liquid crystalline properties of metal alkanethiolates have been studied and they are popularly known as covalent

soaps [54,55]. The flexibility associated with the alkyl chains together with the variable coordinating sulfur assists the formation of various liquid crystalline phases. There are few reports on the electrical and magnetic properties of these systems. Inorganic-organic hybrids like framework silicates, perovskites interspersed with organic layers are reported to exhibit interesting electrical, optical and magnetic properties [56-63]. For instance, the non-linear optical response of organic molecules is shown to increase by confining them in a silicate network thus preventing randomization of their orientations [57]. Also, the restricted environment of silicate networks is found to enhance the quantum yield of organic LEDs [58]. In the case of hybrid perovskites, Guloy and co-workers observed an unusual semiconductor–metal transition in tin(II) halide families as a function of increasing perovskite layer thickness [62]. The conductivity of these systems could also be modified by changing the organic moiety from alkyl group to π-conjugated molecules. In metal alkanethiolate systems, considering the close metal-metal distances (~3 Å), weak interactions are possible across the -S-metal-S- chain [15]. Computational studies on the electronic structure of *tiara* Pd-thiolates have shown that a delocalized Pd-S π bonding orbital exists throughout the Pd ring for even numbered cyclic Pd-thiolates and is responsible for their exceptional stability compared to the odd ones [33]. Similar d-orbital delocalization is found for highly symmetric *tiara* Ni-thiolates as well [32]. Very few experimental reports are available on the properties of lamellar metal thiolates. A lamellar Ni-thiolate has been reported to exhibit semiconducting behavior [64]. There have been reports on the unusual magnetic behavior in the case of layered compounds of Ni such as azides, hydroxides, framework sulfates as well as supramolecular complexes [65-68] at low temperatures that can be related to the geometric structure.

4.2 Scope of the Present Investigation

The present investigation pertains to the study of structural aspects of lamellar bilayer systems of Pd- and Ni-alkanethiolates in relation to their electrical and magnetic properties. Generally obtained as insoluble polymeric complexes, investigations on these systems are rare. Although structural aspects of monothiolates have been well established in earlier studies [2,33,34], little information is available on the properties of such systems.

4.2.1 Hybrid bilayers of Pd(II)-alkanethiolates

Pd(II)-alkanethiolates are unique in that they self-assemble in organic media and remain soluble [36]. We considered it interesting to investigate the nature of the organization that would result when alkane chains of different lengths are introduced during the synthesis. While it is naive to expect a disordered structure, we thought that the self-assembling process might still be influential enough to bring together an organization that is hybrid yet crystalline.

Only a few mixed bilayer sytems such as fullerene-lipid bilayer films [69] and asymmetric phosphatidylcholines [70] with two different acyl chains are known in literature. On the other hand, there have been several investigations on mixed hydrocarbon systems in the form of self-assembled monolayers on metal surfaces [50-53] and two-dimensional condensates [71-73]. In the present study, mixed bilayer systems of Pd-thiolates have been prepared and the XRD data exhibited intermediary layer spacings, indicating the formation of hybrid bilayers. Three binary alkanethiol systems, octane-dodecane (C_8-C_{12}), dodecane-hexadecane (C_{12}-C_{16}), and octane-hexadecane (C_8-C_{16}), have been studied covering the entire composition ranges. The organization and conformation of chains in such hybrid systems probed by FT-IR, indicated that the chains accommodate considerable defect concentration for hybrid systems while they are in all-trans conformation for monothiolates. In fact these systems are analogous to self-assembled monolayers of alkanethiols on metals [74,75] and investigations on the mixed monolayers [52] have indicated a preferential adsorption of longer chains but with no macroscopic phase segregation of the two chain lengths. The chain terminus of the longer one is found to be disordered and degree of disorder can be controlled to impart free volume in the outer part of monolayers. In the case of hybrid bilayers of Pd(II)-alkanethiolate, we have shown that it is possible to control the degree of disorder by changing the relative composition of the shorter and longer chain thiols. The introduction of disorder has caused the trapping of free acetate ions in the bilayers, which is indeed an indication towards the presence of free volume in the system. It had been earlier envisaged that inclusion of smaller ions should be possible in these bilayer systems but had not been accomplished [34].

4.2.2 Pd-alkanethiolates as precursors for nanocrystal synthesis

The polymeric thiolates have been used as precursors for the preparation of nanorods and nanowires of copper and nickel sulfides [29-31] and also nanocrystals of gold [28]. This presents a solventless thermolysis route. Carotenuto *et al*. [26] have established the thermolysis route as a general method for the synthesis of metal and metal sulfide nanocrystals in a polymer matrix. The thermolysis of bilayer organizations of Pd(II)-alkanethiolates should present a simple route for the preparation of Pd nanocrystals. We have explored the influence of bilayer organization on the formation of Pd nanocrystals and studied the stability of Pd nanocrystals produced by this technique without the aid of a matrix. The chain length of constituent thiol (bilayer thickness) indeed seems to affect the size and organization of the Pd nanocrystals. A complete decomposition of palladium alkanethiolate in air that takes place at fairly lower temperatures, gives Pd metallic films.

4.2.3 Electrical properties of Pd-alkanethiolates

Layered metal alkanethiolates can be considered as inorganic-organic hybrids with bilayers of alkyl chains bridging the metal-μS-metal backbones and the layer spacing is tunable by using thiols of different chain lengths. Also, the metal-to-metal distances are in the range of ~3 Å, which is a close distance for electronic interactions through sulfur. The intermixing of sulfur orbitals with metals in thiolates has been shown to be the cause for exceptional stability for even numbered *tiara* Pd- and Ni-alkanethiolates. With close Pd-Pd distances, one is tempted to consider the set of Pd-S-Pd backbones as evenly spaced one-dimensional conductors with an intervening dielectric medium of the hydrocarbon chains. We therefore undertook the study of the electrical behavior of Pd-thiolates of different bilayer thicknesses deposited on HOPG, employing C-AFM. The specific advantages of C-AFM technique are explained in the previous chapters. This method is particularly useful in our study of Pd-thiolates, as in these compounds, though X-ray crystalline, the stacking extension is typically limited to a few hundred nanometer domains. We have examined the morphology of the bilayer structures using AFM and collected current-voltage (I-V) characteristics from individual features. The I-V data exhibit a low-current region near zero-bias, the width of which varies proportionally with the alkyl chain length and an NDR feature prior to a sudden increase in current at higher bias.

4.2.4 Magnetic properties of Ni-alkanethiolates

Nickel alkanethiolates are conventionally thought to be diamagnetic since the stable coordination environment is square planar for Ni(II), a d^8 system [2,3,9]. But there have been reports of structural distortion in the case of well-investigated *tiara* systems [15,76]. We considered it interesting to investigate magnetic interactions in such low dimensional systems exhibiting mesoscopic ordering. We, therefore, carried out an investigation of the magnetic properties of Ni-alkanethiolates of different interlayer spacings at low enough temperatures where new magnetic interactions possibly emerge. A rise in magnetic susceptibility is noticed below 30 K, indicating a structural distortion from the existing square planar phase. They exhibit anti-ferromagnetic coupling along -S-Ni-S-Ni- chain at low temperatures due to super-exchange phenomena. In addition, there has been evidence for dimensional crossover in shorter Ni-alkanethiolates through the interlayer dipolar coupling facilitated by alkylchains. There is a single report on the magnetism in the case of a square planar coordinated Ni-S system, in which the authors mention the possibility of anti-ferromagnetic interaction arising from a high spin Ni(II) or a paramagnetic impurity [77]. We have also found that the antiferromagnetic coupling temperature decreases with increase in bilayer thickness (increase in chain length). Such chain length dependence has not been found in the case of other layered hydroxides or azides of octahedrally coordinated Ni [38,39].

4.3 Experimental Details

4.3.1 Preparation of Pd(II)- and Ni(II)-alkanethiolates

Pd(II)-alkanethiolates were prepared by mixing palladium acetate and alkanethiol in the ratio 1:2 in toluene. Following the reaction, the solution became viscous and the yellow color deepened to orange. The acetic acid released was washed away with water and the organic layer dried over magnesium sulfate. For the preparation of mixed alkanethiolates, toluene solution of two alkanethiols in the desired molar ratio was added to palladium acetate in toluene with stirring. Various binary combinations-10:90, 20:80, 30:70, 40:60, and 50:50-of octane (C_8), dodecane (C_{12}), and hexadecane (C_{16}) thiolates were prepared. The obtained thiolates were freely soluble in organic solvents such as toluene, methanol, and heptane.

Thermolysis of Pd(II)-alkanethiolates were conducted in air as well as argon atmosphere. For preparing Pd metallic films, a few drops of palladium docdecanethiolate was drop cast or spin-coated on a glass plate and heated in a furnace at 250 ºC in air for 2 hr 30 min. Pd nanocrystals were obtained by heating the thiolate precursors with different chain lengths in Ar atmosphere or air for 2 hr. Lower chain length ones were heated at 155 °C and the higher ones at 180-185 °C. The residue was washed with ethanol and redispersed in toluene.

For preparing nickel thiolates, nickel chloride hexahydrate was used as the precursor and the reaction was done in absolute ethanol in the presence of triethyl amine that helped in the generation of alkyl sulfide anion by abstracting a proton. Triethyl amine and alkanethiol were taken in equimolar ratio. The solution turned reddish brown following the reaction and the compound was obtained as sticky brownish black precipitate from ethanol medium. The precipitates were thoroughly washed with methanol, acetonitrile to remove excess reactants. This was done till there was no evidence for chlorine ions in energy dispersive X-ray spectra.

4.3.2 Characterization techniques

X-ray diffraction patterns (XRD) were obtained using Siemens Seifert 3000TT diffractometer employing Cu K_α radiation. A film obtained by evaporating a few drops of the toluene solution on the glass slide and subsequently annealing at 60 °C for a few min was used for XRD measurements. FT-IR measurements were done using an IFS66v/s Bruker spectrometer with a resolution of 2 cm^{-1}. Samples for infrared measurements were prepared by evaporating a few drop of the thiolate solution in toluene on a dry KBr pellet. Ni thiolates were taken in powder form for XRD and FT-IR measurements. UV spectroscopy of thiolate solution was performed using Perkin-Elmer Lambda 900 UV-Vis spectrophotometer.

TEM analysis of the nanocrystals was performed with a JEOL-3010 microscope operating at 300 kV. The samples had been prepared by depositing a few drops of the nanocrystal dispersion in toluene on a holey carbon grid. Selected area electron diffraction (SAED) measurements were also carried out on the same microscope. The diameters of the nanocrystals were obtained from TEM and generally represent averages obtained from a few hundred nanocrystals.

X-ray photoelectron microscopy (XPS) of Pd metal film was carried out with ESCA LAB MKIV spectrometer employing Al K_α radiation (1486.6 eV). The reported binding energies are relative to the 84.0 eV Au ($4f_{7/2}$) level.

STM and AFM were carried out using a Digital Instruments Quadrex Multimode microscope attached to a Nanoscope-IV SPM controller. Samples for imaging were prepared by depositing a droplet of the dilute thiolate dispersion on a freshly cleaved HOPG surface. C-AFM was done in contact mode with one terminal as the gold-coated AFM probe and other as the graphite connected to a Keithley 236 electrometer. After locating the lamellar structures, the tip was positioned on them and the I-V was collected. Bias was applied to the tip with respect to the graphite substrate that was held at ground potential. Imaging was done in contact mode with a Au/Ti coated (resistive thermal evaporation) silicon nitride cantilever. The tip was positioned over the bundles with a nominal force to measure the I–V characteristics. The force applied is an optimum value where the soft contact changes to hard contact. The details of C-AFM can be found in sections 2.3 and 3.3.2. Imaging was done after the I–V measurement to ensure that the feature had not drifted away during the measurement. Several measurements were done on each sample to ensure the reproducibility of the data.

For magnetic measurements, Ni-alkanethiolates were taken in the powder form in a vial and a Quantum Design SQUID magnetometer was used in the temperature range 2-300 K.

Low temperature Raman measurements were performed on a custom-built Raman spectrometer using a Jobin-Yovn 550 Triax monochromator (Instruments SA, Inc., NJ, USA). A holographic 1800 grooves mm^{-1} grating was used with the entrance slit fixed at 500 mm, providing a resolution of ~ 5 cm^{-1}. Laser emission of 532 nm from a frequency doubled Nd-YAG laser (DPSS-400, Coherent Inc., USA) with a power of 70 mW was used as the excitation source. A long working distance 20x objective with numerical aperture (NA 0.25) was used for laser incidence and collection of the Raman signal. A trinocular microscope head (Olympus, Japan) was fiber coupled to the monochromator to complete the collection optics. A notch filter (Kaiser Optical Systems Inc., MI, USA) was used to cut off the laser light. The low temperature experiments were carried out in compressed Helium cryostat (CTI-Cryogenics, MA, USA) with an accuracy of ±1 K. The sample was pelletized and put into the cryostat. The Raman signals were recorded at two

temperatures, 100 K and 30 K (the lowest temperature achievable in this modified cryostat).

4.4 Results and Discussion

4.4.1 Structural aspects of mono- and mixed bilayers of Pd(II)-alkanethiolates

The X-ray powder diffraction patterns from palladium monothiolates with different alkyl chain lengths from 6 carbons to 18 carbons are given in Figure 4.1. The peaks correspond to a series of (00k) reflections, which are typical of a crystalline lamellar mesophase. The *d* spacings of the Bragg peaks vary as 1:2:3 and so on. For example, the

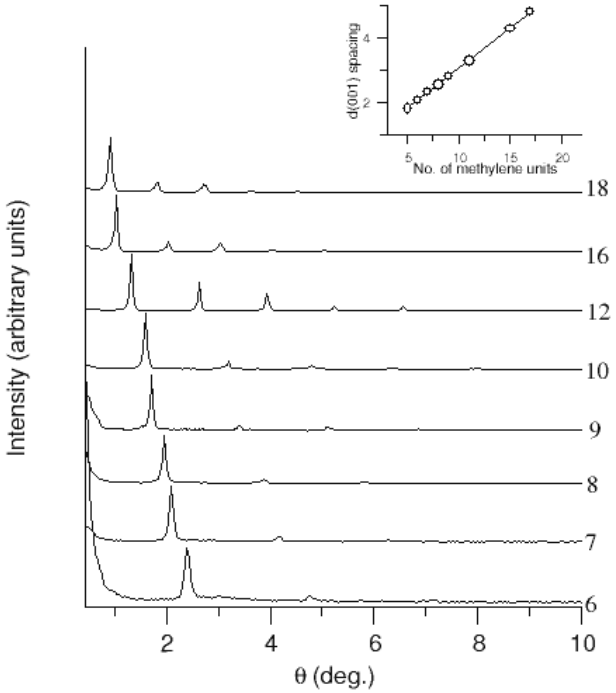

Figure 4.1. X-ray diffraction patterns obtained from nanocomposites of palladium with alkane thiols of different chain lengths (hexyl to octadecyl). The numbers given alongside indicate the number of carbons in the parent thiol. Inset shows the variation of the observed *d*(001) peak position with the number of methylene groups in the alkane chain.

pattern obtained from dodecylthiolate exhibits peaks with *d* values of 34.11, 17.11, 11.04, 8.76, 6.84 Å corresponding to (001) to (005) reflections respectively. The *d* spacing corresponding to the (001) reflection increases from 22.98 Å in the case of hexylthiolate to 47.78 Å in the case of octadecylthiolate. The increase is linear with the number of

methylene groups in the alkyl chain as can be seen from the inset of Figure 4.1. A linear fit of the variation yields a slope of 2.48 Å per methylene and an intercept of 5.62 Å. These values have to be carefully studied to arrive at the structure of diffracting lamellar solid. The C-C distance along the backbone plane of a fully extended all-trans conformer of an alkane chain is 1.24 Å. Hence, the slope corresponds to the contribution from two methylene groups per diffracting unit indicating that twice the length of alkyl chains is involved. The structure of the head group can be ascertained from the intercept. Based on a search through the Cambridge structural database [78] for unstrained sulfur-bridged Pd motifs containing C-S bonds (including palladium ethylthiolate and n-propylthiolate), we obtained the length of the C-μS-Pd motif along the C-S bond as 2.79 Å, which compares well with one half of the experimental intercept (5.62 Å). Hence, *d*(001) is a measure of the bilayer thickness. The van der Waals radius of the methyl end group is taken to be 1.69 Å [34]. Thus, the calculated projected lengths of octane-, dodecane-, and hexadecane thiolates are 11.94, 16.90, and 21.86 Å, respectively. The observed layer

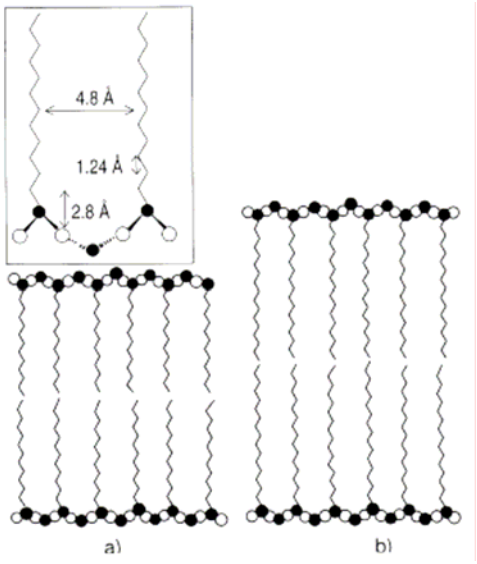

Figure 4.2. Schematics of the lamellar mesoscopic assemblies of Pd(II)-alkanthiolates a) Pd(II)-dodecanethiolate b) Pd(II)-hexadecanethiolate. Alkane chains of the thiols arrange themselves in all-trans conformation into bilayer structures separating rows of sulfur (●) bridged Pd^{2+} atoms (○). The bilayer thickness is estimated on the basis of the known thickness of the C-μS-Pd motif and the number of methylene units assuming no interdigitation of the chains. The inset shows one structural motif. Only long-chain thiols (>C4) tend to form such lamellar structures, while shorter chain thiolates crystallize out into hexameric ring structures [36].

thickness may differ slightly from the estimated value because of small interdigitation of the hydrocarbon chains up to 0.5 Å [27]. Besides, the layer thickness is also sensitive to the annealing conditions; we have observed a variation up to 1 Å routinely. A schematic illustration of the structure of the monothiolate is given in Figure 4.2.

In Figure 4.3, the XRD patterns of a mixed thiolate formed when C_{12} and C_{16} thiols in the ratio 50:50 are mixed with palladium acetate is given along with that of the individual thiolates by the constituent thiols. It is interesting that the mixed thiolate shows a progression of intense reflections similar to monothiolates with their *d* spacings varying as 1:2:3. The diffraction peaks, therefore, correspond to (001), (002), and (003) reflections of a lamellar mesophase, involving two chains per diffracting unit. The *d*(001) spacing is found to be 39.7 Å in the case of the mixed thiolate C_{16}-C_{12}, 50:50. It nearly corresponds to the mean value of the *d*(001) spacings of the individual monothiolates, 34.11 (C_{12}) and 44.03 Å (C_{16}). The subsequent reflections, *d*(002) and *d*(003) of the

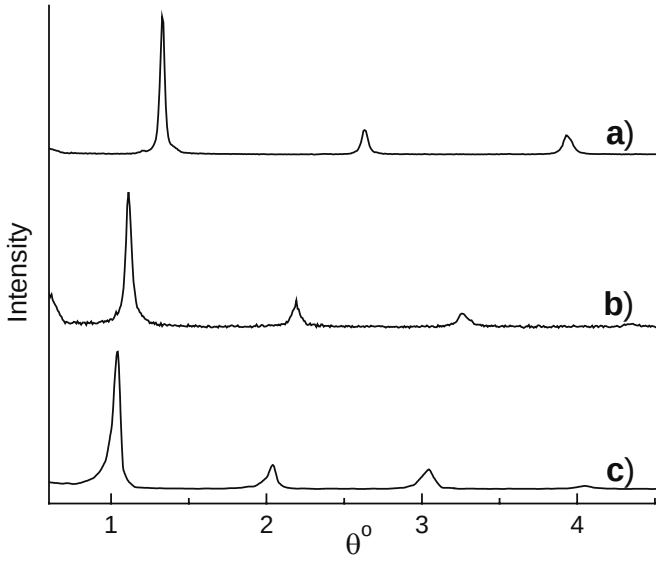

Figure 4.3. XRD patterns of the palladium thiolates: (a) C_{12} monothiolate (b) C_{12}-C_{16} (50:50) mixed thiolate (c) C_{16} monothiolate.

mixed thiolate, also follow a similar trend. Thus, the intermediary *d* spacings and their intensity patterns indicate the presence of a true hybrid phase. We have been successful in preparing hybrid thiolates with various compositions of C_{12}-C_{16} thiols, as well as by employing C_8-C_{12} and C_8-C_{16} thiol mixtures. It is noteworthy that the hybrid thiolates,

when prepared using the toluene solution, contained no noticeable trace of the constituent monothiolate phases. But in highly polar solvents such as acetonitrile, palladium thiolates are insoluble and the XRD patterns from the precipitates showed broad features and even peaks corresponding to monothiolates. Thus, it appears that the solubility of the thiolate plays an important role in determining the formation of hybrid nanocomposites.

Figure 4.4 shows the variation in the *d*(001) spacing with the thiol composition for the three binary systems, C_8-C_{12}, C_{12}-C_{16}, and C_8-C_{16}. The first two systems, in which the constituent thiols differ by four methylene units, the *d* spacing increases gradually as the mole fraction of the longer chain thiol increases. This behavior may be compared with an "ideal" situation in which the two types of molecules organize cooperatively incorporating several defects (Figure 4.5), such that the resulting bilayer thickness is simply an average of the chain lengths of the two molecules weighed with composition, plus a C-μS-Pd layer thickness of 5.62 Å. We see from Figure 4.4a and b that within the experimental uncertainty, the experimental values more or less follow the "ideal", except at higher concentrations of the longer thiol, where the values are slightly on the higher side. This deviation may be due to the reluctance of the longer chain to accommodate a larger number of defects, especially when their population is high. Yet, it is interesting that both systems show a clear tendency to self-assemble, a behavior that is typical of long chain thiols [79]. The C_8-C_{16} system, however, behaves somewhat differently (see Figure 4.4c). The *d* value shows a step-like variation and reaches saturation at 50:50 composition, closely matching that of the C_{16} monothiolate. Intermediate *d* spacings are seen only in C_8-rich compositions (>60%), beyond which the C_{16} thiol dominates the bilayer organization. It is possible that higher disparity in the chain lengths (8 methylene units) and the relatively lower tendency of the C_8 thiol to self-assemble may be the cause of such a behavior.

STM imaging of both mono and mixed thiolates revealed a large number of string-like features generally in bunch, four or five, extending a few tenths of nanometers. We show the images obtained with C_{12} thiolate and a mixed thiolate (C_{16}-C_{12}, 50:50) in Figure 4.6. The typical width of the string of the C_{12} thiolate (Figure 4.6a) was measured to be ~34 Å, closely matching with the bilayer thickness found by XRD. Scanning in smaller regions showed that each string consisted of hair-like features of length ~20 Å

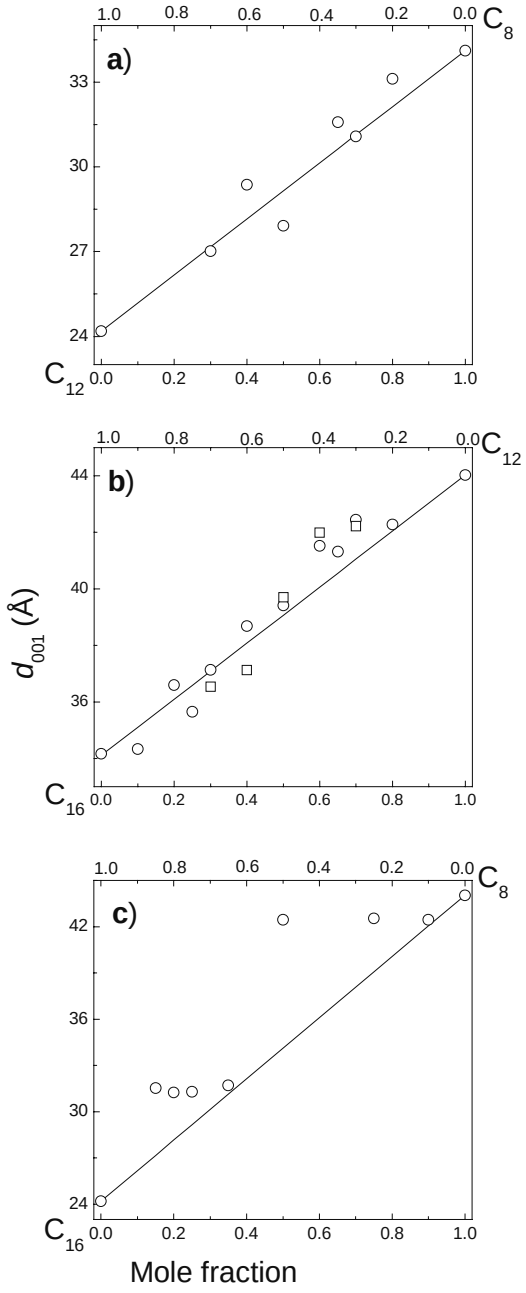

Figure 4.4. Variation in the *d*(001) spacing for the three mixed thiolates with composition (a) C_8-C_{12}, (b) C_{12}-C_{16}, and (c) C_8-C_{16}. Circles denote the experimental data points. The straight lines represent hypothetical bilayers with *d*(001) spacings obtained as weighted averages of the chain lengths of the two constituent thiols plus the C-μS-Pd layer thickness. To ascertain the reproducibility in experiments, a few compositions of C_{12}-C_{16} were repeated (squares in (b)).

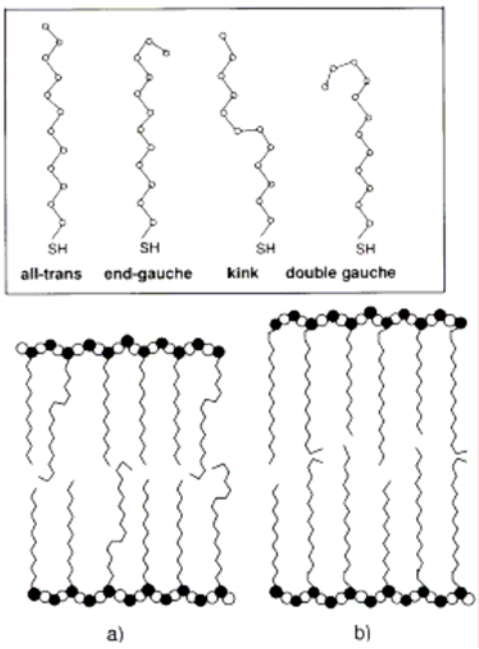

Figure 4.5. A schematic illustration of the structures of mixed palladium thiolates of the C_{12}-C_{16} system, (a) C_{12}-rich and (b) C_{16}-rich. Here, the bilayer thickness corresponds to the weighted average of the chain lengths of the component thiols plus the C-μS-Pd layer thickness. The C_{16} chain adopts disordered conformations to self-assemble into a hybrid bilayer. The C_{12} chain remains defect-free. The inset shows the various defective conformations of the alkyl chains.

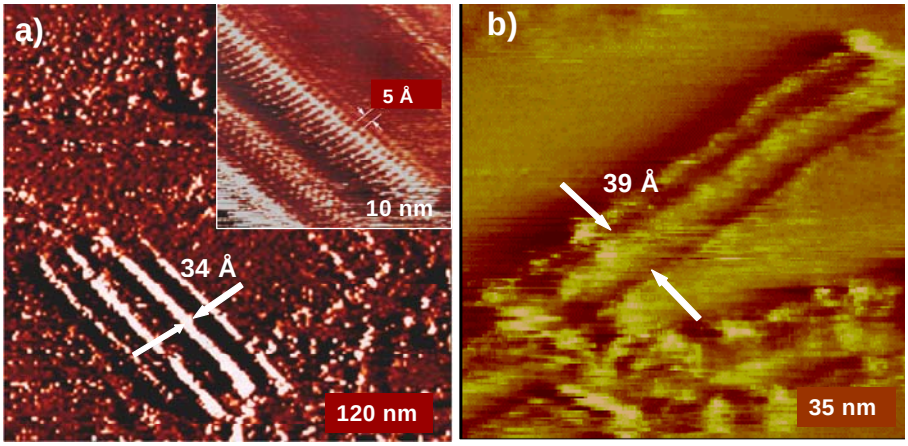

Figure 4.6. STM images of the palladium thiolates (a) C_{12} monothiolate (b) C_{12}-C_{16} (50:50) mixed thiolate. Imaging was carried out with a bias voltage of 188.9 mV, feedback current of 1.2 nA, and a scan speed of 39 nm/s. Inset in (a) shows the internal structure of the monothiolate.

with a uniform separation of ~5 Å. Obviously, these features correspond to the dodecane chains and the separation is typical of alkanethiol molecules in a self-assembled

monolayer [80] and the other known metal thiolates [34,35].The image of the mixed thiolate shown in Figure 4.6b gives a bilayer thickness of ~39 Å, quite comparable to the value obtained from XRD. While STM images showing the internal structure of the hybrid thiolate could have been very informative, all of our attempts in imaging were unsuccessful.

In order to understand the conformations adopted by alkyl chains in these structures, we compared the infrared spectra of the mixed thiolates with those of the monothiolates. Typical spectra from mixed thiolates of various compositions of the C_{12}-C_{16} system are shown in Figure 4.7. The characteristic C-H stretches of the methylene and the end-methyl groups of the alkane chain appear in the 2800-3000 cm^{-1} region. In the case of mixed thiolates (Spectra b, c and d in Figure 4.7), the symmetric (d^+) and antisymmetric (d^-) methylene C-H stretching modes are broad with the mean positions at 2852 and 2922 cm^{-1}, while in monothiolates (Spectra a and e), the peaks appear at 2848 and 2918 cm^{-1} respectively. A shift of 4 cm^{-1} in the vibrational frequency indicates the presence of gauche defects in the mixed thiolates. Support for this observation follows from the work of MacPhail *et al*. who reported the d^+ and d^- modes at 2850 and 2920 cm^{-1}, respectively, for crystalline long-chain n-alkanes [81], whereas in the liquid state [82], where the chains are expected to be disordered, the same modes appeared at 2856 and 2928 cm^{-1}, respectively. The $r^+$and r^- (methyl symmetric and antisymmetric stretch) modes appear around 2873 and 2960 cm^{-1}, respectively, for mono and mixed thiolates (see Figure 4.7). The features being small in intensity, the derivative spectrum method was followed. The derivative spectra in the case of monothiolates revealed the splitting of r^- modes into r_a^- and r_b^- at 2967 and 2956 cm^{-1}, respectively. Thus, the degeneracy of the CH_3 antisymmetric stretch is lifted because of a loss of symmetry of the methyl group. It has been established that for the two antisymmetric stretching vibrations of a methyl group to become degenerate and appear as a single peak, the methyl group must be in at least C_3 symmetry [83]. Such a split of r^- mode was, however, not observed in the case of the mixed thiolates. We believe that for methyl groups present in defective environments, such as in our bilayer assemblies, the methyl groups can adopt a higher symmetry. The scissoring, wagging, twisting, and rocking modes of methylene and methyl groups, as well as the stretching of the skeletal C-C-C backbone, appear in the low-frequency region 600-1700 cm^{-1}) of the spectra. In the case of monothiolates (Spectra f and j in Figure 4.7),

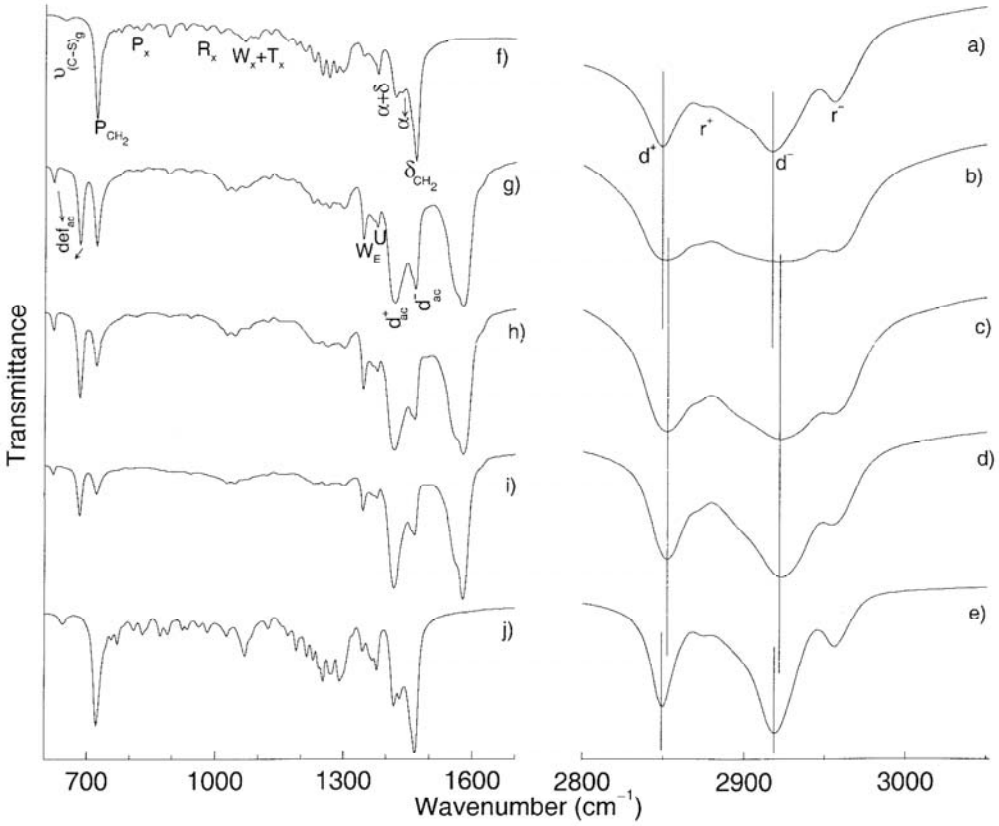

Figure 4.7. FT-IR spectra of the C_{12}-C_{16} system (a,f) C_{16}-monothiolate (b,g) C_{12}-C_{16} (20:80) (c,h) C_{12}-C_{16} (50:50) (d,i) C_{12}-C_{16} (70:30) (e,j) C_{12} monothiolate. The various vibrational modes are denoted in the figure. The modes corresponding to the acetate group are shown with the subscript *ac*. For a detailed description of the modes, see Table 4.1.

the wag-twist progression bands (W_x + T_x, 1175-1350 cm^{-1}) are well-defined (implying that the coupling between the methylene oscillators is unaffected because the chains are all-trans, which is also evident from the C-H stretching modes (Spectra a and e). Interestingly, these bands are greatly diminished in intensity and are broad in the case of mixed thiolates (Spectra g-i in Figure 4.7), which confirms the occurrence of gauche defects in the chains [84-86]. Details of the assignment of the various vibrational modes can be found in Table 4.1.

In all cases, a strong band is observed at ~1467 cm^{-1}, which is assigned to the methylene scissoring mode (δ). The peak at 1419 cm^{-1} may be considered as due to the methylene deformation adjacent to the sulfur. The peaks at 1454 and 1377 cm^{-1} correspond to bending modes of the methyl group, the latter more specifically to the

Table 4.1. Assignment of various vibrational modes in the FT-IR spectra of mono- and mixed thiolates

Vibrational Modes	n =12 (cm^{-1})	n =16 (cm^{-1})	n=12 & n =16 50:50	n =8 &n = 12 50:50	n= 8 &n = 16 65:35	In literature [81-90]
Asymm. CH_3 stretch, r_a^-	2967	2967.7	2960.6	2963	2957	2952
r_b^-	2956	2956.7				2962
Asymm. CH_2 stretch, d^-	2919	2919	2922	2922	2922.5	2920, 2928(crys&liq.n-alkanes)
Symm.CH_3 stretch, r^+	2876	2875	2874	2872.4	2871.2	2870
Symm.CH_2 stretch, d^+	2849	2849	2852	2851.5	2852	2850,2856(crys& liq.n-alkanes)
COO^- asymm.def.	—	—	1578.5	—	—	1577
CH_2 scissor, δ	1467	1467.8	1467	1466.1	1467.3	1467
CH_3 asymm.def., α	1454		1455	1455	1456.5	1458
COO^- symm.stretch	—	—	1422	—	—	1424
α +δ	1416	1417.5	1409	1420	1420.5	1419
CH_3 def	1378	1378	1377	1377.3	1377.3	1375
(umbrella mode),U						
CH_2 $W_{g\text{-}t\text{-}g'}$	1363	—	1365	1365.3	1366	1306 &1366
CH_2, W_E	1343.1	1343	1343	1344	1344	1345,1341
CH_2 wag, W_x			1301	1298.5	1299.2	1294
W_x	1298.1	1292.6			1271.6	1277
CH_2 twist, T_x	1273.1	1278.5				
W_x		1263.4			1257.2	1265
W_x, T_x	1265.2	1246.6		1256		1255
W_x	1251	1228.9		1234	1235.6	1240
W_x, T_x	1240	1224	1225.8			1232
T_x, W_x	1228			1214	1216.4	1211
T_x,W_x	1212	1206.7		1194.8	1196	1201
T_x	1198	1185.5				1190
W_x	1188.1					
C-C-C skeletal,R_x	1167.8	1126	1122	1118	1125	1122
R_x	1123	1097	1044	1092.8	1091	
R_x	1069	1067	1023	1026.7	1026.7	
R_x	1025	1006.7	1008			
CH_2 rocking, P_x	980	975		952	952.3	
P_x	959	955				
P_x	932					
$(P_{CH3},R)_E$						
P_x	921	928	940	925	912.7	943
P_{CH3}	889	888.6	889	888	888	891
P_x	869.4	850.2				
P_x	828.1	823.7				825
P_x	808.9	804.5		804	803	810
$P_{CH2\text{-}CH3}$	771	776				782
P_x	757	763		766	766.2	760
P_x	744	738				
P_l, $\gamma_{(C\text{-}S)\,t}$	720.3	720.4	720.3	720.6	720.6	719
$\gamma_{(C\text{-}S)\,g}$	642	646	645	645	645	640,650
COO^- def.			619,682			612, 636

umbrella deformation (*U*). A peak at 1343 cm^{-1} arises because of an end gauche defect (W_E), the intensity of which is relatively higher in the mixed thiolate [84-86]. The intensity ratio, I_{1343}/I_{1377}, can be taken as a measure of the end gauche population [87]. In Figure 4.8, we show how this ratio varies with the composition of the thiolate. The C_{12} monothiolate shows a value of ~0.5, which increases to ~0.9 with the mixed thiolate containing 20% of C_{16}. When the C_{16} thiol is 30%, the ratio jumps to 4.7 and decreases gradually with further increase in the proportion of C_{16} thiol. Evidently, it is mainly the

C_{16} thiol that accommodates these defects to form crystalline mesophases with intermediate layer thicknesses. At higher proportions of C_{16}, for which the layer thickness approaches that of the C_{16} monothiolate, the defect concentration also decreases gradually. Apart from the above wagging modes, the spectra also exhibit weak bands at 1301 and 1365 cm^{-1} due to $W_{g\text{-}t\text{-}g'}$ [84-86, 88] indicating the presence of a very small population of kinks in the chain.

A series of peaks observed between 1000 and 1150 cm^{-1} are assigned to the skeletal C-C-C vibrational modes (R_x), while the progression bands in the region 700-980 cm^{-1} are assigned to the rocking modes (P_x) of the methylene chains [89]. The main band at 720 cm^{-1} is the head band of the rocking progression. This band is present in all of the cases, whereas the progression series gets diminished in the case of mixed thiolates. A weak peak observed at 646 cm^{-1} is assigned to the C-S stretch to an adjacent gauche methylene unit, $\nu(C\text{-}S)_g$ [44]. The $\nu(C\text{-}S)_t$, which is expected at 719 cm^{-1}, is obscured by the rocking head band. The assignments are tabulated in Table 4.1.

An interesting observation that follows from the infrared spectra of the C_{12}-C_{16} system is the existence of a strong peak at 1577 cm^{-1} in the spectra of mixed thiolates (Spectra g, h and i in Figure 4.7) that is absent in the case of the monothiolates (Spectra

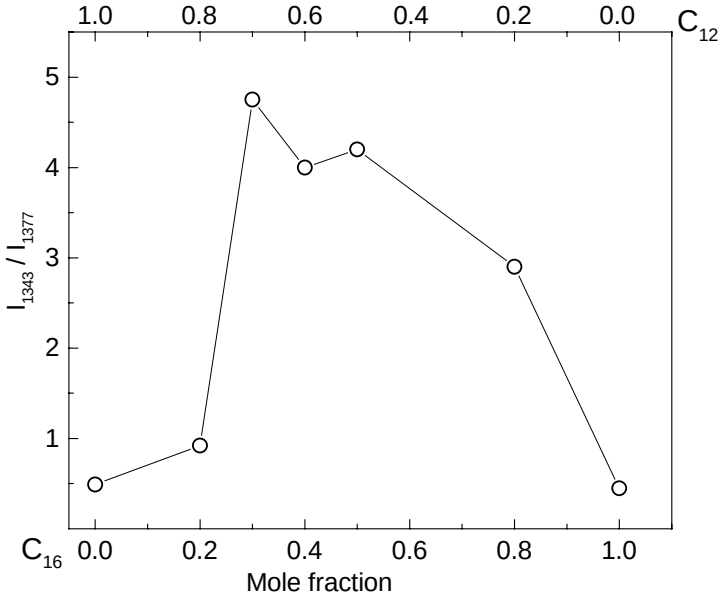

Figure 4.8. Variation in the ratio of the intensities of the end gauche mode (1343 cm^{-1}) and the methyl umbrella mode (1377 cm^{-1}) with the composition of the C_{12}-C_{16} mixed thiolate.

f and j). The peak at 1577 cm^{-1} is assignable to the antisymmetric stretching of acetate groups [89,90]. Further evidence for the presence of an acetate group in the mixed bilayer is drawn from the observation of a distinctly high-intensity region around 1420 cm^{-1}, which is unusual for methylene deformation (which occurs at around the same position). This is taken to correspond to the symmetric stretching of the acetate group. The extra features at 682 and 620 cm^{-1} in the case of mixed thiolate are assignable to the bending modes of the acetate group. These infrared signatures are clearly not due to the liberated acetic acid, for it was carefully washed away while depositing the bilayer film. Moreover, the C=O stretching band of free acetic acid, if present, would appear at 1730 cm^{-1}, distinctly different from the observed bands [89]. The presence of acetate groups amidst the crystalline bilayers is indeed surprising. It arises possibly because of the incomplete displacement of the acetate groups of the palladium acetate by thiols. However, this is not the case with compositions rich in C_{12} (>70%). The spectrum of the C_{12}-C_{16} 80:20 thiolate shown in Figure 4.9 is completely devoid of the acetate modes. Such is the case with all compositions of the other two (C_{12}-C_8 and C_8-C_{16}) mixed thiolate systems (see Figure 4.9).

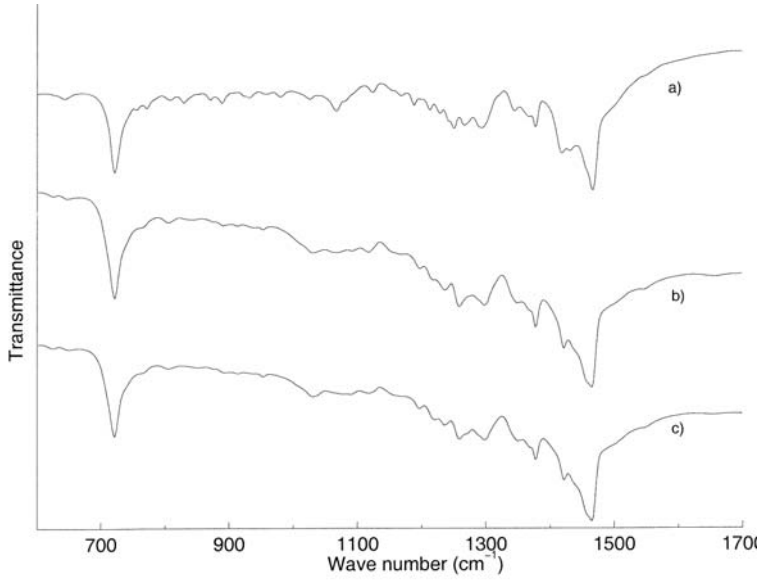

Figure 4.9. FTIR spectra of mixed palladium thiolates (a) C_{12}-C_{16} (80:20) (b) C_8-C_{12} (50:50) (c) C_8-C_{16} (65:35). Spectra b and c are only representative; indeed all compositions of C_8-C_{12} and C_8-C_{16} systems showed no modes corresponding to the acetate group.

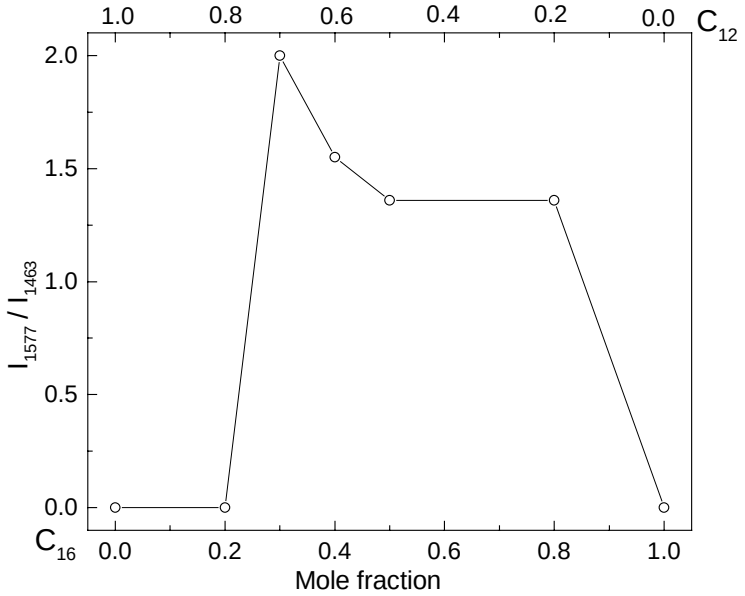

Figure 4.10. Variation in the ratio of the intensities of antisymmetric stretching mode of the acetate group (1577 cm^{-1}) and the methyl scissoring mode (1463 cm^{-1}) with the composition of the C_{12}-C_{16} mixed thiolate. This is taken as a measure of the relative population of undisplaced acetate groups that are present in the bilayer.

On the basis of the above observations and in the absence of any kinetic or mechanistic details of the reaction, we speculate that following the palladium acetate and thiol reaction, some sort of rudimentary assembly builds up spontaneously in solution in which some acetate groups from the palladium acetate precursor may get trapped and become inaccessible for further reaction (even after refluxing the toluene solution of thiolate for extended hours). The population of the undisplaced acetate groups for different compositions of the C_{12}-C_{16} system was calculated from the intensity ratio I_{1577}/I_{1463} (Figure 4.10). It is remarkable that the acetate group population nearly mimics the population of the end gauche defects (compare Figures 4.8 and 4.10). The amount of acetate retained by the structure depends on the composition of the C_{12}-C_{16} mixed thiolate those containing the C_{16} thiol at 30% or greater carry a relatively higher population of the acetate. In contrast, monothiolates of C_{12} and C_{16}, as well as their mixed thiolates rich in C_{12} (>70%), fail to accommodate the acetate groups in the bilayer structure (see Figures 4.7, 4.9, and 4.10). Thus, the two factors-readiness to assemble and adequate disorder leaving some free volume-seem to be important in providing shelter to the acetate groups. The C_{16} thiol in combination with small amounts of C_{12} does it well. It has been

suggested in the literature [34,53] that it may be possible to trap solvent molecules in the voids between alkyl chains of thiolates. The mixed thiolates presented above provide excellent experimental evidence.

4.4.2 Palladium thiolates as single source precursors for Pd nanocrystals and Pd films-a preliminary study

A previous study from this laboratory on the melting behavior of Pd(II)-alkanethiolates of different chain lengths has shown that these mesophases melt in the temperature range of 60 °C to 100 °C, with the melting point increasing linearly with the thiol chain length [36]. When heated to temperatures above the melting point, they undergo decomposition.

The present work is related to the thermolysis of Pd-thiolates to form Pd nanocrystals. Figures 4.11, 4.12 and 4.13 show the TEM images of Pd nanocrystals obtained by heating Pd(II)-alkanethiolates of different chain lengths, octanethiolate ($PdSC_8$, 155 °C), dodecanethiolate ($PdSC_{12}$, 185 °C) and hexadecanethiolate ($PdSC_{16}$, 185 °C) in the solid state, in argon atmosphere. The histograms and SAED patterns corresponding to each system is also given. The particles form a close packed arrangement (see Figures 4.11, 4.12, 4.13a) with mean size decreasing from 8.5 nm in the case of $PdSC_8$ to 2 nm for $PdSC_{16}$ (see histograms in Figures 4.11, 4.12, 4.13c). SAED in each case gives the reflections typical of Pd metal. High resolution TEM (HRTEM) of a Pd nanocrystal reveals a *d*-spacing corresponding to (220) lattice plane (Figure 4.13d). A clear dependence of the particle size on the chain length or bilayer thickness is noticeable, the longer chains forming smaller particles.

In the case of $PdSC_{10}$, the experimental conditions were slightly different, the thermolysis being conducted in air. The Pd nanocrystals obtained from $PdSC_{10}$ are rather irregularly shaped with a mean size of 1.8 nm (Figure 4.14a and c). SAED (Figure 4.14b) shows reflection corresponding to Pd lattice. Hence it is clear that Ar atmosphere is essential for the formation of well-shaped Pd nanocrystals. When the longer thiolates were heated at lower temperatures (155 °C), partial decomposition was observed (Figure 4.14e). Also, the shorter thiolates, for eg. $PdSC_6$ could not produce well-shaped nanocrystals, only aggregates were observed (Figure 4.15). The suggestive mechanism

for the formation of Pd nanocrystals is the reductive elimination of thiols as disulfides forming Pd followed by stabilization of nanocrystals by the disulfide.

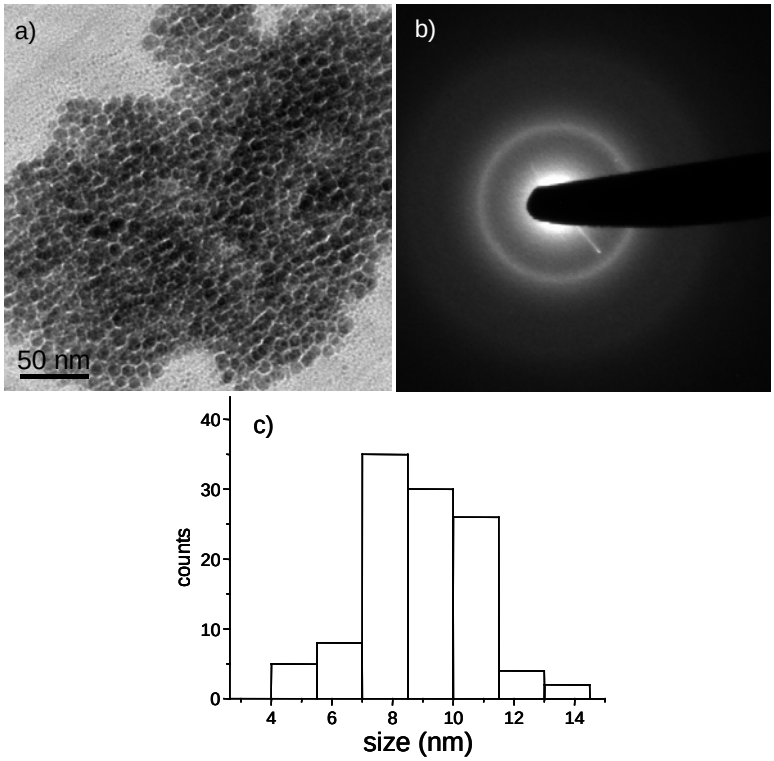

Figure 4.11. a) TEM image of Pd nanocrystals obtained by thermolysis of $PdSC_8$ – Ar atmosphere, 155 °C, 2 hr. b) SAED showing the (111) reflection from Pd nanocrystals. c) Histogram giving the particle size distribution, mean size ~8.5 nm.

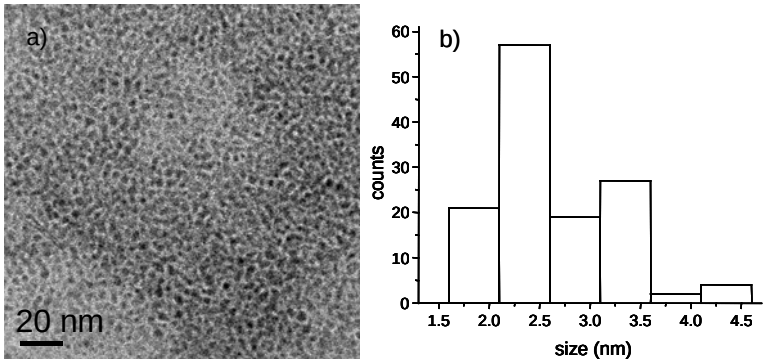

Figure 4.12. a) TEM image of Pd nanocrystals from the thermolysis of $PdSC_{12}$ – Ar, 185 °C, 2 hr. b) Histogram giving the particle size distribution, mean size ~2.5 nm.

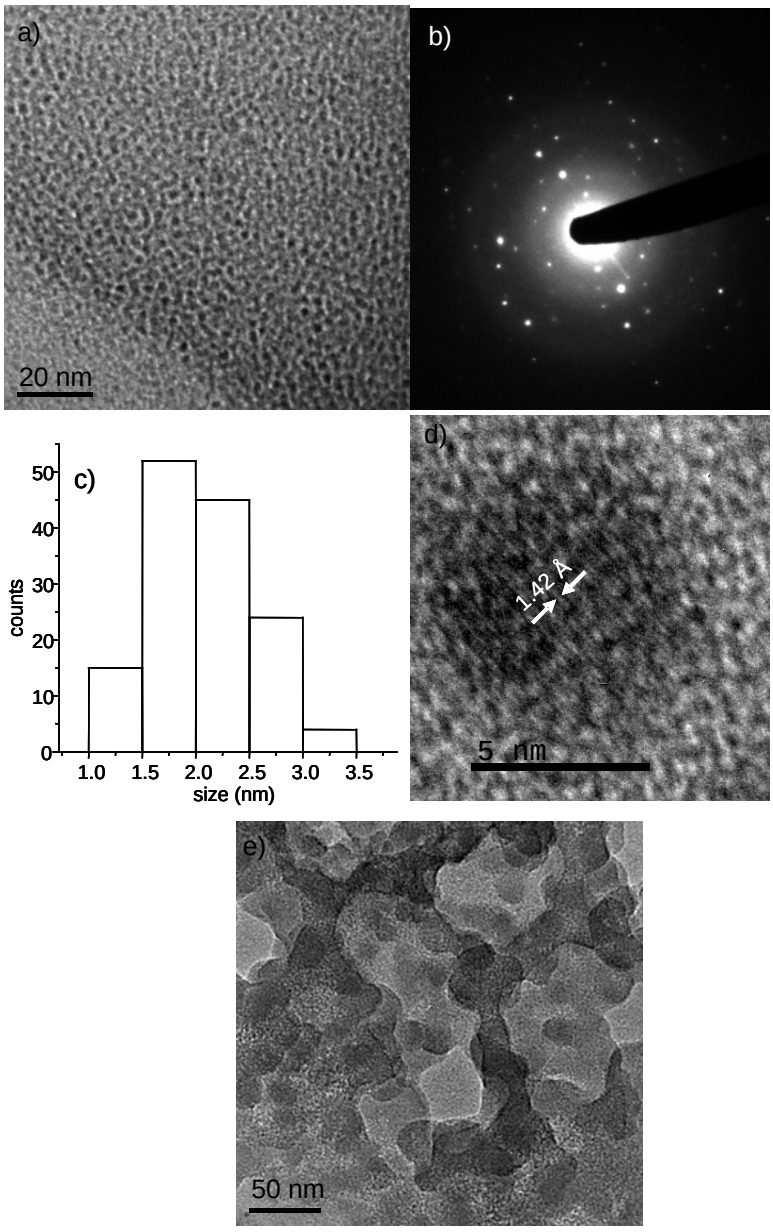

Figure 4.13. a) TEM image of Pd nanocrystals from the thermolysis of $PdSC_{16}$ – Ar, 185 °C, 2 hr. b) SAED from Pd nanocrystals. c) Histogram giving particle size distribution, mean size ~2 nm. d) HRTEM revealing the 220 lattice plane of Pd (1.375 Å in JCPDS). e) TEM image showing partially decomposed $PdSC_{16}$ when heated at 155 °C.

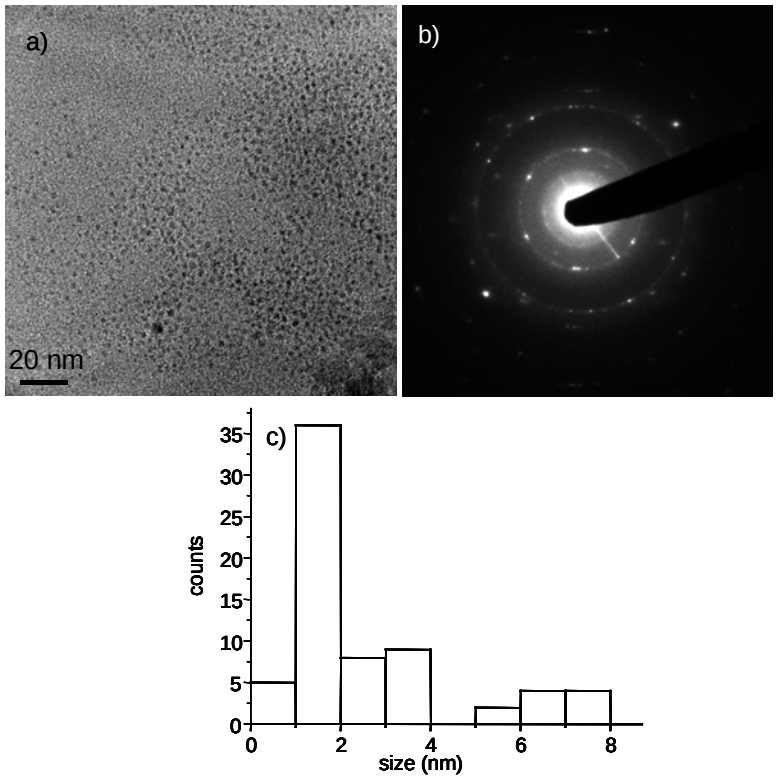

Figure 4.14. a) TEM image of Pd nanocrystals from the thermolysis of $PdSC_{10}$ – air, 185 °C, 2 hr. b) SAED showing reflections from Pd lattice. c) Histogram giving the particle size distribution, majority having a size of 1.5 nm.

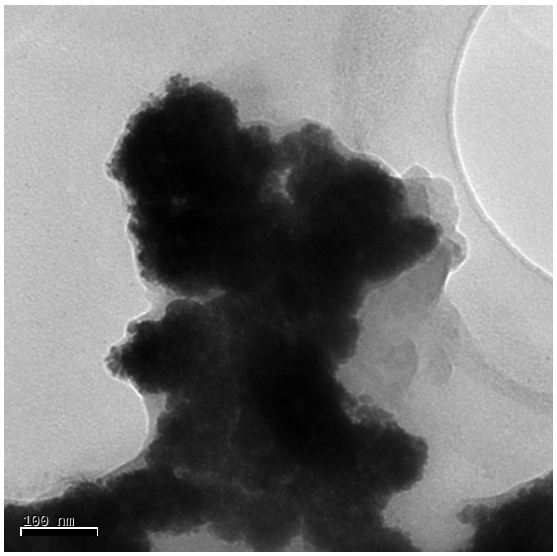

Figure 4.15. TEM image of Pd aggregates obtained from the thermolysis of $PdSC_6$ – air, 155 °C, 2 hr.

Thermal decomposition occurs according to the following reaction scheme:

$$Pd(SR)_2 \longrightarrow Pd + RS\text{-}SR \qquad (4.1)$$

Such a mechanism has been reported in the case of decomposition of Au(I)-alkanethiolate producing Au nanocrystals [28]. Thioethers are the by-products when metal sulfides are formed [22]. A detailed study of the thermal decomposition of metal alkanethiolates by Carotenuto *et al*. [26] using differential scanning calorimetry and thermogravimetry have shown that these systems undergo melting from crystalline phase and then undergo decomposition to either metal or metal sulfides. If the metal-sulfur bond energy is lower than sulfur-carbon bond energy (714.1 kJ/mol), then the thermolysis preferentially leads to metal and disulfide as by-product, while it leads to metal sulfide formation, for higher metal-sulfur bond energy.

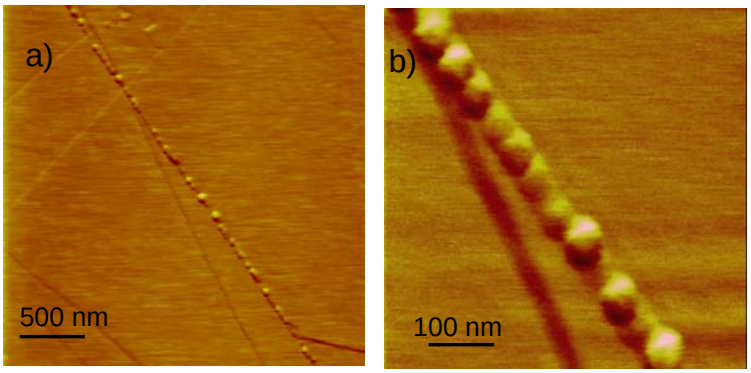

Figure 4.16. AFM images of Pd nanocrystals on HOPG. a) Aggregates of nanocrystals are found to self-assemble along the steps. b) A zoomed in view of the nanocrystal array.

Pd nanocrystals obtained by thermal decomposition method were examined under AFM. Figure 4.16 shows that, the nanocrystals form aggregates and arrange spontaneously along HOPG steps producing necklace patterns.

When the thiolates were heated at higher temperatures above 200 °C in air, they got completely decomposed to form a silvery gray film with high metallic conductivity. Figure 4.17 gives the XRD pattern from the film showing reflections typical of Pd metal. The film is polycrystalline with (111) plane as the preferred orientation. The peaks marked with asterisks do not correspond to Pd and their *d* spacings are not easily identifiable with PdS and PdO either. XPS analysis of the film (Figure 4.18) show that Pd

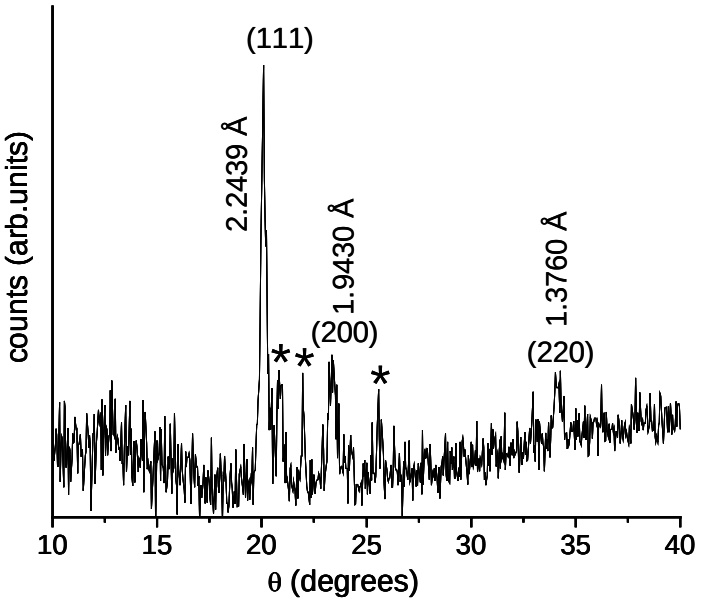

Figure 4.17. XRD pattern from a Pd film obtained by the decomposition of Pd(II)-dodecanethiolate in air at 250 °C for 2 hr. The peaks corresponding to Pd metal are marked. The asterisks correspond to unidentified peaks.

is in the metallic state. The core level binding energy of Pd $3d_{7/2}$ (334.8 eV) corresponds to Pd in the zero oxidation state. The curves in Figure 4.18 are fitted using Gaussian expression. The C 1s level binding energy corresponds to graphitic carbon (284.7 eV) and also a small percentage oxidized alkyl carbons (286.7 eV). The peaks for O 1s level at 531.8 eV (corresponding to O^{2-}) and at 535 eV indicate that a fairly good amount of oxygen is present on the surface in the form of adsorbed species. There is negligible amount of sulfur in the film. Hence, these compounds may be utilized for the production of Pd films by inkjet printing [91].

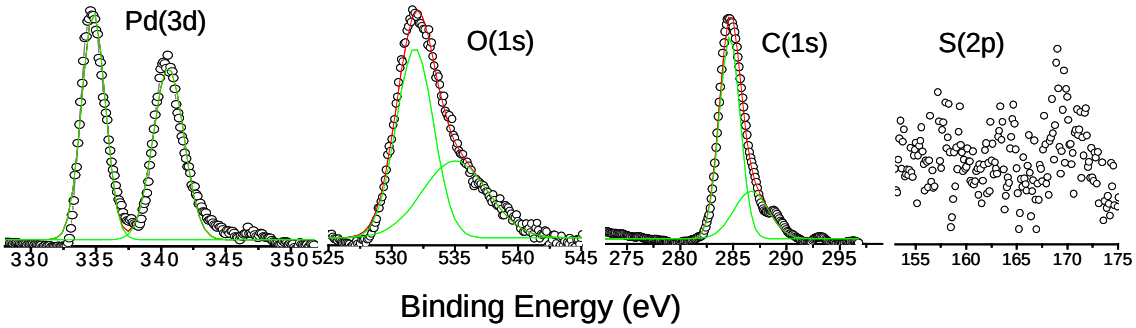

Figure 4.18. XPS analysis of Pd film obtained from the pyrolysis of $PdSC_{12}$ at 250 °C for 2 hr. The core level spectra of Pd(3d), O(1s), C(1s) and S(2p) are shown (intensity scales are different).

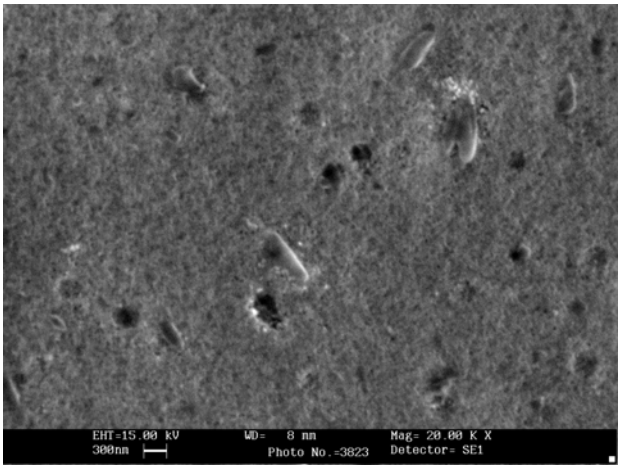

Figure 4.19. SEM image showing the morphology of the Pd film

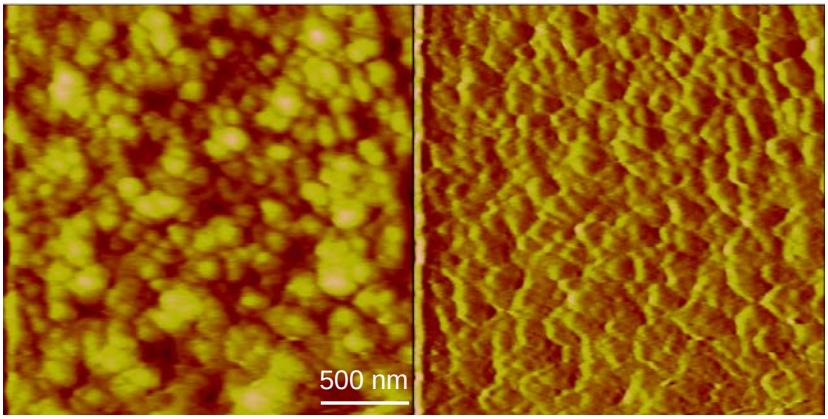

Figure 4.20. Contact mode AFM topography (left image) and lateral force micrograph (LFM, left image) of the Pd film.

The morphology of the Pd film obtained by the pyrolysis of $PdSC_{12}$ spin-coated on a glass plate was examined using SEM and AFM. Figure 4.19 shows the SEM image of the Pd film. AFM images (Figure 4.20) show a granular film similar to that of a sputtered film.

4.4.3 Electrical characterization of Pd(II)-alkanethiolates by C-AFM

Contact mode AFM images of lamellar solids of Pd-alkanethiolates (PdSR) show bundles of elongated features extending over several hundreds of nanometers, the bundles being oriented in different directions. AFM topography of Pd-dodecanethiolate ($PdSC_{12}$) is given in Figure 4.21a. The lateral widths of the features vary from 40 to 17 nm

indicating that they actually consists of 10 to 5 units of bilayers when compared with the *d*-spacing obtained from the XRD (Figure 4.1) and also from high resolution STM image (Figure 4.6a). A zoomed in AFM image of a bundle is shown in Figure 4.21b. LFM image of $PdSC_{10}$ taken in friction mode shows similar features (Figure 4.21c). Due to the poor resolution of the gold-coated tip, the individual units could not be seen in the AFM image.

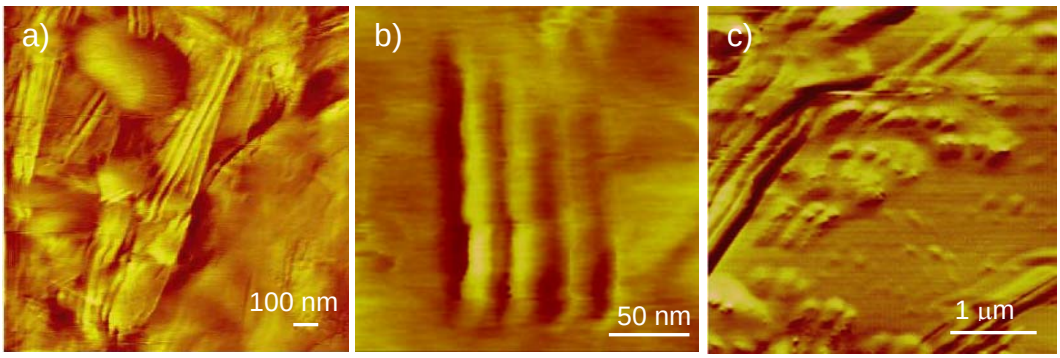

Figure 4.21. a) AFM topography of $PdSC_{12}$ deposited on HOPG. The elongated features represent bilayers. b) A closer view of the bilayers. c) LFM image of $PdSC_{10}$ on HOPG.

A schematic of the configuration used for conducting AFM measurements is given in Figure 4.22a. The tip was biased with respect to the sample that was held at ground potential. A typical I-V curve obtained from a Pd-alkanethiolate, $PdSC_6$ when a bias ramp of ±1 V is applied, is shown in Figure 4.21b. Clearly, the I–V curve exhibit a non-ohmic behavior and is asymmetric. The current is low close to zero bias and increases almost linearly with bias voltage up to ~ ±0.2 V (rectangular region in Figure 4.22b) beyond which there is a sudden increase in the current. The expanded view of the low bias region is given in the inset. The variation in current in the high bias region is also linear with the applied voltage but with a higher slope. The different linear regimes in the spectrum are marked by dotted lines. On the positive bias, at the crossover region (+0.46 V), we observe a small but well-defined peak, corresponding to a negative differential resistance feature.

The I-V characteristics for bilayers with increasing chain lengths, for $PdSC_8$, $PdSC_{10}$, $PdSC_{12}$ and $PdSC_{16}$ i.e, increasing bilayer thicknesses are given in Figure 4.23. It is clearly seen that the current decreases with increasing chain length of the thiolate. The linear variation near zero bias lies between +0.4 and –0.5 V in $PdSC_6$ (Figure 4.22b)

while in $PdSC_{16}$ (Figure 4.23d), it lies between +0.75 and –0.75 V. Accordingly, the NDR feature is shifted to higher bias voltage values of +0.46 V and +0.8 V, respectively and its intensity decreases gradually to eventually disappear like a shoulder in the crossover region in the case of $PdSC_{16}$.

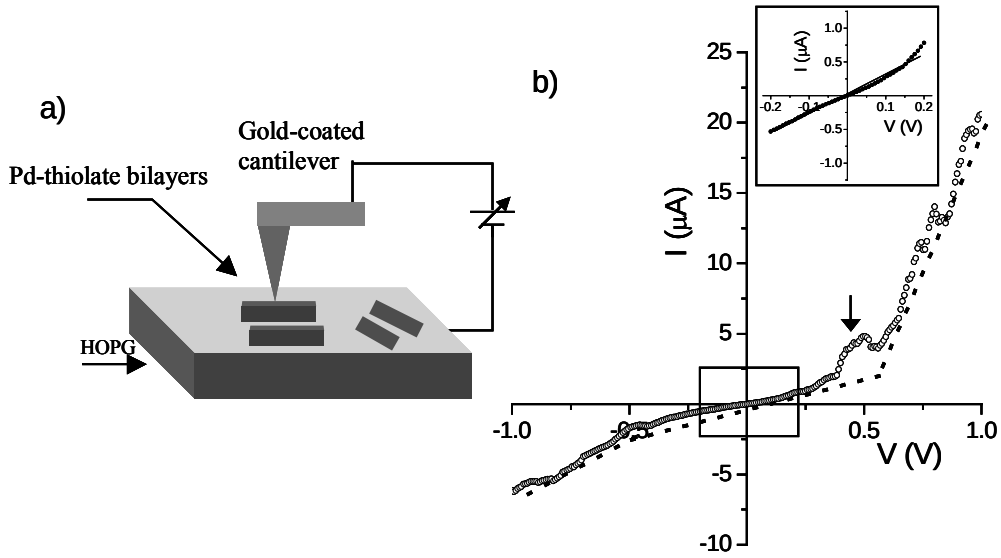

Figure 4.22. a) A schematic of the configuration employed for C-AFM of Pd-thiolate bilayers. b) I-V characteristics of $PdSC_6$. The arrow indicates the NDR region. The linear regimes in the spectrum are marked by dotted lines. The zoomed in view of the rectangular region is given in the inset.

A linear I–V behavior with low current around the zero bias is akin to the transport in alkanethiols [92-97]. Ratner *et al*. [98] have theoretically predicted such a linear variation for small voltages in the case of molecular wires. The most common situation for long range electron transport, as encountered in donor-bridge-acceptor assemblies and metal-insulator-metal junctions, is where the Fermi level of the electrodes occurs in the middle of the HOMO/LUMO gap for the organic material and in this situation, coherent nonresonant tunneling also known as superexchange tunneling is the mechanism of electron transport [97-99]. For alkanes up to a certain length and for low voltages, the current through the junction is given by

$$I = I_0 \; e^{-\beta d} \tag{4.2}$$

where d is the length of the molecular bridge (chain length) and β is an energy-dependent parameter characterizing the molecule known as the decay parameter [97-100].

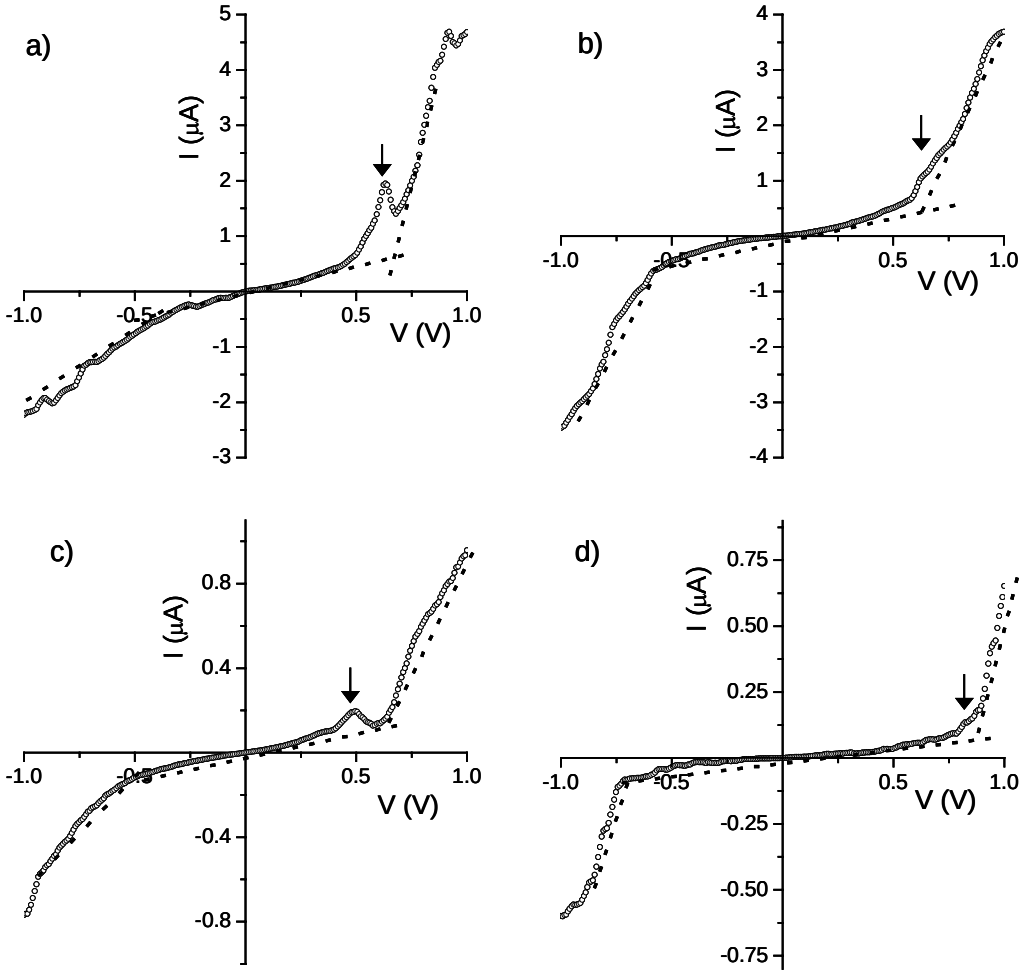

Figure 4.23. I-V characteristics of Pd-alkanethiolates with increasing bilayer thickness from C-AFM a) $PdSC_8$ b) $PdSC_{10}$ c) $PdSC_{12}$ d) $PdSC_{16}$. The different linear regimes are indicated by dotted lines. The arrows indicate NDR positions.

It follows from the above equation that in nonresonant tunneling regime, the current falls exponentially with increasing distance or chain length. β is a measure of the tunneling efficiency through the alkyl chains, a higher value indicating lower tunneling efficiency [100]. Measurements on self-assembled monolayers of alkanethiol junctions by various techniques employing Hg drop electrodes [94,97] and C-AFM [97,101] with varying chain lengths have estimated a β value of 1±0.1 $Å^{-1}$, indicating a lower tunneling efficiency. For conjugated systems, β is found to be small on the order of 0.4±0.2 $Å^{-1}$ and hence tunneling efficiency is high in these systems [102,103].

In the case of Pd-thiolates, the resistance of the thiolate bilayer is calculated from the linear regime of the low bias region in the I-V curve (see inset of Figure 4.22b) as 1/slope. For nonresonant tunneling, the resistance should vary exponentially with chain length or bilayer thickness according to the expression [100]

$$R = R_0 e^{\beta d} \tag{4.3}$$

which follows directly from eq 4.2; d being bilayer thickness in this context. A semilog plot of the resistance vs bilayer thickness ranging from hexyl to hexadecane thiolates gives a linear variation clearly indicating an exponential dependence of resistance/current on chain length/bilayer thickness as depicted in Figure 4.24. β as calculated from the slope of the plot in Figure 4.24 is 0.2±0.04. A lower value of β indicates high tunneling efficiency and long-range transport in Pd-alkanethiolate bilayers. It also gives an idea that the nonresonant tunneling in this case is very different from that through the free space. However, the absolute current is larger than that expected for systems with organic linkers. Since the bilayers are lying on the graphite substrate with chains being parallel to the surface, tunneling from tip to the substrate also contributes to the total current.

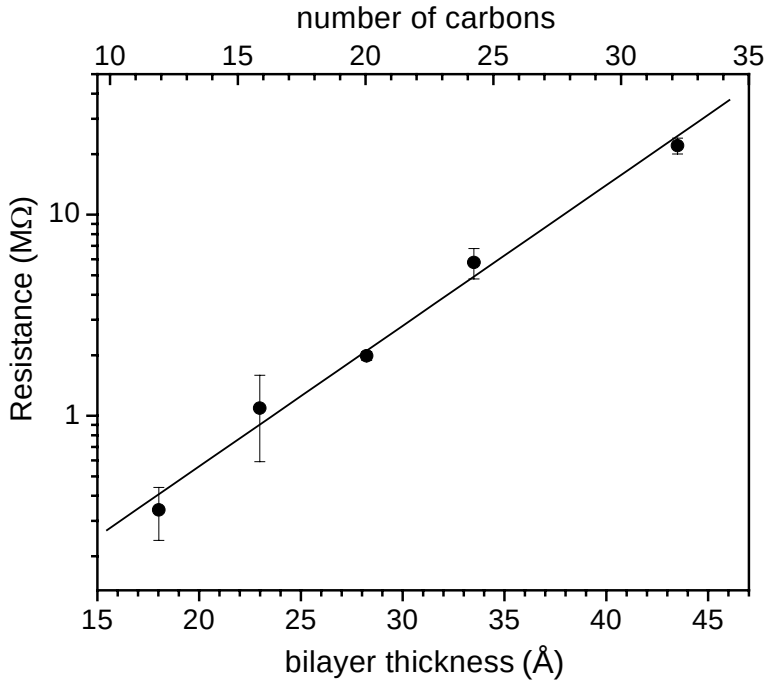

Figure 4.24. A semilog plot of the resistance of Pd-alkanehtiolate bilayers vs the bilayer thickness. The top axis gives the number of carbons constituting the bilayer junction. The error bar is estimated based on several measurements on each bilayer.

A sharp increase in the current with higher biases (>0.6 V) can be attributed to resonant tunneling [97,98]. This happens when the Fermi level of electrode approaches the energy of the molecular orbitals resulting in electrons actually populating the energy levels. It may be noticed from the I-Vs that the bias at which this sudden jump occurs shifts towards higher values for larger bilayer thickness (Figure 4.23). This is because the energy required for resonant tunneling will be more for higher chain lengths having larger barrier widths. Asymmetry in the I-V comes from the difference in the work functions of gold (AFM tip) and graphite electrodes (the substrate).

The appearance of NDR peak may be due to resonant tunneling via interface states arising from hybridization between molecular thiol groups and d orbitals of Pd and hence, a direct consequence of the -Pd-S-Pd- backbone in the system. Dalgeish *et al.* [104] have predicted that single alkane dithiolate molecules bridging transition metal nanoelectrodes (including Pd/Rh, Pt/Rh, and Pt/Pt) can exhibit NDR, on the basis of ab initio and semiempirical calculations. The resonant conduction through interface states happens at specific bias, beyond which the amplitude of resonance decreases and resonant tunneling through molecular levels takes over. Hence, NDR is observed at a crossover from nonresonant to resonant tunneling regimes.

4.4.4. Ni(II)-alkanethiolates: Chain length dependent magnetic interactions

X-ray diffraction patterns from powder samples of nickel alkanethiolates with increasing chain length of the alkanethiol is given in Figure 4.25a. A series of (00k) reflections typical of a lamellar bilayer structure is seen, as is the case with palladium thiolates and other metal thiolates [34,36]. The $d(001)$ spacing varies linearly from 13.53 to 43.5 Å with increase in alkyl chain length from 3 to 15 methylene units (i.e., 4 to 16 carbons). A linear fit to the plot of $d(001)$ spacing vs. number of methylene units (Figure 4.25b) constituting the bilayer gives a slope of 1.279 Å per methylene unit, closely matching with the value of 1.24 Å of an all-trans conformer [34,36]. The intercept of the linear fit, originating from inorganic backbone comes out to be 5.39 Å, comparable with other alkanethiolates [34,36]. Thus, there are two contributions to the bilayer thickness, twice the thickness of inorganic slab consisting of Ni and S ($2t_1$) and twice the alkanethiol chain length ($2t_2$). t_2 is given by $L + r_w(X)$, where L is the length of the

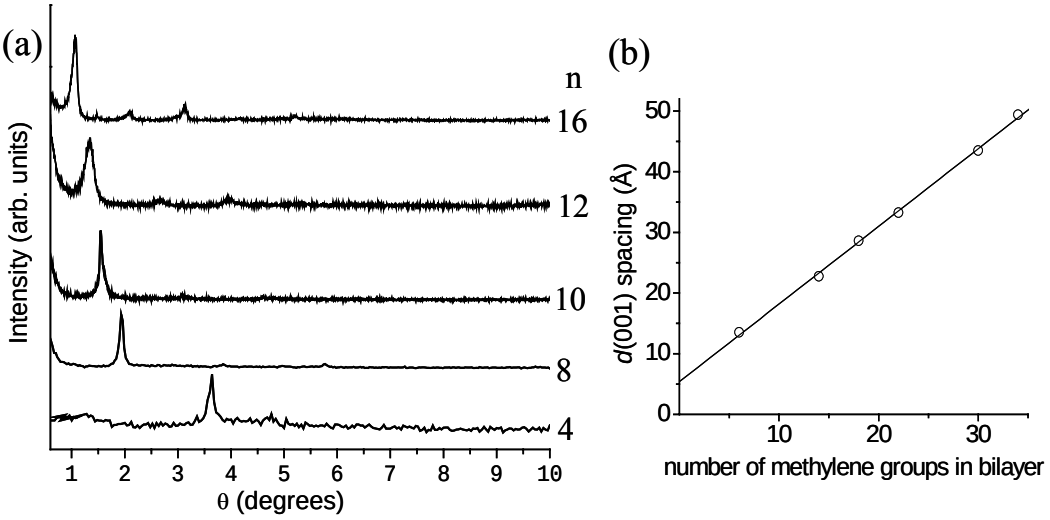

Figure 4.25. a) XRD pattern of nickel alkanethiolates with different chain lengths. n is the number of carbon atoms present in the alkanethiol. b) A linear variation of *d*(001*)* spacing with the chain length. The *d*(001*)* spacing is proportional to twice the alkanethiol chain length and hence, denotes the bilayer thickness.

methylene chain and r_w, the van der Waals radius of the distal atom X (here, -CH_3) [34]. Assuming r_w as 1.69 Å, the calculated value for the backbone thickness of nickel dodecanethiolate is 2.59 Å twice of which (5.18) is close to the intercept value, 5.39 Å obtained from the linear fit in Figure 4.25b. A difference in the value up to 1 Å can be explained as due to the interdigitation of the chains. A similar observation is reported in the case of silver, copper and palladium thiolates and also in the case of silver carboxylates [35,40,47]. The reported structures of toroidal nickel thiolates and also ab-intio calculations indicate that the co-ordination environment of Ni to be square planar and the Ni-Ni non-bonding distance (2.9-3 Å) is very close to the normal Ni-Ni bond length [15,32]. Based on the above observations, a schematic of the lamellar nickel thiolate is given in Figure 4.26 where Ni(II) is in square planar co-ordination.

Infrared spectra of nickel alkanethiolates showed the symmetric and antisymmetric methylene stretches at 2849 and 2918.5 cm^{-1} respectively confirming an all-trans conformation of the alkylchain. Figure 4.27 gives the mid-IR spectra of nickel hexadecanethiolate. The wag-twist (W_x, T_x) progression bands in the region 1175–

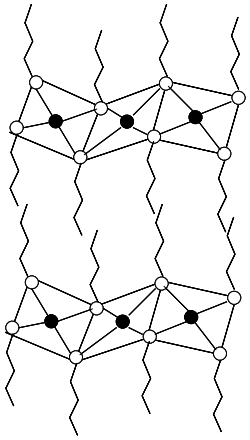

Figure 4.26. A schematic of the bilayer configuration of lamellar nickel alkanethiolate [2,17] nickel butanethiolate. Dark circles represent Ni atoms and hollow ones, sulfur. Ni(II) is shown in square planar coordination.

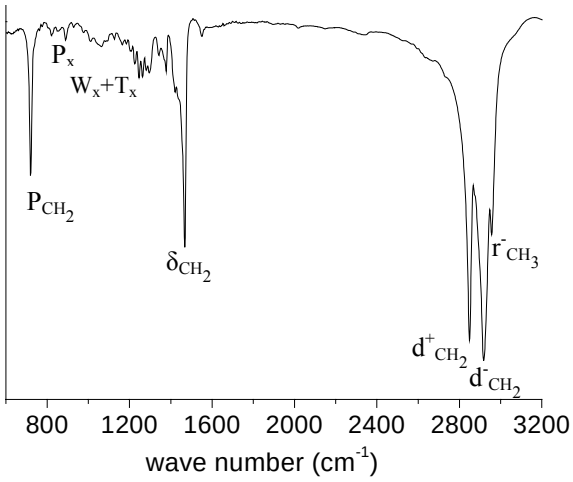

Figure 4.27. FT-IR spectra of nickel hexadecanethiolate. The assignments of different vibrational modes are also given.

1300 cm^{-1} further support the all-trans conformer of the polymethylene chain. Room temperature UV-Visible spectra for nickel butanethiolate in heptane is shown in Figure 4.28. The intense absorptions here correspond to the S(thiolate) $p_\pi \rightarrow$ Ni d-orbital charge transfer transitions. For tetrahedral Ni(II), additional bands in longer wavelength region (>700 nm) are expected due to spin allowed d-d transitions [16,105]. The absence of any prominent d-d transitions is suggestive of a square planar geometry for Ni(II).

Before proceeding with magnetic measurements, the chemical composition of nickel alkanethiolates was estimated by elemental analysis. See Table 4.2 for a comparison with

calculated values, assuming a molecular formula of $Ni(SR)_2$. The thiolates were purified till there no chlorine was observed in the EDX spectra.

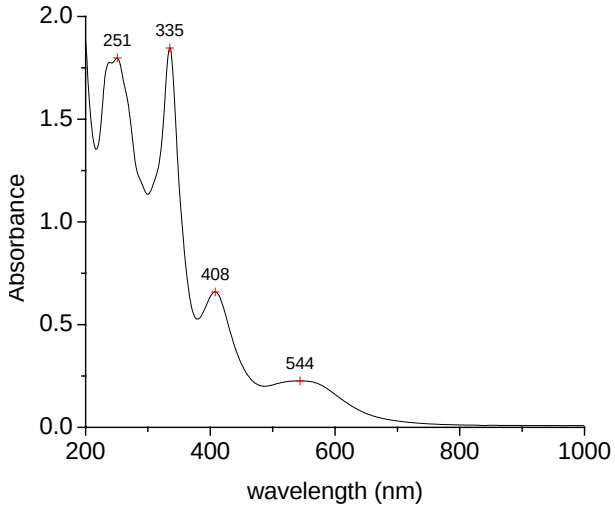

Figure 4.28. UV-Vis absorption spectra of nickel butanethiolate in heptane at room temperature. Other chain lengths also showed similar spectra.

Table 4.2. Elemental analysis of nickel alkanethiolates

	Experimental (%)	Calculated (%)
Nickel butanethiolate	C-39.2, H-7.29, S-25.17	C-40.5, H-7.6, S-27, Ni-24.9
Nickel octanethiolate	C-54.5, H-9.56, S-16.81	C-54.8, H-9.7, S-18.4, Ni-16.8
Nickel decanethiolate	C- 59.78, H-10.37, S-15.9	C-59.24, H-10.36, S-15.8, Ni- 14.5
Nickel dodecanethiolate	C-61.24, H-10.45, S-13.3	C-62.45, H-10.84, S-13.9, Ni-12.78

Magnetic measurements on various nickel thiolates were carried out using a SQUID magnetometer down to 2 K. The temperature variation of both field cooled (FC) and zero-field cooled (ZFC) magnetic susceptibility data for nickel butanethiolate at 100 Oe are shown in Figure 4.29. Both FC and ZFC data exhibit an upward rise in χ as temperature is lowered below 30 K. The system orders antiferromagnetically with a short-range order with χ showing an exponential drop below ~ 11 K, as seen in ZFC curve. The short-range order is identified with the point where the FC data deviates from the ZFC.

Short-range order is generally associated with low-dimensional antiferromagnetic systems [106]. Assuming classical spins, a dimer model for spin-1 particle does not fit the

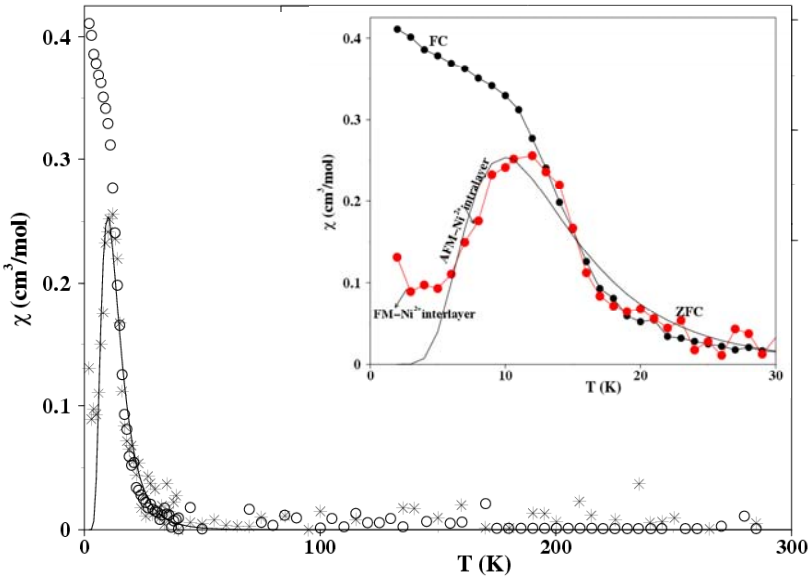

Figure 4.29. FC (circles) and ZFC (stars) as a function of temperature for nickel butanethiolate at 100 Oe field. Solid line is the theoretical fit to the ZFC data (see text). The low-temperature part of the ZFC and FC are shown in the inset for clarity. Note the upward rise of the ZFC data below 4 K.

data below 20 K. Since the lowest excitation in a spin-1 chain consists of magnons, we use a parabolic dispersion to obtain the relation

$$\chi = A\exp(-\Delta/K_BT)/(K_BT)^{\tau} \qquad (4.4)$$

where Δ is the gap, K_B and T are the Boltzmann constant and temperature, respectively. The exponent τ relates to the extended nature of the antiferromagnetic interactions along the NiS_2 chain at low temperatures. By fitting the experimental data with the above form of χ, we obtained values, Δ = 10.5 K and τ = 0.45 (see solid line in Figure 4.29). Since S=1 system corresponds to a Haldane chain, the exchange coupling can be readily obtained (Δ = 0.41J) [107]. While the exponent τ is exactly 1 for a dimer, an infinitely extended structure should give a value close to 0.5 [108]. Clearly, the estimated value of τ gives an idea of the optimal length scales associated with the exchange processes in this system. The magnetization value at the transition temperature (T=11 K) are shown in the Figure 4.30 for three H-field strengths. It may be noteworthy that even at H = 0.1 T, the spins are not completely polarized and the associated Brillouin function corresponds to a chain of particles with spin little smaller than unity. This suggests that the geometry

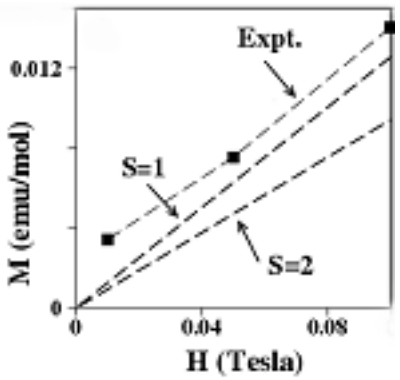

Figure 4.30. Magnetization values at 11 K for three magnetic field strengths (diamonds: Expt), calculated *M* from Brillouin functions for *S*=1 and *S*=2.

associated with Ni^{2+} ion at lower temperature is just a distorted square planar and not perfectly tetrahedral (spin-1). Further, we notice from the inset of Figure 4.29 that at lower temperatures (below 4 K), the susceptibility starts rising as $T \rightarrow 0$, signaling a magnetic polarization.

Using Gaussian-03 optimisation at the DFT based B3LYP/LANL2DZ level [109], we have computed a few molecular-orbitals for an optimized $Ni_2[S(CH_2)_3CH_3]_2$ motif as shown in Figure 4.31. As can be seen, the lowest unoccupied (LUMO) and the immediate higher lying MOs (LUMO+1, LUMO+2), correspond to the substantial charge transfer between Ni^{2+} ions leading to strong super-exchange through the bridging S ions.

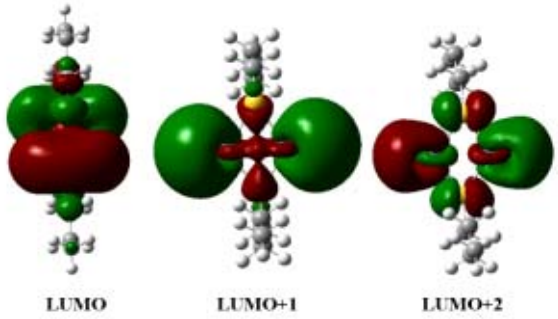

Figure 4.31. Frontier molecular orbitals for the cluster, $Ni_2(SR)_2$, R=butyl. As can be seen, charge transfer occurs between the Ni 3d-orbitals through 3p-orbitals of sulfurs. Atom basin: Ni, blue (cannot be seen due to large contribution from its orbitals to the MOs); S, yellow.

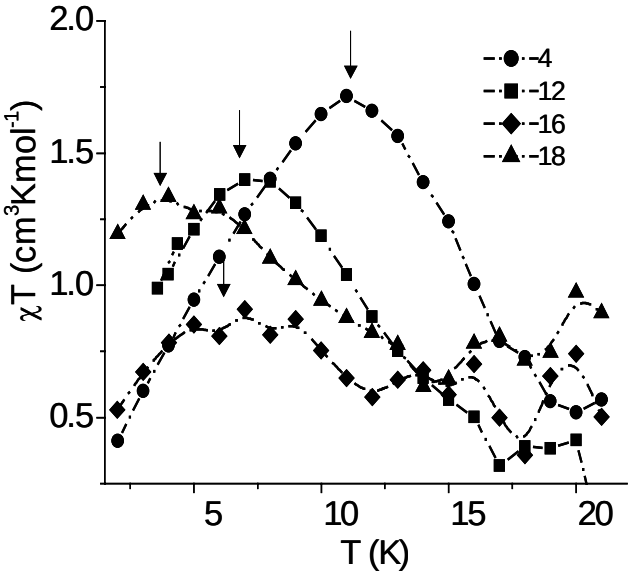

Figure 4.32. Variation in χT with T for various nickel thiolates at a field of 100 Oe. The legend gives the number of carbons in the alkane chain. The arrows indicate the antiferromagnetic ordering temperature. The data for butane thiolate is divided by a factor of 2 to fit to the scale.

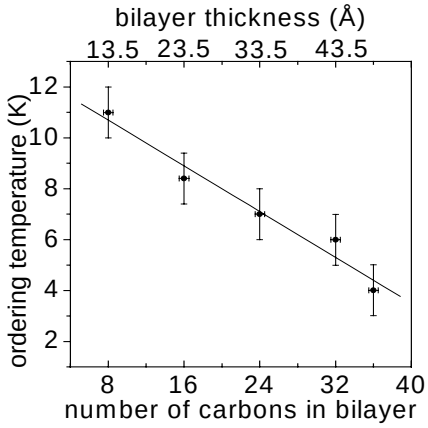

Figure 4.33. The variation of antiferromagnetic ordering temperature with the layer spacing (number of carbons in bilayer) following a linear behaviour. Bilayer thickness values shown on the top axis are the *d*(001) spacings obtained from XRD (see Figure 4.25).

Magnetic data for other nickel alkanethiolates with longer chain lengths are shown in Figure 4.32. Each FC susceptibility data exhibits a maximum corresponding to the short-range order present in the system. Interestingly, the ordering temperature decreases with increase in the chain length of the alkyl group and follows a linear form as shown in the

Figure 4.33. This is accompanied by a decreasing magnitude of the peak. Clearly, longer chains compelled by their self-assembling nature seem to restrain from anti-ferromagnetic coupling along the NiS_2 chain. Our preliminary calculations on bilayer motifs show that there is a slight elongation in Ni-Ni distance with increase in the alkyl chain due to inductive effect of the R groups.

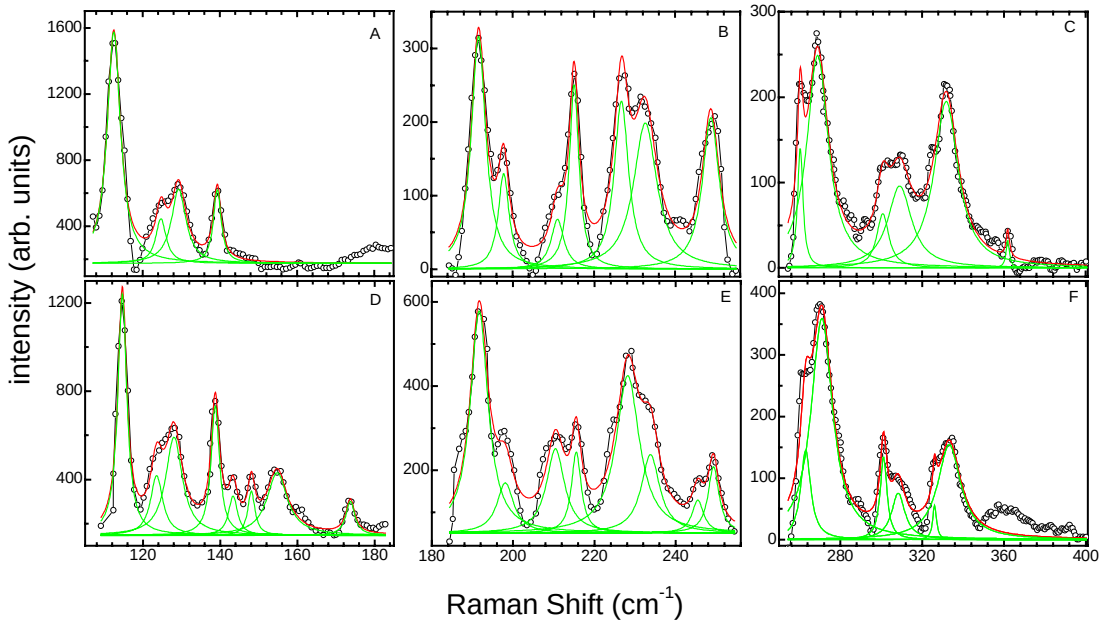

Figure 4.34. Raman spectra of Ni(II)-butanethiolate at 300 K (A, B, C) and 30 K (D, E, F) in Ni-S vibrational region. The green curves are Lorentzian fits to the peaks.

For a better understanding of the structural changes leading to the new magnetic interactions observed in Figure 4.29, we performed Raman measurements at room temperature and 30 K. Raman spectra at 300 K show $\delta(E_g)$ (S-Ni-S), $\delta(T_{2g})$ (S-Ni-S), $\nu(A_{1g})$ (Ni-S) and $\nu(T_{2g})$ (Ni-S-C) modes along with a librational mode around 112 cm^{-1}, C-C-S deformation (246 cm^{-1}) and C-C-C deformations (333 and 361 cm^{-1}) in the range 100 to 400 cm^{-1} as reported earlier for a square planar structure of Ni^{2+} [44,49]. Figure 4.34 gives a comparison of Raman spectra at 30 and 300 K for the Ni-S vibrational region. The assignments of the vibrational modes are given in Table 4.3. In the case of 300 K, the Ni-S structure is square planar and hence the Raman spectra show that most of the modes associated with Ni-S are degenerate due to high symmetry of the Ni-S unit. Upon cooling to 30 K, we observe an increase in the number of Raman modes. It is

Table 4.3. Assignment of different vibrational modes in the Raman spectra of nickel butanethiolate at 300 K and 30 K.

Vibrational Mode	Ni(II)- butanethiolate- Raman Shift (cm^{-1})	
	300 K	30 K
Librational mode	112.55	114.66
$\delta(E_g)$ S-Ni-S	124.76	123.54
	129.35	128.03
$\delta(T_{2g})$ S-Ni-S	139.34	138.73
		143.34
		148.08
		154.76
		160*
		173.71
$\nu(A_{1g})$ Ni-S	191.62	191.65
	197.8	198.08
	211.05	210.42
	215.15	215.55
		224.5*
$\nu(T_{2g})$ Ni-S-C	226.78	228.19
	232.65	233.79
		245.45
C-C-S deformation	248.79	249.31
$\nu(T_{2g})$ Ni-S	260.47	262
	268.95	269
		288.76*
	300.81	301.09
	309.07	308.28
		326.03
C-C-S deformation	331.81	333.21
C-C-C deformation	361.88	361.16*

* peaks are not fitted

important to note that the $\delta(E)$ and $\delta(T_2)$ in the region 120–175 cm^{-1} show a marked change along with softening (decrease in frequency) of the modes. The increase in number of Raman modes at low temperature could be due to lifting of the degeneracy of the corresponding modes of the asymmetric Ni-S unit [49]. The presence of modes related to both the square planar and the distorted geometry at 30 K is clearly an indication of out-of-plane movement of Ni. The above observations imply that the magnetic moment arises due to a slight distortion in the NiS_4 square planar geometry. Similar distortions have been observed in the case of *tiara* structures of nickel alkanethiolates [32].

The square planar arrangement of $Ni(SR)_4$ corresponds to the ground state geometry of the diamagnetic spin structure (S=0) while stable geometry for the paramagnetic state

is associated with a distorted arrangement of the $Ni(SR)_4$ ($1 > S > 0$) unit (see Figure 4.35).

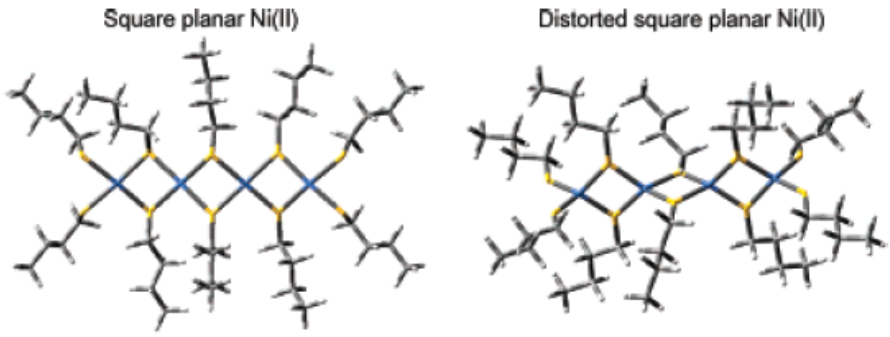

Figure 4.35. Ground state optimized structures for the $Ni_4(SR)_{10}$, R=butyl in its room temperature (square planar) and low temperature (distorted square planar) geometries. Note that the calculation is performed on a finite sized cluster and terminal -SR groups are included to avoid end-group effect.

In the nickel thiolates, the Ni^{2+} ions are bridged *via* S ions along the backbone and the backbones are held together by hydrocarbon spacers. At relatively higher temperatures (~30 K), the exchange processes are along the -Ni-S-Ni- backbone and are thus antiferromagnetic in nature. This exchange path dominates down to the ordering temperature (see Figure 4.33). However at even lower temperatures, the system may go through a dimensional crossover, whereby the exchange between the backbones through hydrocarbon spacers becomes dominant. Magnetic coupling mediated through space is most often considered to be ferromagnetic due to dipolar interactions [66], as can be seen in inset of Figure 4.29, below 4 K. Such a feature may arise as a result of increased proximity of the neighboring layers due to the out of plane displacement of the alternate butyl chains in the distorted geometry compared to square planar structure (Figure 4.35). This is expected to facilitate 'through-space' ferromagnetic coupling between the layers. However, one may also consider the possibility of impurity moment contributing to the rise in χ at very low temperatures. In the case of higher alkyl analogues, we do not observe an upward rise in χ even at the lowest measurable temperatures (~2 K), which clearly implies a dimensional crossover in the magnetic interaction prevalent in the butyl system. With other longer thiolates, the energy corresponding to the two-dimensional

exchange (J_{2D}) is smaller than the lowest temperature (2 K) achieved in these measurements.

4.5 Conclusions

Pd(II)- and Ni(II)-alkanethiolates form a lamellar bilayer structure containing metal-sulfur-metal backbone and intervening hydrocarbon chains in the case of longer alkanethiols (number of carbons >3). Our study has shown that palladium thiolates being soluble in organic media unlike other metal thiolates, self-assemble into hybrid bilayered mesophases when a mixture of thiolates is employed. The hybrid thiolates are crystalline and consist of layered structures of which the thicknesses, as measured by the *d*(001) spacings, are intermediate to the corresponding monothiolates. The bilayer thickness and the internal structure depend on the chain lengths of the constituent thiols and more on the difference in the chain lengths. When the difference is four methylene units as in C_8-C_{12} and C_{12}-C_{16} systems, the bilayer thickness varies continuously with the composition of the thiol mixture. The layer thicknesses closely follow the estimated values, obtained as the weighted averages of the thicknesses of the corresponding monothiolates. When the disparity of the thiol chain lengths is high, as in the case of the C_8-C_{16} system (eight methylene units), bilayers with intermediate layer thicknesses were found only with C_8-rich (>60%) compositions. Below 60%, the layer thickness was nearly equal to that of the C_{16} monothiolate. STM images of both mono- and mixed thiolates showed string-like features extending to tens of nanometers, the widths matching closely the layer thickness obtained from XRD. The monothiolates consist of highly ordered chains in a fully extended all-trans conformation. All hybrid structures, in contrast, consist of disordered chains with fair amounts of gauche defects and kinks. The concentration of defects varies with the composition of the thiol mixture. At a few specific compositions, the C_{12}-C_{16} bilayers incorporate acetate groups in an unusual environment. Thus, the composition and the disparity in the chain lengths of the constituent thiols are the important experimental parameters that govern the structure of the resulting hybrid bilayer.

Pd-monothiolates have been employed as precursors for the production of Pd nanocrystals by solid-state thermal decomposition in inert atmosphere. The nanocrystals obtained were stable and crystalline. The suggested mechanism is that Pd-alkanethiolates

when heated (160-180 °C) above their melting temperatures decompose to give palladium metal and alkyl disulfides, the disufides stabilizing the particles. The chain length of the thiolate or rather the bilayer thickness is found to influence the particle size, the higher ones giving smaller particles. When heated in air at 200 °C, they decomposed to give metallic Pd film.

We have probed the electrical characteristics of lamellar palladium alkanethiolates with varying chain length using C-AFM. I-V curves are nonlinear consisting of a low current region followed by a high current one, at the interface of which NDR peak appears. The resistance measured from the low bias (low current) region varies exponentially with the chain length as in the case of other alkanethiol monolayers but the β value is five times lower suggesting a different nonresonant tunnel mechanism. The NDR peak arises due to resonant conduction through interface states provided by mixing of orbitals of thiol molecule and Pd. At higher biases, resonant tunneling occurs through molecular states leading to a sudden jump in the current. The bias value at which the current jumps increases with increase in bilayer thickness.

Layered Ni-alkanethiolates exhibited unusual magnetic interactions at low temperatures accompanying distortions in the Ni(II) square planar coordination. The magnetic susceptibility showed a rise below 30 K, reaching a maximum at a particular temperature indicating antiferromagnetic ordering along the Ni-S-Ni chain through superexchange interaction. The ordering temperature is found to decrease linearly with increase in bilayer thickness i.e., for higher alkylchain thiolates. For smaller thiolates such as nickel butanethiolate, interlayer dipolar coupling emerged at further low temperatures (below 4 K) giving rise to a ferromagnetic ordering.

References

[1] P. J. Blower & J. R. Dilworth, *Coord. Chem. Rev.*, 76, 121 (**1987**).

[2] I. G. Dance, *Polyhedron*, 5, 1037 (**1986**).

[3] K. A. Jensen, *Z. Anorg. Chem.*, 252, 227 (**1944**).

[4] N. R. Kunchur, *Acta Crystallogr. B*, 24, 1623 (**1968**).

[5] R. G. Hayter & F. S. Humiec, *J. Inorg. Nucl. Chem.,* 26, 807 (**1964**).

[6] P. Woodward, L. F. Dahl, E. W. Abel & B. C. Crosse, *J. Am. Chem. Soc.*, 22, 5251 (**1965**).

[7] R. O. Gould & M. M. Harding, *J. Chem. Soc. A*, 875 (**1970**).

[8] A. D. Watson, C. Pulla Rao, J. R. Dorfman & R. H. Holm, *Inorg. Chem.*, 24, 2820 (**1985**).

[9] M. Kriege & G. Henkel, *Z. Naturforsch.*, 42b, 1121 (**1987**).

[10] J. D. Higgins, III & J. W. Huggs, *Inorg. Chim. Acta*, 145, 247 (**1988**).

[11] T. Krüger, B. Krebs & G. Henkel, *Angew. Chem. Int. Ed. Engl.*, 31, 54 (**1992**).

[12] A. Silver, S. A. Koch & M. Millar, *Inorg. Chim. Acta*, 205, 9 (**1993**).

[13] A. H. Mahmoudkhani & V. Langer, *Polyhedron*, 18, 3407 (**1999**).

[14] S. A. Ivanov, M. A. Kozee, W. A. Merrill, S. Agarwal & L. F. Dahl, *J. Chem. Soc., Dalton Trans.*, 4105 (**2002**).

[15] P. Alemany & R. Hoffmann, *J. Am. Chem. Soc.*, 115, 8290 (**1993**).

[16] S. I. Gorelsky, L. Basumallick, J. Vura-Weis, R. Sarangi, K. O. Hodgson, B. Hedman, K. Fujisawa & E. I. Solomon, *Inorg. Chem.*, 44, 4947 (**2005**).

[17] B. Krebs & G. Henkel, *Angew. Chem. Int. Ed. Engl.*, 30, 769 (**1991**).

[18] A. F. Kolodziej, *Prog. Inorg. Chem.*, 41, 493 (**1994**).

[19] A. Volbeda, M. H. Charon, C. Piras, E. C. Hatchikian, M. Frey, J. C. Fontecilla-Camps, *Nature*, 373, 580 (**1995**).

[20] Z. Li, Y. Ohki & K. Tatsumi, *J. Am. Chem. Soc.*, 127, 8950 (**2005**).

[21] N. Herron, J. C. Calabrese, W. E. Farneth & Y. Wang, *Science*, 259, 1426 (**1993**).

[22] K. Osakada & T. Yamamoto, *J. Chem. Soc., Chem. Commun.*, 1117 (**1987**).

[23] G. Krauter, P. Favreau & W. S. Rees, Jr., *Chem. Mater.*, 6, 543 (**1994**).

[24] G. Krauter B. Neumuller, V. L. Goedken & W. S. Rees, Jr., *Chem. Mater.*, 8, 360 (**1996**).

[25] A. N. MacInnes, M. B. Power & A. R. Barron, *Chem. Mater.*, 5, 1344 (**1993**).

[26] G. Carotenuto, B. Martorana, P. Perlob & L. Nicolais, *J. Mater. Chem.*, 13, 2927 (**2003**).

[27] G. Carotenuto, L. Pasquini, E. Milella, M. Pentimalli, R. Lamanna & L. Nicolais, *Eur. Phys. J. B*, 31, 545 (**2003**).

[28] M. Nakamoto, M. Yamamoto & M. Fukusumi, *Chem. Commun.*, 1622 (**2002)**.

[29] T. H. Larsen, M. Sigman, A. Ghezelbash, R. C. Doty & B. A. Korgel, *J. Am. Chem. Soc*., 125, 5638 (**2003)**.

[30] A. Ghezelbash, M. B. Sigman Jr. & B. A. Korgel, *Nano Lett.*, 4, 537 (**2004)**.

[31] L. Chen, Y-. B. Chen & L-. M. Wu, *J. Am. Chem. Soc*., 126, 16334 (**2004**).

[32] A. Datta, N. S. John, G. U. Kulkarni & S. K. Pati, *J. Phys. Chem. A*, 109, 11647 (**2005**).

[33] K. Nobusada & T. Yamaki, *J. Phys. Chem. A*, 108, 1813 (**2004**).

[34] I. G. Dance, K. J. Fisher, R. M. H. Banda & M. L. Scudder, *Inorg. Chem.,* 30, 183 (**1991**).

[35] N. Sandhyarani & T. Pradeep, *J. Mater. Chem.*, 11, 1294 (**2001**).

[36] P. J. Thomas, A. Lavanya, V. Sabareesh, G. U. Kulkarni, *Proc. Indian Acad. Sci., Chem. Sci*., 113, 611 (**2001**).

[37] S-. H. Park & C. E. Lee, *J. Phys. Chem. B*, 109, 1118 (**2005**).

[38] M. Taibi, S. Ammar, N. Jouini, F. Fiévet, P. Molinié & M. Drillon, *J. Mater. Chem.*, 12, 3238 (**2002**).

[39] C. Guillot, M. R- . Plouet & S. Vilminot, *J. Mater. Chem.*, 12, 851 (**2002**).

[40] S. J. Lee, S. W. Han, H. J. Choi & K. Kim, *J. Phys. Chem. B*, 106, 2892 (**2002**).

[41] Y. Ishikawa, H. Kuwahara & T. Kunitake, *J. Am. Chem. Soc.*, 116, 5579 (**1994**).

[42] N. Kimizuka, N. Oda & T. Kunitake, *Chem. Lett.*, 695 (**1998**).

[43] T. Kunitake, *Angew. Chem. Int. Ed. Engl.* 31, 709 (**1992**).

[44] H. G. Fijolek, J. R. Grohal, J. L. Sample & M. J. Natan, *Inorg. Chem.*, 36, 622 (**1997**).

[45] H. G. Fijolek, P. G. Duarte, S. H. Park, S. L. Suib & M. J. Natan, *Inorg. Chem.*, 36, 5299 (**1997**).

[46] J. -F. Bardeau, A. N. Parikh, J. D. Beers & B. I. Swanson, *J. Phys. Chem. B*, 104, 627 (**2000**).

[47] A. N. Parikh, S. D. Gillmor, J. D. Beers, K. M. Beardmore, R. W. Cutts & B. I. Swanson, *J. Phys. Chem. B*, 103, 2850 (**1999**).

[48] H. G. Fijolek, T. A. Oriskovich, A. J. Benesi, P. G-. Duarte & M. J. Natan, *Inorg. Chem.*, 35, 797 (**1996**).

[49] Y. –H. Huang, I. Moura, J. J. G. Moura, J. LeGall, J. –B. Park, M. W. W. Adams & M. K. Johnson, *Inorg. Chem.*, 32, 406 (**1993**).

[50] C. D. Bain & G. M. Whitesides, *J. Am. Chem. Soc.*, 110, 3665 (**1988**).

[51] C. D. Bain, J. Evall & G. M. Whitesides, *J. Am. Chem. Soc.*, 111, 7155 (**1989**).

[52] C. D. Bain & G. M. Whitesides, *J. Am. Chem. Soc.*, 111, 7164 (**1989**).

[53] P. E. Laibinis, R. G. Nuzzo & G. M. Whitesides, *J. Phys. Chem.*, 96, 5097 (**1992**).

[54] M. J. Baena, P. Espinet, M. C. Lequerica & A. M. Levelut, *J. Am. Chem. Soc.*, 114, 4182 (**1992**).

[55] P. Espinet, M. C. Lequerica & J. M. M- . Alvarez, *Chem. Eur. J.*, 5, 1982 (**1999**).

[56] K. G. Sharp, *Adv. Mater.*, 10, 1243 (**1998**).

[57] H. K. Kim, S. -J. Kang, S. -K. Choi, Y. -H. Min & C. -S. Yoon, *Chem. Mater.*, 11, 779 (**1999**).

[58] T. D. de Morais, F. Chaput, K. Lahlil & J. -P. Boilot, *Adv. Mater.*, 11, 107 (**1999**).

[59] D. B. Mitzi, K. Chondroudis & C. R. Kagan, *IBM J. Res. & Dev.*, 45, 29 (**2001**).

[60] X. Hong, T. Ishihara & A. V. Nurmikko, *Solid State Commun.*, 84**,** 657 (**1992**).

[61] M. Era, S. Morimoto, T. Tsutsui & S. Saito, *Appl. Phys. Lett.*, 65, 676 (**1994**).

[62] D. B. Mitzi, C. A. Feild, W. T. A. Harrison & A. M. Guloy, *Nature*, 369, 467 (**1994**).

[63] H. R. Heulings IV, X. Huang, J. Li, T. Yuen & C. L. Lin, *Nano Lett.*, 1, 521 (**2001**).

[64] Y. Zhao, M. Hong, Y. Liang, R. Cao, W. Li, J. Weng & S. Lu, *Chem. Commun.*, 1020 (**2001**).

[65] M. Monfort, I. Resino, J. Ribas & H. S- . Evans, *Angew. Chem. Int. Ed.*, 39, 191 (**2000**).

[66] M. Drillon & P. Panissod, *J. Mag. Magn Mater.*, 188, 93 (**1998**).

[67] J. N. Behera, K. V. Gopalkrishnan & C. N. R. Rao, *Inorg. Chem*. 43, 2636 (**2004**).

[68] O. Waldmann, J. Hassmann, P. Müller, D. Volkmer, U. S. Schubert & J. –M. Lehn, *Phys. Rev. B*, 58, 3277 (**1998**).

[69] T. Nakanishi, M. Morita, H. Murakami, T. Sagara & N. Nakashima, *Chem. Eur. J.*, 8, 1641 (**2002**).

[70] H. Xu & C. -H. Huang, *Biochemistry*, 26, 1036 (**1987**).

[71] M. Castro, S. M. Clarke, A. Inaba, R. K. Thomas & T. Arnold, *J. Phys. Chem. B*, 102, 10528 (**1998**).

[72] M. Castro, S. M. Clarke, A. Inaba, R. K. Thomas & T. Arnold, *Phys. Chem. Chem. Phys.*, 3, 3774 (**2001**).

[73] N. Ulagappan & C. N. R. Rao, *Chem. Commun.*, 2759 (**1996**).

[74] S. –C. Chang, I. Chao & Y. –T. Tao, *J. Am. Chem. Soc.*, 116, 6792 (**1994**).

[75] J. C. Love, L. A. Estroff, J. K. Kriebel, R. G. Nuzzo & G. M. Whitesides, *Chem. Rev.*, 105, 1003 (**2005**).

[76] H. Miyamae & T. Yamamura, *Acta Cryst.* C, 44, 606 (**1988**).

[77] A. Berkessel, J. W. Bats, M. Hüber, W. Haase, T. Neumann & L. Seidel, *Chem. Ber.*, 128, 125 (**1995**).

[78] F. H. Allan & O. Kennard, *Chem. Des. Automata News*, 8, 131 (**1993**).

[79] D. S. Everhart, in *Handbook of Applied Surface and Colloid Chemistry*; K. Holmberg, Ed.; John Wiley and Sons. Ltd: Chichester, U.K. (**2001**).

[80] L. H. Dubois & R. G. Nuzzo, *Annu. Rev. Phys. Chem.*, 43, 437, (**1992**).

[81] R. A. Macphail, H. L. Strauss, R. G. Synder & C. A. Elliger, *J. Phys. Chem.*, 88, 334 (**1984**).

[82] R. G. Synder, H. L. Strauss & C. A. Elliger, *J. Phys. Chem.*, 86, 5145 (**1982**).

[83] R. G. Synder, M. Maroncelli, H. L. Strauss & V. M. Hallmark, *J. Phys. Chem.*, 90, 5623 (**1986**).

[84] R. G. Synder, M. Maroncelli, S. P. Qi & H. L. Strauss, *Science*, 214, 188 (**1981**).

[85] M. Maroncelli, S. P. Qi, H. L. Strauss & R. G. Synder, *J. Am. Chem. Soc.*, 104, 6237 (**1982**).

[86] N. V. Venkataraman & S. Vasudevan, *J. Phys. Chem. B*, 105, 7639 (**2001**).

[87] N. V. Venkataraman & S. Vasudevan, *J. Phys. Chem. B*, 105, 1805 (**2001**).

[88] M. J. Hostetler, J. J. Stokes & R. W. Murray, *Langmuir*, 12, 3604 (**1996**).

[89] C. N. R. Rao, *Chemical Applications of Infrared Spectroscopy*; Academic Press Inc. London (**1963**).

[90] S. H. Chen & F. W. Curtis, *Langmuir*, 5, 978 (**1989**).

[91] C. Curtis, T. Rivkin, A. Miedaner, J. Alleman, J. Perkins, L. Smith & D. Ginley, NCPV Program Review Meeting, October **2001,** *http://www.osti.gov/bridge*.

[92] C. Miller, P. Cuendet & M. Gratzel, *J. Phys. Chem.*, 95, 877 (**1991**).

[93] A. M. Becka & C. Miller, *J. Phys. Chem.*, 96, 2657 (**1992**).

[94] K. Slowinski, R. V. Chamberlain II, R. Bilewicz and M. Majda, *J. Am. Chem. Soc*., 118, 4709 (**1996**).

[95] X. D. Cui, A. Primak, X. Zarate, J. Tomfohr, O. F. Sankey *et al.*, *J. Phys. Chem. B*, 106, 8609 (**2002**).

[96] D. J. Wold & C. D. Frisbie, *J. Am. Chem. Soc.*, 123, 5549 (**2001**).

[97] R. E. Holmlin, R. Haag, M. L. Chabinyc, R. F. Ismagilov, A. E. Cohen, A. Terfort, M. A. Rampi & G. M. Whitesides, *J. Am. Chem. Soc.*, 123, 5075 (**2001**).

[98] M. A. Ratner, B. Davis, M. Kemp, V. Mujica, A. Roitberg & S. Yaliraki, *Ann. N. Y. Acad. Sci.*, 852, 22 (**1998**).

[99] J. R. Heath & M. A. Ratner, *Physics Today*, 5, 43 (**2003**).

[100] A. Salomon, D. Cahen, S. Lindsay, J. Tomfohr, V. B. Engelkes & C. D. Frisbie, *Adv. Mater.*, 15, 1 (**2003**).

[101] V. B. Engelkes, J. M. Beebe & C. D. Frisbie, *J. Am. Chem. Soc.*, 126, 14287 (**2004**).

[102] S. Creager, C. Y. Yu, C. Bamdad, S. O'Connor, T. MacLean *et al.*, *J. Am. Chem. Soc.*, 121, 1056 (**1999**).

[103] S. B. Sachs, S. P. Dudeek, R. P. Hsung, L. R. Sita, J. Smalley, M. D. Newton, S. W. Feldberg & C. E. D. Chidsay, *J. Am. Chem. Soc.*, 119, 10563 (**1997**).

[104] H. Dalgleish & G. Kirczenow, *Nano Lett.*, 6, 1274 (**2006**).

[105] A. Storr, D. A. Summers & R. C. Thompson, *Can. J. Chem.*, 76, 1130 (**1998**).

[106] S. K. Pati, S. Ramasesha & D. Sen, in *Magnetism: molecules to materials IV*, J. S. Miller, M. Drillon, Eds. Wiley-VCH, Weinheim (**2003**).

[107] S. R. White*, Phys. Rev. Lett.*, 69, 2863 (**1992**).

[108] M. Troyer, H. Tsunetsugu & D. Wurtz, *Phys. Rev. B*, 50, 13515 (**1994**).

[109] Gaussian 03, Revision B.05, M. J. Frisch *et al*., Gaussian, Inc., Pittsburgh PA, (**2003**).

Chapter 5

Femtoliter Metal Cups by Pulsed Laser Ablation: Deposition, Characterization and Applications*

SUMMARY

Laser ablation has become a popular method for producing nanomaterials as well as thin films of compounds due to its versatility, especially its ability of congruent transfer of materials. We have employed this method to obtain cup-like structures of various metals such as Au, Ag, Cu, Zn, Nb, Cd, Al, In and Sn in the size range of 300 nm to few microns with an internal volume of a few femtoliters. The obtained cups have been characterized by a host of techniques, SEM, EDX, AFM. A metal target when ablated in vacuum produces molten droplets that impinge on a flat substrate to form blobs and cups. With optimal laser energy and substrate temperature, the droplets spread and exhibit a sudden discontinuity in height–termed as hydraulic jump, before solidifying to form cups. With the kind of length and velocity scales involved in our experiment, gravity is negligible and surface tension is considered as the sole driver of the jump. The optimum conditions of obtaining femtoliter cups are found to be moderate laser energies, ~100 mJ/pulse and substrate temperatures close to but lower than the melting point of the metal. The general nature of the process is supported by the facile formation of cups of a variety of metals on many flat, non-reacting substrates such as silicon, graphite and glass. The formation of elliptical cups with inclined substrates further support the flow dynamics.

The metal cups can be functionalized with biomarkers, filled with nanoparticle sols, oxidized to crucibles or detached from the substrate without causing noticeable deformation. Further, the oxidative transformation of metal cups (Sn, In, Nb) has been monitored employing spatially resolved Auger electron spectroscopy and microscopy. We, therefore, envisage their potential applications as femtoliter metal containers.

---

* A paper based on this work has appeared in J. Phys. Chem. B (2006). Two manuscripts are accepted for publication in Phys. Rev. Lett. and Appl. Phys. A (2007).

5.1 Introduction

The growing interest in single molecule detection and kinetics has given impetus to the technology of making ultra-small containers. Femto or picoliter capacity containers are useful while dealing with cellular systems [1,2] and provide control on diffusion and kinetics [3]. Such small volumes are also economical while handling expensive reagents. Developments in lithography and nanotechnology have offered several tools for producing ultra-small containers. Conventional photolithography has been used to produce picoliter wells in silicon wafers for the detection of single metal ions and enzyme molecules [4,5] while soft lithography has been used to fabricate femto and picoliter containers in an elastomer which has been demonstrated for its use in monitoring the enzyme action [2,6]. Arrays of wells of zeptoliter (10^{-21} L) capacity have been fabricated on silica [7] as well as titania nanobowls [8] by employing nanosphere lithography and have been used for growing nanoparticles. Such small vials also find applications as inkwells, in the developing technique of dip pen nanolithography for patterning in sub-nanometer dimensions [9]. Oxide nanopores grown on Si employing focused ion beam lithography have been used for localized functionalization and further immobilization of biomolecules [10]. Other reported techniques for obtaining ultra-small containers include layer by layer assembly of polyelectrolytes [11,12], electrospraying of polymers and polymer-inorganic nanocomposites [13] and emulsion based synthesis of inorganic nanoparticle embedded polymer microcapsules [14]. Recently, there have been a lot of developments in using self-assembled biomimetic systems such as phospholipid vesicles, hydrosomes and liposomes for carrying out single cell reactions [15,16].

In this chapter, a simple method to produce metal containers of femtoliter capacity employing pulsed laser ablation of metal targets is presented. Nano or femtosecond pulsed lasers emitting pulses of high fluence (~1 J/cm^2), when focused, can induce local melting and ejection of virtually any material including refractory compounds [17-19]. The plume emanating from the target is essentially a hot plasma consisting of cluster ions, molten droplets and particles from secondary collisions. The laser ablation method has been used extensively to produce thin films of high T_c ceramic superconductors and other electronic materials [20]. Well-defined clusters of molecules [21], metals [22] and many interesting compounds [23] have been generated using lasers in tandem with

supersonic gas pulses. Laser ablation has been used to pattern catalytic metal particles for the growth of aligned carbon nanotubes [24] and in producing ropes of carbon nanotubes [25]. Similarly, nanotubes, nanorods and nanowires of various inorganic compounds have been obtained [26,27]. Laser ablation has also been carried out in liquid media to obtain alloy nanoparticles [28] and onion shaped nanomaterials [29,30]. Recently, the method has been extended to the realm of biomaterials and polymers [31]. The local heating induced by the laser has also been utilized for the study of nanoparticle dynamics [32] and shape transformation of Au nanorods [33].

In the laser ablation method employed here, the metal droplets from the laser plume impinge on the substrate and exhibit a sudden height discontinuity during spreading, termed as hydraulic jump in fluid dynamics. When a vertical jet of liquid from a nozzle hits a flat surface, a discontinuity appears in a ring created by the flow. At this deformation the depth of the water alters abruptly (the 'circular hydraulic jump') at some distance from the jet [34,35]. The jump height is generally, an order of magnitude higher than the height of the fluid close to jet. This is a commonly encountered phenomenon for example, in the case of water from a faucet striking a kitchen sink and also tidal bores (see Figure 5.1 for a picture of circular hydraulic jump). In this case, gravity is the key ingredient for the occurrence of a jump and the jump radius is of the order of millimeter scales [34-39].

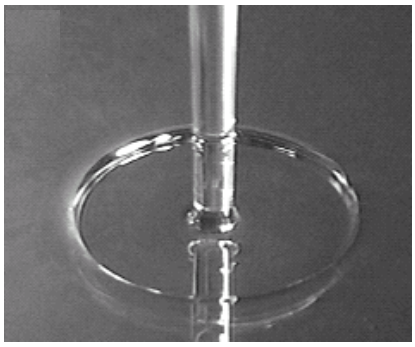

Figure 5.1. A picture of circular hydraulic jump occurring in a kitchen sink [adopted from ref. 35].

5.2 Scope of the Present Investigation

The present investigation deals with the development of a method based on pulsed laser ablation and deposition and optimization of experimental parameters to generate

femtoliter cups of a variety of metals on different substrates. The various utilities of these cups as ultra-small containers have also been explored.

5.2.1 Deposition and applications of femtoliter metal cups

The urge to understand single cell reactions and enzyme kinetics when they are in isolation has given rise to strategies to limit detection volumes and hence various methods to prepare ultra-small containers [1,2]. Our laser ablation method provides a facile way to consistently obtain femtoliter cups of any kind of metal. Laser ablation of materials produces a plume containing atom clusters and droplets of the target material [17,18]. The plume can be entrained in vacuum under controlled conditions to obtain clusters [40] and fullerenes [41] as well as thin films [18,19]. In the absence of entrainment, the molten droplets, if made to impinge upon a solid substrate, would normally solidify into lump-shaped structures. We have noticed from the literature a few instances of ring or cup-like structures on thin films produced by laser ablation but they have neither been commented upon nor there is an explanation for their formation [42,43]. The presence of such structures on thin films increases the roughness and hence these are unwanted and care is taken to avoid their formation by various modifications to the technique. But we have optimized the experimental conditions such as laser energy and substrate temperature that favours the formation of cups and the mechanism responsible for the formation is also proposed. Since the substrate being held vertical and length scales small, a novel hydraulic jump driven by surface tension is the proposed mechanism unlike the gravity-driven jump in conventional cases.

The utility of the cups as containers has been illustrated by filling them with nanoparticle sols and biomolecules and functionalizing with other molecules. The metal cups could also be converted to stable ceramic crucible by oxidation.

5.2.2 Chemical mapping of oxidized metal cups by SR-AES

The transformation of cups to their oxides is interesting, as it will produce more inert cups for use as containers. It is important to study the conditions under which a desired composition is obtained during chemical transformation without affecting morphology and also worthwhile to understand the chemical nature of the surface of the as-prepared cups. A surface-sensitive probe with good spatial resolution is required for monitoring

such local changes. Auger spectroscopy is capable of good spatial resolution, since the incident electron beam can be focused to small spot sizes with high current density [44]. In general, this high lateral resolution makes it possible to use the Auger electrons at particular energy for imaging (microscopy) and has been extensively used in the field of metallurgy to study diffusion process at grain boundaries [45], geology as a microanlaytic tool [46] and lately, to characterize nanostructures [47-50]. In the present study, with the help of SR-AES, the oxidation behavior of the metal cups at center and rim of the cups and also substrate region could be compared which are usually hidden in the ensemble averaging of bulk spectroscopic measurements.

5.3 Experimental Details

5.3.1 Preparation and characterization of metal cups

A Q-switched frequency tripled Quanta-Ray (GCR-170) Nd:YAG laser (spectra-Physics, USA) λ=355 nm, 100 mJ/pulse, pulse width, 5 ns and repetitive frequency of 10 Hz, was focused on a rotating metal disc in a vacuum chamber (10^{-7} Torr). A convex lens of 30 cm focal length was used to focus the laser beam on to the target, through a quartz window fastened to the deposition chamber. The metal foil/disc was fixed onto a holder held at 45° to the laser beam. The target holder was driven externally by a linear rotary motion using a stepper motor arrangement such that the laser beam ablate a spiral groove on the target exposing it evenly. A schematic of the experimental set-up is given in Figure 5.2. The substrate was placed directly opposite to the target at ~4 cm, fixed to a molybdenum boat whose temperature could be varied up to 1350 ºC. The temperature calibration was done using an optical pyrometer (Mikron Instrument Co., Inc. USA). The laser plume was collected for 5-20 min on the clean substrate held at a desired temperature. Silicon, glass and HOPG were used as substrates. Prior to deposition, the Si surface was subjected to standard cleaning procedures involving washing with acetone, deionized water and finally using piranha solution (1:2 H_2O_2:H_2SO_4, *Caution: this mixture reacts violently with organic matter*) followed by deionized water. The cleaned surface was then etched with very dilute HF and rinsed with deionized water and mounted in the chamber. HOPG was freshly peeled and glass substrate was sonicated in acetone and ethanol before use. The deposition was carried out at different temperatures,

varying from room temperature to 1000 °C and laser pulse energies, 60, 100, 150 and 200 mJ.

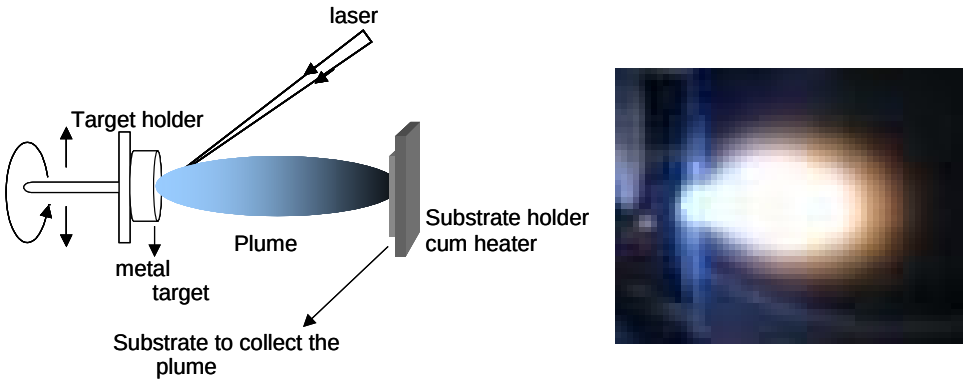

Figure 5.2. A schematic of the experimental set-up used for pulsed laser ablation and deposition. The whole arrangement excluding the laser is enclosed in a UHV chamber held at a pressure of 10^{-7} Torr. A photograph of the laser plume is also shown alongside.

The metal cups obtained were characterized by field-emission scanning electron microscopy (FESEM), EDX (Nova nanoSEM 600, FEI, The Netherlands), and AFM (Nanocope IV-Multimode, Digital Instruments, Santa Barbara). AFM imaging was done in contact mode using silicon nitride cantilevers under ambient conditions. A Carl Zeiss LSM510 confocal microscope was used to image fluorescent molecules in the cups.

5.3.2 Oxidation of metal cups and SR-Auger spectroscopy and microscopy

The metal cups (In, Sn & Nb) were oxidized either by external treatment in a furnace with a high oxygen flow or by exposing to thousands of Langmuirs of oxygen in a UHV chamber (*in situ* treatment). In the case of In, the substrate carrying the cups was placed in a furnace and heated to 350 °C (higher than the melting point of In, 156.6 °C) at the rate of 2.5 °C /min in oxygen flow and held there for 1 hour. Then it was cooled down to room temperature.

In the case of Sn, clean Sn cups (native oxide removed by Ar^+ ion sputtering) were treated *in situ* with oxygen in the UHV chamber. Oxygen was introduced into the system via a leak valve. The substrate was held at a temperature of 227 °C (close to the melting point of Sn) for 15 min and the heating rate was 8 °C/min. The heating was performed

using a filament kept in contact with the substrate. Another Sn sample, as described previously for In, was externally treated in oxygen in a furnace heated to 220 °C at the rate of 5-8 °C/min and held under these conditions for half an hour and then brought to room temperature.

Nb was exposed to oxygen in UHV at a substrate temperature of 800 °C for 15 min. In this case, the heating was performed by passing current directly through the Si substrate. The oxidation of the cups was monitored by AFM, SEM, and SR-AES.

The AES has been performed in a UHV chamber consisting of a preparation chamber maintained at a base pressure of $\leq 2 \times 10^{-10}$ mbar, where samples can be sputtered, annealed, or exposed to dosage of gases, and of an analysis chamber held at a base pressure of $\leq 3 \times 10^{-11}$ mbar equipped with a SEM and a spatially resolved Auger electron spectroscopy system [51,52]. Electrons are provided by a FEI electron gun with a nominal beam diameter of 20 nm and a lateral resolution of the order of some 10 nm. The working conditions used in this experiment were beam voltage 10 keV, beam current 2 nA, and analyzer pass energy 80 eV, giving an instrumental resolution of ~0.25 eV. Before the introduction into the analysis chamber, the samples were washed with acetone followed by ethanol. Auger energies have been calibrated on the Si LVV line on clean Si at a kinetic energy of 92 eV [53].

The samples were sputtered in the preparation chamber by bombarding with Ar^+ ions of 1 keV for 1 hr. The absence of carbon and oxygen KLL auger lines in the AES was taken as the reference for a clean surface.

In order to take SR-AES spectra, the sample is scanned in SEM mode and an image of the sample is recorded. The electron beam is then moved to a selected area of the cup structure, and then the scan raster is turned off. Spectra have been obtained by averaging a series of 10 scans taken either on the same spot or on adjacent spots. We did not observe any shift in energy from scan to scan, and therefore we can safely exclude both charging and degradation effects during the measurements. After acquiring the spectrum, SEM was done to ensure that the point had not drifted away.

5.4. Results and Discussion

5.4.1 Deposition of cups by pulsed laser ablation

The substrate after collecting the laser plume from the metal target when examined in FESEM showed a higher population of ring-like structures along with some blobs. Figure 5.3a shows the FESEM image of Ag structures obtained by laser ablation at a substrate

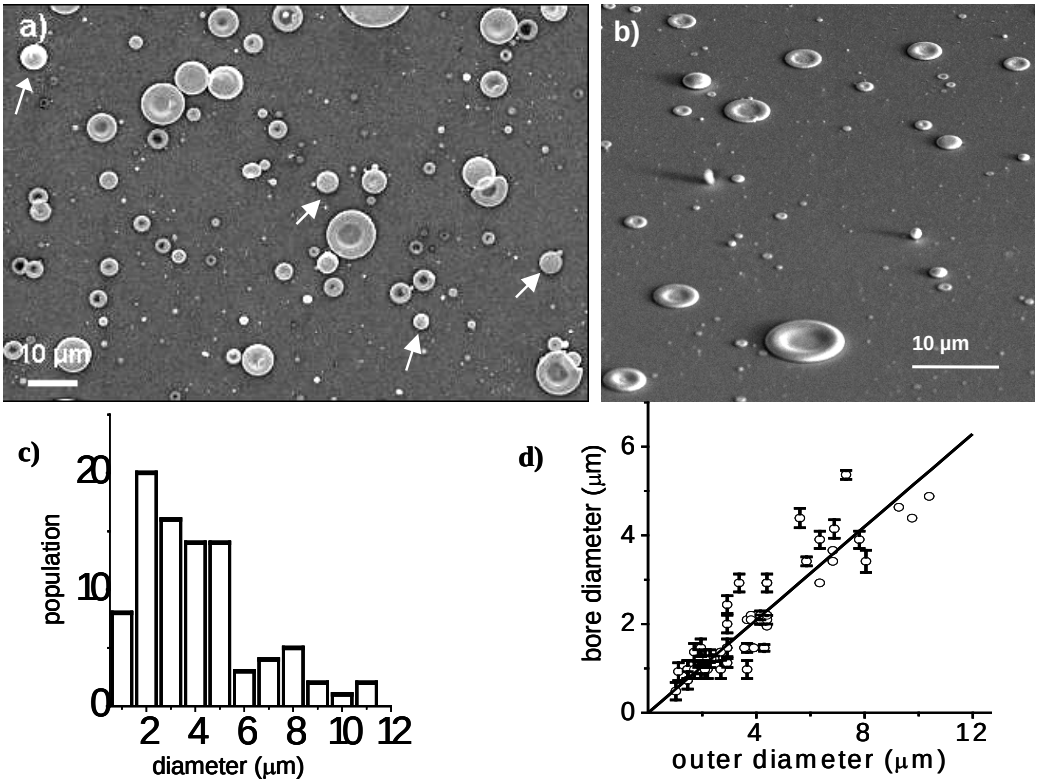

Figure 5.3. a) SEM image of ring-like structures of silver on a silicon substrate obtained by laser ablation. An Ag foil was ablated with a laser energy of 100 mJ/pulse and the substrate was held at a temperature of 900 ºC, deposition time, 20 min. Rings of various sizes are seen spread over a large area of the substrate. Arrows indicate a few blobs. b) A tilted view of the substrate (view angle, 45º) revealing that the structures are more cup-like. c) The histogram gives the distribution of the ring diameter under given conditions. d) A plot of the total diameter against the bore diameter for a number of structures. A straight line is fitted with the total diameter as twice the bore diameter.

temperature, 900 °C and laser energy, 100 mJ/pulse. Majority of them have ring-like shapes with outer diameters varying from 300 nm to 10 µm. A few blobs are indicated by arrows. A 45° tilted view of the substrate reveals that the structures are more cup-like

than ring-like (Figure 5.3b). The histogram shown in Figure 5.3c gives the distribution of the cup diameters. A large percentage of the cups have diameters in the range 2-5 μm. Incidentally, the bore diameter of most of the cups is half the total diameter (Figure 5.3d). A closer look at these structures (see Figure 5.4) confirms that the central region of the rings is not devoid of the metal. EDX spectra given alongside give the ratio of Si (from the substrate) to Ag at various regions of the cup. The amount of Ag is maximum at the rim of the cup and is less towards the center. There is some amount of Ag on the

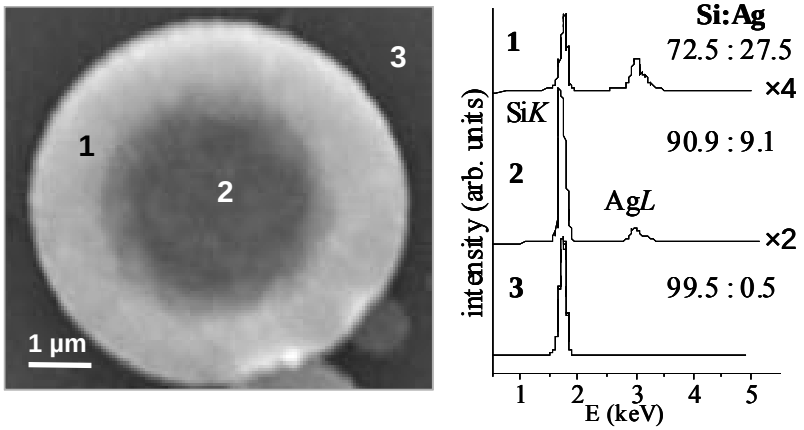

Figure 5.4. SEM image of a Ag cup giving a closer view. EDX spectra provide Ag to Si ratios from different locations of the cup as marked in the image.

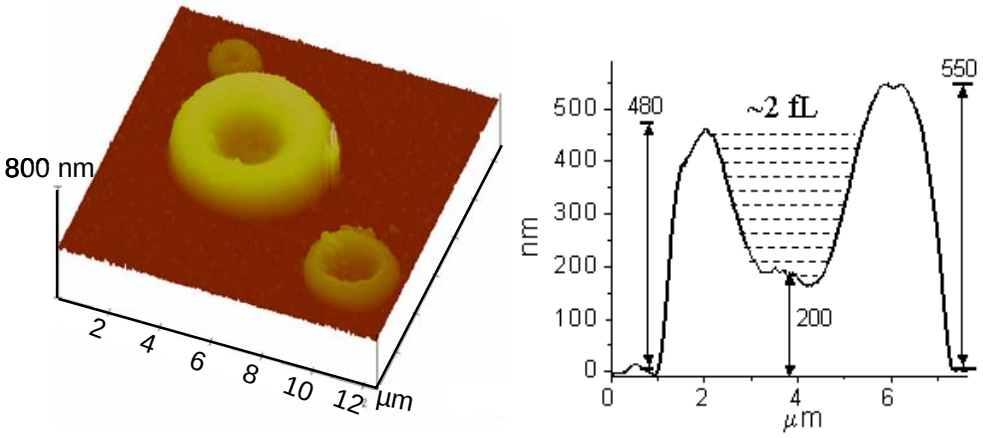

Figure 5.5. 3D projection of an AFM image showing cups of three different sizes. The height profile of the central cup shown. The hashed region gives an estimate of the inner volume, 1 fL = 1 μm^3.

substrate and reveals that a very thin layer of Ag covers the substrate as well. The cup shape is further supported by the AFM image and the associated height profile given in

Figure 5.5. The central region is raised from the substrate by a thickness of ~ 200±10 nm and the rims on either side of the profile exhibit heights of ~ 490 and 550 nm and widths of ~ 2.0 µm. The internal volume of the cup indicated by the hashed region, assuming a cylindrical volume, in the figure is thus ~ 2 fL. Hence the cups of different sizes will have a volume varying from 25 attoliter to 6 fL.

EDX and AFM analysis of a typical blob formed along with cups are given in Figure 5.6. As expected, the central region has more silver in the case of blobs.

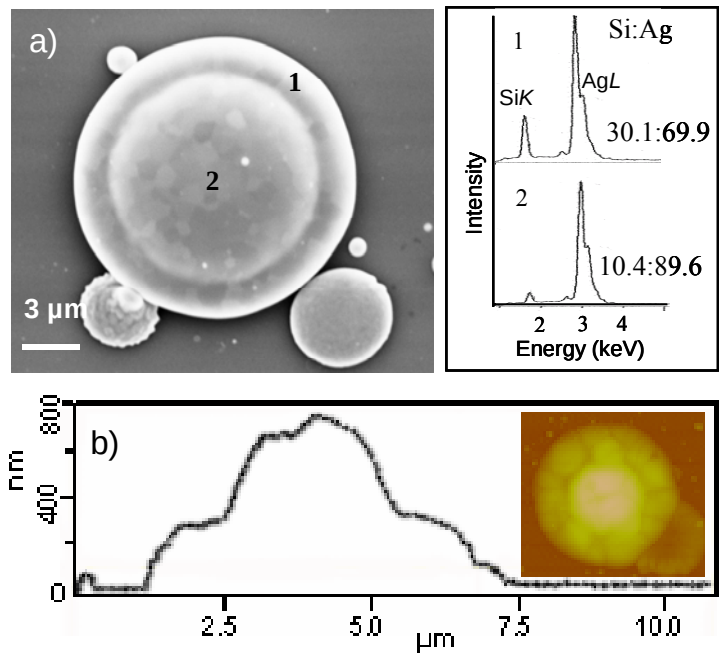

Figure 5.6. a) SEM image image of a silver blob on Si obtained during laser ablation and the corresponding EDX gives Si (from substrate) to Ag ratio. b) AFM topography of a blob and the height profile.

Hence, at any time of deposition, both cups and blobs are observed. The ratio of cups to blobs can be controlled by varying the deposition conditions such as substrate temperature and pulse energy. Figure 5.7 show the distribution of cups and blobs in the case of Ag on Si at different substrate temperatures, 27, 500, 700, 820 and 1000 °C for a given pulse energy, 100 mJ (see Figure 5.3a for 900 °C deposition). The SEM images of a typical sampling area in each case are shown. It is clearly seen that at lower temperatures, the population of blobs is higher compared to those deposited above

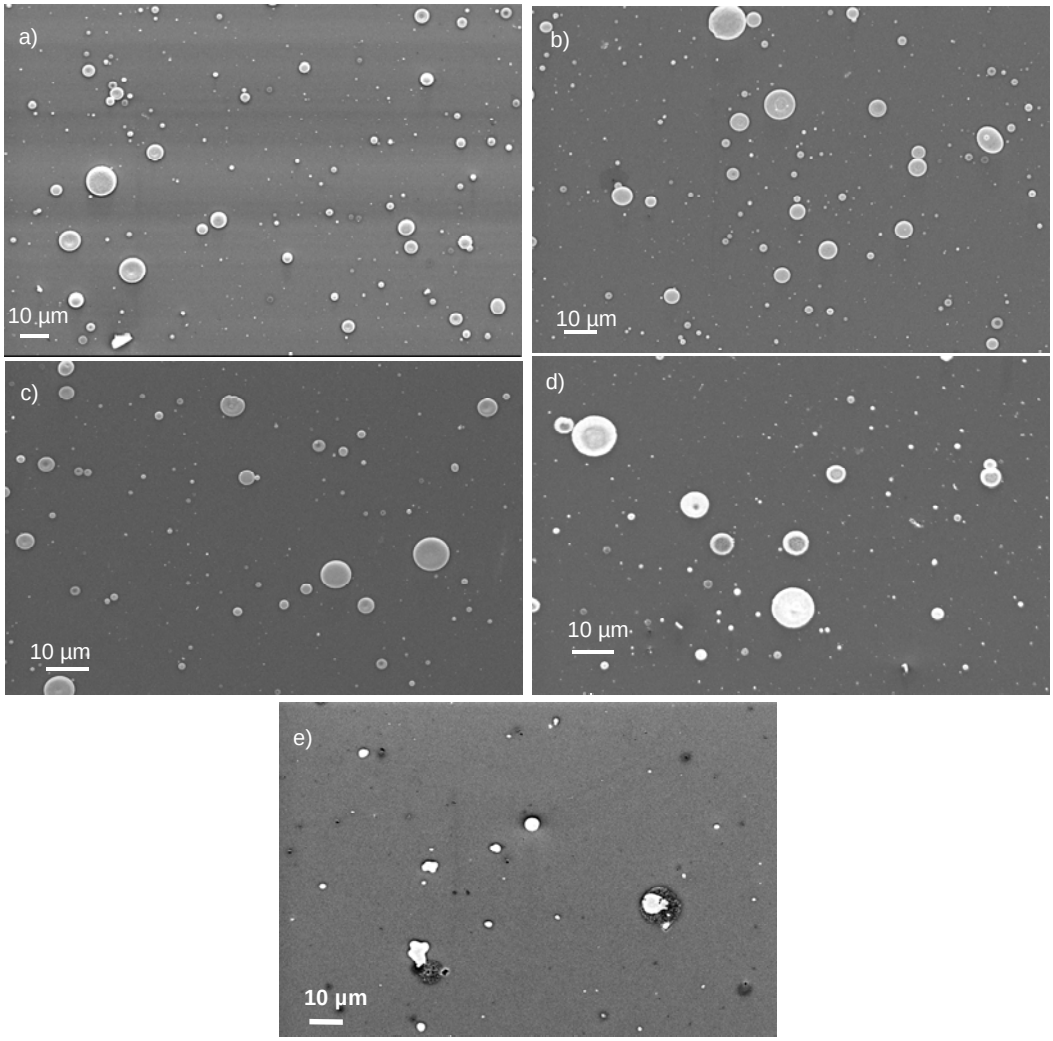

Figure 5.7. SEM images of Ag cups on Si obtained by laser ablation at different substrate temperatures, laser energy, 100 mJ/pulse a) 27 °C (room temperature) b) 500 °C c) 700 °C d) 820 °C e) 1000 °C. See Figure 5.3a for 900 °C.

500 °C. Cups with well-defined depressions are formed at 820 and 900 °C. The formation of blobs is greatly suppressed at 900 °C. In fact this temperature is close to the melting point (M. P.) of Ag, 961 °C. As the substrate temperature is increased above the M. P. to 1000 °C, a few patchy features are observed (Figure 5.7e). Figure 5.8 shows the influence of laser pulse energy on the formation of Ag cups on Si substrate held at a given substrate temperature, 820 °C. As the pulse energy is increased from 60 (Figure 5.8a) to 100 mJ (Figure 5.7d), there is a tremendous increase in the number of features obtained and also

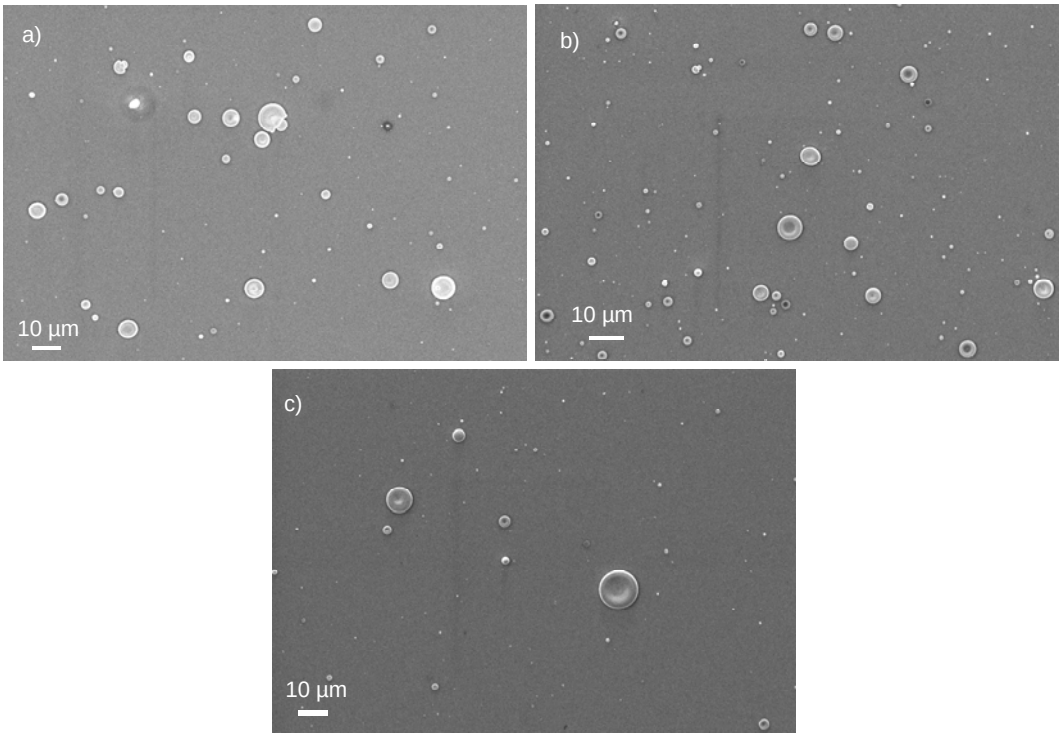

Figure 5.8. SEM images of Ag cups on Si obtained by laser ablation at different pulse energies, substrate temperature, 820 °C a) 60 mJ b) 150 mJ c) 200 mJ. See Figure 5.7d for pulse energy, 100 mJ.

the cups become more well-defined. Increase in laser fluence has an effect of increase in the number of particulates and droplets and hence, the increase in the number of features With 150 mJ per pulse, again well-shaped cups are produced (Figure 5.8b). When the pulse energy is increased further to 200 mJ, as seen in Figure 5.8c, the population of features/cups has come down drastically. This observation is consistent with earlier studies of droplet emission from metal targets at high laser fluences [54]. It is reported that above threshold laser fluence, the surface roughening of target is suppressed resulting in a reduction in the number of droplets. Thus, we have been able to optimize the experimental conditions to obtain well-formed metal cups and the optimum conditions are found to be moderate laser fluence (~100 mJ/pulse) and substrate temperatures slightly lower than M. P. of the metal employed.

Well-shaped cups could be obtained in the case of other metals such as Au, Cu, Cd, Zn, Nb, Sn, In, Al on silicon by laser ablation. A few examples are given in Figure 5.9. Metal cups could also be obtained on substrates other than Si, such as HOPG and glass

(Figure 5.10). The morphology of the cups is essentially similar on the different substrates used in this study. It appears that any non-reactive, flat substrate will do for the

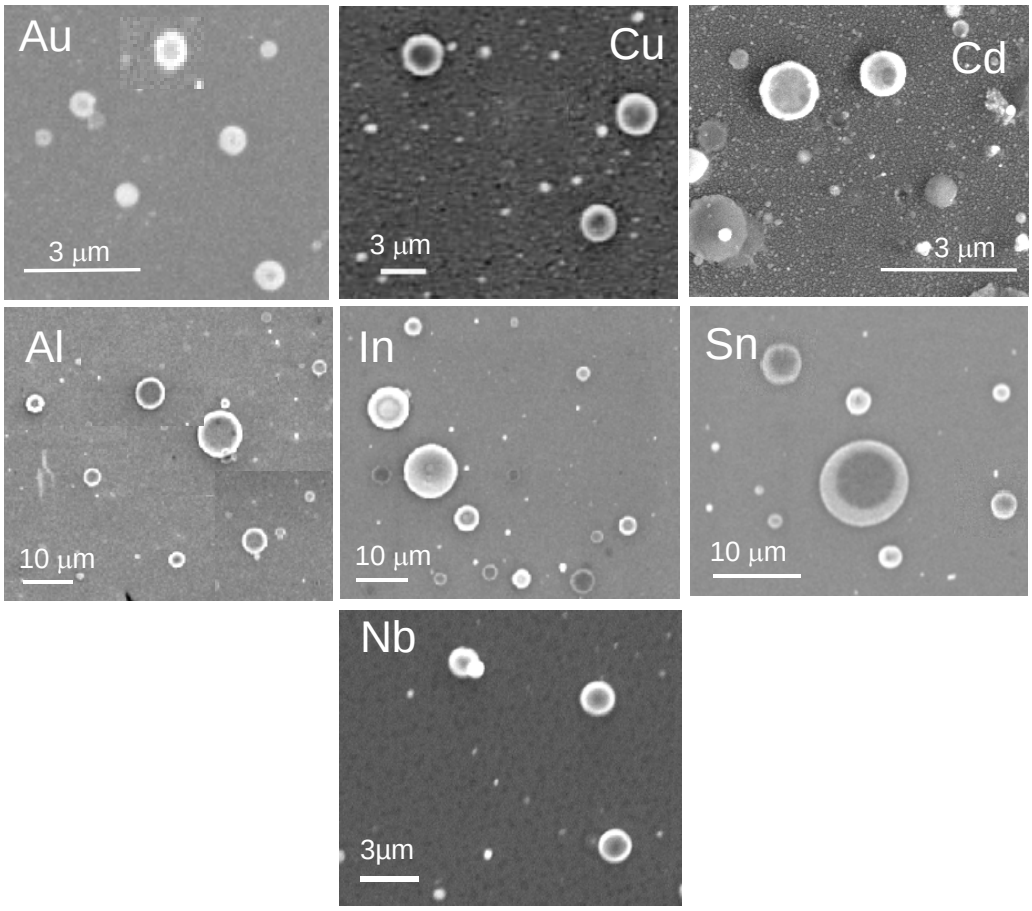

Figure 5.9. SEM images of femtoliter cups formed by other metals on Si by laser ablation. Laser energy-100 mJ/pulse, substrate temperatures: Au-720 ºC, Cu, Cd, Al, In, Sn-27 ºC and Nb-1000 ºC.

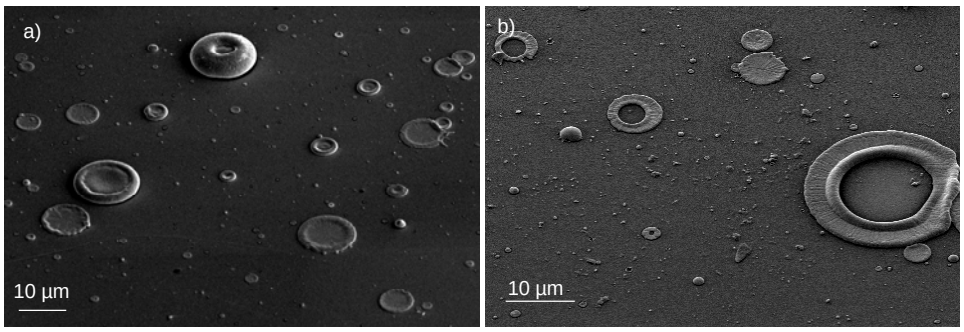

Figure 5.10. FESEM image of Sn cups obtained by laser ablation, substrate temperature-27 ºC, laser energy-100 mJ/pulse a) on HOPG b) on cover glass.

deposition. The experimental conditions for obtaining femtoliter cups of various metals on different substrates are given in Table 5.1. 3D AFM image of a well-formed Sn cup on Si and the height profile is given in Figure 5.11. An interesting observation with most of these cups is the appearance of radial striations after solidification.

Table 5.1. Experimental conditions for cup formation

Metals (M.P. ºC)	Substrate	Substrate temperature (ºC)	Laser energy (mJ/pulse)	Remarks
Ag (961.7)	Silicon	820	60 —	Cups and blobs. Less number of well-defined cups.
	Silicon	27, 500, 700, 820, 900	100 —	Both cups and blobs. Well-defined cups above 500°C.
	Silicon	820	150 —	well-defined cups.
	HOPG	800	100 —	Cups and blobs
	Cover glass	500	100 —	Cups and blobs
Au (1064)	Silicon	720	—	Well-defined cups
	HOPG	720	100 —	Well-defined cups
	Cover glass	500	—	Cups and blobs
Sn (231.9)	Silicon	27	—	Well-defined cups
	HOPG		100 —	Well-defined cups
	Cover glass		—	Cups and blobs
Al (660.3)	Silicon	500	—	Well-defined cups
In (156.6)		27	—	Well-defined cups
Cu (1084.6)		800	—	Well-defined cups
Zn (419.5)		300	100 —	Well-defined cups
Nb (2477)		1000	—	Cups and blobs
Cd (321.2)		27	—	Cups and blobs

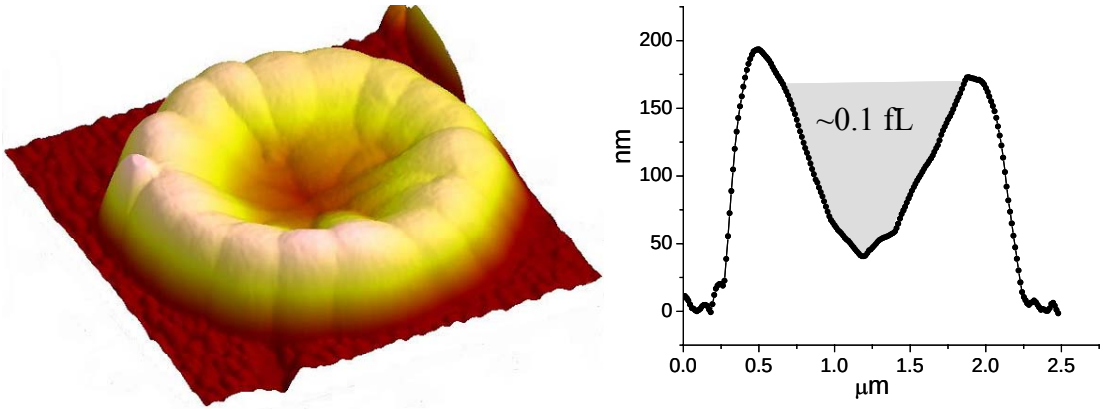

Figure 5.11. AFM image of a Sn cup, a 3D view. The height profile across the diameter of the cup is also shown alongside. Note the presence of radial striations on the surface.

5.4.2 Mechanism of cup formation

We have attempted to understand the mechanism behind the formation of femtoliter cups. It is possible that tiny hot metal droplets impinging on the substrate undergo a peculiar flow pattern before freezing into a cup-like structure. The droplet dynamics is such that rather than make solid blobs on the surface, there is a strong preference, over a range of substrate temperatures, to spread out thinly initially and then display a hydraulic jump. Large scale jumps are always caused by a balance of inertial, gravitational and viscous forces [36,37]. In our experiment, however, gravity is irrelevant, since the length scales are small and besides, the substrate is held vertical. We find that at small scales, hydraulic jumps can be caused by a balance of inertial, surface tension and viscous forces. This is because surface tension can offer an adverse pressure due to the azimuthal curvature analogous to the adverse pressure gradient created by gravity.

The relative magnitudes of gravity and surface tension may be estimated by the Bond number, given by

$$Bo=\frac{\rho a^2 g}{\sigma} \tag{5.1}$$

where ρ and σ respectively are the density and surface tension of the fluid, a is a typical length scale in the problem, and g is the acceleration due to gravity. In the kitchen sink, Bo is of the order of 10, while in our experiment with molten silver, Bo is of the order of 10^{-7} to 10^{-8} ($a=10^{-7}$ m, $\rho=5000$ kg/m^3, $\sigma=0.9$ N/m). Thus gravity is the driver in the former flow, and surface tension plays that role in the latter. Note that azimuthal curvature is required. Unlike gravity, surface tension cannot create a planar jump.

Thus, the surprising cup structure is consistent with the proposed dynamics, of a droplet spreading out thinly initially and then undergoing a height discontinuity. At larger scales hydraulic jumps are known to occur even when the incoming flow is in droplets rather than jets [55]. The general nature of the process creating the jump is supported by our experiments with different metals and substrates, cups are observed in all cases (Figures 5.9 and 5.10). Although, effect of gravity is negligible, inertia is considerable since velocities are high. That the jump is directly related to droplet dynamics is confirmed by varying the substrate orientation with respect to the incoming jet (see schematic in Figure 5.12). As θ, the inclination of the substrate away from the normal, is increased, the structures become increasingly elliptical, especially beyond 40º. The

variation is expressed as the ratio of major axis to minor axis vs. θ in the plot given in Figure 5.12. SEM images of the structures at various θ are also given.

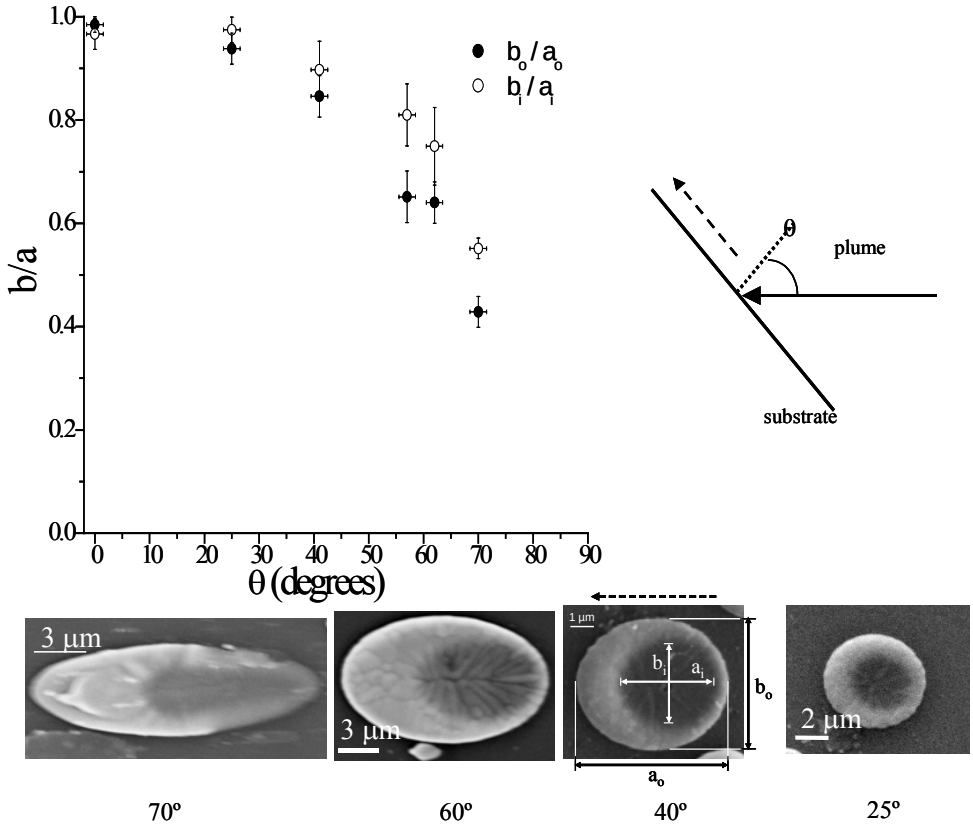

Figure 5.12. Experiments with varying substrate orientation with respect to plume. The ratio of the minor to the major axis, *b/a*, of the elliptical structures as a function of θ. Each data point is an average on several cup-like structures. A schematic of the arrangement employed in the experiment is shown alongside. SEM images of the elliptical Sn cups obtained on Si at various θ are shown. *a* and *b* are defined in the image. The error bar denotes the error in the angle measurements (± 1.5º) and also the deviation from the average *b/a*. The dashed arrows indicate the direction of maximum flow, which lies along the major axis of the ellipse.

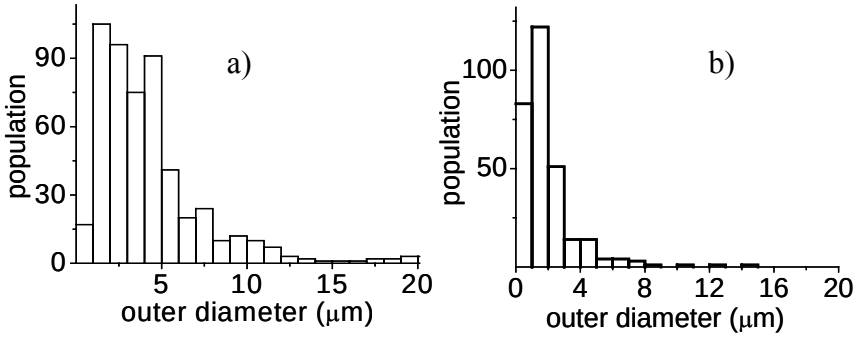

Figure 5.13. Histograms of Sn cups on (a) silicon and (b) glass, deposited simultaneously.

Table 5.2. Ratio of height of the center to rim for Ag and Sn cups on Si estimated from AFM height profiles.

Ag	Sn
1.75	2.13
2.38	2.93
2.60	3.02
2.61	3.36
2.67	3.48
2.86	3.80
2.96	3.84
3.17	4.01
3.20	4.54
3.25	5.65
3.54	6.20

Since the experiment includes additional complexity in the form of solidification, we estimate relative time-scales of jump formation t_j and solidification of a droplet t_c. For the experimental values of substrate thickness, t_c ranges from ~3×10^{-4} s on silicon to ~10^{-2} s on glass (taking into consideration conduction, radiation and latent heat), while $t_j \sim r_j/u_j$ ~10^{-6} s or less. Contact-line freezing can give rise to an increase in height in the vicinity, typically amounting to a small percentage of the height in the central region. Contrast this to our jump where the height at the rim is several-fold larger than that in the central region. An idea of the spread in the ratio of height of the center to rim may be obtained from Table 5.2, for Ag and Sn cups deposited on Si. In spite of this, and the disparity in time scales, we cannot rule out a role for local freezing at the contact line [56]. We do notice a dependence on the substrate of the size distribution of cups (Figure 5.13) and also some visual differences in the shape of the cups.

5.4.3 Applications of femtoliter cups as containers

To illustrate the utility of the cups as containers or reaction vessels, we have filled them with nanometals and biomolecules. Figure 5.14 shows a Sn femtoiter cup holding a drop of Pt metal from electron beam induced deposition of a volatile organometallic precursor, cyclopentadienyl trimethyl platinum (Nova nanoSEM 600, FEI, Netherlands). The subsequent EDX analysis shows the presence of Pt at the center of the cup. Figure 5.15 shows a confocal fluorescence image of a biomarker adsorbed in an Au cup. To do this, we deposited Au cups on a cover glass with pre-defined markers and soaked them

with Alexa 488 dye and examined under a confocal microscope. In this experiment, the biomarker seems to be adsorbed all over the cup. Similarly, we were successful in

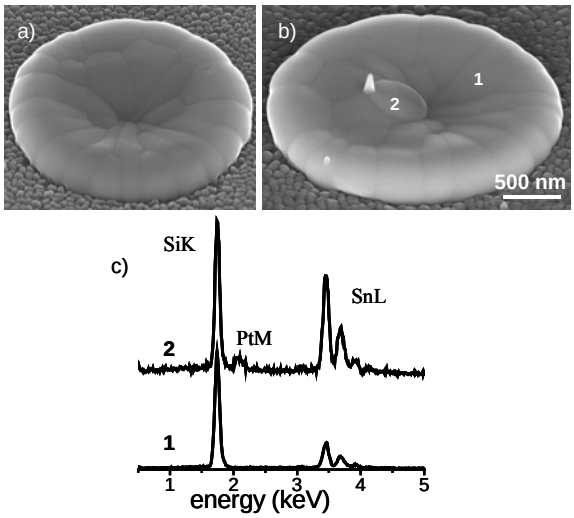

Figure 5.14. Filling a Sn cup with Pt metal by e-beam assisted metal deposition, FESEM images a) before and b) after deposition. c) The EDX spectra from the rim and the center of the cup after Pt deposition.

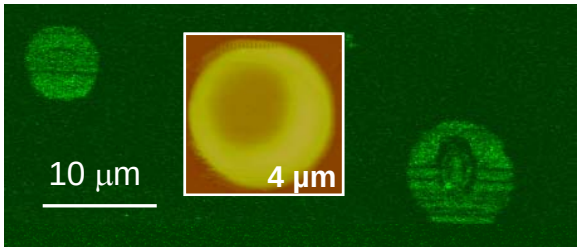

Figure 5.15. Confocal fluorescence image of femtoliter Au cups (deposited on cover glass) filled with dye molecules. Inset gives the AFM topography of the cup located with the help of markers.

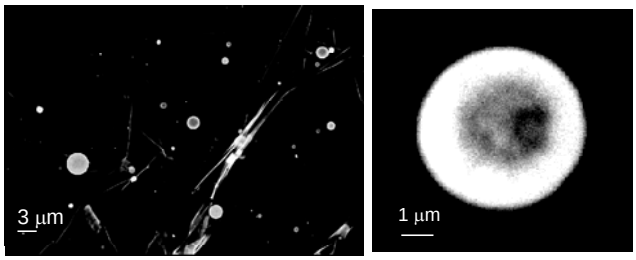

Figure 5.16. SEM image of Au cups lifted on to HOPG after leaching out the substrate, a microscopy cover glass, by dissolving in HF. A closer view of a cup is also given.

imaging a green fluorescent protein marker (GFP) as well. A more efficient way of filling these cups would be to use a suitable injection pump. Alternatively, we have employed DPN to selectively functionalize inside of an Ag cup with octanedithiol molecules followed by adsorption of Au nanoparticles. The technique of DPN for patterning nanostructures is explained in detail in the next chapter.

The cups could be detached by leaching out the substrate. This was possible in the case of Au cups prepared on a cover glass, the latter removed by dissolving in HF. Figure 5.16 shows an SEM image of Au cups lifted on to HOPG. We see that the cup morphology is intact, from the closer view.

5.4.4 Chemical transformation of femtoliter metal cups to oxide cups and chemical mapping by scanning Auger spectroscopy

We could convert metal cups to their oxides by oxidizing them externally in a furnace with oxygen flow. Figure 5.17 shows AFM and SEM images of ceramic cups of alumina by oxidizing the Al cups deposited on a Si surface. We see that following the transformation, the overall shape is retained, but the surface had become slightly non-uniform. EDX analysis confirmed the formation of the oxide.

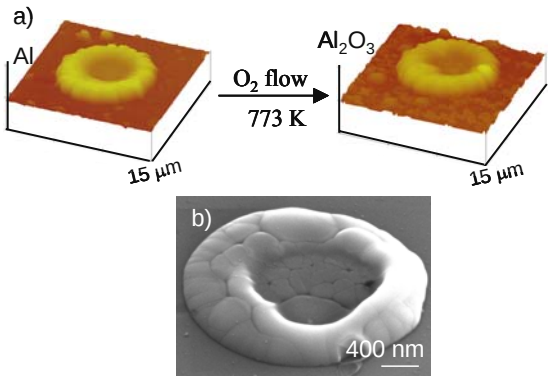

Figure 5.17. a) AFM images of an Al cup on a Si surface (left) and after oxidation to form an alumina cup (right). The feature of interest was monitored with the aid of pre-defined markers on the substrate. b) SEM image after oxidation.

Following this, we studied the oxidation behavior of In, Sn and Nb cups. When the as-deposited In cups were heated externally in oxygen, they showed large variations in morphology although the overall shape was retained. The AFM images shown in Figure

5.18a reveal a bulging of the cup, on one side, as though the material has been driven towards the rim during heating. Accordingly, the thickness of the metal in the center of the cup decreased as seen from the height profiles (Figure 5.18b). However, the outer diameter remains unchanged. In order to understand whether morphological changes are associated with variations in local chemical compositions, we monitored the oxidation process of In, Sn and Nb cups employing SR-AES. AES studies of as-deposited, sputtered and oxidized cups were performed.

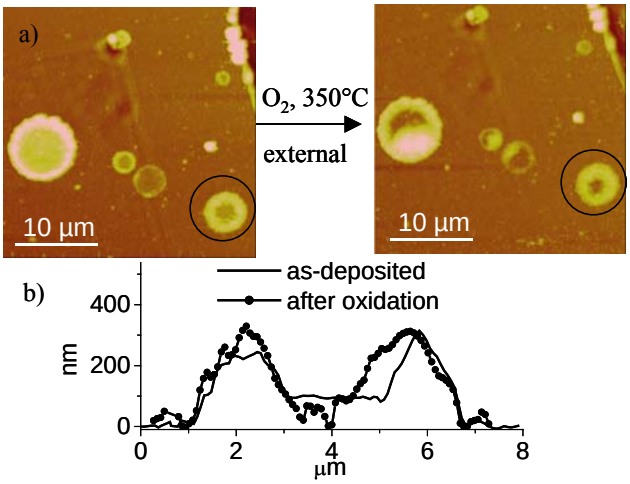

Figure 5.18. a) AFM images of In cups before and after external oxidation. b) Height profiles of a cup, marked by a circle in (a), before (solid line) and after oxidation (dotted line).

i) SR-AES of as-deposited cups

Figure 5.19a shows a set of spectra of In MNN Auger transitions obtained from the central region of an In cup (curve 1) as well as from the substrate region (curve 2) of an as-deposited sample. The inset shows an SEM image of the cup with the positions marked from where Auger spectra have been acquired. Curve 2 shows that a thin In film covers the substrate. The spectrum from the rim of the cup is similar to that from the central region.

To determine the chemical shifts, we have followed the conventional concept of taking the position of the negative excursion peak from the differential spectrum as the Auger electron kinetic energy for a particular transition [57,58]. Hence for the as-deposited sample, In MNN transitions from the center of a cup are at 400.5 and 407.2 eV (Figure 5.19a, right inset). These values are in accord with that for oxidized In, In_2O_3 [58,59]. A further 1 eV shift of the In line to lower kinetic energy (KE) is observed for

the substrate (see the differential spectrum in the inset) and the peak is found to be a little broader compared to that from the cup, presumably due to local charging of the thin film on the native SiO_2 on substrate. The corresponding O KLL transition is similar to that from SiO_2 (see the direct spectrum in the inset of Figure 5.19a) [58]. Similar observations

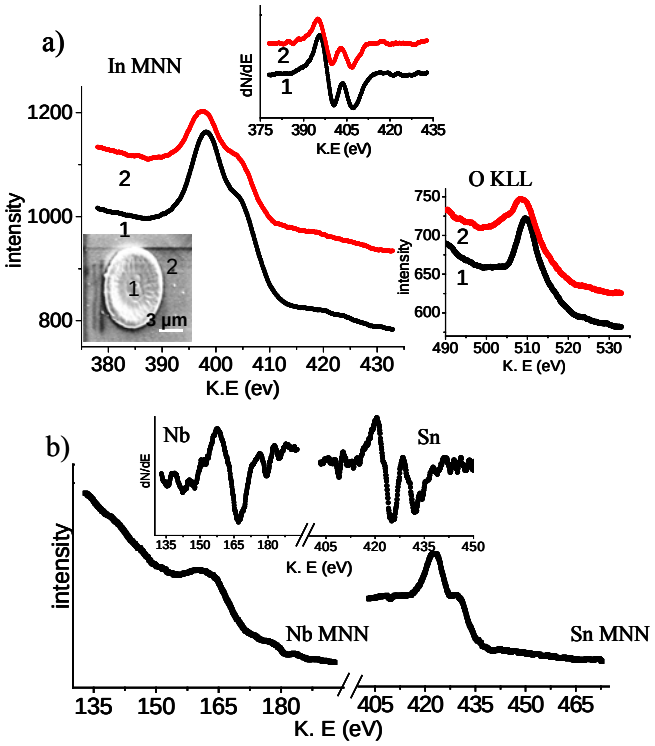

Figure 5.19. a) In MNN AES from various regions of as-deposited In cups: (1) from the central region of the cup, (2) from the substrate (outside the cup). Left inset gives the SEM image of an In cup in the tilted mode for acquiring AES. Right top inset gives the differential spectra from 1 and 2 positions. O KLL from as-deposited In cup from 1 and 2 regions is also given. b) MNN AES for as-deposited Nb and Sn cups from the center region. The inset gives the corresponding differential spectrum. Spectra from the rim of the cup showed similar characteristics.

have been made in the case of Sn and Nb cups. Figure 5.19b shows the AES from central regions of as-deposited Sn and Nb cups in the direct and differential mode. A shift of 4 eV towards lower KE in the case of Sn MNN with respect to pure Sn, 429 eV [53] and a broad peak in the direct Nb MNN with a shoulder at lower KE (as seen in the derivative spectrum given in inset) shows the presence of a native oxide layer. These results are in accordance with what is reported in literature [53,60,61]. In the case of Sn, the oxide can be SnO_2 or SnO, the chemical shifts for both compounds being same in AES [60]. For

Nb, the oxide layer mainly consists of Nb_2O_5, the broad peak consists two lines, 167 and 160.5 eV. The splitting of the MNN line is indicative of the presence of pentoxide of Nb [62]. Rao *et al*. have reported that such a splitting of the MNN line occurs due to the interatomic transition involving the oxygen valence level in the hole decay of the metal valence level [63]. Depth profiling studies on superconducting cavities of Nb has shown that the oxide layer consists of various suboxides of Nb as well [64]. Hence, the metal cups when exposed to ambient conditions get passivated with a native oxide layer. Oxygen KLL spectra from Sn and Nb cups and that from the substrate in each case are similar to the case of In. Acquired C KLL spectra indicate that carbon contamination is present in all the cases. For Nb alone, we found the presence of small amount of Si on the surface of cups. This is due to the high temperature treatment of Si substrate while depositing Nb.

ii) Ar^+ ion sputtering of as-deposited cups

The MNN Auger transitions from the central region of an In cup after Ar ion sputtering are given in Figure 5.20a. From the Auger spectra it is clear that oxygen and carbon are completely removed by sputtering. The KE values at 402.8 and 409.3 eV (right inset of Figure 5.20a) correspond to clean metallic In, which are shifted by 2.3 eV with respect to those from as-deposited cups (compare with Figure 5.19a). Importantly, the In MNN signal from the substrate disappears after sputtering indicating that the thin In film covering the substrate has been removed. But interestingly, the cup shape and morphology are found to be intact after sputtering (see the SEM image in inset of Figure 5.20a). Similar observations may be made in the case of Sn and Nb cups from the SEM images in Figures 5.20c and 5.20d.

Some In cups got transformed into In rings after sputtering due to the removal of metal from the central region. Figure 5.20b shows the SEM and SAM images of an In ring of 3.7 μm diameter. The SAM image was acquired at the peak value of In MNN of 397 eV. The bright red color denotes the presence of In. Ring structures of metals and semiconductors are of importance and are known to exhibit unusual optical and magnetic properties [65-68].

Figure 5.20c gives the Sn MNN Auger line from the central region of a Sn cup after

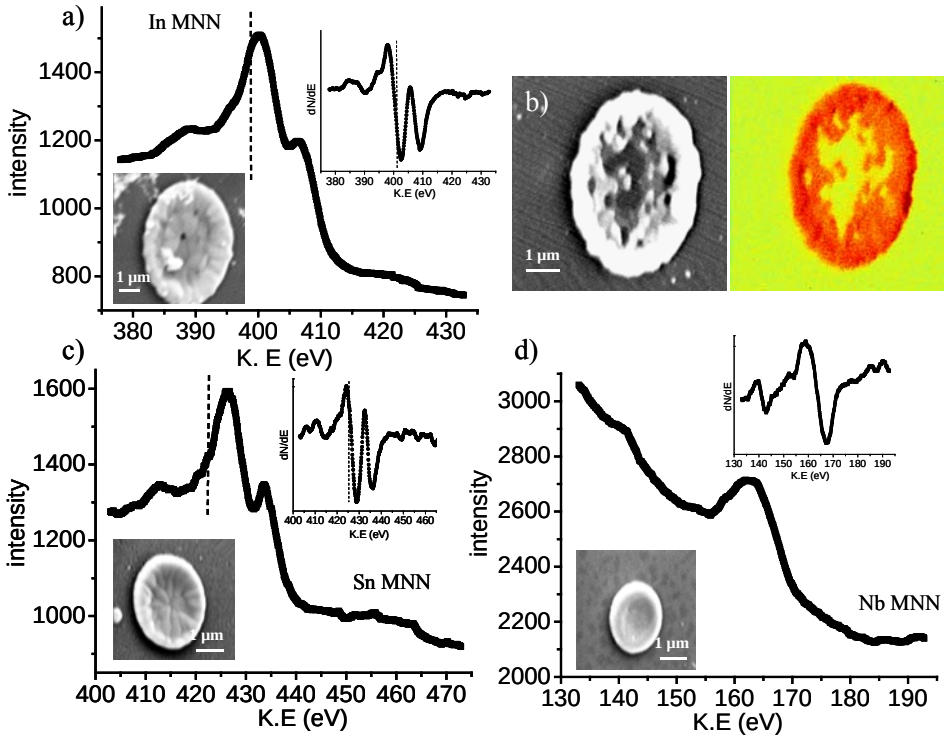

Figure 5.20. a), c) and d) In MNN, Sn MNN and Nb MNN from the central region of the sputtered In, Sn and Nb cups, respectively. Left insets give the SEM images of the sputtered cup and right insets, the differential spectra in each case. The dashed lines indicate the shift in Auger line positions with respect to the as-deposited cases (with native oxide layer). b) The SEM and SAM images of an In ring obtained after sputtering. The SAM image was acquired at the In MNN line energy. The red colour denotes the presence of indium.

sputtering. A shift of 4 eV towards higher KE with respect to the as-deposited cups is observed indicating the removal of native oxide layer. In the case of Nb, despite a longer duration of sputtering a small amount of oxygen was still present. However, the broad spectrum due to the oxide component of Nb became narrower following sputtering (Figure 5.20d). The splitting of MNN becomes less prominent. Hence in most cases, the native oxide layer and other contaminants could be removed by sputtering to obtain clean femtoliter cups in UHV.

iii) Chemical mapping of oxide cups-in situ vs. external oxidation

SR-AES from the central and rim regions of the oxidized In cups (curves 2 and 3 in Figure 5.21) showed a negative 0.5 eV shift with respect to the as-deposited ones. The

shift is 2.8 eV when compared with the clean In cups. In addition to the morphological variations described in Figure 5.18, it is noticed that the radial morphology seen in the case of as-deposited cups is lost during external oxidation, and an unusually dark contrast is observed at the central region of the cups. This is clear when one compares the SEM images shown in the insets of Figures 5.19a and 5.21.

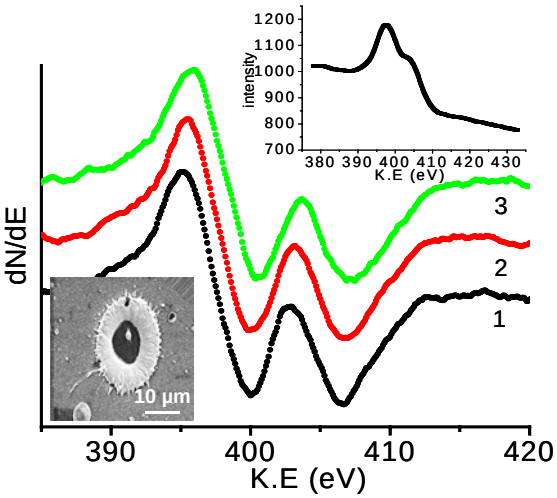

Figure 5.21. Differential SR-AES from different regions of the oxidized cups: (2) center and (3) rim. Curve (1) from the as-deposited cup is given for comparison. Right inset gives the direct spectrum from the oxidized cup and left inset, SEM image of the oxidized In cup.

To understand the oxidation process more clearly, we undertook a systematic study of oxidizing clean Sn cups in UHV as well as externally. Figure 5.22 gives a comparison of AES from externally and *in situ* oxidized Sn cups with respect to the sputtered ones. Externally oxidized ones showed considerable shifts in the KE values indicating the formation of a thicker oxide layer as compared to the *in situ* oxidation (Figure 5.22 b and c). The O KLL transitions are much more intense in this case (Figure 5.22 d). The KE values of the Sn MNN transition from various regions of the differently treated cups are given for comparison in Table 5.3.

The SEM image in Figure 5.22a reveals that after *in situ* oxidation, larger cups underwent some shrinkage, while the smaller ones altogether lost their shape and turned to blobs. An unusual dark contrast is observed in the center of the rings, as was observed in the case of externally oxidized In cups (see inset SEM image of Figure 5.21). Figure

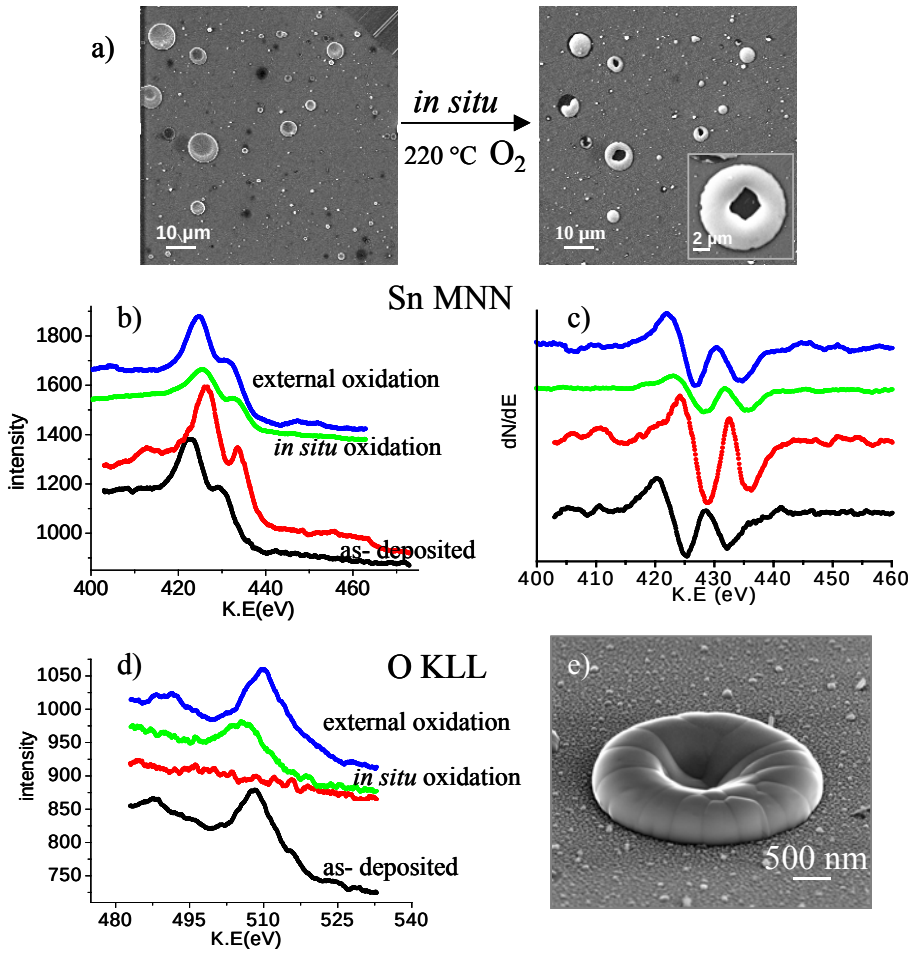

Figure 5.22. Sn cups after oxidation. a) SEM images before (left) and after (right) *in situ* oxidation. A closer view of an *in situ* oxidized cup is given as the inset of right image. b) A comparison of Sn MNN lines from the central region of cups after different treatments. c) The differential spectra of the curves in (b). d) O KLL lines from the center of Sn cups subjected to different treatments. e) SEM image of an externally oxidized Sn cup.

5.22b reveals that the Auger lines from the oxidized cups have broadened compared to those from a clean cup for *in situ* oxidation. There is a negative shift of only 0.5 eV but only for the central region. For the rim region, there is no shift in the KE values before and after the *in situ* oxidation. In addition, we see a Si signal from the central region of oxidized cups. Hence this small shift in MNN from the center and the appearance of dark contrast might be arising from the formation of an oxidized Sn-Si alloy. A similar explanation may be given for the dark contrast seen at the center of oxidized In cups. The melting of Sn in the center and interdiffusion of Si is further supported by the O KLL spectra (Figure 5.22d), wherein the underlying SiO_2 contributes to the total spectrum

(similar to the O KLL from substrate region, see O KLL spectra in Figure 5.20a). This was not observed for the rim region. In contrast to the case of In cups, Sn is seen on the substrate even after sputtering, and a Si line is also observed with AES.

Another noticeable aspect is that the externally oxidized Sn cups are intact in size and shape as can be seen from the SEM image given in Figure 5.22e. Hence a higher flux of oxygen is found to be necessary throughout the oxidation step to prevent the deformation of cups and retain the shape, even when the oxidation is carried out below the melting point of the metal. Also there is no contribution from SiO_2 in the AES of O KLL from the central region after external oxidation. The KE values of the Sn MNN transition from various regions of the differently treated cups are given for comparison in Table 5.3.

Table 5.3. MNN Auger transition positions from various regions of In, Sn and Nb cups subjected to different treatments. The error is estimated to be ± 0.2 eV.

KE values (eV) from the derivative spectra				
	as-deposited	sputtered	*in situ* oxidation	external oxidation
In MNN				
Center	400.5, 407.1 (O present, Si not seen, C seen)	402.6, 409.3 (no O and C, Si seen only in some cases)	Not performed	400, 406.6 (O present)
Rim	400.5, 407.1 (O present, Si not seen, C seen)	402.6, 409.3 (no O, Si and C)		400, 406.7 (O present)
Substrate	400, 406.7 (O, Si and C seen)	No In, O and Si seen, no C		399.3, 406.2 (O and Si seen)
Sn MNN				
Center	425.2, 432 (O present, Si not seen, C seen)	428.8, 435.9 (O not present, Si not seen, no C)	428.2, 435.4 (O present, Si seen, C seen)	426.8, 434.5 (O and C seen, Si not seen)
Rim	424.9, 432.4 (oxygen seen, Si not seen, C seen)	428.9, 435.9 (O not seen, Si not seen, no C)	428.9, 435.8 (O seen, no Si and C)	427, 434.2 (O and C seen)
Substrate	424.9, 431.5 (O present, Si not seen, carbon seen)	429, 435.6 (O present, Si seen & C removed)	426.6, 434 (O seen, Si seen)	426.8, 434.4 (O seen, Si and C not seen)
Nb MNN				
Center	167.2 (O, Si and C seen)	167.5 (O and Si seen, no C)	166.4 (O and Si seen, no C)	Not performed
Rim	168 (O, Si and C seen)	168.1 (O and Si seen, no C)	166.4 (O and Si seen, no C)	
Substrate	167.9 (O, Si and C seen)	167.1 (O and Si seen, no C)	167.1 (O and Si seen, no C)	

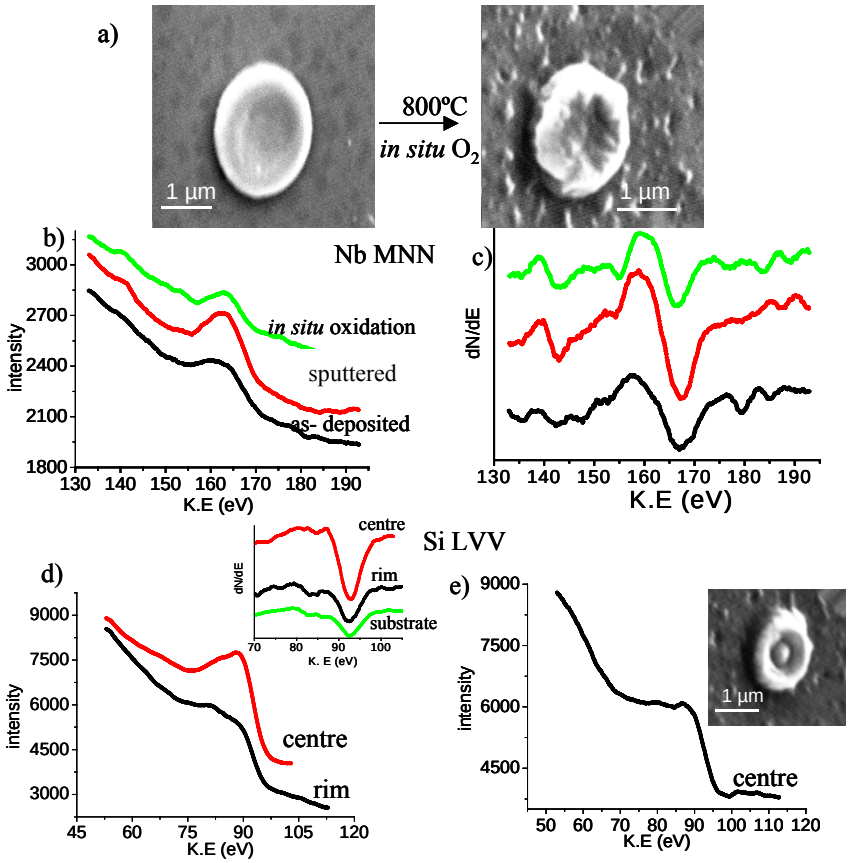

Figure 5.23. *In situ* oxidation of Nb cups. a) The SEM image of Nb cups before and after oxidation b) Nb MNN spectra acquired from the central region of the Nb cup before and after oxidation. c) The differential spectra of AES given in (b). d) Si LVV Auger transitions from different regions of the oxidized cups. The corresponding differential spectra are shown in the inset. e) SEM image of a Nb cup with a Si feature inside, following oxidation. The corresponding Si LVV spectrum is also shown.

Figure 5.23a gives the SEM images of Nb cups before and after oxidation. Although the shape is retained, the surface roughness has increased after oxidation. A comparison of the Nb MNN transitions from the center of the cups after various treatments is given in Figure 5.23b. It can be noticed that after *in situ* oxidation, the intensity of the Nb signal decreased drastically. The KE values from the differential spectra (Figure 5.23c) showed a 0.8-1 eV shift towards lower KE after oxidation at higher temperature with respect to the sputtered one (167.8 eV) and the one with the native oxide layer. The oxygen peak intensity after oxidation is very small. In contrast to the case of In and Sn, sputtered Nb cups when subjected to *in situ* oxidation at 800 ºC showed the presence of Si at the

surface of the cups. Figure 5.23d shows that the reduced intensity of Nb after oxidation and annealing is due to the large segregation of elemental Si (92 eV) to the surface of the Nb cups. Hence the 1 eV shift for Nb after *in situ* treatment can be attributed to the formation of a Nb-Si alloy. A small shift in metal Auger transitions is generally observed for metal silicides [69]. A shoulder in the Si LVV line at 84.5 eV from the rim and central region also support the formation of alloy [70]. It can be noted from the differential spectra (inset of Figure 5.23d) that the Si LVV line from the substrate has an oxide component in addition to the alloy and pure Si peaks. Some of the cups even appear to hold a drop inside, which is presumably the alloy (Figure 5.23e). Examples of metal induced segregation of Si while annealing at high temperatures are known [71,72]. Higher temperatures increase the mobility of metal in Si and finally promote Si segregation.

5.5 Conclusions

In conclusion, we have established, employing pulsed laser ablation, a simple and straightforward method to produce femtoliter cup structures of various metals (Ag, Au, Cu, Sn, Cd, Zn, Nb, In, Al) on flat substrates such as Si, HOPG and glass. The method is, in principle, extendable to other materials. The formation of these cups is attributed to the dynamics of the molten metal droplets, with the right combination of size and velocity, which translate to experimental conditions of laser pulse energy and substrate temperature. Optimal conditions for the formation of cups are thus, moderate laser energies (100-150 mJ/pulse) and substrate temperatures close to but below the melting point of the metal under study. A hydraulic jump solely driven by surface tension is found to be the underlying mechanism in shaping these microstructures. However, the laser ablation process provides little control on their size distribution. With a proper metal injection system designed to deliver uniform droplets, it should be possible to produce patterned cup structures with well-defined size. The utility of the cups as femtoliter containers is demonstrated by filling them with fluorescent biomarkers and metal nanoparticles. We envisage potential applications for the metal cups ranging from nanoscale synthetic chemistry to single cell biology.

The novelty of the metal cups is that they could be chemically transformed to more robust oxide cups, retaining the shape. SR-AES is employed for local chemical mapping of different regions of metal cups. In particular, the oxidation behavior of In, Sn, and Nb cups on a Si substrate is monitored. Clean metal cups without the native oxide layer and carbon impurities were obtained in UHV by sputtering, retaining the shape and morphology of the cups. In the case of In, a few cups with a thin layer of metal at the central region transformed into ring structures after sputtering. SR-AES on Sn and In, after oxidation showed that externally treated cups in high oxygen flow have thicker oxide layers compared to the *in situ* treatment. In contrast, precipitation of Si from the substrate to the surface is observed for *in situ* oxidized Nb cups. Interdiffusion of metal and silicon, especially at the thinner central region of the cups, is observed for *in situ* treated Sn and Nb cups.

References

[1] D. Stamou, C. Duschl, E. Delamarche & H. Vogel, *Angew. Chem. Int. Ed.,* 42, 5580 (**2003**).

[2] Y. Rondelez, G. Tresset, K. V. Tabata, H. Arata, H. Fujita, S. Takeuchi & H. Noji, *Nat. Biotechnol.*, 23, 361 (**2005**).

[3] K. Jensen, *Nature*, 393, 735 (**1998**).

[4] W. Tan & E. S. Yeung, *Anal. Chem.*, 69, 4242 (**1997**).

[5] Z. Wang, H. Shang & G. U. Lee, *Langmuir*, 22, 6723 (**2006**).

[6] R. J. Jackman, D. C. Duffy, E. Ostuni, N. D. Willmore & G. M. Whitesides, *Anal. Chem.*, 70, 2280 (**1998**).

[7] J. E.Barton & T. W. Odom, *Nano Lett.*, 4, 1525 (**2004**).

[8] X. D. Wang, E. Graugnard, J. S. King, Z. L. Wang & C. J. Summers, *Nano Lett.*, 4, 2223 (**2004**).

[9] C. A. Mirkin, K. S. Ryu, X. Wang, K. Shaikh, D. Bullen, E. Goluch, J. Zou & C. Liu, *Appl. Phys. Lett.*, 85, 136 (**2004**).

[10] J. I. Nilsson, J. R. Lee, T. V. Ratto & S. E. Létant, *Adv. Mater.*, 18, 427 (**2006**).

[11] F. Caruso, R. A. Caruso & H. Möhwald, *Science*, 282, 1111 (**1998**).

[12] L. Dähne & C. S. Peyratout, *Angew. Chem. Int. Ed.*, 43, 3762 (**2004**).

[13] P. B. Deotare & J. Kameoka, *Nanotechnology*, 17, 1380 (**2006**).

[14] H. Y. Koo, S. T. Chang, W. S. Choi, J. –H. Park, D. -Y. Kim & O. D. Velev, *Chem. Mater.*,18, 3308 (**2006**).

[15] D. T. Chiu, C. F. Wilson, F. Ryttsén, A. Strömberg, C. Farre et al., *Science*, 283, 1892 (**1999**).

[16] D. M. Vriezema, A. M. Comellas, J. A. A. W. Elemans, J. J. L. M. Cornelissen, A. E. Rowan & R. J. M. Nolte, *Chem. Rev.*, 105, 1445 (**2005**).

[17] P. R. Willmott & J. R. Huber, *Rev. Mod. Phys.*, 72, 315 (**2000**).

[18] M. N. R. Ashfold, F. Claeyssens, G. M. Fuge & J. S. Henley, *Chem. Soc. Rev.*, 33, 23 (**2003**).

[19] D. B. Chrisey & G. K. Hubler, *Pulsed Laser Deposition of Thin Films*, Wiley, New York (**1994**).

[20] D. H. Lowndes, D. B. Geohegan, A. A. Puretzky, D. P. Norton & C. M. Rouleau, *Science*, 273, 898 (**1996**).

[21] G. Raina, G. U. Kulkarni, & C. N. R. Rao, *J. Phys. Chem. A*, 105, 10204 (**2001**).

[22] U. Heiz, & E. L. Bullock, *J. Mater. Chem.*, 14, 564 (**2004**).

[23] B. C. Guo, K. P. Kerns & A. W. Castleman, *Science*, 255, 1411 (**1992**).

[24] M. Terrones, N. Grobert, J. Olivares, J. P. Zhang, H. Terrones et al., *Nature*, 388, 52 (**1997**).

[25] A. Thess, R. Lee, P. Nikolaev, H. Dai, P. Petit et al., *Science*, 273, 483 (**1996**).

[26] X. Duan, & C. M. Lieber, *Adv. Mater.*, 12, 298 (**2000**).

[27] Y. Zhang, K.Suenaga, C. Colliex & S. Iijima, *Science*, 281, 973 (**1998**).

[28] I. Lee, S. W. Han & K. Kim, *Chem. Commun.*, 1782 (**2001**).

[29] M. Nath, C. N. R. Rao, R. P. Biro, A. A. Yaron & R. Tenne, *Chem. Mater.*, 16, 2238 (**2004**).

[30] U. K. Gautam, S. R. C. Vivekchand, A. Govindaraj, G. U. Kulkarni, N. R. Selvi, & C. N. R. Rao, *J. Am. Chem. Soc.*, 127, 3658 (**2005**).

[31] S. Link, M. B. Mohamed & M. A. El-Sayed, *J. Phys. Chem. A*, 103, 1165 (**1999**).

[32] C. J. K. Richardson, M. H. Wisnioski, J. B. Spicer, J. D. Demaree, M. W. Cole et al., *Mat. Res. Soc. Symp.*, 617, J7.4.1 (**2000**).

[33] J. S. Henley, M. N. R. Ashfold & S. R. J. Pearce, *Appl. Surf. Sci.*, 217, 68 (**2003**).

[34] Lord Rayleigh, *Proc. R. Soc. Lond. A*, 90, 324 (**1914**).

[35] C. Ellegaard, A. E. Hansen, A. Haaning, K. Hansen, A. Marcussen, T. Bohr, L. J. Hansen & S. Watanabe, *Nature*, 392, 767 (**1998**).

[36] E. J. Watson, *J. Fluid Mech.*, 20, 481 (**1964**).

[37] T. Bohr, P. Dimon & V. Putkaradze, *J. Fluid Mech.*, 254, 635 (**1993**).

[38] J. W. M. Bush & J. M. Aristoff, *J. Fluid Mech.*, 489, 229 (**2003**).

[39] T. Bohr, V. Putkaradze & S. Watanabe, *Phys. Rev. Lett.*, 79, 1038 (**1997**).

[40] H. Haberland, *Clusters of Atoms and Molecules I*, Springer Series in Chemical Physics, Springer-Verlag, Berlin (**1995**).

[41] H. W. Kroto, J. R. Heath, S. C. O'Brien, R. F. Curl & R. E. Smalley, *Nature*, 318, 162 (**1985**).

[42] D. B. Chrisey, A. Piqué, R. A. McGill, J. S. Horwitz & B. R. Ringeisen, *Chem. Rev.*, 103, 553 (**2003**).

[43] A. Habenicht, M. Olapinski, F. Burmeister, P. Leiderer, & J. Boneberg, *Science*, 309, 2043 (**2005**).

[44] N. C. MacDonald, *Appl. Phys. Lett.,* 16, 76 (**1970**).

[45] A. Joshi, L.E. Davis & P.W. Palmberg, in *Methods of surface analysis*, A.W. Czanderna, Ed., Elsevier, New York, Pg. 159 (**1975**).

[46] M. F. Hochella, Jr., D. W. Harris & A. M. Turner, *Amer. Miner.*, 71, 1247 (**1986**).

[47] M. Lazzarino, M. Padovani, G. Mori, L. Sorba, M. Fanetti & M. Sancrotti, *Chem. Phys. Lett.*, 402, 155 (**2005**).

[48] W. Li, G. S. Hsiao, D. Harris, R. M. Nyffenegger, J. A. Virtanen & R. M. Penner, *J. Phys. Chem.*, 100, 20103 (**1996**).

[49] A. Folch, J. Tejada, C. H. Peters & M. S. Wrighton, *Appl. Phys. Lett.*, 66, 2080 (**1995**).

[50] F. S. -S. Chien, Y. C. Chou, T. T. Chen, W. -F. Hsieh, T. -S. Chao & S. Gwo, *J. Appl. Phys.*, 89, 2465 (**2001**).

[51] A. Wiessner, J. Kirschner, G. Schaefer & Th. Berghaus, *Rev. Sci. Instrum.*, 68, 3790 (**1997**).

[52] M. Padovani, E. Magnano, G. Bertoni, V. Spreafico, L. Gavioli & M. Sancrotti, *Appl. Surf. Sci.*, 212, 213 (**2003**).

[53] L. E. Davis, N. C. MacDonald, P. W. Palmberg, G. E. Riach & R. E. Weber, *Handbook of Auger electron spectroscopy*, 2nd edition, Physical Electronics Division, Minnesota (**1976**)**.**

[54] E. Van de Riet, C. J. C. M. Nillesen & J. Dieleman, *J. Appl. Phys.*, 74, 2008 (**1993**).

[55] S. Chandra & C. T. Avedisian, *Proc. R. Soc. Lond. A*, 432, 13 (**1991**).

[56] S. Schiano & A. A. Sonin, *Phys. Fluids*, 9, 2227 and 2217 (**1997**).

[57] M. P. Seah, I. S. Gilmore, H. E. Bishop & G. Lorang, *Surf. Interface Anal.*, 26, 701 (**1998**).

[58] H. Öfner, Y. Shapira & F. P. Netzer, *J. Appl. Phys.,* 76, 1196 (**1994**).

[59] G. Kiriakidis, N. Katsarakis, M. Bender, E. Gagaoudakis & V. Cimalla, *Mater. Phys. Mech.*, 1, 83 (**2000**).

[60] Y. Zhang & A. J. Slavin, *Phys. Rev. B*, 49, 2005 (**1994**).

[61] Y. Wang, X. Wei, Z. Tian, Y. Cao, R. Zhai, T. Ushikubo, K. Sato & S. Zhuang, *Surf. Sci.*, 372, L285 (**1997**).

[62] T. T. Lin & D. Lichtman, *J. Mater. Sci.*, 14, 455 (**1979**).

[63] C. N. R. Rao & D. D. Sharma, *Phys. Rev. B*, 25, 2927 (**1982**).

[64] H. Hahn & H. J. Halama, *J. Appl. Phys.*, 47, 4629 (**1976**).

[65] M. M-. Almazo, D. G-Gutierrez, X. Gao, J. L. Elechiguerra, V. A. Kusuma et al., *Nano Lett.*, 4, 1365 (**2004**).

[66] F. J. Castano, C. A. Ross, C. Frandsen, A. Eilez, D. Gil, H. I. Smith, M. Redjdal & F. B. Humphrey, *Phys. Rev. B*, 67, 184425 (**2003**).

[67] H. W. Choi, C. W. Jeon, C. Liu, I. M. Watson, M. D. Dawson, P. R. Edwards, R. W. Martin, S. Tripathy & S. J. Chua, *Appl. Phys. Lett*., 86, 021101 (**2005**).

[68] J. Aizpurua, P. Hanarp, D. S. Sutherland, M. Kall, G. W. Bryant & F. J. G. de Abajo, *Phys. Rev. Lett.*, 90, 057401 (**2003**).

[69] R. T. Tung, J. M. Gibson & J. M. Poate, *Phys. Rev. Lett.*, 50, 429 (**1983**).

[70] V. M. Bermudez, *Appl. Surf. Sci.*, 17, 12 (**1983**).

[71] Z. Jin, G. A. Bhat, M. Yeung, H. S. Kwok & M. Wong, *J. Appl. Phys.*, 84, 194 (**1998**).

[72] J. Y. Wang, D. He, Y. H. Zhao & E. J. Mittemeijer, *Appl. Phys. Lett.*, 88, 061910 (**2006**).

Chapter 6

Generating Patterned Nanostructures by Dip Pen Nanolithography*

SUMMARY

Dip pen nanolithography (DPN), an AFM based patterning technique, is employed to produce nanopatterns of various colloids like luminescent Eu^{3+} doped lanthanum phosphate, zinc oxide etc on various substrates like mica and silicon. The nanocrystal patterns were independently characterized by electron beam based techniques like low energy electron microscopy (LEEM) and X-ray photoemission electron spectroscopy (XPEEM). We have demonstrated patterning of zinc acetate and potassium tetrachloroaurate in mild HF that act as precursors for ZnO and Au. $KAuCl_4$/HF undergoes spontaneous reduction even on a Si surface covered with native oxide layer forming stable Au patterns. The patterns could be relocated in AFM and SEM. Constructive lithography has been performed by patterning amino propyl trimethoxy silane (APTMS) on Si substrate using DPN followed by adsorption of nanocrystals and thereafter further metallization in a electroless deposition process. DPN patterning of a biopolymer, poly L-lysine is also demonstrated. Filling of femtoliter metal cups employing DPN is also demonstrated.

In the context of integrating micro- and nanopatterns, we have developed a laboratory method to produce AFM tips of different sizes based on laser irradiation of the commercial silicon nitride tips, for application in DPN. A few shots of 60 mJ at 355 nm were found adequate to induce the desired bluntness from 40 nm to 500 nm in a controlled way. DPN has been performed with the blunt tips using a colloidal ink consisting of Pd nanocrystals coated with poly(vinylpyrrolidone). The line patterns drawn bear a direct relation with the tip size, wider the tip, broader are the patterns, in general. The rate of deposition also increases with the tip dimension.

---

*Papers based on this work have appeared in Int. J. Nanosci. (2005) and J. Nanosci. Nanotech. (2007).

6.1 Introduction

Novel methods for micro- and nanofabrication are essential for the scientific progress in the fields ranging from catalysis to molecular electronics to biomedicine [1]. The future of nanotechnology depends on the efficient means of integrating various nanostructures. Although synthesis pathways for making nanocrystals [2], nanotubes and nanowires [3] are well established, assembling them to form circuits and devices is still an intensive area of research. Recent activities utilize various lithographic techniques to pattern nanostructures and build up circuits on site [4-6]. The lithographic tools available today are based on modified optics [7], e-beam [8], elastomer [9] and scanning probe microscope (SPM) [10]. Originally developed as a high resolution imaging technique, SPM has become popular lately as a powerful tool for constructing, modifying and patterning nanostructures [10,11] and various genres of lithography based on SPM have been developed like electrochemical, near-field optical, local anodic oxidation and dip pen, which are collectively termed as scanning probe lithography (SPL). Dip pen nanolithography (DPN) has gained much attention among SPL methods due to its capability to pattern and image with sub-100 nm resolution and also versatility [12]. DPN pioneered by Mirkin and co-workers [13], exploits the water-meniscus formed between a slowly scanning AFM tip and a substrate to transfer the fluid material (ink) coated on the tip (nib) to the substrate (paper). Its ability as a direct-write method for a chosen ink combined with its simplicity and resolution, makes it an attractive tool for nanolithography.

Early experiments with alkanethiol molecules on gold substrates have revealed that humidity, temperature and contact time can influence the feature size formed during DPN [14,15]. Following this, patterning of many self-assembling molecules has been demonstrated on a variety of substrates [16]. These, in turn, serve as resists for fabrication of metal and semiconducting nanostructures [17]. The direct writing of precursors and generating solid structures is also possible with DPN [18]. This was further utilized to fabricate miniature gas sensors [19]. Magnetic barium hexaferrite ($BaFe_{12}O_{19}$) and CdS structures were obtained from a sol-based precursor deposited via DPN on a SiO_2 substrate [20,21]. The deposition of optically active fluorescent materials and conducting polymers by DPN opened new opportunities for miniaturized optical

devices [22,23]. Both electrochemical and electroless versions of DPN were used for direct writing of metals [24,25]. Recently the delivery of solid inks was demonstrated by heating a coated AFM tip to the melting temperature of the ink [26].

The importance of oligonuleotide or protein arrays in bioinformatics for quantifying gene expression and genomic structures has led to the fabrication of DNA arrays using DPN. The resulting patterns could be hybridized to both fluorophore-labeled oligonucleotides as well as to DNA functionalized gold nanocrystals. Such tagged arrays were screened in an optical microscope [27,28]. DPN has been employed to carry out chemical reactions at selective sites for further applications. GaN nanowires were grown on DPN patterned Ni-catalyst sites on SiO_2 [29]. Recently, Mirkin and co-workers demonstrated the blending of top down approach with bottom up approach by patterning electrodes with e-beam and then derivatizing it with DNA via DPN. DNA modified 20 and 30 nm gold nanocrystals were adsorbed on these to form a nanoscale circuit [30].

Ali *et al*. [31] have reported DPN based procedure to deposit small volumes of a sol containing Au nanocrystals on a surface, which upon evaporation of the solvent leads to circular nanocrystal patterns. Other reported methods in this context include shaving of thiol monolayers on Au using an AFM tip followed by further deposition of Au nanocrystals coated with a mixture of thiol and dithiol molecules [32]. Experiments with hydrosols of different metals by Thomas *et al*. offered a broad choice of inks [33]. Thus, nano-patterns of gold and palladium nanocrystals on substrates of mica and silicon were obtained. Each pattern consists of a collection of nanocrystals, several layers thick. The patterns are stabilized by weak interactions of the nanocrystals with mica surface. Colloids with magnetic (γ-Fe_2O_3) properties [34] were also patterned to exploit their specific functions. Magnetic force imaging performed on the drawn patterns indicated the weak magnetic nature of these nanocrystals.

The major challenges faced with the DPN technique are large area patterning with a good writing speed and supply of ink to the tip as it gets depleted. These problems have been circumvented in the recent years, by integrating several probes on a single chip capable of parallel writing and combining with microfluidic technology for replenishing inks [35]. Salaita *et al*. [36] demonstrated the use of such a parallel pen plotter for generating patterns in cm-scale areas. Since the technique is centered on the nature and resolution of the AFM probe, there have been many studies on the modification of the

probes to diversify its applications [37,38]. Another commendable development is the introduction of nano-fountain pen technology for DPN [39]. This technique uses a cantilever tip with an aperture (300 nm diameter) to dispense the ink and is integrated with ink reservoirs through microchannels and works independent of the humidity conditions.

6.2 Scope of the Present Investigation

The present chapter pertains to the study of nanopattern formation by DPN with a wide variety of inks and also the ink deposition process from tips of varying sizes.

Photoluminescent, nanocrystals of $LaPO_4$ doped with Eu^{3+} have been patterned on various substrates and the lateral diffusion of the colloid due to the interactions with the substrate is studied. Since the nanocrystals emit in the visible red region when illuminated by UV light, they have potential applications as security keys. Conduits of Au have been obtained on Si by DPN of a dilute HF solution of potassium tetrachloroaurate, which is extensively used for the controlled growth of Au(111) films on silicon [40,41]. Maynor *et al*. [25] and Porter *et al*. [42] have previously employed metal hydrochlorides to produce metal patterns on semiconductor surfaces. The use of metal chlorides need a stringent condition of bare Si surface (with no native oxide) for galvanic deposition. This is a difficult situation since DPN is performed in ambient conditions and oxide layer immediately forms on Si surface. We have found that a mixture of HF and $KAuCl_4$ function well even in the presence of surface oxide layer. Deposition of precursor compounds that can be transformed to important functional materials of nanoscale dimensions in a further simple treatment is also demonstrated. For example, zinc acetate nanopatterns were produced by DPN, which may be thermally decomposed to produce zinc oxide nanopatterns. Alternatively, ZnO nanocrystals could be patterned directly. ZnO nanomaterials find applications in gas sensor devices [43]. Among several ways to assemble nanocrystals, Au nanocrystals were assembled on DPN patterns of a bifunctional molecule, aminopropyl trimethoxy silane in a constructive fashion. In the context of patterning cell molecules and monitoring their growth under isolated conditions [44], DPN patterning of polylysine, which is generally used for

adsorbing cell molecules is successfully demonstrated. More interestingly, AFM tip is employed as a fountain pen to fill nanocrystals inside metal femtoliter metal cups.

The DPN technique holds the promise of integrating nano- and microelectronics, as it provides an opportunity of employing pens of different nib thicknesses. This becomes handy especially when large area patterning is attempted. A simple calculation by Schwartz has shown that the thiol molecules diffuse from the AFM tip at a rate of ~10^5 molecules/s, corresponding to a patterning time of 100 years/cm^2 [45]. In this context, tip modifications leading to both faster rates of deposition and well-controlled DPN features are highly desirable. Blunt tips of various sizes have been prepared by a simple method of laser ablation starting from a commercial tip. The DPN study employing blunt tips and Pd sol as the ink has given an insight into the ink deposition process from the tips of varying sizes.

6.3 Experimental Details

6.3.1 Preparation of inks for DPN

i) Nanocrystal synthesis

$LaPO_4:Eu^{3+}$: $LaPO_4$ nanocrystals doped with 5 mol% Eu were prepared by a hydrothermal method reported by Haase *et al* [46]. Lanthanum nitrate hexahydrate (5.7 mmol, 2.5 g) and europium nitrate pentahydrate (0.3 mmol, 0.13 g) were dissolved in water (20 mL) and poured into NaOH (1 M, 10 mL). To the well-stirred suspension, a solution of ammonium hydrogen phosphate (5.4 mmol, 1.78 g) in 10 mL water was added. The mixture was adjusted to pH 12.5 using 4 M NaOH and heated to 200 ºC for 2 hrs with stirring in a teflon-lined autoclave. The resulting suspension was centrifuged and the supernatant was discarded. The precipitate was suspended in 0.1 M HNO_3 for a few hrs to dissolve any lanthanum hydroxide formed. The pH was adjusted to 1.0 from time to time. The suspension was centrifuged and the colorless supernatant containing the by-products was discarded. Distilled water was added to the precipitate with stirring resulting in the peptization of the solid. The resulting milky colloid was centrifuged and the supernatant was collected. The peptization step was repeated 3-4 times and finally the combined supernatants were centrifuged to obtain a weakly opalescent colorless colloid containing the smallest nanocrystals.

ZnO: Colloidal ZnO was prepared by the spontaneous hydrolysis of zinc acetate in a polar basic aprotic solvent, dimethyl sulfoxide (DMSO) [47]. A 0.2 mM solution of zinc acetate in anhydrous DMSO with 3 % water was heated to 50 ºC for 20 min.

Au: Au nanocrystals were prepared by reducing a solution of $HAuCl_4$ and cetyl trimethyl ammonium bromide (CTAB) taken in the ratio Au:CTAB, 1:5, with sodium borohydride solution.

Pd: Pd nanocrystals capped with poly(vinylpyrrolidone) (PVP, M.W-40,000) were synthesized following the method of Teranishi *et al* [48]. H_2PdCl_4 solution (2 mM, 15 mL) in the presence of PVP (Pd:PVP mole ratio 1:10) was reduced with an aqueous ethanolic solution (20%, 35 mL) by refluxing for 3 hrs [49]. The nanocrystals were precipitated from the brownish black sol by adding ether, washed and redispersed in water.

ii) Preparation of precursor and molecular inks

$KAuCl_4$: A 5 mM solution of $KAuCl_4$ in 1 M HF [40] was employed for electroless deposition via DPN.

Zinc acetate: A freshly prepared 20 mM solution of zinc acetate dihydrate in deionized water or ethylene glycol was used.

APTMS: 5 μL of aminopropyl trimethoxy silane (APTMS) was dissolved in 5 mL HPLC grade methanol for DPN purpose.

Poly L-lysine: A 5% aqueous solution of poly L-lysine hydrobromide was used.

6.3.2 Preparation of substrate and design of markers

Freshly cleaved mica and silicon were used as substrates with and without the native SiO_x layer. Si was subjected to standard procedures of cleaning, first with acetone, followed by ethanol and deionized water and then few minutes in piranha solution, finally with deionized water. The oxide layer was stripped using dilute HF.

Prior to laying DPN patterns, guiding markers were set on the substrate, following a procedure developed in our laboratory [50]. These markers help to relocate the patterns for further characterization. Briefly, a TEM grid (type G200HS obtained from Ted Pella Inc., USA) with a strand width of 15 μm was placed on the Si substrate to act as a mask. A single laser shot of 100 mJ was fired on to the substrate, which left an impression on the exposed regions due to surface melting. SEM and AFM images of the grid pattern on

Si are given in Figure 6.1. The areas shadowed by the grid wire were utilized for performing DPN. The above method of laying markers on the substrate has a distinct advantage in that the substrate can be subjected to severe cleaning procedures without causing any damage to the markers themselves.

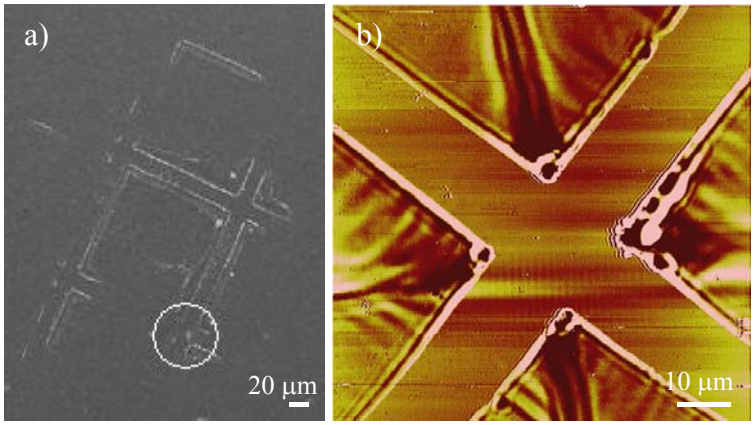

Figure 6.1. Markers formed on Si by laser ablation. a) SEM image of the grid pattern. b) AFM image of the marked region in (a).

6.3.3 Lithography

DPN experiments were carried out under ambient conditions (~20 °C, humidity ~35 – 50%) by employing a Nanoscope-IV controller attached with a Digital instruments multimode-head. Contact mode imaging was carried out in both normal and lateral force modes at different scan angles. Standard silicon nitride cantilevers were coated with ink by immersing them in the solution of desired ink followed by drying in nitrogen. A region of the substrate between the markers was chosen with the aid of the CCD camera.

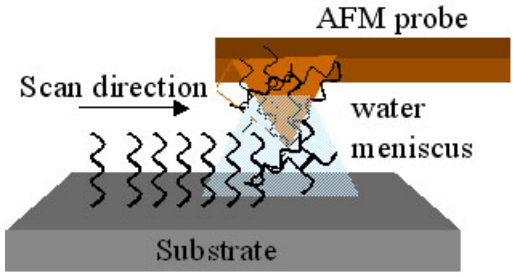

Figure 6.2. Schematic illustration of DPN. As the tip moves slowly across the substrate, the ink gets deposited by diffusion through water meniscus.

Line patterns were drawn by dragging the coated tip along a pre-defined area at a rate of 0.25 Hz. At such slow scan speeds, the water meniscus formed between the tip and the substrate will remain undisturbed and the nanocrystals get deposited on the hydrophilic surface by diffusion. A scan time of a few min was found to be necessary to make a well-defined pattern. A schematic of the DPN process is given in Figure 6.2. The patterns were imaged using a fresh cantilever tip. A photograph of the AFM set up is given in Chapter 2 (Figure 2.2)

6.3.4 Preparation of blunt tips

A frequency tripled Nd:YAG laser (Quanta-Ray GCR-170, Spectra-Physics, USA, λ = 355 nm) was operated in the Q-switch mode to generate laser pulses of width ~ 5 ns. The laser beam was directed with the aid of a CCD camera, towards the tip of the AFM cantilever through a 50 cm lens, such that the tip was slightly out of focus. A schematic of the set up is shown in Figure 6.3. Commercial silicon nitride tips (~40 nm diameter, Nanoprobes, Digital Instruments) were used for this study. The laser was operated in single shot mode. We tried out different laser energies (60-150 mJ/pulse) and varying number of shots in order to arrive at optimal conditions. Usually, a few shots of 60 mJ were found to be adequate to remove the material at the tip-nose and make them blunt. Since the beam spot size is large ~100 μm, in a few cases the cantilevers got bent or blew off. Following exposure to laser, the cantilevers were cleaned in methanol for further use in DPN.

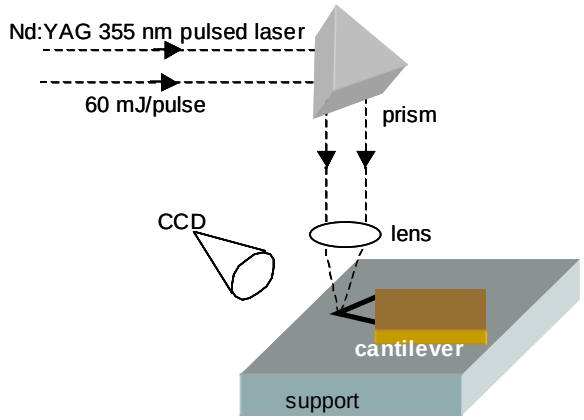

Figure 6.3. A schematic of the set up used for exposing the tip of an AFM cantilever towards laser.

6.3.5 Characterization

Transmission electron microscopic (TEM) measurements of nanocrystals were carried out with a JEOL 3010 TEM, operating at 300 kV. Samples for TEM were prepared by depositing a drop of the nanocrystals on a holey carbon copper grid. Room temperature fluorescence spectra of $LaPO_4:Eu^{3+}$ colloid and absorption spectra for ZnO was obtained using a Perkin-Elmer (LS50B) spectrophotometer.

The Nanospectroscopy Beamline at the synchrotron radiation facility Elettra in Trieste was employed for the characterization of the nanopatterns [51]. Electron beam-based techniques are ideal for such studies [52] in that they have a lateral resolution of 10 nm and atomic depth resolution. Low Energy Electron Microscopy (LEEM) is used to identify the patterns and X-ray Photo-Emission Electron Microscopy (XPEEM) was used to characterize the chemical identity of the patterns. In LEEM, a low energy electron beam (1–100 eV) is incident on the sample and the backscattered beam is used for imaging in the dark or bright field. In the XPEEM mode the sample is illuminated by monochromatic soft X-rays (20-1000 eV). This leads to the emission of a whole spectrum of photoelectrons with kinetic energies, from which electrons with a certain kinetic energy, for example, characteristic core or valence electrons, are used for imaging. In order to reduce surface charging, doped Si substrates were used. The DPN patterns were relocated at the beamline using the preformed markers.

High-resolution scanning electron microscopy of the laser-exposed tips was performed using a field emission SEM (Nova NanoSEM600, FEI, Netherlands) in the low vacuum mode in order to avoid charging of silicon nitride. In this mode, water vapor is leaked into the chamber at a pressure of 0.38 Torr and the imaging was done at 5 kV beam voltage employing ‘through the lens’ detector.

6.4 Results and Discussion

6.4.1 Nanopatterns by DPN

i) $LaPO_4:Eu^{3+}$ colloid

Figure 6.4a shows the TEM image of the nanocrystals of photoluminescent $LaPO_4:Eu^{3+}$ used for DPN. A high-resolution image (HRTEM) of an individual nanocrystal given in Figure 6.4b reveals the lattice spacing corresponding to $LaPO_4$

lattice. The nanocrystals have a prismatic shape and have diameters between 8-15 nm. In Figure 6.5, fluorescence spectra of the colloid at an excitation wavelength of 260 nm, is given. The prominent emissions are at 587 nm and 618 nm (red region). The spectrum is comparable with that reported in the literature [46]. The main emission lines in the spectra are due to $^5D_0$–^7F_J transitions in the europium levels. Inset shows an optical micrograph of the red emission from a drop of the colloid on a glass plate, when illuminated by UV light.

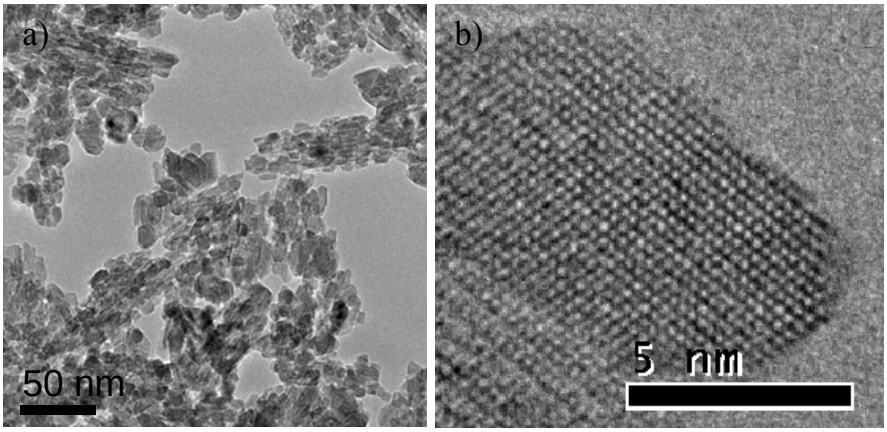

Figure 6.4. a) TEM image of $LaPO_4:Eu^{3+}$ nanocrystals revealing a distribution of particle size between 8-15 nm. b) HRTEM image of a single nanocrystal (d = 2.53 Å) showing the lattice planes and the crystalline nature.

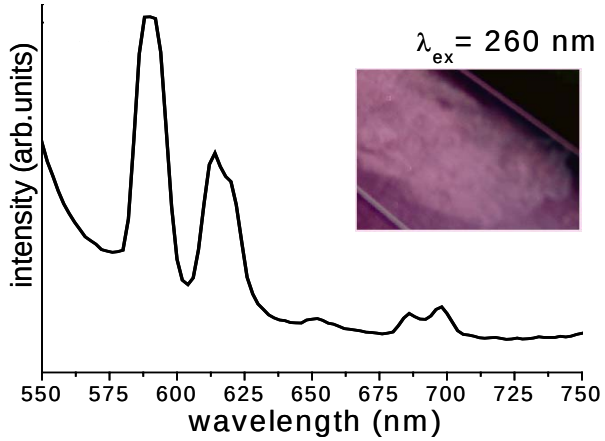

Figure 6.5. The fluorescence spectra of the nanocrystal colloid along with an optical micrograph showing red emission from the particles when excited by UV light.

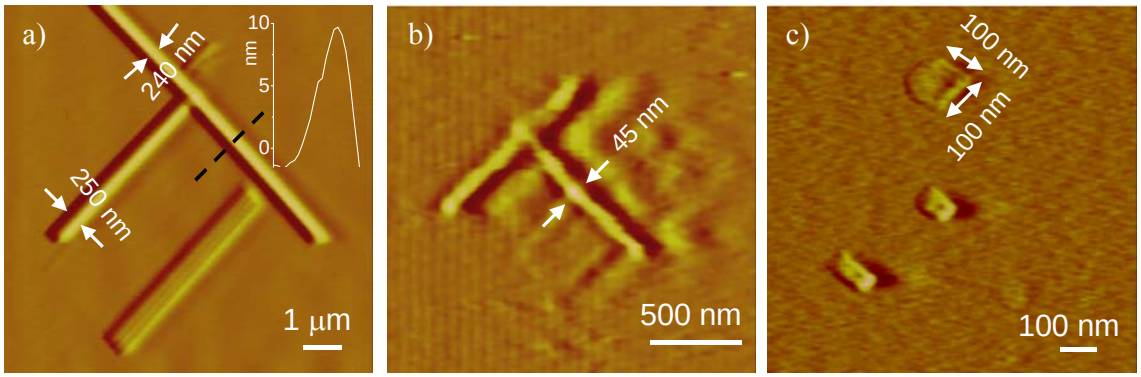

Figure 6.6. AFM topography of nanopatterns of $LaPO_4:Eu^{3+}$ colloid on mica formed by DPN. a) Line patterns of large aspect ratios with the height profile (inset) along the dashed line in the image. b) Patterns with smaller line width of 45 nm. c) Rectangular patterns with smaller aspect ratios.

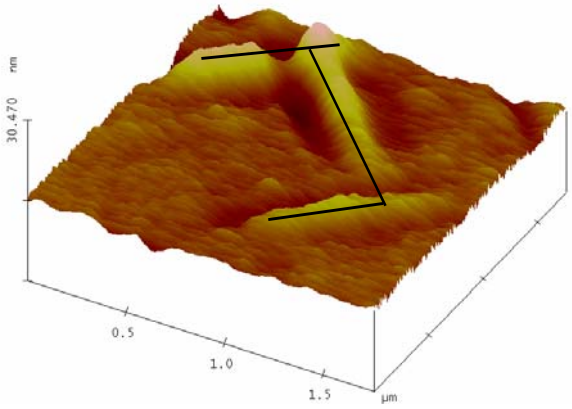

Figure 6.7. 3D AFM image of a nanopattern of luminescent colloid on mica forming the letter 'J'.

The luminescent colloid could be patterned on mica as well as on silicon substrates. Figure 6.6 shows the AFM image of DPN patterns of various aspect ratios on mica. Figure 6.6a shows an open ladder pattern comprising of two parallel 4.7 μm long lines of widths 250 and 500 nm and a perpendicular line of length 8 μm and width 240 nm. The height of the pattern estimated from the height profile as 9.7 nm given in the inset, corresponds to the diameter of nanocrystals. Hence the nanopattern consists of approximately a monolayer of nanocrystals. In Figure 6.6b are shown the line patterns with the smallest width obtained using a commercial silicon nitride tip of ~40 nm diameter. Rectangular patterns of smaller aspect ratios, 100 nm × 100 nm, 86 nm × 45 nm

and 110 nm × 50 nm are shown in Figure 6.6c. The spreading due to lateral diffusion of the aqueous colloid on mica can be clearly seen from the 100 nm × 100 nm pattern. A 3D topographical view of a letter 'J' written on mica using the luminescent colloid is given in Figure 6.7. The line width is 130 nm.

A grid type nanopattern formed on Si/SiO_x surface by DPN is given in Figure 6.8a. These patterns were characterized independently by electron beam-based techniques using synchrotron radiation [51,53]. They are ideal for such studies in that they have a lateral resolution of 10 nm and atomic depth resolution. In LEEM, a low energy electron beam is incident on the sample and the backscattered beam is used for imaging in the dark or bright field. The image of Figure 6.8b was acquired in the LEEM mode and the contrast arises from variation in topography. The LEEM image corresponds exactly with the AFM image. These studies were carried out typically a few weeks after patterning of the nanocrystals on Si surfaces with native oxide layers, demonstrating thereby that the patterns are robust.

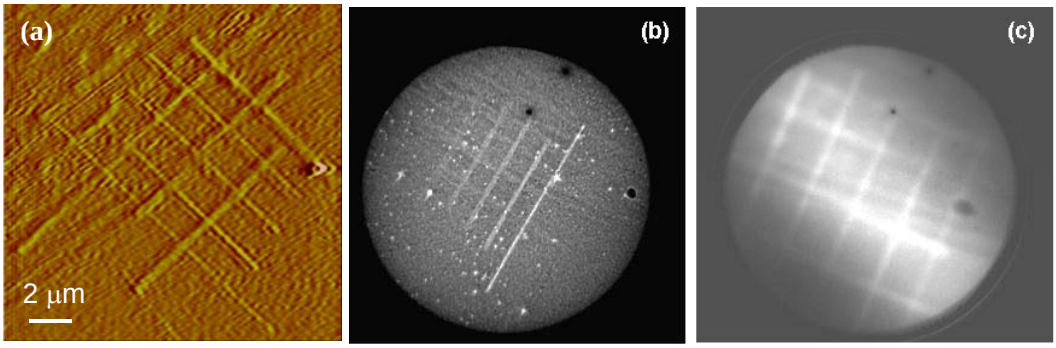

Figure 6.8. a) Topographic image of a grid pattern drawn on Si surface with fluorescent $LaPO_4$: Eu^{3+} nanocrystals. b) LEEM image of the pattern. The field of view is 20 μm. c) XPEEM image obtained by collecting secondary electrons. Field of view is 10 μm.

We have ascertained the chemical nature of the species by recording XPEEM images. The image in Figure 6.8c was obtained in X-ray absorption spectroscopy mode using secondary electrons for imaging. The image obtained with secondary photoelectrons corresponds exactly to the AFM image. However, core-level mapping was not successful because of a surface contamination of the sample.

ii) ZnO colloid

Figure 6.9a gives the TEM image of the ZnO nanocrystals obtained in DMSO. The size of the nanocrystals varies in the range 3-5 nm. The selected area electron diffraction

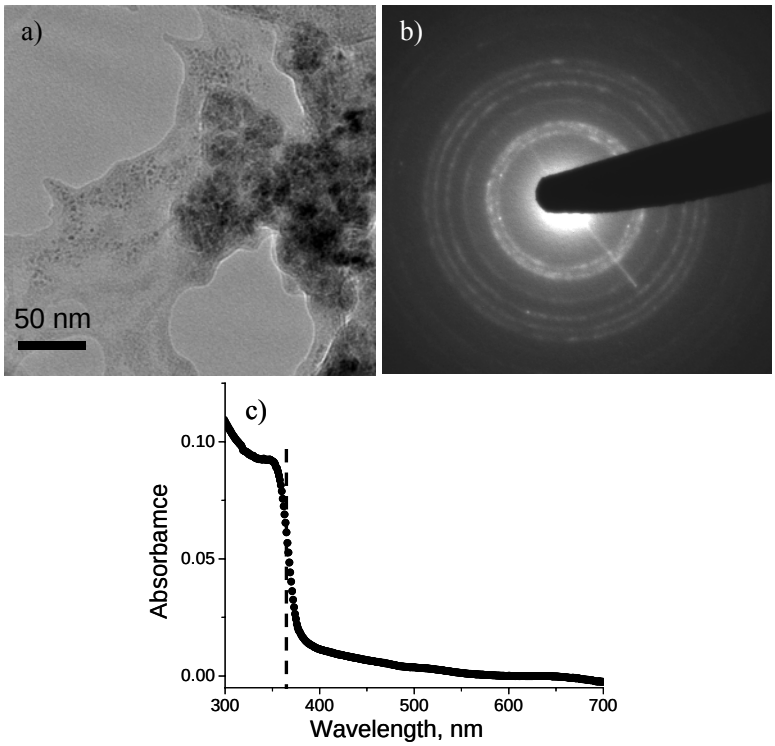

Figure 6.9. a) TEM image of ZnO-DMSO nanocrystal dispersion. b) Electron diffraction obtained from a collection of nanocrystals. c) UV absorption spectra of ZnO nanocrystals in DMSO.

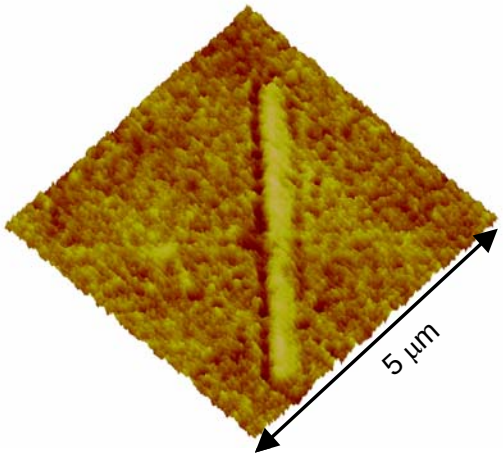

Figure 6.10. 3D AFM view of ZnO nanocrystal pattern on Si substrate.

pattern given in Figure 6.9b gives diffraction from (100), (101), (102), (110) and (112) planes of ZnO indicating the polycrystalline nature. The UV absorption spectra in Figure 6.9c show the typical band edge absorption at 360 nm [47]. DPN patterns of ZnO-DMSO nanocrystal dispersion could be obtained on Si/SiO_x substrate. A typical line pattern of width 450 nm is shown in Figure 6.10.

iii) Zinc acetate precursor

Another method of obtaining ZnO nanopatterns is to form patterns of zinc acetate, followed by heat treatment. As the first step, we have employed DPN to obtain patterns of zinc acetate on Si/SiO_x substrate. Figure 6.11a and b gives the AFM image of line patterns of various dimensions. The patterns could be relocated in SEM with the help of markers and the SEM image is given in Figure 6.11c. Earlier, Su *et al.* had utilized the hydrolysis of chlorides of Zn, Sn and Al to prepare their respective oxides by DPN [18].

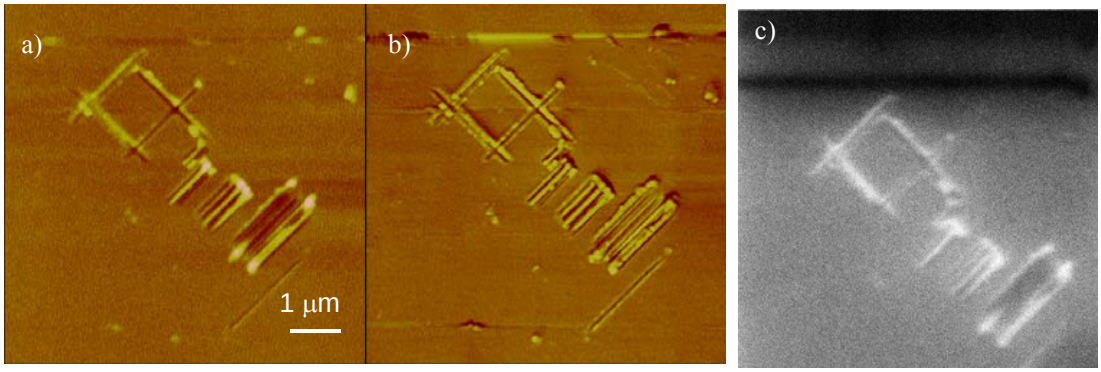

Figure 6.11. a) Tapping mode AFM image of zinc acetate nanopatterns. b) AFM image in phase mode. c) Relocated image in SEM.

iv) Potassium tetrachloroaurate precursor

We have used a mild HF solution of $KAuCl_4$ to produce nanopatterns of metallic Au on Si or Si/SiO_x substrate. When deposited on Si surface, it undergoes spontaneous galvanic reduction [40] to produce Au patterns. Unlike Liu's method [25] of using $HAuCl_4$ on etched Si and perform DPN within an hour of exposure to ambient, this method has the advantage that etching is not necessary and hence the patterning time is not limited with little effect on the efficiency of the electroless process. Figure 6.12 shows a few line patterns of Au of ~550 nm width. The height profile taken perpendicular

to the three line patterns reveals the mean height of Au as ~2 nm. Figure 6.13 shows AFM and SEM images of Au patterns obtained with smaller line widths, the smallest being achieved in our experiments was 60 nm.

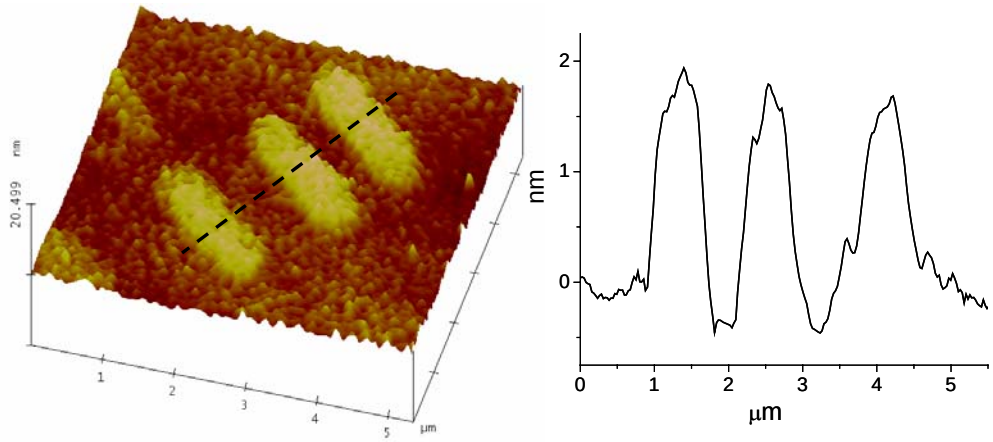

Figure 6.12. A 3D AFM view of the line patterns of Au obtained by DPN of $KAuCl_4$/HF on Si/SiO_x substrate. The height profile across the three line patterns is also given.

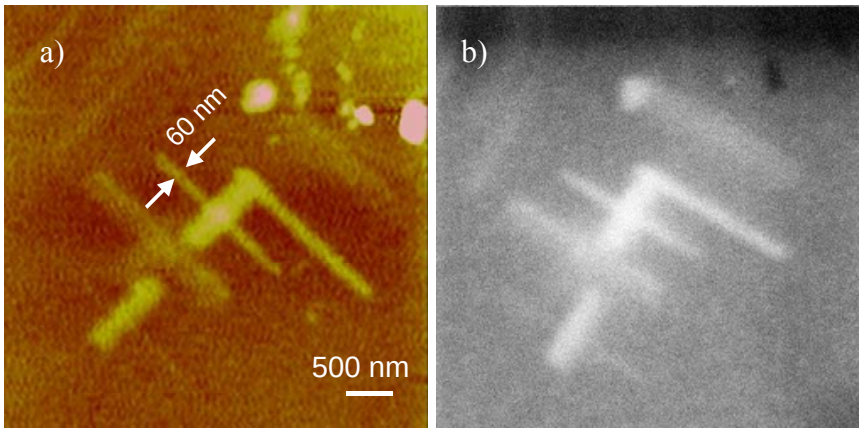

Figure 6.13. a) AFM image of Au patterns on Si with smaller line widths. b) Relocated SEM image.

v) Constructive lithography

A bifunctional molecule, APTMS was patterned by DPN and employed it for assembling nanocrystals. During DPN, the silane group of APTMS binds to the native oxide on the silicon surface and the amino group of the molecule will be free. Hence it was utilized to adsorb Au NCs capped with CTAB and finally these nanocrystals were

used as nucleation centers for further metallization in presence of $HAuCl_4$ and hydroxylamine solution. Constructive lithography has been demonstrated for the first time by Sagiv and co-workers, by adsorbing silver salt on a bifunctional molecular system, followed by reduction reaction to produce Ag patterns [54].

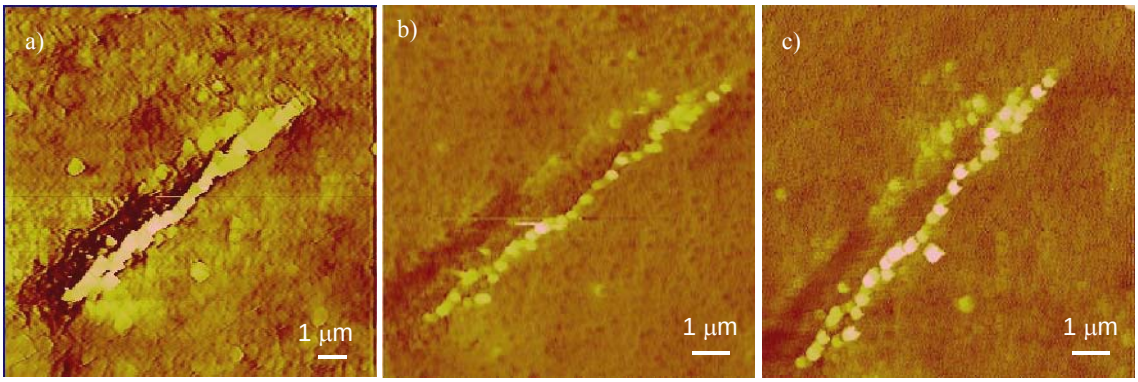

Figure 6.14. a) AFM topography of a line pattern of APTMS on Si/SiO_x produced by DPN. b) The same line pattern after Au-CTAB nanocrystal adsorption and wash. c) (b) after electroless deposition with $HAuCl_4/NH_4OH$ solution and wash.

In Figure 6.14, the results of this sequential assembly are shown. All the AFM images were obtained by relocating with a fresh tip after washing the substrate in each adsorption step to remove unadsorbed material. DPN pattern of a 10 μm long, ~350 nm width, APTMS line on Si/SiO_x is shown in Figure 6.14a. The mean height of the pattern is 26 nm, which reveals that several layers of molecules are adsorbed that remains even after washing. This indicates a lot of nonspecific adsorption of APTMS on the surface along with chemical binding. Figure 6.14b gives the status of APTMS line after adsorption with Au-CTAB nanocrystals (polydisperse, diameter range 5-20 nm). For this, the whole substrate was dipped in the nanocrystal solution for 30 min. From the AFM image, one can clearly see that the nanocrystals got adsorbed on the pattern. But the line width got reduced to 190-220 nm and height varies from 50 nm (the highest point) to 25 nm (the lowest point). Hence, although particles got adsorbed there is no apparent height increase in some regions. This might be due to the removal of nonspecifically bound APTMS, when they bind to Au NCs that ultimately goes into the solution. After nanocrystal adsorption, the substrate was dipped in a solution of $HAuCl_4/NH_4OH$ solution for 30 min,

capable of electroless deposition of Au. Figure 6.14c show that the Au NCs have grown laterally, increasing the line width to 300-350 nm. Along the line, it can be noticed that the lateral growth has resulted in improving the connectivity of the particles. The rise in the height of the line pattern after electroless deposition is very less and is in the range ~28-42 nm.

vi) Poly L-lysine

For biological applications, nanopatterns of polylysine were produced on silicon with native oxide layer and coverglass by DPN. Figure 6.15 shows the AFM images of the patterns. Here, the electrostatic interaction between positively charged polyL-lysine and negatively charged SiO_2 helps in obtaining robust patterns.

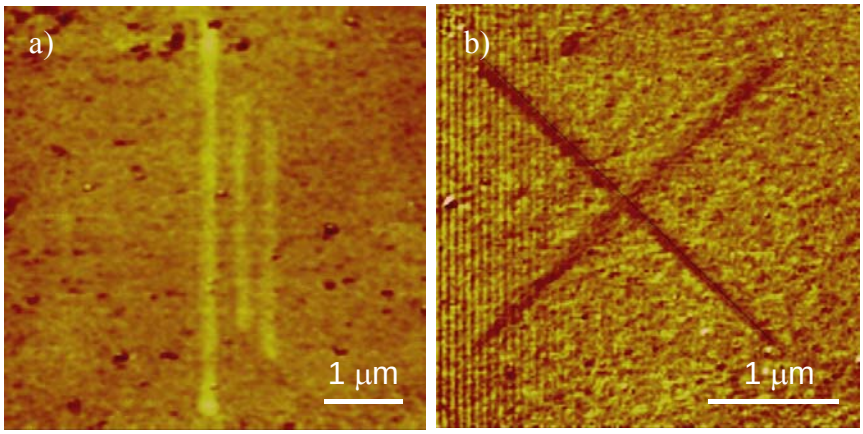

Figure 6.15. AFM images of DPN patterns of polyL-lysine on a) Si/SiO_x substrate, topography, line width 150 nm. b) Coverglass, LFM mode, line width 50 nm.

vii) DPN inside femtoliter metal cups

DPN has been used to fill metal cups. The cups with femtolitre capacity were prepared by a laser ablation technique, as described in the previous chapter. In this experiment, Ag cups were deposited on to a Si substrate with predefined markers and adsorbed with octanedithiol molecules. Following this, a silicon nitride tip soaked in citrate stabilized Au NCs (mean size ~20 nm) was positioned inside the cup and held typically for 15 min. The filled cups were relocated with the help of markers using a fresh tip. Figure 6.16 shows the AFM image of the Ag cup filled with Au NCs. The height

profiles alongside show an increase in the height at the center of the cup by ~20 nm following deposition of nanocrystals.

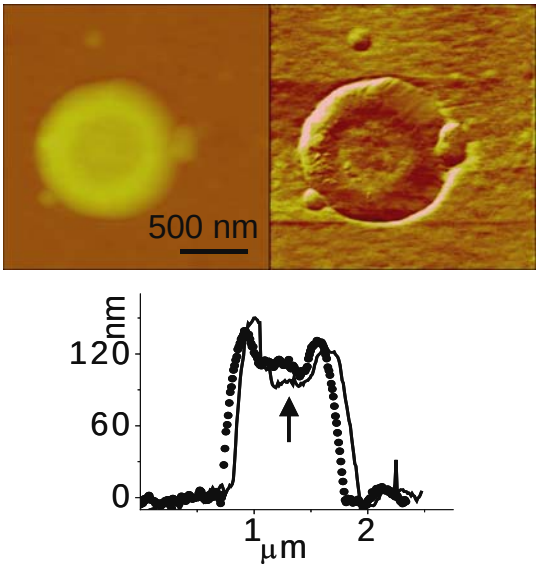

Figure 6.16. AFM and LFM images of an Ag cup functionalized with octanedithiol molecules followed by dip pen lithography of Au NCs in the bore region. The height profile after DPN (dotted line) is raised in the center than before DPN (solid line), showing pick up of nanocrystals in the cup (see arrow).

6.4.2 DPN using pens of different thicknesses

AFM tips of varying bluntness were prepared by ablating the commercially available silicon nitride tips employing laser pulses of different energy, as described in Section 6.3.4. In Figure 6.17 are shown, SEM images of the AFM tips subjected to laser shots, along with that of an as-supplied tip. In contrast to the sharpness of tip in Figure 6.17a, the eroded regions of tips exposed to laser is clearly evident in Figures 6.17b and c. It appears that the laser energy pounds on the tip giving rise to a square-like cross section of its pyramidal shape (as marked by dashed lines in the figure). Accordingly, the tip dimension has increased from less than 40 nm (Figure 6.17a), to ~250 nm × 270 nm and ~400 nm × 500 nm (Figures 6.17b and c) following exposure to single and couple of shots of 60 mJ, respectively. The pronounced rectangular cross-section in the Figure 6.17c might be due to an inclined angle at which tip was exposed to laser.

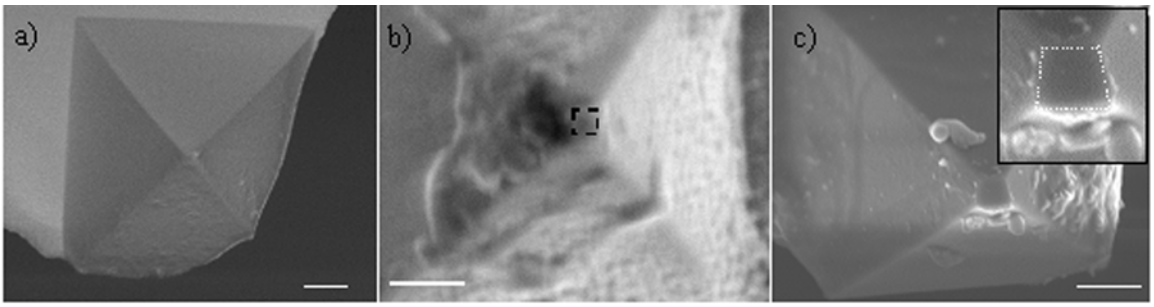

Figure 6.17. FESEM images of AFM tips. a) As-supplied b) Exposed to a 60 mJ laser shot and c) Exposed to a few shots. Inset shows a closer view of the blunt tip. The eroded region is marked. The particulates seen on the tips in b and c are aggregates of Pd-PVP nanocrystals from the ink used for DPN. Scale bar-1μm.

In order to demonstrate the variation in tip size and study the ink diffusion from blunt tips, we performed DPN employing the above-mentioned laser exposed tips. The ink used was an aqueous colloid of PVP capped Pd and the substrate, hydrophilic Si/SiO_x. While performing DPN with different tips, parameters such as scan rate (0.25 Hz), humidity (45±2%) and temperature (22±1 ºC) were maintained constant so that the pattern dimensions depend solely on the diameter of the tip. In Figure 6.18, we have shown AFM images of typical DPN patterns filled with Pd-PVP nanocrystals, using the blunt tips. The pattern obtained with the 60 nm tip has a line width of 90 nm (Figure 6.18a) while that with 400 nm wide tip has a much wider line width of 390 nm (Figure 6.18b), as illustrated by the line profile analysis shown below. While the lengths of the patterns correspond to the pre-defined values, 3 μm and 2 μm respectively, the widths are clearly related to the tip contact areas. In the case of narrower line widths, a gradation in the height profile is noticeable (Figure 6.18a). Several such line patterns were drawn using these tips. Similarly, tips bearing intermediate dimensions of 150 nm and 250 nm were also prepared and subjected to DPN (Figure 6.19a and b). All the images shown are patterns relocated with a fresh tip.

The dimensions of the patterns obtained with different tips are given in Table 6.1 along with the corresponding pre-defined values and the scan duration. We readily observe from Table 6.1 that for a given tip, the obtained line widths are varied, often higher than the tip dimension itself. A variation in the line widths for repeated

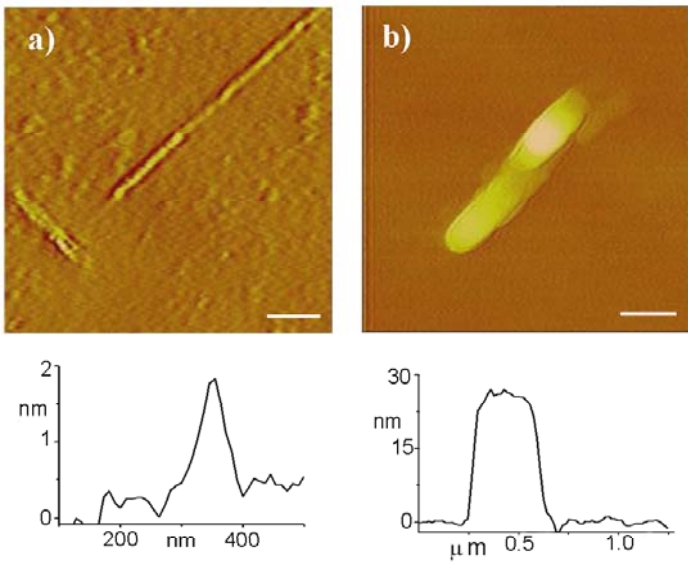

Figure 6.18. AFM topography of DPN patterns of Pd-PVP on Si obtained with probes of different dimensions a) ~60 nm. c) ~400 nm. Height profiles across the patterns are shown below. Scale bar-500 nm.

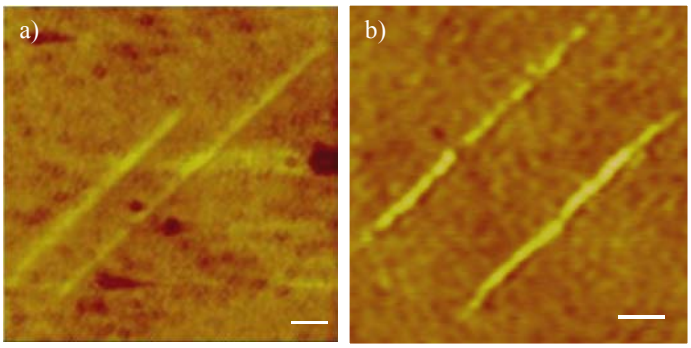

Figure 6.19. AFM topography of DPN patterns obtained with probes of size a) 150 nm b) 250 nm. Scale bar-500 nm.

experiments has been reported in earlier experiments with alkanethiols [14,45]. The lengths also show similar variations, sometimes being even smaller than the pre-set value. The thickness of the depositions did not show a clear dependence on the scan duration, although higher durations and larger tips yielded patterns with higher thicknesses. The increase in the feature size is in accord with earlier experiments involving alkanethiols, where in an increase in the dot size was achieved by employing higher contact times [13,55,56]. The DPN process mainly involves two steps- transport of ink from AFM tip

to the substrate and surface diffusion on the flat substrate [57]. It appears that molecules, which bind strongly to the substrate, diffuse less [58] compared to those that bind weakly [59]. Even the strongly bound ones diffuse to some extent creating a halo around the pattern especially with a dull tip [55]. Such a spreading of the pattern was also found in this study, especially at higher scan durations.

Table 6.1. DPN patterns obtained with different tips.

Tip dimension (nm × nm)	Pre-defined length (μm)	Scan duration (min)	DPN pattern dimension Length (μm)	width (nm)	height (nm)
as-supplied tip	0.75	10	0.728	50	3.5
	0.75	10	0.728	50	9.5
	0.1	10	0.095	58	5
60 × 60	1	7	0.95	77	2
	3	10	3	90	2
	1	12	1	60	2
150 × 150	5	15	4.9	156	5.4
	3	15	3.1	167	3.8
	2	15	1.9	148	2.9
	1	18	1	162	3.4
	2	5	2	206	2.9
250 × 270	5	10	5	273	2
	3	10	3.1	253	2
	5	5	5.3	215	2.3
	3	5	3.35	273	4
400 × 500	2	18	1.9	390	24.5
	1	7	1.16	405	2.5
	2	7	1.6	500	3.6
	2	18	1.8	400	7.8
	3	5	2.85	445	3
	1	5	1.1	512	2

The rate of deposition of the ink is estimated from the volume of the deposited pattern and the scan duration. Here, the thickness of the patterns is included in the calculation, unlike earlier reports where only lateral dimensions were considered [14,66]. The estimated values from different tips are plotted against the widths of the patterns in Figure 6.20. We observe from Figure 6.20 that the rate of deposition is typically small for tips of smaller dimensions while it increases gradually as the tip dimension increases, accompanying a greater spread in both the rate of the deposition and the width of the patterns. Jang *et al*. [58] have reported that a slower deposition rate yields narrower line widths. From the plot in Figure 6.20b, we see that the mean deposition rate exhibits a

linear increase initially with increase in the tip contact area but seem to level off for higher contact area. It appears that the transfer of ink through diffusion becomes less effective at larger contact areas. In other words, the ink flow may be restricted to mainly the periphery of the flattened tip with the middle region (see inset of Figure 6.17c) remaining passive, once the initial meniscus is formed. This is clear from the plot in Figure 6.20c where the rate of deposition per unit area of the tip is similar for tips of smaller dimensions while drops considerably for the larger tip.

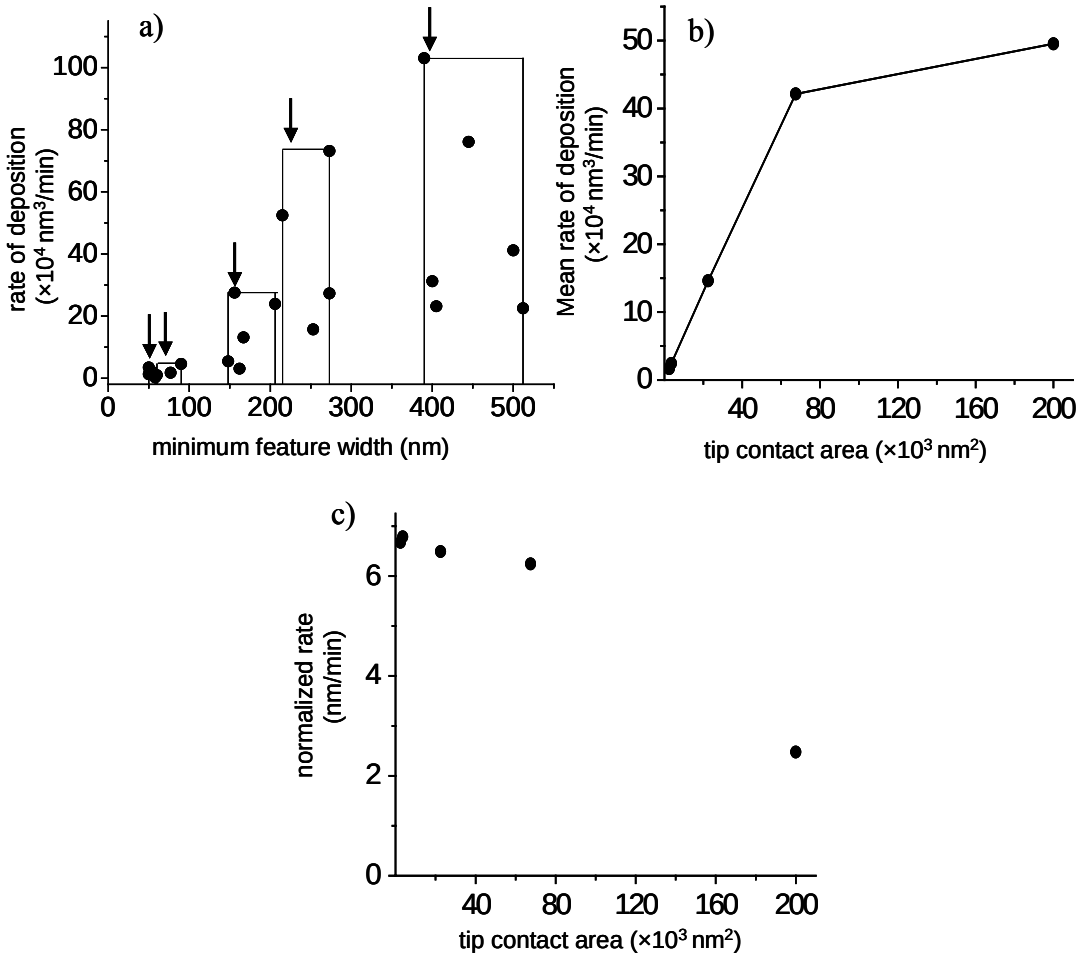

Figure 6.20. (a) Rate of deposition of the colloidal ink versus the widths of the patterns obtained. Boxes enclose data points from the different tips. The arrows indicate the minimum feature size obtained with a particular tip and it corresponds to the tip dimension. (b) The variation of the mean rate of deposition with the tip contact area. (c) The normalized (with respect to tip contact area) mean rate of deposition vs. the tip contact area.

6.5 Conclusions

A versatile DPN method is demonstrated for patterning a wide range of inks on various substrates. Patterns of luminescent $LaPO_4:Eu^{3+}$ nanocrystals and also ZnO nanocrystals have been achieved with widths ranging from 45 to 500 nm and different aspect ratios to form rectangles, squares or lines, on various substrates such as mica and silicon. The patterns are stabilized by weak physisorption and yield well-resolved LEEM and XPEEM images. The patterning of zinc acetate and potassium tetrachloroaurate in mild HF has also been demonstrated that can act as precursors for obtaining ZnO and Au patterns, respectively. In this manner, Au conduits of widths in the range 60-550 nm and lengths of several microns with 2 nm thickness could be obtained on Si. DPN patterns of a bifunctional molecule, APTMS have been utilized for assembling Au nanocrystals to obtain nanocrystal line patterns of ~200 nm width and 50 nm height. Further metallization by electroless deposition, using nanocrystals as nucleation centers resulted in improving the lateral connectivity between them. Line patterns of polyL-lysine molecules with 50 and 150 nm widths have been achieved and have the potential as anchors for cells. DPN has also been employed to fill metal cups of femtoliter capacity with nanocrystals, following functionalization with dithiol molecules.

In order to make DPN useful for patterning from macro to micro to nano, AFM probes of different sizes were prepared. A simple method of exposing AFM probes to high-energy nanosecond laser pulses was adopted. Thus, starting with commercial tips of ~40 nm diameter, tips with lateral dimensions of ~150, 250 and 400 nm were successfully prepared by exposing to increasing number of laser shots. The tips when utilized for DPN using a Pd sol (mean, ~2 nm), produced line patterns characteristic of their dimensions. A comparison of the rate of deposition of the ink with different probe sizes is also presented. It was observed that the rate of deposition of the ink increased with the tip dimension, from 40 to 250 nm, but for the 400 nm wide tip, the deposition per unit contact area decreased as ink diffusion was limited to only the periphery of the tip.

References

[1] C. A. Mirkin & J. A. Rogers, Eds., *MRS Bull.,* 506, (**2001**).

[2] C. N. R. Rao, G. U. Kulkarni, P. J. Thomas & P. P. Edwards, *Chem. Eur. J.*, 8, 30 (**2002**).

[3] C. N. R. Rao & A. Govindaraj, *Nanotubes and Nanowires*, The royal society series in nanoscience, London (**2005**).

[4] A. Batchtold, C. Dekker, P. Hadley & T. Nakanishi, *Science*, 294, 1317 (**2001**).

[5] D. Long, C. H. Patterson, M. H. Moore, D. S. Seferos, J. G. Kushermerick & G. C. Buzan, *Appl. Phys. Lett*., 86, 153105 (**2005**).

[6] C. -H. Oon & J. T. L. Thong, *Nanotechnology*, 15, 687 (**2004**).

[7] G. L. –T. Chin, *IBM J. Res. Dev.*, 41, 3 (**1997**)

[8] C. R. K. Marrian & D. M. Tennant*, J. Vac. Sci. Technol. A,* 21, S207 (**2003**).

[9] B. D. Gates, Q. Xu, M. Stewart, D. Ryan, C. G. Wilson & G. M. Whitesides, *Chem. Rev.*, 105, 1171 (**2005**).

[10] R. Garcia, R. V. Martinez & J. Martinez, *Chem. Soc. Rev.*, 35, 29 (**2006**).

[11] D. Wouters & U. S. Schubert, *Angew. Chem. Int. Ed.*, 43, 2480 (**2004**).

[12] D. S. Ginger, H. Zhang & C. A. Mirkin, *Angew. Chem. Int. Ed.*, 43, 30 (**2004**).

[13] R. D. Piner, J. Zhu, F. Xu, S. Hong & C. A. Mirkin, *Science*, 283, 661 (**1999**).

[14] S. Rozhok, R. D. Piner & C. A. Mirkin, *J. Phys. Chem. B*, 107, 751 (**2003**).

[15] M. Su, Z. Pan, V. P. Dravid & T. Thundat, *Langmuir*, 21, 10902 (**2005**).

[16] A. Ivanisevic & C. A. Mirkin, *J. Am. Chem. Soc*., 123, 7887 (**2001**).

[17] G. S. Metraux, Y. C. Cao, R. Jin & C. A. Mirkin, *Nano Lett.*, 3, 519 (**2003**).

[18] M. Su, X. Liu, S. –Y. Li, V. P. Dravid & C. A. Mirkin, *J. Am. Chem. Soc.*, 124, 1560 (**2002**).

[19] M. Su, S. Li & V. P. Dravid, *J. Am. Chem. Soc.*, 125, 9930 (**2003**).

[20] L. Fu, X. Liu, Y. Zhang, V. P. Dravid & C. A. Mirkin, *Nano Lett*., 3, 757 (**2003**).

[21] L. Ding, Y. Li, H. Chu, X. Li & J. Lin, *J. Phys. Chem. B*, 109, 223337 (**2005**).

[22] A. Noy, A. E. Miller, J. E. Klare, B. L. Weeks, B. W. Woods & J. J. Deyoreo, *Nano Lett*., 2, 109 (**2002**).

[23] M. Su, M. Aslam, L. Fu, N. Wu & V. P. Dravid, *Appl. Phys. Lett.*, 84, 4200 (**2004**).

[24] Y. Li, B. W. Maynor & J. Liu, *J. Am. Chem. Soc.*, 123, 2105 (**2001**).

[25] B. W. Maynor, Y. Li & J. Liu, *Langmuir*, 17, 2575 (**2001**).

[26] P. E. Sheehan, L. J. Whitman, W. P. King & B. A. Nelson, *Appl. Phy. Lett.*, 85, 1589 (**2004**).

[27] J. –H. Lim, D. S. Ginger, K. –B. Lee, J. Heo, J. –M. Nam & C. A. Mirkin, *Angew. Chem. Int. Ed.*, 42, 2309 (**2003**).

[28] J. –M. Nam, S. I. Stoeva & C. A. Mirkin, *J. Am. Chem. Soc.*, 126, 5932 (**2004**).

[29] J. Li, C. Lu, B. Maynor, S. Huang & J. Liu, *Chem. Mater.*, 16, 1633 (**2004**).

[30] S. –W. Chung, D. S. Ginger, M. W. Morales, Z. Zhang, V. Chandrasekhar, M. A. Ratner & C. A. Mirkin, *Small*, 1, 1 (**2005**).

[31] M. B. Ali, T. Ondarcuhu, M. Brust & C. Joachim, *Langmuir*, 18, 872 (**2002**).

[32] J. C. Garno, Y. Yang, N. A. Amro, S. C-. Dupeyrat, S. Chen & G. -Y. Liu, *Nano Lett.*, 3, 389 (**2003**).

[33] P. J. Thomas, G. U. Kulkarni & C. N. R. Rao, *J. Mater. Chem.*, 14, 625 (**2004**).

[34] G. Gundiah, N. S. John, P. J. Thomas, G. U. Kulkarni, C. N. R. Rao & S. Heun, *Appl. Phys. Lett.*, 84, 5341 (**2004**).

[35] B. Rosnera, T. Duenasb, D. Banerjeeb, R. Shileb, N. Amroa & J. Rendlena, *Proc. of SPIE*, 5275, 213 (**2004**).

[36] K. Salaita, S. W. Lee, X. Wang, L. Huang, T. M. Dellinger, C. Liu & C. A. Mirkin, *Small*, 1, 940 (**2005**).

[37] K. –H. Kim, N. Moldovan, C. Ke, H. D. Espinosa, X. Xiao, J. A. Carlisle & O. Auciello, *Small*, 1, 866 (**2005**).

[38] X. Wang, K. S. Ryu, D. A. Bullen, J. Zou, H. Zhang, C. A. Mirkin & C. Liu, *Langmuir*, 19, 8951 (**2003**).

[39] K. -H. Kim, C. Ke, N. Moldovan & H. D. Espinosa, *Proc. of Society of Experimental Mechanics Annual Conference*, Charlotte, USA, 235, (**2003**).

[40] Bhuvana & G. U. Kulkarni, *Bull. Mater. Sci.*, 29, 505 (**2006**).

[41] I. B. Krileshlopaitis & Z. P. Kudzhmauskaiti, *Elektrokhimiya*, 7, 1679 (**1971**).

[42] L. A. Porter, Jr., H. C. Choi, J. M. Schmeltzer, A. E. Ribbe, L. C. C. Elliot & J. M. Buriak, *Nano Lett.*, 2, 1369 (**2002**).

[43] Z. L. Wang, *J. Phys.: Condens. Matter*, 16, R829 (**2004**).

[44] H. G. Craighead, C. D. James & A. M. P. Turner, *Curr. Opin. Solid Stat. Mater. Sci.*, 5, 177 (**2001**).

[45] P. V. Schwartz, *Langmuir*, 18, 4041 (**2002**).

[46] H. Meyssamy, K. Riwotzki, A. Kornowski, S. Naused & M. Haase, *Adv. Mater.*, 11, 840 (**1999**).

[47] G. R-. Gattorno, P. S-. Jacinto, L. R-. Vázquez, J. Németh, I. Dékány & D. Díaz, *J. Phys. Chem. B*, 107, 12597 (**2003**).

[48] T. Teranishi & M. Miyake, *Chem. Mater.*, 10, 54 (**1998**).

[49] P. J. Thomas, G. U. Kulkarni & C. N. R. Rao, *J. Phys. Chem. B*, 105, 2515 (**2001**).

[50] T. Vijaykumar, N. S. John & G. U. Kulkarni, *Solid State Sci*., 7, 1475 (**2005**).

[51] A. Locatelli, A. Bianco, D. Cocco, S. Cherifi, S. Heun, M. Marsi, A. Pasqualetto & E. Bauer, *J. Phys. IV*, 104, 99 (**2003**).

[52] M. Lazzarino, S. Heun, B. Ressel, K. C. Prince, P. Pingue & C. Ascoli, *Appl. Phys. Lett.*, 81, 2842 (**2002**).

[53] T. Schmidt, S. Heun, J. Slezak, J. Diaz, K. C. Prince, G. Lilienkamp & E. Bauer, *Surf. Rev. Lett.*, 5, 1287 (**1998**).

[54] R. Maoz, E. Frydman, S. R. Cohen & J. Sagiv, *Adv. Mater.*, 12, 424 (**2000**).

[55] P. E. Sheehan & L. J. Whitman, *Phys. Rev. Lett.*, 88, 156104 (**2002**).

[56] B. L. Weeks, A. Noy, A. E. Miller & J. J. De Yoreo, *Phys. Rev. Lett.*, 88, 255505 (**2002**).

[57] N. Cho, S. Ryu, B. Kim, G. C. Schatz & S. Hong, *J. Chem. Phys.*, 124, 024714 (**2006**).

[58] J. Jang, S. Hong, G. C. Schatz & M. A. Ratner, *J. Chem. Phys.*, 115, 2721 (**2001**).

[59] P. Manandhar, J. Jang, G. C. Schatz, M. A. Ratner & S. Hong, *Phys. Rev. Lett.*, 90, 115505 (**2003**).

LIST OF PUBLICATIONS

1. **Self-Assembled Hybrid Bilayers of Palladium Alkanethiolates,** Neena Susan John, P. John Thomas, and G. U. Kulkarni, *J. Phys. Chem. B* 2003, 107, 11376.
2. **Deposition of a Metal-Organic Heterostructure to Form Magnetic-Nonmagnetic Bilayer Films**, Sudipta Pal, Neena Susan John, P. John Thomas, G. U. Kulkarni, and Milan K. Sanyal, *J. Phys. Chem. B* 2004, 108, 10770.
3. **Gold-Coated Conducting-Atomic Force Microscopy Probes**, Neena Susan John and G. U. Kulkarni, *J. Nanosci. Nanotech.* 2005, 5, 587.
4. **Formation of a Rectifier with Gold Nanoclusters: X-ray Rreflectivity and Atomic force Microscopy Measurements**, S. Pal, M. K. Sanyal, Neena S. John, G. U. Kulkarni, *Phys. Rev. B* 2005, 71, 121404(R).
5. **A Resistless Photolithography Method for Robust Markers and Electrodes**, T. Vijaykumar, Neena Susan John, G. U. Kulkarni, *Solid State Sci.* 2005, 7, 1475.
6. **Dip-pen Nanolithography Using Colloidal Inks**, Neena Susan John, Gautam Gundiah, P. John Thomas, G. U. Kulkarni and S. Heun, *Int. J. Nanosci.* 2005, 4, 921.
7. **Aromaticity in Stable Tiara Nickel Thiolates: Computational and Structural Analysis**, A. Datta, Neena S. John, G. U. Kulkarni, and S. K. Pati, *J. Phys. Chem. A* 2005, 109, 11647.
8. **A Facile Method for the Production of Femtoliter Metal Cups by Pulsed Laser Ablation**, Neena Susan John, N. R. Selvi, Rama Govindarajan and G. U. Kulkarni, *J. Phys. Chem. B* 2006, 110, 22975.
9. **Dip-pen Lithography Using Pens of Different Thicknesses**, Neena Susan John and G. U. Kulkarni, *J. Nanosci. Nanotech.* 2007, 7, 977.
10. **Magnetic Interactions in Layered Nickel Alkanethiolates**, Neena Susan John, G. U. Kulkarni, A. Datta, S. K. Pati, F. Komori, C. Narayana, G. Kavitha and M. K. Sanyal, *J. Phys. Chem. C* 2007, 111, 1868.
11. **Gravity-Free Hydraulic Jumps and Femtoliter Metal Cups**, Manikandan Mathur, Ratul Dasgupta, N. R. Selvi, Neena Susan John, G. U. Kulkarni and Rama Govindarajan, *Phys. Rev. Lett*. 2007 (in press).

12. **Transformation of Femtoliter Metal Cups to Oxide cups- Chemical Mapping by Scanning Auger Spectroscopy**, Neena Susan John, N. R. Selvi, G. U. Kulkarni, S. Heun, E. Cavaliere, M. Fanetti, I. Kholmanov, L. Gavioli and M. Sancrotti, *Appl. Phys. A* 2007 (in press).
13. **A Conducting-AFM Study of Electronic Transport in Bilayer Assemblies of Palladium Alkanethiolates**, Neena Susan John and G. U. Kulkarni, - submitted.
14. **Solventless Thermolysis Method for Producing Pd Nanocrystals and Pd Films from Pd-alkanethiolate Bilayers,** Neena Susan John, Bhuvana and G. U. Kulkarni (under preparation)

Other Publications

1. **Dip-pen Nanolithography with Magnetic Fe_2O_3 Nanocrystals**, Gautam Gundiah, Neena Susan John, P. John Thomas, G. U. Kulkarni, and C. N. R. Rao, S. Heun, *Appl. Phys. Lett.* 2004, 84, 5341.
2. **Nature and Electronic Properties of Y-junctions in CNTs and N-doped CNTs Obtained by the Pyrolysis of Organometallic Precursors**, F. L. Deepak, Neena Susan John, A. Govindaraj, G. U. Kulkarni, C. N. R. Rao, *Chem. Phys. Lett.* 2005, 411, 468.
3. **Pyramidal Nanostructures of Zinc Oxide**, S. Angappane, Neena Susan John and G. U. Kulkarni, *J. Nanosci. Nanotech.* 2006, 6, 101.